Universidade do Minho
I3Bs - Instituto de Investigação em Biomateriais, Biodegradáveis e Biomiméticos

Bárbara Bruna da Silva Mendes

Micro/Nano-structured hydrogels based on platelet lysate for tissue engineering and regeneration

Junho de 2020

Micro/ Nano-structured hydrogels based on platelet lysate for tissue engineering and regeneration

Bárbara Mendes

UMinho | 2020

Universidade do Minho

I3Bs - Instituto de Investigação em Biomateriais, Biodegradáveis e Biomiméticos

Bárbara Bruna da Silva Mendes

Micro/Nano-structured hydrogels based on platelet lysate for tissue engineering and regeneration

Tese de Doutoramento

Doutoramento em Engenharia de Tecidos, Medicina Regenerativa e Células Estaminais

Trabalho efetuado sob a orientação de

Prof. Doutora Maria Manuela Estima Gomes

Doutor Rui Miguel de Andrade Domingues

Junho de 2020

ACKNOWLEDGMENTS

In my first class of the PhD program, the lecturer said: “Throughout your PhD you will not change the world. You will only get a driver license to work on science”. Indeed, the PhD is such a journey in which you always need to learn how to go in the right direction, the same way you need while driving a car. You need to use the brakes and speed as needed. As is common in Europe, you need to choose the right manual gear. But, as a young and ambitious person, you always want to work fast so that everything will happen. You only want to use the highest gear. But sometimes, the other cars are in a different gear, so you need to adapt your speed. This is a process in continuous learning and making decisions to successfully get your driver license.

I want to thank all of those that were able to show me the right directions, the green lights, and that at every pit stop helped me with a refill of energy, wisdom and kindness. You truly were my map towards success.

Ortiga, June 1st 2020

The funding contribution of ‘Fundação para a Ciência e Tecnologia’ is truly appreciated through my PhD scholarship PD/BD/113807/2015.

STATEMENT OF INTEGRITY

I hereby declare having conducted this academic work with integrity. I confirm that I have not used plagiarism or any form of undue use of information or falsification of results along the process leading to its elaboration.

I further declare that I have fully acknowledged the Code of Ethical Conduct of the University of Minho.

Micro/nano-structured hydrogels based on platelet lysate for tissue engineering and regeneration

ABSTRACT

Native tissues are represented by a complex collection of bidirectional interactions between cells and the microenvironment in which they are compartmentalized. Such dynamic reciprocal communications are one of the main modulators of cell responses and extracellular matrix (ECM) remodelling, playing a central role in tissue development, hemostasis, and regeneration. Tissue engineering strategies have been attempting to recreate the ECM microarchitecture, viscoelastic behavior, and biochemical cues by designing biomaterials with modular properties to guide cell responses towards regeneration. However, the translation of engineered tissue substitutes to clinics still anticipates new developments in ECM heterogeneity biomimicry as well as replacement of animal origin products in cell culture media.

Inspired by the mechanisms that promote tissue healing, this thesis proposes the use of intrinsically bioactive materials based on platelet lysate (PL), as a native source of biologically-active and structural proteins (e.g., fibrinogen), combined with cellulose nanocrystals (CNC) or hyaluronic acid (HA). Specifically, we investigate how to improve PL structural integrity, mechanical properties, and biomolecules profile release while preserving proteins biofunctionality. We demonstrate that CNC incorporation modulates microstructure, mechanical properties and biochemical environment of injectable systems (Chapter 3), hemostatic cryogels (Chapter 4), and advanced bioinks (Chapter 6) to guide cell responses under xeno-free cell culture conditions. Moreover, the modulation of CNC sulfation degree leads to defined nanoparticle PL-derived protein coronas that can trigger different cell signaling events (Chapter 5). Finally, we produce jammed microgels inks that tailor PL properties and greatly improve HA bioactivity (Chapter 7). In summary, the spatiotemporal presentation of PL bioactive proteins combined with ECM mimetic fibrillar matrices, displaying key cell instructive cues, results in a range of unique human-based biomaterials that can find multiple applications in regenerative medicine.

Keywords: Cellulose nanocrystals, Hyaluronic acid, Platelet lysate, Tissue Engineering.

Hidrogéis micro/nano-estruturados à base de lisado de plaquetas para engenharia e regeneração de tecidos

RESUMO

Os tecidos humanos podem ser representados por um conjunto complexo de interações bidirecionais entre as células e o microambiente que as rodeia. Estas comunicações dinâmicas e recíprocas atuam como moduladores da resposta celular e da remodelação da matriz extracelular (MEC), desempenhando um papel crucial no desenvolvimento, hemóstase e regeneração dos tecidos. A engenharia de tecidos procura mimetizar a estrutura, o comportamento viscoelástico e bioquímico da MEC ao desenvolver biomateriais com propriedades que possam ser ajustadas e assim controlar a resposta celular no sentido de promover a regeneração. No entanto, a sua translação clínica ainda antecipa novos desenvolvimentos na recriação da heterogeneidade da MEC, bem como na substituição de produtos de origem animal em cultura celular.

Ao inspirar-se nos mecanismos de reparação dos tecidos, esta tese propõe o uso de materiais com propriedades biológicas à base de lisado de plaquetas (LP), como uma fonte natural de proteínas bioativas e estruturais (e.g., fibrinogénio), em combinação com nanocristais de celulose (NCC) ou ácido hialurónico (AH). Em particular, explora como melhorar a integridade estrutural, as propriedades mecânicas e o perfil da libertação do PL, enquanto a sua função biológica é mantida. Foi demonstrado que a incorporação de NCC regula a microestrutura, propriedades mecânicas e bioquímicas dos sistemas injetáveis (Capítulo 3), criogéis hemostáticos (Capítulo 4) e 'bioinks' (Capítulo 6) para direcionar a resposta celular sem suplementos xenogénicos. A modulação dos graus de sulfatação dos NCN determina as interações entre as proteínas do PL e os NCN, o que desencadeia diferentes tipos de sinalização celular (Capítulo 5). Por último, nós desenvolvemos 'inks' de microgéis que gerem as características do PL e melhoram significativamente a bioatividade do AH (Capítulo 7). Em suma, a libertação espácio-temporal das proteínas do PL em conjunto com a sua matriz fibrilar semelhante à MEC, que contém fatores cruciais para as funções celulares, resulta em biomateriais únicos á base de PL, com inúmeras aplicações em medicina regenerativa.

Palavras-chave: Ácido Hialurónico, Engenharia de Tecidos, Lisado de Plaquetas, Nanocristais de Celulose

TABLE OF CONTENTS

LIST OF ABBREVIATIONS

2D – Two-dimensional

3D – Three-dimensional

αMEM – α Minimum essential medium

A

A/A – Antibiotic/Antimycotic

a-CNC – Aldehyde-modified cellulose nanocrystals

ACTA2 – α-smooth muscle actin

AFM – Atomic Force Microscopy

ALP – Alkaline phosphatase

APOB – Apoliprotein B

APOE – Apoliprotrein E

B

BCA – Bicinchoninic acid protein

BD – Blood derivatives

BMP-2 – bone morphogenic protein 2

C

CCL – C-C motif chemokine ligand

cDNA – Complementary deoxyribonucleic acid

CNC – Cellulose nanocrystals

CO_2 – Carbon dioxide

COLA1 – Collagen Type I Alpha 1 chain

COMP – Cartilage oligomeric matrix protein

CXCL – C-X-C motif chemokine ligand

D

DAPI - 6-Diamidino-2-phenyindole dilactate

DI – Deionized water

DO – Degree of oxidation

DTT – Dithiothreitol

E

E. Coli - Escherichia coli

ECM – Extracellular matrix

EDC – 1-ethyl-3-(3-dimethylaminopropyl)-carbodiimide

EGF – Endothelial growth factor

ELISA - Enzyme-linked immunosorbent assay

F

FBS – Fetal bovine serum

FG – Fibrin glue

FGF-2 – Fibroblast growth factor-2

FITC – Fluorescein isothiocyanate

FTIR - Fourier transform infrared spectroscopy

G

G' – Storage modulus

G'' – Loss modulus

GADPH - Glyceraldehyde-3-phosphate dehydrogenase

GAG – Glycosaminoglycan

GelMA - Gelatin-methacrylate

GFs – Growth factors

GH – Growth hormone

GM-CSF - Granulocyte-macrophage colony-stimulating factor

H

H&E – Hematoxylin & eosin

HA – Hyaluronic acid

hASCs – Human adipose-derived stem cells

HGF – Hepatocyte growth factor

HMPs – Hydrogel microparticles

HO – Hydroxide

HUink - Human-based nanocomposite bioink

I

IGF-1 – Insulin growth factor-1

IL-1 – Interleukin-1

L

LAP – Lithium phenyl(2,4,6-trimethylbenzoyl) phosphinate

LEP – Leptin

LPL – Lipoprotein lipase

L-PRP – Leukocyte-rich PRP

M

MCC – Microcrystalline cellulose

Micro-CT – Micro-computed tomography

MKX – Mohawk

MMP – Matrix metalloproteinases

MSC – Mesenchymal stromal cell

N

NaCl – Sodium Chloride

$NaIO_4$ – Sodium Periodate

nano LC-MS/MS - nanoscale liquid chromatography coupled to tandem mass spectrometry

NMR – Magnetic Resonance Spectroscopy

NorHA - norbornene-modified hyaluronic acid

P

PBS – Phosphate-buffered saline

PC – Platelet concentrate

PDGF-BB – Platelet-derived growth factor – BB

PEx – Platelet-derived exosomes

PG – Platelet gel

Phalloidin-TRITC - Phalloidin-Tetramethylrhodamine B isothiocyanate

pI – Isoelectric point

PL – Platelet lysate

PLG – Platelet lysate gel

PPARγ - peroxisome proliferator-activated receptor γ

PPP – Platelet-poor plasma

P-PRP – Leukocyte-poor plasma

PRGF – Plasma-rich in growth factors

PRP – Platelet-rich plasma

R

RBC – Red blood cell

RNA – Ribonucleic acid

RT – Room temperature

RT-PCR – Real-time polymerase chain reaction

RUNX2 – Runt-related transcription factor-2

S

S. aureus - Staphylococcus aureus

SDS-PAGE - Sodium dodecyl sulfate–polyacrylamide gel electrophoresis

SEM – Scanning electron microscopy

SOX-9 - SRY-box transcription factor 9

SP3 - Solid-phase-enhanced sample-preparation

T

TBA – Tetrabutylammonium salt

TCEP – Tris(2-carboxyethyl)phosphine

TE – Tissue engineering

TERM – Tissue engineering and regenerative medicine

TGF-β1 – Transforming growth factor β 1

TIMP – Tissue inhibitors of metalloproteinase

TNF α – Tumor necrosis factor α

U

U – Units

UV – Ultraviolet

V

VEGF – Vascular endothelial growth factor

VWF – von Willebrand factor

W

WBC – White blood cell

LIST OF EQUATIONS

LIST OF SUPPLEMENTARY EQUATIONS

LIST OF FIGURES

LIST OF SUPPLEMENTARY FIGURES

LIST OF SCHEMES

LIST OF TABLES

LIST OF SUPPLEMENTARY TABLES

SHORT *CURRICULUM VITAE*

Bárbara B. Mendes is 28 years-old and was born in Fátima. She concluded her three years Biomedical Sciences graduation in 2012 in the University of Beira Interior. That same year, she enrolled in a Biomedical Engineering Master's Program from the University of Porto, which she finished by 2014. Her master thesis was developed under supervision of Professor Bruno Sarmento and Professor Domingos Ferreira entitled "Development and characterization of a co-culture two-dimensional blood-brain barrier for the study of nanoparticle permeation". In September of 2015 she was accepted to the PhD Program in Tissue Engineering, Regenerative Medicine & Stem Cells of the University of Minho (Portugal) and awarded the PhD scholarship from Portuguese Science Foundation under the scope of this program. Since then she is conducting her PhD research at the 3B's Research Group, I3Bs Institute of the University of Minho, under the supervision of Prof. Manuela Gomes and Dr. Rui Domingues, and in collaboration with the University of Pennsylvania (USA) under the supervision of Professor Jason Burdick. For nearly five years, she has been researching and engineering intrinsically bioactive systems as mimics of the native extracellular matrix that find multiple research and clinical applications in regenerative medicine.

Bárbara B. Mendes mentored 2 undergraduate students and she has been actively participating in other works of 3B's research group such as in the organization of several symposiums/workshops. She has also been involved in research projects such as the ERC Cog 'MagTendon' and, more recently, on the international collaborative projects ITI 'Nanoplant' and RCN project 'InjecTE'. Bárbara B. Mendes is a student member of several International Scientific Organizations and she has been acting as referee of international peer review journals. Moreover, she was an elected member of I3Bs Institute Council, and she was a founder member of the team of students ('PhDynamics') that are responsible for science dissemination and 'soft' skills program for the 3B's research group.

As result of her research work, she authored and co-authored 8 full length papers published in international scientific journals (8 in Q1 journals, plus 3 under revision), 3 book chapters, 8 oral communications and 19 poster presentations. In addition, she is inventor of 1 international patent. She has an h-index of 6 according to Google Scholar, and 5 for Scopus, and her work was cited 100 times (May 20th, Google Scholar).

Ciência iD:BD10-2F99-9DD9; Scopus author iD:57195102619; ORCID iD:0000-0001-8630-1119

LIST OF PUBLICATIONS

The work performed during the PhD period resulted in the publications listed below.

Work incorporated in the present Thesis:

Papers in international scientific journals with referees (as first author):

B. B. Mendes, A.C. Daly, R. L. Reis, R. M. A. Domingues, M. E. Gomes. J. A. Burdick. Injectable hyaluronic acid and platelet lysate-derived granular hydrogels for biomedical applications. (Submitted)

B. B. Mendes, M. Gómez-Florit, A. C. Araújo, J. Prada, P. Babo, R. M. A. Domingues, R. L. Reis, M. E. Gomes. Intrinsically bioactive cryogels based on platelet lysate nanocomposites for hemostasis and wound regeneration applications. (Submitted)

B. B. Mendes, M. Gómez-Florit, H. Osório, A. Vilaça, R. M. A. Domingues, R. L. Reis, M. E. Gomes. Cellulose nanocrystals of variable sulfation degree can sequester specific platelet lysate-derived biomolecules to modulate stem cells response. 2020. Chemical Communications. DOI: 10.1039/D0CC01850C.

B. B. Mendes, M. Gómez-Florit, A. G. Hamilton, M. S. Detamore, R. M. A. Domingues, R. L. Reis, M. E. Gomes. Human platelet lysate-based nanocomposite bioink for bioprinting hierarchical fibrillar structures. 2019. Biofabrication. 12 (1), 015012.

B. B. Mendes, M. Gómez-Florit, R. M. A. Domingues, R. L. Reis, M. E. Gomes. Human-based fibrillar nanocomposite hydrogel as bioinstructive matrices to tune stem cell behavior. 2018. Nanoscale. 10 (36), 17388-17401.

B. B. Mendes, M. Gómez-Florit, P. S Babo, R.MA Domingues, R.L Reis, M. E Gomes. Blood derivatives awaken in regenerative medicine strategies to modulate wound healing. 2017. Advanced Drug Delivery Reviews. 129, 376-393.

Patent:

B. B Mendes, R. M. A. Domingues, P. Babo, R. L. Reis, M. E. Gomes. Blood derivatives composite material, methods of production and uses thereof. Patent application: WO 2018/078586 A1, EP 3532114 A1 and US 2019/0282621 A1. Priority date: 27 Oct 2016, PT.

Conference oral presentations (as first author and as speaker):

B. B. Mendes, M. Gómez-Florit, A. C. Daly, R. M. A. Domingues, R. L. Reis, M. E. Gomes, J. A. Burdick. 16 to 19 October 2019. Platelet Lysate-Based Bioinks for 3D Printing Applications. BMES 2019 Annual Meeting Philadelphia, USA.

B. B. Mendes, M. Gómez-Florit, R. M. A. Domingues, R. L. Reis, M. E. Gomes. 09 to 13 September 2018. Platelet lysate fibrillar nanocomposite bioink for soft tissues bioprinting. ESB 2018. 628. Maastritcht, Netherlands.

B. B. Mendes, R. Costa-Almeida, P. S. Babo, R. M. A. Domingues, R. L. Reis and M. E. Gomes. 26 to 30 June 2017. Injectable platelet lysate/cellulose nanocrystals hydrogels: a novel combined approach for regenerative medicine strategies. In eCM Meeting Abstracts 2017, Collection 2: Personalized Therapies for Regenerative Medicine, TERMIS-EU 2017. 0105. Davos, Switzerland.

B. B. Mendes, R. M. A. Domingues, R. L. Reis, M. E. Gomes. 5 to 9 June 2017. Incorporation of modified cellulose nanocrystals in platelet lysate-based hydrogels for 3D microenvironment sequestration of platelet lysate bioactive molecules. CHEM2Nature - Second School. Porto, Portugal.

B. B. Mendes, R. M. A. Domingues, R. L. Reis, M. E. Gomes. 21 to 25 November 2016. Sulfated cellulose nanocrystals: synthesis and application on growth factors sequestering biomaterials. CHEM2Nature - First School. Guimarães, Portugal.

Other collaborative works:

Papers in international scientific journals with referees (as co-author):

S. Araújo-Custódio, M. Gómez-Florit, A. R. Tomás, **B. B Mendes**, P. S. Babo, S. M. Mithieux, A S. Weiss, R. M. A. Domingues, R. L. Reis, M. E. Gomes. Injectable and magnetic responsive hydrogels with bioinspired ordered structures. 2019. ACS Biomaterials Science & Engineering. 5 (3), 1392-1404.

T. Pesqueira, R. Costa-Almeida, S. M. Mithieux, P. S. Babo, A. R. Franco, **B. B. Mendes**, R. M. A. Domingues, P. Freitas, R. L. Reis, M. E. Gomes and A. S. Weiss. Engineering magnetically responsive tropoelastin spongy-like hydrogels for soft tissue regeneration. 2018. Journal of Materials Chemistry B. 6 (7), 1066-1075.

E. Silva, P. S. Babo, R. Costa-Almeida, R. M. A. Domingues, **B. B. Mendes**, E. Paz, P. P. Freitas, M.T. Rodrigues, P. L. Granja and M. E. Gomes. Multifunctional magnetic-responsive hydrogels to engineer

tendon-to-bone interface. 2017. Nanomedicine Nanotechnology Biology and Medicine. 14 (7), 2375-2385.

Book Chapter:

M. Gómez-Florit, R. M. A. Domingues, S. M. Bakht, **B. B. Mendes**, R. L. Reis, M. E. Gomes, Chapter 1.3.6. Natural Materials, in Biomaterials Science: An Introduction to Materials in Medicine, Fourth Edition, edited by William Wagner, Shelly Sakiyama-Elbert, Guigen Zhang and Michael Yaszemski, Elsevier, ISBN: 9780128161371, 2020.

Conference oral presentations (as co-author):

M. Gómez-Florit*, **B. B. Mendes***, R. M. A. Domingues, R. L. Reis, M. E. Gomes. 12 to 14 June 2019. Platelet Lysate-Based Nanocomposite Biomaterials for Tissue Engineering & Regenerative Medicine. In eCM Online Periodical 2019, Collection 2: Scandinavian Society for Biomaterials 2019 Conference. Page 13. Kirkkonummi, Finland. (*contributed equally to this work).

S. M. Bakht, T. Lamers, M. Gomez-Florit, M. Sixt, **B. B. Mendes**, R. L. Reis, R. M. A. Domingues and M. E. Gomes. 04 to 05 November 2019. Combining 3D Printing with Nanoparticles Self-Assembly for the Fabrication of Fibrillar, Perfusable and Transparent Microfluidics Devices. Second Achilles Conference. Braga, Portugal.

M. Gómez-Florit*, **B. B. Mendes***, A. Hamilton, R. M. A. Domingues, M. S. Detamore, R. L. Reis, M. E. Gomes. 03 to 08 June 2018. Human-based nanocomposite bioink for freeform structures printing. CHEM2Nature – Summer School. Porto, Portugal. (*contributed equally to this work).

Conference posters (as first author):

B. B. Mendes, A. Vilaça, M. Gómez-Florit, R. M. A. Domingues, R. L. Reis, M. E. Gomes. 07 to 08 November 2019. Cellulose nanocrystals of variable sulfation degree for sequestering specific growth factors. TERMSTEM 2019. Braga, Portugal.

B. B. Mendes, M. Gómez-Florit, L. Randall, P. S. Babo, R. C. Almeida, Michael S. Detamore, R. M. A. Domingues, R. L. Reis, M. E. Gomes. 9 to 13 September 2019. Intrinsically bioactive cryogels for

hemorrhage hemostasis and regenerative wound healing applications. 30th Annual Meeting of the European Society for Biomaterials. Dresden, Germany.

B. B. Mendes, M. Gómez-Florit, L. Randall, P. S. Babo, R. C. Almeida, Michael S. Detamore, R. M. A. Domingues, R. L. Reis, M. E. Gomes. 3 to 6 April 2019. Human-based nanocomposite cryogels for hemostatic and wound healing applications. In Transactions of the Annual Meeting of the Society for Biomaterials and the Annual International Biomaterials Symposium: 42nd Society for Biomaterials Annual Meeting and Exposition 2019. P. 597. Seattle, United States of America.

B. B. Mendes, M. Gómez-Florit, L. Randall, P. S. Babo, R. C. Almeida, Michael S. Detamore, R. M. A. Domingues, R. L. Reis, M. E. Gomes. 23 to 26 October 2018. Human-based hemostatic cryogels for wound healing applications. CHEM2Nature – Final Conference. Guimarães, Portugal.

B. B. Mendes, R. M. A. Domingues, Rui L. Reis, M. E. Gomes. 02 to 04 July 2018. Human-based nanocomposite scaffolds towards new bioinstructive matrices to TERM strategies. Encontro de Ciência 2018. Lisboa, Portugal.

B. B. Mendes, M. Gómez-Florit, R. M. A. Domingues, R. L. Reis, M. E. Gomes. 15 to 17 November 2017. Platelet lysate loaded in nanocomposite bioinks towards a new generation of bioinks for TERM strategy. Forecast 2017. Porto, Portugal.

B. B. Mendes, R. Costa-Almeida, P. S. Babo, R. M. A. Domingues, R. L. Reis and M. E. Gomes. 27 and 28 October 2016. Platelet lysate hydrogels enriched with oxidized cellulose nanocrystals. TERM STEM 2016. Guimarães, Portugal.

Conference posters (as co-author)

S. M. Bakht, T. Lamers, M. Gomez-Florit, M. Sixt, **B. B. Mendes**, R. L. Reis, R. M. A. Domingues and M. E. Gomes. 25 to 27 September 2019. Combining 3D Printing with Nanoparticles Self-Assembly for the Fabrication of Fibrillar, Perfusable and Transparent Microfluidics Devices. 1st Discoveries Forum on regenerative and precision medicine. Porto, Portugal.

R. M. A. Domingues, S. Araújo-Custódio, A. Tomás, **B. B. Mendes**, M. Gómez-Florit, P.S. Babo, R. L. Reis, M.E. Gomes. 09 to 13 September 2018. Injectable and Magnetic Responsive Hydrogels with Bioinspired Ordered Structures for the Regeneration of Anisotropic Tissues, 29th Annual Meeting of the European Society for Biomaterials. P842. Maastricht, Netherlands.

M. Gómez-Florit*, **B. B. Mendes***, R. M. A. Domingues, R. L. Reis, M. E. Gomes. 04 to 07 September 2018. Platelet Lysate-based Nanocomposite Bioink for 3D Printing in Tissue Engineering. 5TH World TERMIS congress 2018. 01-P066. Kyoto, Japan. (*contributed equally to this work).

R. M. A. Domingues, S. Araújo-Custódio, **B. B. Mendes**, M. Gómez-Florit, P. S. Babo, R. L. Reis, M. E. Gomes. 04 to 07 September 2018. Cellulose nanocrystals as nanostructuring tools to modulate the artificial cell microenvironment in nanocomposite hydrogels. 5TH World TERMIS congress 2018. 02-P447. Kyoto, Japan.

M. Gómez-Florit*, **B. B. Mendes***, R. M. A. Domingues, R. L. Reis, M. E. Gomes. 4 to 8 September 2017. Tunable Nanocomposite Bioactive Bioinks for 3D Printing in Tissue Engineering. 28th Annual Conference of the European Society for Biomaterials 2017. PP494. Athens, Greece. (*contributed equally to this work).

S. M. Bakht, R. M. A. Domingues, **B. B. Mendes**, R. L. Reis, M. E. Gomes. 15 to 17 November 2017. Development of tunable supramolecular nanocomposite hydrogels as nanoinks for tissue specific needs in bioprinting. FORECAST 2017. Porto, Portugal.

E. Silva, P. S. Babo, R. Costa-Almeida, R. M. A. Domingues, **B. B. Mendes**, P. L. Granja and M. E. Gomes. 26 to 30 June 2017. Multifunctional magnetic-responsive hydrogels modulate platelet lysate-derived growth factor release and guide cell fate. In eCM Meeting Abstracts 2017, Collection 2: Personalized Therapies for Regenerative Medicine, TERMIS-EU 2017. P37. Davos, Switzerland.

M. Gómez-Florit, **B. B. Mendes**, R. M. A. Domingues, R. L. Reis, M. E. Gomes. 5 to 9 June 2017. Research road map towards the development of scaffolds for tendon tissue engineering. CHEM2Nature - Second School. Porto, Portugal.

E. Silva, P. S. Babo, R. Costa-Almeida, R. M. A. Domingues, **B. B. Mendes**, P. L. Granja and M. E. Gomes. 27 and 28 October 2016. Multifunctional magnetic-responsive hydrogels to engineer tendon-to-bone interface. TERM STEM 2016. Guimarães, Portugal.

Awarded grants

Fundação para a Ciência e Tecnologia PhD scholarship –PD/BD/113807/2015.

Deus quer, o homem sonha, a obra nasce.
Deus quis que a terra fosse toda uma,
Que o mar unisse, já não separasse.
Sagrou-te, e foste desvendando a espuma.

E a orla branca foi de ilha em continente,
Clareou, correndo, até ao fim do mundo,
E viu-se a terra inteira, de repente,
Surgir, redonda, do azul profundo.

Quem te sagrou criou-te português.
Do mar e nós em ti nos deu sinal.
Cumpriu-se o Mar, e o Império se desfez.
Senhor, falta cumprir-se Portugal!

Fernando Pessoa, "O Infante" na Mensagem

.

SECTION 1

GENERAL INTRODUCTION

Chapter I

Blood derivatives awaken in regenerative medicine strategies to modulate wound healing

Chapter I

Blood derivatives awaken in regenerative medicine strategies to modulate wound healing

ABSTRACT

Blood components play key roles in the modulation of the wound healing process and, together with the provisional fibrin matrix ability to selectively bind bioactive molecules and control its spatial-temporal presentation, define the complex microenvironment that characterize this biological process. As a biomimetic approach, the use of blood derivatives in regenerative strategies has awakened as a source of multiple therapeutic biomolecules. Nevertheless, and despite their clinical relevance, blood derivatives have been showing inconsistent therapeutic results due to several factors, including proper control over their delivery mechanisms. Herein, we highlight recent trends on the use biomaterials to protect, sequester and deliver these pools of biomolecules in tissue engineering and regenerative medicine approaches. Particular emphasis is given to strategies that enable to control their spatiotemporal delivery and improve the selectivity of presentation profiles of the biomolecules derived from blood derivatives rich in platelets. Finally, we discussed possible directions for biomaterials design to potentiate the aimed regenerative effects of blood derivatives and achieve efficient therapies.

This chapter is based on the following publication: ***B. B Mendes***, *M. Gómez-Florit, P. S Babo, R.MA Domingues, R.L Reis, M. E Gomes. Blood derivatives awaken in regenerative medicine strategies to modulate wound healing. Adv. Drug Del. Rev., 129, 376-393. 2017.*

I-1. INTRODUCTION

Wound healing following injury is a highly complex and dynamic process that can either lead to the formation of a scarred (repaired) or a regenerated tissue, depending on the multicellular organism, tissue and local signals [1, 2]. Regenerative medicine holds the promise of promoting tissue regeneration in the body by therapeutically manipulating its natural ability to heal after injury or disease. As a concept, it applies various strategies for the management of diseases or healing processes, including the tissue engineering triad: biomaterials, cells, and signaling molecules [3-5]. These tools should control the swing between tissue regeneration and scar formation, promoting the regenerative pathway and avoiding the formation of fibrotic tissue [2]. In this context, blood components and their blood derivatives (BD) formulations can provide a wide range of biological elements (cells, growth factors (GFs), cytokines and scaffold-forming elements) that are essential in the regulation of wound healing mechanisms [6].

The use of different types of BD has shown positive clinical effects in several fields of regenerative medicine such as in the treatments of tendon injures and pathologies [7], cartilage disorders [8], as well as in periodontal [9] and soft tissue [10] wound healing. However, the systematic review of the literature shows conflicting results in the therapeutic outcomes, mainly due to the lack of standardization and poor characterization of formulations, which has led to an open debate on their real potential within the field [11, 12]. Indeed, BD are a variable pool of cellular, sub-cellular and molecular components, making it difficult to draw strong conclusions on which formulation and therapeutic regime should be applied in a specific regenerative strategy. To overcome these limitations, the development of more controllable systems for the delivery of well characterized populations of biomolecules will certainly improve many clinical aspects on the use of BD. In vivo, GFs are protected and stabilized via their binding to different extracellular matrix (ECM) components [13] that regulate their availability and signaling [14]. In a biomimetic strategy, researchers have combined BD with different biomaterials to modulate the delivery of bioactive molecules in order to guide the wound healing process.

In this introduction, we provide a theoretical and investigational framework to improve our understanding on the use of BD to modulate the wound healing process towards tissue regeneration as opposed to simple repair. Firstly, it is presented a brief overview of the fundamental molecular mechanisms of wound healing and tissue regeneration (section I-2). Subsequently, in section I-3, it is provided a general introduction to the methods of preparation and classification of the different BD. In section I-4, the recent strategies and findings on the modulation of BD delivery in a spatio-temporal, selective and concentration-dependent fashion are analyzed in detail. In the final section (section I-5)

unresolved issues are critically discussed, providing possible directions for the progression of the field looking towards the future.

I-2. MECHANISMS OF WOUND HEALING AND TISSUE REGENERATION

The natural reaction to injury is the immediate activation of the wound healing cascade, which primarily intends to restore tissue integrity and homeostasis. In healthy individuals, this process is relatively fast and effective, although it is often associated with scar formation, which can be anesthetic and impair the tissue function [2, 15]. Research in the field of cutaneous wound healing [16] has made significant contributions to unveil the fundamental principles of tissue regeneration process [1, 2]. Nevertheless, wound healing stages and key principles are shared among different tissues [2, 17]. For example, the events that follow a myocardial infarction are remarkably similar to that following a tendon or cartilage injury, a spinal-cord injury, a burn or a gunshot wound despite the different types of insult, the different organs affected, and the sterility of the wound [2, 18, 19]. Likewise, scar formation that occurs during wound repair leads to similar tissue dysfunction wherever it takes place.

Wound healing can be divided in three overlapping phases: (i) hemostasis (seconds-minutes) and inflammation (hours-days); (ii) proliferation or new tissue formation (days-weeks); and (iii) tissue remodeling (weeks-months-years, depending on wound type), (Figure I-1). The orchestration of these complex process is precisely regulated by multiple cytokines, chemokines, and GFs secreted by multiple cell types, including platelets, neutrophils, macrophages, fibroblasts, endothelial and resident stem cells [2, 17].

I-2.1. Inflammatory phase

Immediately after tissue damage, the coagulation cascade is activated to prevent fluid and blood loss, leading to homeostasis. The extravasation of blood components triggers the formation of a platelet plug followed by a fibrin matrix, which provides a provisional scaffold for cell infiltration and proliferation [20, 21]. At the same time, toll-like receptors at immune cells surface are activated by blood extravasation elements, ECM degradation products and bacteria. This causes the downstream activation of transcription factor nuclear factor kappa B, which induces the expression of proinflammatory mediators [18].

Platelets not only participate in the clot formation but also release large amounts of a wide variety of cytokines, chemokines, and GFs, extending their role beyond hemostasis to the participation in the innate immune system [22], inflammatory response [23], and tissue repair and regeneration [24-27].

Neutrophils are recruited to the wound in response to the activation of complement cascade, the degranulation of platelets, and bacterial products. These immune cells sterilize the wounds, phagocytizing bacteria and clearing cellular debris at the sites of tissue damage. However, its excessive activation may result in the killing of many otherwise-healthy host cells, a behavior which is particularly prevalent in chronic wound situations [28]. In addition, neutrophils activate other cells through the release of inflammatory mediators, such as transforming growth factor-β 1 (TGF-β1), interleukin (IL)-1 and -4. As a key player in the initial inflammatory phase, TGF-β1 induces the expression of proinflammatory genes that activates the recruitment of monocytes. At the injury site, monocytes differentiate into macrophages, which phagocytize dead cells and debris and coordinate tissue repair [28]. Macrophages also produce numerous cytokines (IL-1 and IL-6) and GFs (fibroblast growth factor (FGF), endothelial growth factor (EGF), TGF-β1, and platelet derived growth factor (PDGF)) crucial for fibroblast recruitment and angiogenesis in the proliferative phase [29]. As the first inflammatory phase ends, pro-inflammatory macrophages (M1 macrophages), in response to IL-4, adopt an anti-inflammatory and reparative phenotype (M2 macrophages) to finalize the inflammation [30].

I-2.2. Proliferative phase

The proliferative phase consists on the formation of granulation tissue, ECM deposition, and angiogenesis. An interleukin in particular, IL-6, has important functions in the new tissue formation phase. IL-6 binding to its receptor activates the signal transducer and activator of transcription – Janus kinase pathway, which indirectly induces neutrophil and monocyte infiltration, fibroblasts migration and collagen deposition, and promotes angiogenesis by the induction of TGF-β1, IL-1, vascular endothelial growth factor (VEGF), and hepatocyte growth factor (HGF) production [31]. In the case of skin, early migration of keratinocytes into the fibrin matrix leads to re-epithelialization. This process is aided by fibroblasts, which, attracted by TGF-β1, among others, invade the fibrin network and progressively replace it for a collagen-rich connective tissue [25]. This provisional matrix or granulation tissue invades the wound space and serves as a support for angiogenesis and later collagen remodeling [16]. Simultaneously, endothelial cells migrate into the wound attracted by VEGF and FGF-2 to form new blood vessels. Some fibroblasts undergo transformation into contractile myofibroblasts through TGF-β1 pathway. These cells secrete copious

amounts of collagen and express α-smooth muscle actin, which allows the physical contraction of the wound [32, 33]. However, excessive activation of myofibroblasts has been related to fibrotic diseases [34].

I-2.3. Remodeling phase

The final phase of wound repair involves a decrease in cellular content and is characterized by significant collagen remodeling. Most of the endothelial cells, macrophages, and myofibroblasts undergo apoptosis or exit the wound [2] while collagen type III in the ECM is replaced by stronger collagen type I [17]. Remaining cells coordinate this process producing new collagen, matrix metalloproteinases (MMP) and their inhibitors, tissue inhibitors of metalloproteinases (TIMP), which work together to form collagen bundles and achieve the native tissue structure and strength [35]. In conclusion, a proper balance between degradation and synthesis of ECM is indispensable for normal wound healing. However, the repaired ECM of mature scar tissue differs considerably from that of unwounded tissue and is generally characterized by their comparatively lower biomechanical properties and functionality [36].

I-2.4. Towards Tissue Regeneration

In some eukaryotic organisms, the response to injury can completely recapitulate the original tissue architecture through regeneration. Though this process is poorly understood, researchers are beginning to uncover the individual components of tissue regeneration trough the study of animal models of regeneration and human tissues with self-regeneration ability [37].

A leading hypothesis is that immune cells have a prominent role in the swing between regeneration and repair [28]. Efficiently regenerating organisms, such as zebrafish, depend on macrophages to efficiently resolve inflammation and facilitate tissue remodeling and regrowth [38]. Furthermore, recent findings indicate that the sequential conversion of macrophages from M1 to M2 phenotype might have an important role in tissue regeneration [30]. For example, in skeletal muscle, the polarization of M2 macrophages promotes the release of IGF-1, that supports satellite cell growth and fusion to form new muscle fibres, and IL-10 and TGF-β, that suppress inflammation, stimulate angiogenesis and promote ECM remodeling, suggesting that modulation of macrophage polarization could improve muscle regeneration [39, 40]. Indeed, inflammation is necessary for the effective defense against pathogens and

to set in motion the tissue repair mechanisms following injury, although excessive inflammation delays healing and results in increased scarring, compromising tissue regeneration [41].

As an example of the role of GFs in tissue regeneration, researchers showed that IGF and FGF signaling pathways are up-regulated during the fin regeneration in zebrafish. TGF-β family members have as well an important role in the balance between wound repair and regeneration [33, 42]. While TGF-β1 increases the expression of genes associated with ECM synthesis in fibroblasts, it also down-regulates MMP-1 [43] and induces the acquisition of the contractile myofibroblast phenotype to close the wound [32, 44], showing both anti-inflammatory and profibrotic activity. In addition, TGF-β1 is also involved in the up-regulation of the angiogenic VEGF expression [45, 46]. On the other hand, while TGF-β2 plays a similar role to TGF-β1, the third isoform TGF-β3, inhibits scarring and promotes better collagen organization in vivo [47]. In a clinical scenario, wounds that heal by scar formation, as opposed to tissue regeneration, have been shown to produce increased amounts of TGF-β [2].

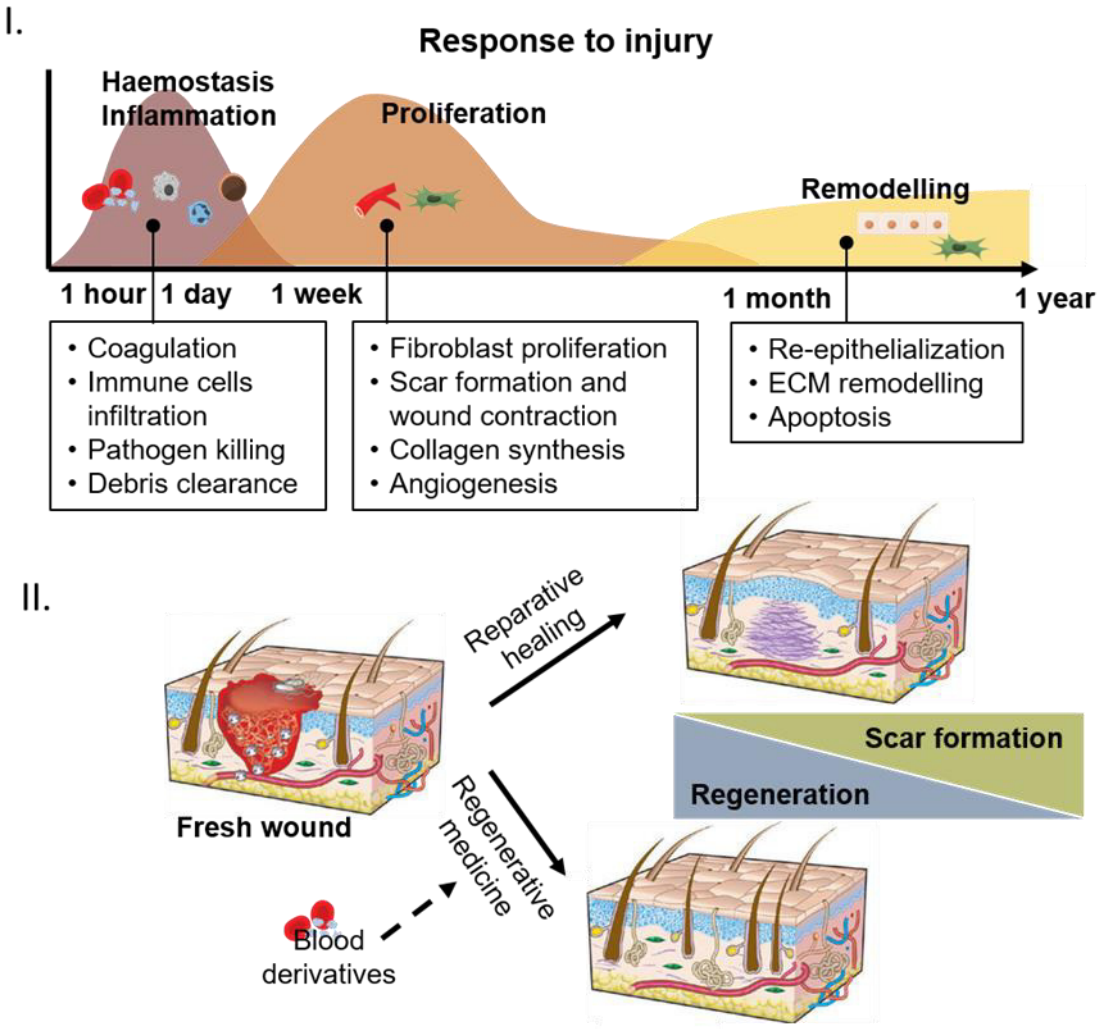

Figure I-1 Overview of the classical wound healing phases vs regenerative medicine therapy approach. (I) Major wound healing events in a controlled spatial and precisely temporal response to injury. (II) The balance of these events plays an important

role in the swing between tissue repair (scar formation) and tissue regeneration after injury. Considering BD content, rich in key biomolecules involved in the regulation wound healing mechanisms, its use will potentially alter the outcomes of this process. Adapted with permission from [2]. Copyright 2008, Nature Publishing Group.

In addition, the liver is one of the few organs in the human body that regenerates efficiently after acute or even repetitive damage. Non-parenchymal cells in the liver, including macrophages and endothelial cells, are central in the coordination of the regenerative process. In particular, activation of VEGF receptor-2 in endothelial cells, stimulates the production of angiocrine factors and HGF, triggering hepatocyte proliferation and liver regeneration [48].

Mammals have retained much of the molecular machinery used by efficiently regenerating organisms, but their regenerative potential is only limited. In part, this seems to result from the rapid formation of fibrotic tissue, which probably conferred a survival advantage but prevented subsequent tissue regeneration [2, 37]. In order to improve human health, GFs from BD could be a potential therapeutic strategy to transform fibrotic healing processes into regenerative ones.

I-3. PREPARATION AND CLASSIFICATION OF BLOOD DERIVATIVES

Blood is composed of different cellular, sub-cellular and molecular components that are involved in essential stages of wound healing [49-51] and regenerative processes [52-54]. The separation of blood components results on the easy and fast production of different BD formulations, being classically produced by the double centrifugation technique (Figure I-2) [55]. Generally, it starts with a whole blood centrifugation, called the hard centrifugation, in order to separate the blood into three phases: 1) a lower layer rich in red blood cells (RBCs); 2) an interface layer (buffy coat) rich in white blood cells (WBCs) and platelets; and 3) an upper layer corresponding to the blood plasma with platelets in suspension (Figure I-2IA). Alternatively, if an anticlotting agent (e.g., heparin or citrate) was previously added, it can be collected (alone or in combination with the buffy coat) and submitted to a further centrifugation step, called the soft spin (Figure I-2IC), to produce a fraction poor in platelets (platelet-poor plasma (PPP)) and a fraction rich in platelets (platelet concentrate (PC) or platelet rich plasma (PRP)) [55]. Table I-1 summarizes the most relevant biomolecules found in BD with therapeutic interest along with their main cellular sources. These soluble factors regulate important cell functions such as chemotaxis, proliferation and differentiation [52-54]. Moreover, some BD are rich in structural proteins, such as fibrinogen [56] (or its polymerized product fibrin), and fibronectin [57], which may act as a provisional matrix for cell adhesion and migration [51]. Fibrinogen of platelet concentrates is commonly activated by calcium and

exo- or/and endogenous thrombin producing a stable fibrin matrix [58]. Both the fibrinogen content and activation strategy have a marked impact over the physical properties of the resulting fibrin matrix, namely on the fibre diameter and network density that will define the in vitro and in vivo stability of the clot, its mechanical properties and its ability to sequester the bioactive molecules released by the platelets [59]. Additionally, BD have also been reported to exhibit antimicrobial properties [60-63], attributed to the presence of β-lysin [64], neutrophil activating protein-2 [65, 66], CXC chemokine ligand-4 [67, 68], or complement proteins [63] which can contribute for maintaining the prophylaxis of the wound site.

The lack of standardization in origin (auto-, allo- or xenogenous) and preparation methods (donors number, anticoagulant agent, activation method) of BD generally leads to marked differences in the composition of the formulations, particularly in terms of cellularity mainly characterized by the platelet concentration and the presence/absence and concentrations of WBCs and RBCs [59, 69-71]. At the end, the presence, concentration, protection, release and diffusion of bioactive molecules of interest (Table I-2) from BD will be affected by all these parameters and therefore, their preparation is of utmost importance as the first step to control and ultimately achieve the aimed therapeutic effect.

I-3.1. Platelet-poor blood derivatives

The PPP is a liquid solution of blood plasma with very low cellular content. It is obtained, as above described, from whole blood supplemented with an anti-clotting agent, after cycles of centrifugation The PPP is generally used in clinics mainly as a wound patch termed as fibrin glue (FG), after induction of the coagulation cascade (Figure I-2ID) [55]. It has been shown to be hemostatic and to improve the wound healing [72]. FG is produced by polymerizing the fibrinogen contained in PPP with thrombin and calcium [72] or other coagulation activator. Given the low platelet content, FG is almost depleted of GFs of platelet origin (summarized in Table I-2) [73, 74], although some GFs, such as insulin growth factor-1 (IGF-1) and HGF, can be found in FG [73]. Despite the lack of GFs of platelet origin, FG was shown to be more effective than activated PRP or PRF for the preservation of sockets with buccal dehiscence [74]. The authors hypothesized that the absence of anti-morphogenic factors of platelet origin, such as the PDGF [75], and the higher fibrin content (Table I-2) [74] would enhance the osteoconductive and/or osteoinductive properties of FG over PRP and PRF.

I-3.2. Platelet-rich blood derivatives

As mentioned before, the fraction rich in platelets is termed as platelet-rich BD. During the last two decades, several platelet-rich BD have been developed using the same generic name "PRP". Further than the nomenclature controversy, the ambiguous outcomes reported for the in vitro and clinical application of these different "PRPs" have early unleashed the discussion on the need of an adequate classification method [55, 59, 76].

I-3.3. Platelet-rich plasma

PRP is generally defined as a volume of autologous plasma with a platelet concentration above blood baseline (between $1.5x10^5$ /μL and $3.5x10^5$ /μL) [55]. PRP can be used directly as a liquid formulation or activated through different methods, including the addition of thrombin [77], thromboplastin [78], calcium salts [77-80] or collagen [81] promoting the formation of a fibrin network containing activated platelets, termed platelet gel (PG) (Figure I-2IE) [82]. The supernatant, a solution of GFs released upon platelets activation in blood plasma, herein termed plasma rich in growth factors (PRGF), has also been explored [54, 61]. The activation of platelets contained in PRP induce the degranulation of α-granules and the release of several cytokines and growth factors, including TGF-β-1 and -2, PDGF-A and -B, EGF, VEGF, and FGF [54, 73, 83, 84] (Table I-1). However, their relative concentration varies considerably between batches and activation products.

Four major factors were identified to influence the composition of the PRP and PRP products: 1) the platelet content; 2) the presence of other cells of blood origin, namely WBCs; 3) platelet activation protocol; and 4) donor-to-donor variability. The first three factors are the basis for most of the PRP classification systems, namely those proposed by Ehrenfest [76] and DeLong [85]. Nevertheless, among these factors, platelet content will have a major effect in the concentration of GFs of platelet origin [86], and thus in the possible therapeutic outcomes. Therefore, Marx and colleagues [55] proposed that, for clinical applications, PRP should be defined as a concentration of platelets with a consistent therapeutic efficacy, while all the suspensions of platelets in plasma above the blood baseline could be generally termed PC. Since the concentration of platelets that has been proven to have therapeutic efficacy for bone healing is around $1x10^6$ /μL [55, 87], this has been proposed as the platelet content that defines a platelet suspension as PRP. However, in literature, some works using products termed "PRP" either overlook the platelet concentration [88] or use PC with different platelets concentration [89].

Commercially available kits (e.g. PRGF®-Endoret®, PCCS®, Harvest® SmartPrep®) have aimed at establishing good manufacturing practice protocols for PRP derivatives production, particularly to reduce the protocol-related variability. Nevertheless, different PRP preparation kits still yield significantly different platelets concentration [86, 89]. For example, the preparation of PRP from a single donor using PCCS® or PRGF® kits yielded differences in leukocytes, platelets and GFs content. PCCS® collects 1,641,800 ± 426,820 platelets/μL, which results in a significantly higher content of TGF-β1 and PDGF-AB, in comparison with PRGF® that collects 513,630 ± 139,470 platelets/μL [89]. These results might be explained by the collection protocol, since in the PRGF® kit the buffy coat (contains leukocytes and platelets) is not used and a second centrifugation (hard spin for platelet concentration) is not performed. Therefore, differences in the PRP preparation method might explain the conflicting therapeutic results [11], which emphasizes the need to standardize the platelet concentration and/or the use of a pool of donors to obtain reliable therapeutic effects.

The leukocytes, mainly neutrophils and macrophages, are usually isolated from the whole blood together with platelets during PRP preparation [90]. These cells can contribute with cytokines, GFs and proteases involved in the modulation of inflammation and clot remodeling [91-93] (Table I-1). Based on the potential effect of the WBCs content, Ehrenfest and co-workers have defended the necessity to classify PRP based on their leukocytes content: leukocyte-rich PRP (L-PRP) and the leukocyte-poor PRP or "pure"-PRP (P-PRP) (and, generalizing, all the platelet-rich BD and PRP activated products) [59, 76] (Figure I-2II). Studies comparing the releasate of leukocyte-rich PG and leukocyte-poor PG clots, reported no differences in the released concentration of several relevant GFs, namely PDGF, VEGF, and TGF-β1 [94, 95] (Table I-2). On the other hand, due to their higher WBCs contents, leukocyte-rich PG released higher concentrations of proinflamatory cytokines, namely IL-1β [94, 95] and TNFα [95].

Although results tend to suggest that presence of WBCs in BD might foster undesired proinflammatory effects, systematic reviews have shown inconclusive results in the use of L-PRP and P-PRP [12]. For example, L-PRP might be less suitable for acute tendon conditions because of its catabolic and inflammatory features. On the other hand, P-PRP could induce the formation of excessive scar tissue due to its potent anabolic action [96]. This exemplifies the current gaps of knowledge on the optimal BD formulations to be applied in the treatment of inflammatory diseases or in regenerative strategies. Furthermore, there is a clear difference between the PG clot and the PRGF liquid solution formulates, mainly because of the platelet activation protocol. Besides the fibrin content, differences can be observed in the concentration of some growth factors [73] (Table I-2). For instance, while the concentration of TGF-

β1 is pretty similar between PG and PRGF obtained by PRP activation with either calcium or thrombin, the concentration of e.g. EGF is consistently higher in PRGF than in PG regardless the activation method [73], as a result of their different affinities for the fibrin matrix [97]. The activation method has also been shown to influence the structural characteristics of PRP activated products and consequently the composition of their releasates. PG clots formed using type I collagen exhibited far less retraction than those formed with bovine thrombin [98]. Moreover, while both PGs activation protocols resulted in similar PDGF and VEGF release profiles between 1 and 10 days, thrombin activation resulted in a comparatively higher release of TGF-β1 during the first 5 days [98].

Finally, there is a considerable variability between the proteins released from different platelet donors [73, 99], which should be a major concern when PRP is envisioned for autologous therapies. For instance, Kalén and co-workers observed a remarkably high variability between donors on the release of bone morphogenetic proteins (BMPs)-2, -4, -6, and -7 from P-PRP [99]. In fact, platelets of only one of thirty donors released BMP-2 at physiologic pH [99]. This variability is of paramount relevance for GFs with a major function in the regeneration of the targeted tissue such as, in this particular case, the activation of BMPs signaling pathway for osteogenic differentiation [100, 101]. In order to mitigate this problem, in last few years the use of PRP pools from different donors in alternative to single-donor PRP has been proposed, as they yield PRP preparations with more consistent GFs and cytokine contents than single-donor batches [73].

I-3.4. Platelet lysate

Platelet lysate (PL) is obtained by freeze/thaw cycles [83, 84] or by ultrasounds [102] to disrupt the platelets contained in PC batches, either produced by centrifugation cycles [84] or by apheresis [83, 84]. PL is a liquid solution of biomolecules, and although its platelet content release is obtained by cellular disruption instead of α-granules degranulation, it contains most of the GFs commonly found in another platelet-rich BD [83, 84]. Nevertheless, the concentration of some GFs, namely PDGF, is significantly lower in PL than in PRGF [103] (Table I-2) emphasizing the relevance of BD production method on their bioactive molecules composition.

PL offer several advantages for therapeutic applications: 1) the clot and platelet debris are removed during PL processing, therefore, the PL is a solution that hardly forms spontaneously a gel or retracts; 2) the freeze/thaw cycles are easy to standardize and do not require the addition of any clot activator to

release the platelet factors; 3) the concentration of the growth factors and cytokines is highly reproducible between batches, which can contribute for more predictable outcomes; 4) it can be frozen and stored to be readily available for further use [83].

For TE applications, PL can be processed into a PL gel (PLG) using thrombin [102] or loaded into carriers for the sustained release of PL GFs [104, 105]. These constructs incorporating PL have shown potential to induce neovascularization [102], osteogenesis [104, 105] and to enhance periodontal re-attachment [106]. PL has also been proposed as a prevailing alternative to fetal bovine serum supplement for culture of several human cell types [83, 107].

I-3.5. Platelet-rich fibrin

PRF is a second generation platelet-rich BD proposed by Choukroun [108] as an easier to prepare and completely autologous alternative to PRP. Dohan classified PRF as an autologous leukocyte-PRF matrix [109] termed L-PRP by some authors. Since PRF is produced by the spontaneous coagulation of the upper layers obtained after the hard spin of whole blood (Figure I-2IB), in addition to platelets, it also incorporates all the cells that remain entrapped within the fibrin clot, namely RBCs and WBCs [108-110]. In fact, contrarily to other platelet-rich BD which are produced from homogeneous suspensions of platelets, PRF clots have a cell gradient starting from the bottom, which is highly rich in RBCs, WBCs and platelets, to the top, which is almost depleted from cells [110]. Therefore, the WBCs or RBCs content of PRF can be easily reduced by cutting the bottom end of the clot [111, 112]. PRF contains several of the GF and biomolecules with therapeutic interest found in another platelet-rich BD [110, 112] (Table I-2). However, the GFs distribution throughout the PRF clot follows the cellular gradient, being more concentrated in the lower portion than in the upper portion of the clot [110, 112].

I-3.6. Platelet-derived exosomes

The platelet-derived exosomes (PEx) are extracellular vesicles with sub-micrometer diameter (40-100 nm) characterized for expressing the specific markers CD9, CD63, CD81 and the marker of platelet origin CD41 [113-115]. Blood circulating exosomes, from which the platelet-derived should represent about 25% [116], are known to be involved in vascular remodeling [117]. In fact, PEx mediate platelet atherogenic interactions with endothelial cells and monocytes [118].

PEx are true effectors within the overall platelet function and have been shown to be highly modulated by the environmental conditions. They carry several of the most important GFs of platelet origin, namely PDGF-BB, TGF-β1, VEGF, and FGF-2 [115]. Moreover, PEx incorporate mRNA [113] and might be responsible for the paracrine modulation of ICAM-1 gene expression in endothelial cells mediated by miRNAs [118, 119] (Table I-1). Despite being produced constitutively, their number and cargo depend on the platelets' activation process [114]. Aantonen and co-workers demonstrated that the activation of platelets with calcium produced higher number of exosomes than the thrombin combined with collagen or lipopolysaccharides activation [114].

For biomedical applications, PEx can be easily isolated from PL [113] or from activated PRP [115] by ultracentrifugation and ultrafiltration. Recent studies demonstrated the internalization of PEx by mesenchymal stem cells (MSCs) and its dose-dependent positive effect on cell migration, and osteogenic differentiation [113]. However, before implement PEx as a regenerative medicine approach, future research needs to explore the content of these vesicles and understand their fundamental role on tissue development.

Table I-1 Summary of cellular, sub-cellular and molecular components of BD relevant for wound healing.

	Main components	Key functions	Ref.
Plasma			
Adhesive proteins	Albumin, globulins, fibrinogen, complement proteins, and clotting factors	Haemostasis, clot maturation, cell adhesion, activation of the immune response	[73, 120]
Electrolytes	Chloride, sodium, and calcium	Haemostasis	
Growth factors	IGF-1, HGF, FGF-2, GH	Regulation of cell proliferation	
Platelets			
Alpha granules			
Adhesive proteins	Fibronectin, vitronectin, fibrinogen, vWF, P-selectin	Platelet aggregation, platelet-endothelial cell interaction, thrombus formation	[73, 99, 119-126]
Clotting factors	Factors V, XI, and XIII	Haemostasis, thrombus formation	
Growth factors	PDGF, TGF-β, VEGF, FGF-2, EGF, and BMPs	Regulation of cell proliferation, differentiation, and angiogenesis	
Cytokines/ Chemokines	IL4, IL8, TFNα, CXCL4, CXCL7, CCL2, CCL3, and CCL5	Chemotaxis, inflammatory response modulation, antimicrobial activity	
Complement proteins	Complement C3 and complement C4 precursor	Antimicrobial activity	

Others	α2-macroglobulin, α2-antiplasmin, microbicidal proteins	Protease inhibitors, antimicrobial activity	
Dense granules	ADP, ATP, calcium, serotonin, and pyrophosphates	Platelet activation, vasoconstriction	
Lysosomes	Proteases, hydrolases	Matrix degradation, antimicrobial activity	
Exosomes	Adhesion proteins (P-selectin), genetic material (mRNA, miRNA), growth factors (VEGF, PDGF, TGF-β1, FGF-2) chemokines (CXCL4, CXCL7)	Cell adhesion, paracrine communication, angiogenesis, regulation of cell fate, modulation of inflammatory response	
Leukocytes			
Neutrophils	Cytokines (IL-1, IL-4, IL-6, and TNF-α), growth factors (TGF-β1), and proteases	Phagocytosis, chemotaxis, and matrix remodelling	[93, 127]
Monocytes/ Macrophages	Cytokines (IL-6, IL-1β, IL-8, IL-10, TNF-α, GM-CSF), growth factors (TGF-β1, FGF, EGF, PDGF), proteases	Phagocytosis, modulation of inflammatory response, and matrix remodelling	
Erythrocytes	ATP, nitric oxide, haemoglobin, free radicals	Vasodilatation, antimicrobial activity	[128]

Abbreviations: bone morphogenic proteins (BMPs); C-C motif chemokine ligand (CCL); CXC chemokine ligand (CXCL); endothelial growth factor (EGF); fibroblast growth factor-2 (FGF-2); granulocyte-macrophage colony-stimulating factor (GM-CSF); growth hormone (GH); hepatocyte growth factor (HGF); insulin growth factor-1 (IGF-1); interleukin (IL); platelet derived growth factor (PDGF); tumour necrosis factor alpha (TNFα); transforming growth factor-β (TGF-β); vascular endothelial growth factor (VEGF); von Willebrand factor vWF).

Table I-2 Qualitative comparison of the most relevant GFs and fibrin present in BD relative to the physiological blood serum levels.

GFs	Platelet-poor BD	Platelet-rich BD				PEx	Refs
	FG	PG	PRGF	PRF	PL		
PDGF	-	++	+++	+++	++	+++	[56, 63, 71-73, 91, 93, 03, 115, 29-138]
VEGF	-	++	++	++	++	+++	
TGF-β1	-	+++	+++	++	++	+++	
FGF-2	-	+	+	+	++	+++	
IGF	+	+	+	+	++	u	
EGF	+	+	+++	+	+	u	

Fibrin/fibrinogen	+	++	N/A	+	+	N/A

Abbreviation: "-" ≤ 1-fold; "+" > 1-fold; "++" ≥ 5-fold; "+++" ≥ 10-fold "N/A" non-applicable; "u" unknown.

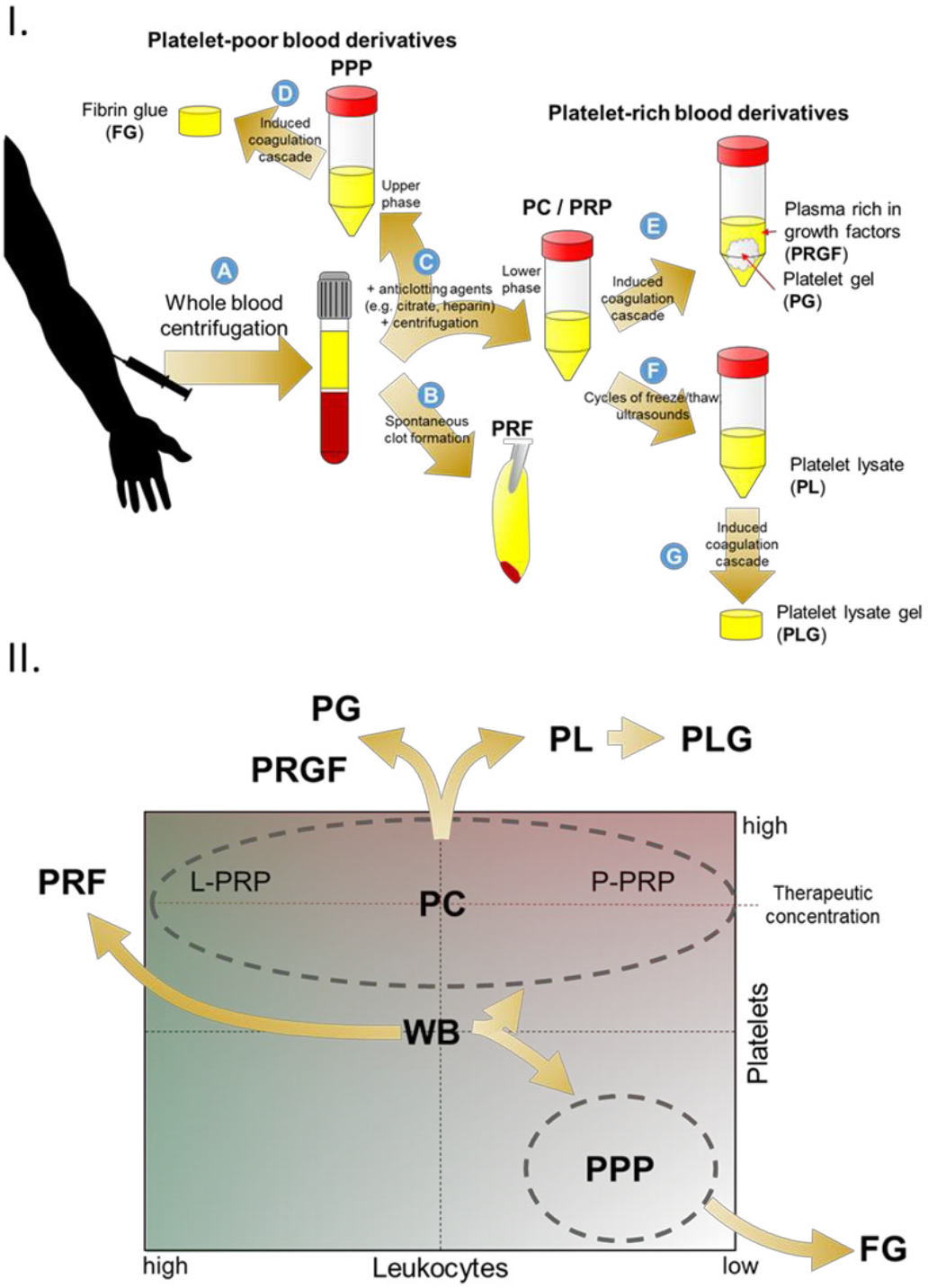

Figure I-2 Blood derivatives production and content differences. I. Conventional (manual) method for the production of different BD. A) The centrifugation of whole blood (WB) induces the separation of the blood components into 3 layers. B) The upper layer, a yellowish solution composed mainly of plasma and platelets, coagulates spontaneously if no anticlotting agent is previously added to the whole blood, originating a fibrin mesh rich in platelets and leucocytes termed platelet rich fibrin (PRF).

C) The whole blood supplementation with anticlotting agents allows the upper layer to remain liquid. It can be therefore collected (together or not with the buffy coat) and further centrifuged to produce platelet-poor plasma (PPP) or platelet concentrate (PC), also called platelet-rich plasma (PRP). D) The induction of PPP clotting originates fibrin glue (FG). Likewise, E) the induction of PC or PRP clotting originates the platelet gel (PG), and plasma rich in growth factors (PRGF). Alternatively, F) the platelets of PC/PRP can be disrupted by freeze/thaw cycles or by ultrasounds, originating a solution of platelet lysate (PL), which can produce platelet lysate gel (PLG) by fibrinogenesis activation. II. Diagram depicting the relative cellular content of each blood derivative and their precursors, compared to the physiologic levels (—) in whole blood, throughout the preparation and activation processes.

I-4. MODULATION OF BLOOD DERIVATIVES DELIVERY

Along the last few decades, the use of BD formulations in clinical applications has relied on 1) direct injection of a liquid form and activation by tissue collagen and thromboplastin, which form a gel in situ [139]; or 2) induction of the coagulation cascade prior to administration to produce a fibrin matrix-based scaffold [140]. Despite the numerous positive reports on the use of BD as biomaterial free strategies in tissue regeneration and decades of research on this field, some inconsistent and sometimes contradictory results are still frequently found [11]. The clear cause-effect relationship of these results is difficult to establish due to the complexity and also conflicting presence of multiple biomolecules in these formulations, showing that new strategies are necessary to overcome these limitations.

As previously described, the normal wound healing process involves the formation of a fibrin network that acts as a sequestering matrix for the blood cellular components and its secretome, while providing a temporary scaffold that will support tissue repair. This matrix protects the bioactive soluble cargo from fast clearance and proteolytic degradation, thus, controlling its release profile, which will ultimately dictate the overall wound biological response. In a biomimetic regenerative medicine approach, the combination of BD with biomaterial platforms might enable the control of the spatiotemporal and selective delivery of signaling biomolecules [2]. This strategy would potentiate their therapeutic effect and enhance tissue healing, shifting the normal reparative response, generally leading to non-functional scar tissue formation, towards a regenerative outcome (Figure I-1). This concept is being developed using a wide range of natural and synthetic polymers, inorganic materials, or their blends combined with BD. Several strategies have been explored to tune the biomaterial/BD interactions ranging from BD covalent (chemical or enzymatic crosslinking) and non-covalent immobilization (affinity-based systems, including electrostatic/ionic interactions, hydrogen bonding and van der Walls forces, mimicking the ECM binding mechanisms) to simple physical entrapment [14, 141]. Therefore, each specific combination of biomaterials and BD will show unique biomolecular binding affinities and release profiles, suggesting that numerous engineering

possibilities are open to be explored within this field [142-147]. In addition to the biological cues provided by BD, biomaterial intrinsic properties (physical, mechanical and chemical cues) can also add an additional level of control over cellular behavior (recently defined as Materiobiology) [148], and therefore synergistically potentiate the regenerative process.

In this section, we survey the application of specific combinations of biomaterials with BD that are intended to deliver bioactive molecules in mechanisms mimicking the cascade of natural signaling events guiding to wound healing process. These include strategies to control the selective, temporal, spatial, and concentration-dependent release profiles of BD biomolecules in order to foster tissue/organ regeneration (Figure I-3 and Table I-3). It should be noted that strategies comprising only components of the BD, are not under the scope of this review. For further information on the topic the readers are referred to other recent and comprehensive reviews [6, 107, 149-151].

I-4.1. Temporal profile

The time frame in which a beneficial therapeutic effect can be achieved with bioactive molecules is limited. For example, soluble GFs have short *in vivo* half-lives (in the order of minutes), degrading or being deactivated via several distinct pathways, including denaturation, oxidation or proteolysis, which restricts their dose and temporal bioactivity [143, 146]. On the other hand, the extended presence of GFs within a local microenvironment can lead to abnormal tissue growth. Therefore, the modulation of the temporal delivery profile of bioactive molecules from BD is crucial to control their therapeutic efficiency during the wound healing phases.

Nano - and micro-particles based carriers have been widely used in drug delivery and tissue engineering approaches in order to protect the cargo and control its release to the cells' extracellular fluid or directly within the cells [152-154]. This type of carriers has also been explored for the controlled deliver of BD. For example, PL was adsorbed on the surface of positively charged chitosan/chondroitin sulphate nanoparticles prepared by polyelectrolyte complexation of the two oppositely-charged polysaccharides [104]. Chitosan, a bioresorbable and positively charged natural polymer, has been traditionally applied to develop different carrier systems and has shown to be able to regulate the release of bioactive agents, including GFs [155, 156]. On the other hand, chondroitin sulphate is an anionic sulphated glycosaminoglycan that act as a stabilizer and also interacts with different biomolecules in the ECM [157]. Exploring their polyelectrolyte nature and biological function, chitosan/chondroitin sulphate nanoparticles allowed to modulate the temporal release profile of electrostatically adsorbed PL proteins which extend

up to 1 week. As the nanoparticles undergo fast cellular internalization (in part due to their positive surface charge), this system might be applied as an intracellular delivery vehicle of PL bioactive agents [104]. Interestingly, besides their application as carriers, these nanoparticles were also used to produce three-dimensional (3D) structures. In a bottom-up strategy, chitosan/chondroitin sulphate nanoparticles loaded with PL spontaneously self-assembled (at high concentrations) into stable 3D structures, simultaneously entrapping human adipose-derived stem cells (hASCs) [158]. The system showed an initial burst release of PDGF-BB and TGF-β1 after one day (92% and 80% of their initial amount). This release pattern was correlated with the higher hASCs proliferation observed at early time points, compared to cultures on unload particles and in form of cell pellets. The PL function was not only to be a source of bioactive molecules, but also acted on the physical stabilization of the system, creating a more appropriate 3D environment for hASCs survival and ECM synthesis. In contrast, the incorporation of the aforementioned nanoparticles within scaffolds (foams processed by supercritical CO_2) of poly(D,L-lactic acid) slowed the initial burst release of PDGF-BB, TGF-β1 and VEGF to 50% after one day, prolonging its sustained delivery up to 28 days [159]. The 3D hybrid scaffolds promoted the earlier osteogenic differentiation of hASCs compared to the controls, demonstrating the potential of the proposed combinatory approach for bone regeneration. Similarly, PL adsorbed on microparticles of hyaluronic acid (HA), a negatively charged non-sulphated glycosaminoglycan, were incorporated in calcium phosphate cements pastes for bone regeneration applications [105]. The use of HA microparticles as carrier clearly maximized the amount of PL that is possible to load into the composites cements without affecting their setting properties and also had a significant impact on the protein release profiles. Compared to direct mixing with the cements, the preloading of PL into HA microparticles resulted in higher total protein but lower TGF-β release from the composite. Interestingly, the osteogenic potential of the system was enhanced when PL was directly mixed with the cement formulation, which might be correlated with their higher release rates of TGF-β. These studies are representative of how biomaterial engineering strategies may explore the electrostatic interactions between proteins and polyelectrolyte polymeric matrices to modulate the release kinetics of BD molecules. For example, albumin, which is the main soluble protein of PL [160] and has an acidic isoelectric point (at pH 4.7), is expected to be non-specifically adsorbed and easily washed out from negatively charged polymers, such as HA [161]. On the other hand, since most of the GFs present in PL with therapeutic interest have basic isoelectric point (e.g. TGF-β at pH 8.90; PDGF-B at pH 9.39), they can electrostatically bind to negatively charged polymers, such as sulphated glycosaminoglycan, as it naturally occurs in the native ECM [162].

The different processing techniques applied to incorporate BD into scaffolding biomaterials has also shown to significantly impact the temporal release profile of GFs. For example, in chitosan based scaffolds produced by freeze-drying, adding PRP to chitosan gel before the freeze-drying process improved the scaffold structural properties and provided a more controlled release of PDGF-BB, IGF-1 and TGF-β1 for 20 days, as compared to PRP post-embedding in the scaffold [163]. On the other hand, no major differences were observed when PL was loaded before or after freeze-drying in sponge scaffolds made of chitosan glutamate, sericin and glycine, both showing similar positive outcomes in an ex vivo human skin biopsy model [164].

During the last few decades, hydrogels became one of the most popular types of biomaterials in TERM due to their inherent similarities (structural, chemical and compositional) with the native ECM of soft tissues [165, 166]. A representative example of this strategy is the recently proposed photoinducible imine crosslinking hydrogel glue system based on the imine crosslinking of o-nitrobenzyl alcohol modified-HA (which generates aldehyde groups upon light irradiation) with amine groups of the proteins present on autologous PRP and also with the tissue surface [167]. The proposed system allowed the sustained release of PDGF, TGF-β and FGF over 14 days, alleviating the burst release of GFs (2 days) observed on PG (thrombin activated). These differences might be explained by the fact that platelets in the hydrogel were not disrupted while platelets in PG were activated with thrombin, which leads to fast platelet content secretion [168], but also by the positive contribution of the modified-HA matrix on the sequestration of platelet-released GFs. Considering that platelets secrete 80-100% of their content during the first hour after activation [168], these results tend to suggest that the incorporation of inactivated platelets (PRP) in a hydrogel matrix might prolong the sustained release of bioactive molecules, improving the overall wound healing in the long-term. Interestingly, the aforementioned HA-PRP hydrogel also enhanced chondrocyte and stem cell long-term proliferation and migration, resulting as well in stronger tissue adhesiveness and integration in vivo than PG formulation [167]. In a different application, freeze-dried chitosan solubilized in L-PRP was used to form stable, non-retracting and homogenous injectable implants that coagulate in situ [169]. In a subcutaneous animal model, these chitosan-PRP implants remained physically stable for at least 2 weeks, while PRP controls lost up to 80% of their original mass and were quickly degraded in one day. Moreover, the chitosan-PRP formulations induced cell recruitment (macrophages) and angiogenesis after 14 days in vivo, suggesting a strong potential for their application in meniscus, cartilage or rotator cuff repair.

The type of BD and their nature (gel or soluble factors) in combination with biomaterials might be an interesting option to modulate the GFs temporal release profile and sequestering pattern. For example, PG and PRGF (both calcium activated) were incorporated into gelatin-nanohydroxyapatite nanofibrous composite scaffolds as a coating or lyophilized within the scaffold nanofibers, respectively [170]. Although both formulations could release GFs (VEGF and PDGF) during 4 weeks, scaffolds incorporating PRGF within the polymer matrix exhibited a steady release profile for both VEGF and PDGF whereas PG coated scaffolds exhibited an initial burst release which gradually declined over time, demonstrating that BD loading method in the biomaterials has a pronounced impact over the release patterns of their bioactive molecules. Overall, these results have been showing that by rationally selecting the biomaterials and processing technique it is possible to modulate the delivery profiles of biomolecules from BD in a time frame that can spam from days (burst release) to weeks (sustained release).

Nonetheless, these approaches still present limitations to reproduce the sequential presentation and time-dependent release of GFs involved in specific phases of wound healing. For example, TGF-β1 promotes cell recruitment during the inflammatory phase, however its presence in latter stages induces scar formation. Besides controlling this transient release, it is as well important to control the delivery of multiple GFs to allow tissue regeneration. Namely, in order to promote angiogenesis at the proliferative phase, VEGF and FGF-2 are required to form immature blood vessels. To enable this biochemical signaling at the required time, the polymer composition, type of crosslinker and crosslinking density can be manipulated to control their swelling behavior and degradation rate. Using an implant composed of PLGA microspheres loaded with BMP-2 embedded in a poly(propylene) scaffold, which was 0surrounded by a gelatin hydrogel loaded with VEGF, a sequential delivery of angiogenic factors, within the first three days, and osteogenic factors, in later stages, was achieved, which resulted in ectopic bone formation [171]. Other biomaterials that could be explored in the future are stimuli responsive materials (pH, temperature or magnetic fields) that might be used to trigger the on-demand delivery of specific biomolecules at desired healing phases [172]. At the end, these properties will engineer the temporal release of bioactive molecules to fit in the chronologic events of the wound healing process and ultimately enhance the regenerative response [141].

I-4.2. Spatial microenvironment

The spatial microenvironment of a healing wound is affected by ECM remodeling, autocrine and paracrine cell signaling, and cells fate, including proliferation, differentiation, migration and apoptosis

[141]. Along with the available tools to engineer the intrinsic physical and chemical properties of biomaterials, the precise spatial control over bioactive molecules delivery will more closely recapitulate the heterogeneity and physical/chemical gradients occurring in native ECM, and therefore, boost the regenerative process. BD have been combined with different scaffold fabrication strategies in order to promote cell migration over and to the scaffold, or to produce well defined 3D architecture that can better replicate the several length scales of the complex architecture of native tissues by the introduction of hierarchical structures in the developed composite biomaterials. Representative examples of these strategies are highlighted in the next paragraphs.

I-4.2.1. Impact on cell migration

Nano- microfiber non-woven scaffolds show unique architectural characteristics that are considered biomimetic analogues of native ECM due to their dimensional similarities to natural collagen fibres [173, 174]. These fibres meshes are usually produced by electrospinning, resulting in biomaterials with high porosity and surface area-to-volume ratios with potential applications in a wide range of tissue engineering strategies. However, they are typically based on polymeric biomaterials with limited bioactivity [174]. The incorporation of biological cues, such as BD, in their compositions has been proposed as a strategy that might promote cellular migration and proliferation, enabling an indirect control over cell behavior [174]. The incorporation of biomolecules into electrospun nanofibers can be achieved by simple blending with the polymeric spinning solution or using emulsion and coaxial electrospinning strategies [175, 176]. As an example of these approaches, PL was blended with chitosan and poly(ethylene) oxide to produce electrospun nanofiber meshes [177]. Remarkably, the biological activity of PRP was not affected by the processing conditions. Although 70% of total protein content was released within 3 hours and the remaining content after 24 hours, the nanofibrous-PL membrane stimulated cell proliferation and, in formulations with higher concentration of PL, keratinocytes showed a more spread morphology, indicating a synergistic positive effect of nanotopography and biological cues. Liu and co-workers incorporated PRGF (using dextran as emulsion stabilizer) into polycaprolactone (PCL)/gelatin nanofibers by emulsion electrospinning technique in order to minimize the denaturation of PRGF proteins and increase the bioactivity of the scaffolds [178]. Although the release of bioactive GFs from the scaffold showed a burst in the first 24 hours, it lasted for nearly 30 days, resulting in improved proliferation and chemotactic effects on bone marrow MSCs, and more interestingly, promoted in vitro chondrogenic differentiation.

The enhanced bioactivity of the scaffolds was also demonstrated in vivo in rabbit osteochondral defects, improving cartilage wound healing and suggesting to have anti-inflammatory effects in the joint cavity.

The persistent presence of bacteria and endotoxins at the wound site is known to prolongs the inflammatory phase and may lead to chronic wound infections [179]. An injectable hydrogel system composed of chitosan and freeze-dried PG (calcium activated) combined with antibiotic nanoparticles (tigecycline) was explored as a convenient and effective therapeutic alternative to treat chronically infected wounds [180]. Tigecycline sustained release inhibited bacterial growth over time and reduced the inflammatory phase, whereas the addition of PG enhanced proliferation and migration of fibroblasts in vitro. Interestingly, other studies have also shown that the combination of BD with biomaterials might have a positive impact on resolving the subsequent inflammatory response occurring after their implantation. For example, PRGF (calcium activated) was impregnated into gelatin hydrogels incorporating micelles of sphingosine-1-phosphate agonist to induce macrophages recruitment [181]. Within 7 days, about 90% of TGF-β1 and stromal cell derived factor-1 was delivered and both soluble factors were detectable after 14 days in vivo. Gelatin hydrogels incorporating micelles and PRGF recruited higher number of macrophages that lead to an initial increase of pro-inflammatory cytokines (TNF-α) level, while 10 days after implantation they increased the production of anti-inflammatory cytokines (IL-10 and TGF-β1) and osteoprotegerin, an osteoclastogenesis inhibitory factor. Thus, sphingosine-1-phosphate agonist and PRGF showed a synergistic enhancement effect on the migration and recruitment of macrophages to the wound site that modulated the production of inflammatory mediators and induced granulation tissue formation and bone regeneration [181].

In order to recreate the biological gradients of the ECM, which are known to modulate the directional migration and overall cellular physiological behavior [182], photocrosslinkable methacrylated gellan gum was combined with PL to generate concentration gradients of bioactive molecules along 3D hydrogel fibres produced by microfluidic strategies [183]. Using fibres containing inverse gradients of human umbilical vein endothelial cells and PL, it was shown that areas with lower PL content decreased cell viability whereas the PL-enriched section increased cell viability and induced cell adhesion and colonization after 12 hours and 7 days in culture. In a different approach, coating of hydroxyapatite/ β-tricalcium phosphate scaffolds with PL also showed to increase chemo-attraction and adhesion of MSCs and endothelial cells on the scaffold and to induce MSCs to produce and secrete pro-angiogenic proteins [184].

I-4.2.2. Controlled architecture

The regeneration of complex tissue interfaces has been explored by the combination of different materials in biphasic systems. These systems are designed to regenerate both the soft and hard regions of tissue interfaces by controlling the gradients of properties that define heterogeneous spatial microenvironments [185]. Bi-layered gelatin/β-tricalcium phosphate sponges loaded with either MSCs, chondrocytes and L-PRP (chondrogenic layer) or MSCs and BMP-2 (osteogenic layer) were explored to repair osteochondral defects of the talus in horses [186]. This study demonstrated that the bilayer sponges combined with cell and biological factors promoted significantly higher osteochondral regeneration and reduced the defect size, as observed by radiography, quantitative computed tomography and macroscopic and histological evaluation 4 months after surgery, than the control group (unloaded bilayer sponges). In a similar approach, a bilayered system has been explored for the regeneration of periodontium in a critical 3-wall intrabony periodontal defect in rats [187]. Calcium phosphate cement incorporating HA microspheres loaded with PL was used to promote the regeneration of alveolar bone side while PL-genipin self-crosslinking membrane was used for the regeneration of periodontal soft tissue. The combination of both systems was degraded within 6 weeks after implantation, showing a lower epithelial downgrowth and formation of periodontal ligament by the immobilization of PL proteins over the tooth root surface [187].

In recent years, advanced additive manufacturing technologies, such as 3D printing and bioprinting, have emerged in the field of TERM as fabrication strategies that have the potential to engineer patient personalized scaffolds and living constructs with finely-tuned physicochemical properties and tailored components along defined positions of the 3D space [188]. As an example of the combination of these technologies with the incorporation of BD, 3D printed collagen/PCL/bioceramic scaffolds were explored to control the release of GFs from recombinant origin and from PRP [189]. After optimizing the composition and processing parameters that maximized the osteogenic potential of collagen/PCL biocomposite scaffolds and resulted in a sustained release of protein biomolecules (tested with BSA), the biomaterials were loaded with bioceramic, bioceramic/recombinant human BMP-2 or bioceramic/PRP. Interestingly, the sustained release of bioactive molecules from PRP-loaded formulation resulted in increased ALP activity, calcium deposition and osteocalcin activity by osteoblast-like-cells in comparison with other control groups, demonstrating that the proposed strategy might have the potential to enhance bone regeneration. In an attempt to recreate the different length scales and functions of native ECM, 3D printing (microscale control) was combined with other fabrication approaches such as layer-by-layer

surface coating (nano/meso scale control) and freeze-drying (fibrillar structures) to produce 3D hierarchical scaffolds for bone tissue engineering [190]. Combining these different top-down and bottom-up methodologies, 3D printed structures based on PCL were coated by layer-by-layer assembly of marine-origin polysaccharides (carrageenan and chitosan) and PL, and subsequently freeze-dried to shape the layer-by-layer structures into nano/submicron-fibrils and nanocoatings. The sulphated and aminated nature of carrageenan and chitosan, respectively, increases the similarity to native ECM, being good candidates for the attraction and stabilization of GFs as mimetics of native glycosaminoglycans [191, 192]. Remarkably, the PCL- layer-by-layer -PL scaffolds could induce the osteogenesis of hASCs without relying on supplementation of culture media with osteogenic factors. The promising results of this methodology open the door to develop tunable PL hierarchical scaffolds to instruct stem cells towards different lineages.

I-4.3. Selection of specific bioactive molecules

The ability to control the delivery of specific bioactive molecules is highly important to precisely modulate the biological signals of the local cell microenvironment. The use of recombinant GFs in combination with finely engineered scaffolds might be a possible solution, however these are very expensive strategies having several technical and biological drawbacks [193]. Therefore, the components of BD, a cost-effective source of bioactive proteins, might be selectively and non-covalently bond to biomaterials constructs following different functionalization strategies.

Besides structural protein, ECM is composed of proteoglycans containing polysaccharides with different sulfation patterns, which specifically interact with soluble bioactive molecules and regulates their availability and functionality within cellular microenvironment [143, 145]. For example, heparin, a highly sulphated glycosaminoglycan, is known to play a major role on the specific binding, sequestration and presentation of GFs containing heparin-binding domains [13]. In a recent work, PRP was combined with heparin-conjugated PLGA nanospheres and commercial fibrin gels [194]. This strategy prolonged the retention of heparin-binding GFs such as PDGF-BB (39% for formulations containing nanospheres vs 88% for PRP control in the first 6 h), while preserving their bioactivity. It is reasonable to expect that it might also have similar impact on the release profile of other heparin-binding GFs (e.g. FGF-2 and VEGF) present in PRP [195, 196]. Furthermore, the proposed system showed superior healing outcomes, specifically dermal and epidermal regeneration and angiogenesis acceleration, as compared to the controls in a mouse skin wound model [194]. Moreover, PLGA degradation produces lactate that accelerates

angiogenesis, activates pro-collagen factors and recruits endothelial progenitor cells to the wound site, which could have a synergistic positive impact on the obtained results [152]. Despite the obvious benefits of applying heparin as binding motif for certain GFs, the use of high doses of heparin is associated with several health risks due to its anticoagulant activity [197] that should not be disregarded in materials design.

The protein binding specificity of sulphated glycosaminoglycans is highly influenced by the sulfation position and patterns [198]. Therefore, the influence of charge and sulfation degree of different polysaccharides on the selective sequestration of bioactive molecules from BD have been studied using self-assembled PL-polysaccharide multilayered nanocoatings [199]. While the intermediate sulphated polysaccharide (ι-carrageenan) achieved high levels of FGF-2, VEGF and PDGF adsorption, the low sulphated polysaccharide (κ-carrageenan) adsorbed high amounts of PDGF and intermediate levels of VEGF. On the other hand, heparin (highly sulphated) showed only high levels of VEGF adsorption while unsulfated polysaccharides (alginate and chitosan) general led to the adsorption of low levels of all tested GFs. These results highlight the potential of surface engineering strategies to selectively incorporate BD components into biomaterials and to modulate cell-material interactions. It is well known that the maintenance of adequate concentrations of appropriate biological factors is of key importance for the outcomes of the wound healing events. For example, the presence of the PDGF is important in MSCs proliferation, however its anti-morphogenic properties might impair the bone regrowth [200]. Therefore, in a regenerative approach, highly sulphated polymer-PL nanocoatings might be more adequate to promote the vascularization of tissue engineered constructs or to induce the vascular differentiation of stem cells since they lead to the incorporation of lower levels of PDGF and higher levels of VEGF than their less sulphated analogues [199]. This hypothesis has been tested in human umbilical vein endothelial cells, where the highly sulphated polysaccharides-PL nanocoatings induced cells to rapidly form tube-like structures accompanied by an increased expression of angiogenic associated genes [201].

The immobilization of antibodies on the surface of biomaterials to recognize and recruit specific GFs from BD is another design option being explored with impressive results. For example, Custódio and co-workers immobilized anti-PDGF-BB antibody on chitosan microparticles surface [202]. After incubation of the microparticles with PL, it was observed a significantly decrease of PDGF-BB (68%) in the remaining PL solution, whereas the content of VEGF (18%) and TGF-β1 (20%) only registered a slight decrease, demonstrating the expected highly selective GF recruitment capability of this strategy. Furthermore, the proposed system allowed a faster attachment of hASCs, which lead to the formation of 3D constructs

after 12 hours while control groups were not able to form stable aggregates. Similar approaches have been adopted for the immobilization of antibodies on the surface of electrospun nanofibers [176, 203]. With this strategy, it was possible to selective bind VEGF, TGF-β1 or FGF-2 from a pool of proteins (PL) without affecting its bioactivity [203]. Furthermore, the simultaneous immobilization of multiple antibodies, distributed in a mixed or in a spatially controlled fashion, was also shown [203]. Although authors did not target any specific tissue, it can be foreseen that this strategy can be customized for specific regenerative medicine strategies, allowing, for example, the immobilization of GFs in a single or multiple binding approach, or the production of GFs patterns and gradients.

I-4.4. Blood derivatives concentration

The amount of BD delivered to the wound niche and, thus, bioactive molecules concentration, will affect the number of ligand-receptor events occurring in a given time frame and the extent of downstream intracellular signaling cascades driving tissue regeneration. Although, to the best of our knowledge, the specific GFs concentrations that trigger the regenerative pathways are not described yet, previous studies using PRP formulations in in vitro cultures, have reported that there is a dose-dependent effect of BD concentration on e.g. cell proliferation and differentiation [204], being therefore a relevant parameter that should be optimized when combined with biomaterials. For instance, collagen/gelatin scaffolds were impregnated with reconstituted freeze-dried PL in order to study the optimal PL concentration (1x, 2x, 3x, or 4x concentrated) to promote wound healing in vivo [205]. The release of GFs from the scaffolds increased in a concentration-dependent fashion and correlated with the scaffold degradation profile. Moreover, the 2x formulation effectively accelerated wound healing, enhancing cell proliferation and vessel growth in granulation tissue without obvious inflammatory reactions in a full-thickness skin defect. In a similar approach, gelatin sponges with different concentrations of PRGF (1x, 3x and 5x) were implanted in alveolar bone defects in rats and 3x PRGF sponges enhanced bone regeneration outcomes compared with the other formulations [206]. Remarkably, when PRP was used without the gelatin, it detached from the injury site and did not contribute to the regenerative process, evidencing the importance of biomaterials to allow the retention of BD at the injury site and the localized delivery of their signaling molecules.

More recently, photocrosslinkable methacrylated-HA hydrogels were blended with different concentrations of PL (0, 50 and 100%) [62]. Both PL formulations exhibited a similar release profile, although the amount of total released protein was proportional to the initial amount of protein incorporated

in the hydrogels. Surprisingly, the amount of FGF-2 released, after enzymatic degradation of the hydrogels, was negatively correlated with the initial protein loading. Similarly, PL incorporation positively impacted human periodontal ligament fibroblasts proliferation and metabolic activity. Furthermore, using the same system, it was possible to safely preserve and store hASCs and PL-derived GFs under standard cryopreservation protocols, showing the potential of this system as off-the-shelf injectable formulation [207].

The use of remote magnetic stimulation combine with magnetic responsive biomaterials might be a novel strategy to modulate the released kinetics in a timely and a controlled space that can potentiate the regenerative process [208]. For example, magnetic nanoparticles were incorporated in a methacrylated chondroitin sulphate hydrogel loaded with PL. Under magnetic stimulation, PDGF-BB release was faster and higher compared to the non-stimulated group. Besides enabling the localized control of GFs release, magnetic stimulation showed to modulate the swelling, matrix stability and degradation, which in combination with PL bioactivity, had a synergistic impact on cell morphology and synthesis of tendon- and bone-like matrix in an in vitro interfacial co-culture model (hASCs and tendon-derived stem cells).

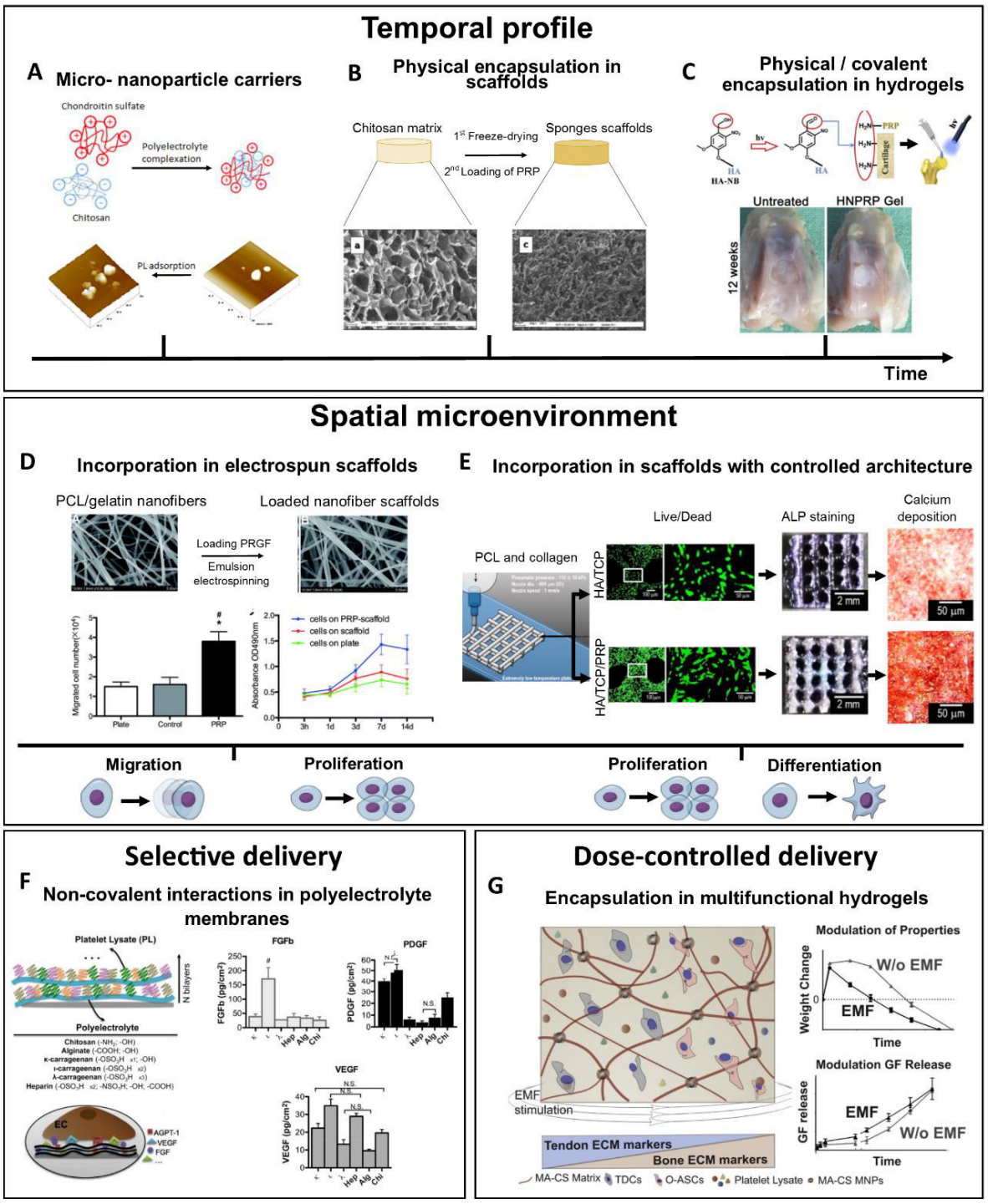

Figure I-3 Strategies incorporating blood derivatives into biomaterials in order to modulate BD temporal profile: A) PL was loaded into chitosan/chondroitin sulphate nanoparticles, adapted from [104]. Copyright 2012, John Wiley and Sons. B) PRP was loaded into sponges composed of chitosan, reproduced with permission [163]. Copyright 2013, John Wiley and Sons. C) PRP was covalent crosslinked and physical encapsulated into modified HA injectable hydrogels. Reproduced with permission [167]. The control over cellular spatial distribution by D) PRGF proteins incorporation in electrospun meshes, reproduced with permission [178]. Copyright 2017, Elsevier. E) PRP incorporated into 3D printed polycaprolactone scaffold, reproduced with permission [189]. Copyright 2017, Elsevier. Finally, the modulation of selective bioactive molecules by EF) polysaccharides presenting different sulfation degrees and charges, reproduced with permission [199]. Copyright 2015, Elsevier. BD

concentration-dependent delivery by G) PL incorporation in magnetic responsive hydrogels, reproduced with permission [208]. Copyright 2017, Elsevier.

I-5. TOWARDS A CLINICAL TRANSLATION

Previous *in vitro* and *in vivo* studies have consistently showed that the combination of BD with biomaterials might be a suitable strategy to modulate the delivery of their bioactive molecules and maximizes the synergistic biomaterial/BD therapeutic efficacy. Some of those therapeutic products are on the way to clinical translation. In this section, we review biomaterials loaded with BD that have been or are currently undergoing clinical studies for skin, maxillofacial, orthopedic, and wound healing related applications. In a case report, three patients with chronic pressure ulcers were treated with PG (calcium activated) and PRP loaded in alginate beads for the sustained delivery of BD bioactive molecules [209]. Despite the small patient sample size, this approach increased granulation tissue in-growth and vascularity, improving wound healing. In a different case study, one patient with a two years nonhealing ulcer was treated with activated PRP covered by a gelatin sheet over 5 days [210]. The treatment improved granulation tissue formation over the wound. After thirty-three days, a new gelatin sheet impregnated with freeze-dried PRP was applied into the injury site, which healed without recurrent ulceration after 9 months. In the maxillofacial research area, a clinical study with ten patients used PG (thrombin and calcium activated) combined with MSCs and HA scaffold as a periodontal regenerative therapy for soft-tissue augmentation [211]. No adverse effects were observed during the follow-up time and all patients reported high satisfaction, demonstrating various degrees of regeneration and defect filling. The involvement of progenitor cells in this process might have an influence in the different outcomes. Currently, a randomized clinical trial (NCT03227367) composed of healthy individuals and chronic periodontitis patients is investigating biphasic calcium phosphate combined with PRF for inhibiting osteoclasts differentiation and bone loss [212].

Some commercial products using BD in combination of biomaterials are already approved and distributed for musculoskeletal disorders. One example is Vergenix™ STR (CollPlant Ltd., Ness-Ziona, Israel) composed of plant derived recombinant human type I collagen mixed with PRP for lateral epicondylitis [213]. In the clinical trial, the product showed to have a clinical success rate (>25% improvement in pain and motion) significantly better than corticosteroids or PRP (standard treatments) and reduction in pain and recovery of motion using standard evaluation methodology at 3 months and 6 months post treatment. Another commercial product, BST-CarGel® (Smith and Nephew, MA, USA), is

composed of chitosan gel and PRP (uncoagulated) [214]. This medical device is used to stabilize the microfracture-based blood clot (standard and first-line surgical treatment) and it was shown to be an effective mid-term cartilage repair treatment, having a significantly higher therapeutic outcome compared with the microfracture alone in a randomized controlled clinical trial.

Table I-3 Summary of the most relevant preclinical studies using combinations of BD with biomaterials.

	Type of material	Animal Model	Major results	Target tissue	Ref.
Time	Autologous PRP covalently bound to photoresponsive HA hydrogel	Rabbit full-thickness osteochondral defect	In situ hydrogel filled and adapted to the injury shape. After 12 weeks, regenerated hyaline cartilage integrated well with adjacent tissue.	Cartilage	[167]
	Chitosan solubilized in allogenic L-PRP	Subcutaneous rabbit model	Chitosan-PRP implants resided for at least 14 d and induced cell recruitment (macrophages), angiogenesis and showed tissue building capacity.	Meniscus, Cartilage, Rotator Cuff	[169]
Space	Autologous PRGF and dextran incorporated in PCL/gelatin nanofibers	Rabbit full-thickness cartilage and subchondral bone defect	Increased collagen II, aggrecan, and Sox9 synthesis, while decreased collagen I. Regenerated cartilaginous matrix was observed around the clusters of regenerated chondrocytes, and also relieved inflammatory reactions.	Cartilage	[178]
	Autologous PRGF loaded in gelatin hydrogel with sphingosine-1-phosphate agonist micelles	Rat bone defect	Promoted migration and recruitment of macrophages and induced granulation tissue formation and bone regeneration.	Bone	[181]
	Bilayer sponges: gelatin/β-tricalcium phosphate loaded with MSCs, chondrocytes and autologous L-PRP or MSCs and BMP-2.	Equine full-thickness osteochondral defect	4 months after surgery, the defects were covered with smooth white tissue. The upper part was filled with cartilage-like tissue and better bone regeneration was observed in the lower part.	Joint disorder (Osteochondrosis)	[186]
	Bi-layered system: allogeneic PL loaded in calcium phosphate cement with HA- microspheres and PL-genipin	Rat critical 3-wall intrabony periodontal defect	The construct was completely degraded after 6 weeks and was substituted by highly vascularized aligned connective tissue. It restricted the formation of long epithelial junctions and enabled the formation of periodontal ligament.	Alveolar bone	[187]

Selective	Autologous PRP with FG loaded in heparin-conjugated PLGA nanospheres	Mouse skin wound model	Enhanced keratinocyte migration, superior healing properties (dermal and epidermal regeneration) and angiogenesis acceleration.	Skin	[194]
Concentration	Allogeneic freeze-dried PL (1x, 2x, 3x, or 4x concentrated) impregnated in collagen/gelatin scaffolds	Mouse full-thickness skin defect	2x formulation effectively accelerated wound healing, enhancing cell proliferation and vessel growth in granulation tissue without obvious inflammatory reactions	Skin (dermis-like tissue)	[205]
	Autologous PRGF (1x, 3x and 5x concentrated) impregnated in gelatin sponges	Rat alveolar bone defect	3x PRGF hydrogel increased new bone regeneration.	Alveolar bone	[206]

Abbreviations: PRP (platelet rich-plasma); HA (hyaluronic acid); L-PRP (leukocyte PRP); PRGF (platelet rich-in growth factors); PCL (polycaprolactone).

I-6. CONCLUDING REMARKS AND FUTURE DIRECTIONS

The use of BD from autologous sources as therapeutic strategies, particularly targeting the regeneration of musculoskeletal tissues, rapidly moved into clinical trials due to their inherent advantages in terms of translation potential. However, these efforts to rapidly translate fundamental science into medical applications lead to the poor understanding of the biological and cellular mechanisms behind their use. The need for standardization of PRP preparation methods continues to be a common argument raised to explain discrepancies among studies and the lack of efficacy of some PRP based therapies in clinical settings [215-217]. While standardization issues may be solved by the definition of good manufacturing practice protocols that generate reproducible BD formulations and the use of platelets from a pool of donors, establishment of clear relationships between the overwhelming numbers of bioactive molecules present in different BD formulations with the resulting therapeutic effects may be a herculean task. As highlighted in this review, the development of more controllable systems for the delivery of a well characterized population of bioactive molecules to target cell niches will certainly improve many clinical aspects behind the use of BD.

The combination of BD with biomaterials has emerged as a synergistic strategy to modulate the selective spatio-temporal and dose-controlled release of signaling molecules that will orchestrate the swing between tissue regeneration and scar formation. Taking in consideration the complex microenvironment present in wound healing, the co-delivery of several bioactive molecules (e.g. GFs and cytokines) from BD will most likely result in a more efficient regenerative microenvironment than the delivery of a single type of biomolecule. To date, most of the proposed strategies to deliver and release BD in a temporal controlled

fashion relied on the use of nano- microparticulate systems as carriers. These systems enabled the delivery of encapsulated bioactive molecules in short periods (hours), showing a temporary effect. In a bottom-up strategy, the physical encapsulation of BD in sponges and hydrogels showed to prolong the release (weeks to months) of biomolecules, enhancing their stability and therapeutic efficiency. Implementing these relatively simple strategies, it is possible to modulate the release profile of different biomolecules by the rational selection of biomaterials (tuning the matrix/biomolecule interactions) and by controlling their degradation rates. However, most of these systems remain as proof-of-concept, since their design considerations and physicochemical properties still require further optimization. In particular, it is necessary to add control over the delivery of multiple bioactive factors at distinct release kinetics in order to enable a dynamic temporal release that matches with the wound healing events.

Regarding the spatial coordination, we have considered systems where the incorporation of BD influences cell fate towards tissue regeneration, mainly cellular migration, proliferation and differentiation. For example, in 3D hydrogel fibres, BD increased cellular colonization and adhesion to the biomaterials as well as cell viability. However, these systems have limitations in terms of mimicking the native tissues complexity and wound healing microenvironment (different cells types, signaling molecules and biochemical/biomechanical properties). The advent of 3D printing/bioprinting technologies in TERM applications might help to overcome some of the reported limitations by enabling to fabricate customized constructs with precise 3D patterns of different biomaterials, cells and signaling molecules [188]. At the moment, only a few studies explored the potential of these fabrication techniques in combination with BD as bioinstructive cues. Therefore, this is an interesting research topic open to be explored in which we foresee major developments in the near future.

The selective delivery of biomolecules from BD can be modulated by different strategies, including the non-covalent immobilization within biomaterial nanocoatings (mimicking the natural interactions occurring in the ECM) or by the covalent functionalization of the biomaterial surface with antibodies, which enables the specific binding of targeted bioactive molecules. In particular, due to their inherent high molecular specificity and affinity, the bioconjugation of antibodies to biomaterials is a promising approach to selectively bind GFs of interest and modulate cell fate, avoiding the conflicting co-delivery of bioactive molecules with opposite roles that might have an undesired outcome, such as anti-morphogenic (e.g. PDGF-BB) and morphogenic factors (e.g. VEGF). Antibodies immobilization has however several limitations that hider their practical application and clinical translation such as high cost, low shelf stability or the associated immunological risk for humans [218]. In order to explore the full potential of GFs

sequestering biomaterials in combination with BD, molecular imprinting method can create in synthetic polymers selective recognition sites for a specific molecular template, resulting in materials that mimic antibody combining sites [219, 220]. By exploring the molecular imprinting technology, it would be conceptually feasible to produce intelligent biomaterials able to remove undesired components or selectively recruit the bioactive molecules of interest (single or multiple) from a pool of proteins (BD). Another important aspect in order to modulate the selective delivery of GFs is the processing of BD. Fibrinogen present in different BD formulations and coagulation cascade inductors will have a marked impact over the physical properties of the resulting fibrin matrix and the ability to retain and present GFs [58]. Moreover, this will also affect the downstream temporal platelet degranulation profile (fast with thrombin and slow with calcium) [168]. Thus, different activation strategies will affect GFs bioavailability which will lead to differences in wound healing process [162, 221] and to various effects at cellular level [60].

Due to the emerging research highlighting the importance of cell-derived exosomes in tissue development and homeostasis regulation [222], the use of platelet-derived exosomes could be a simple and safe alternative to modulate tissue regeneration. However, despite their promising benefits, there is still a lack of comprehension on the biological relevance of the activation process to produce populations with defined cargos, which should be addressed in future research. Additionally, in the authors opinion, future studies should also invest more research efforts on studying the release profile of multiple therapeutic molecules (GFs, cytokines and others bioactive molecules) in order to improve the general understanding on the affinities between the biological cues of BD and biomaterial matrices. This data would provide the necessary knowledge to rationally select systems that enable a tissue-specific spatio-temporal, selective and dose-dependent release profile of bioactive molecules present on BD, more than only controlling the quantity of GFs that is loaded.

Currently, the major challenge in the field is the translation of these approaches to clinical use. Clinical cases are based in small study samples that showed heterogeneous degree of regeneration, thus, being difficult to understand the potential of each formulation. Despite the fast translation of BD to clinical use, the combination with biomaterials is challenging, because they require an approval as new biomaterial-based products, even when using materials already approved in other applications due to the different properties and possible different outcomes [223]. Although, this process will necessarily slow its translation to the clinics, in our opinion, it is the right direction in order to get the best of BD's therapeutic potential.

Major advances have been made over the recent years to develop these systems, but there remain a number of challenges that will need to be addressed in the future. As a strategic pipeline, the definition of good manufacturing practice protocols to standardize the production method of BD formulations, together with the continuous understanding of the basic biology of BD in wound healing modulation will provide robust and reproducible therapeutic results. Moreover, specifically designed biomaterials incorporating BD that bind to and sequester biomolecules, and the full understanding of the nature of these interactions will enable engineering the wound healing environment towards tissue regeneration.

I-7. REFERENCES

[1] S.A. Eming, P. Martin, M. Tomic-Canic, Wound repair and regeneration: mechanisms, signaling, and translation, Sci. Transl. Med., 6 (2014) 265.

[2] G.C. Gurtner, S. Werner, Y. Barrandon, et al., Wound repair and regeneration, Nature, 453 (2008) 314.

[3] G.C. Gurtner, M.J. Callaghan, M.T. Longaker, Progress and potential for regenerative medicine, Annu. Rev. Med., 58 (2007) 299.

[4] J.A. Hubbell, Biomaterials in tissue engineering, Nat. Biotechnol., 13 (1995) 565.

[5] R. Langer, J. Vacanti, Advances in tissue engineering, J. Pediatr. Surg., 51 (2016) 8.

[6] S. Padilla, M. Sánchez, G. Orive, et al., Human-Based Biological and Biomimetic Autologous Therapies for Musculoskeletal Tissue Regeneration, Trends Biotechnol., (2016).

[7] A. Mishra, J. Woodall, A. Vieira, Treatment of tendon and muscle using platelet-rich plasma, Clin. Sports Med., 28 (2009) 113.

[8] Y. Zhu, M. Yuan, H. Meng, et al., Basic science and clinical application of platelet-rich plasma for cartilage defects and osteoarthritis: a review, Osteoarthr. Cartil., 21 (2013) 1627.

[9] P.S. Babo, R.L. Reis, M.E. Gomes, Periodontal tissue engineering: current strategies and the role of platelet rich hemoderivatives, J. Mater. Chem., 5 (2017) 3617.

[10] R.J. Miron, M. Fujioka-Kobayashi, M. Bishara, et al., Platelet-rich fibrin and soft tissue wound healing: a systematic review, Tissue Eng. Part B Rev., 23 (2017) 83.

[11] R.-J. de Vos, J. Windt, A. Weir, Strong evidence against platelet-rich plasma injections for chronic lateral epicondylar tendinopathy: a systematic review, Br. J. Sports Med., 48 (2014) 952.

[12] V.Y. Moraes, M. Lenza, M.J. Tamaoki, et al., Platelet-rich therapies for musculoskeletal soft tissue injuries, Cochrane Database Syst Rev., 12 (2013) CD010071.

[13] I. Capila, R.J. Linhardt, Heparin–protein interactions, Angew. Chem. Int. Ed. Engl., 41 (2002) 390.

[14] L. Macri, D. Silverstein, R.A. Clark, Growth factor binding to the pericellular matrix and its importance in tissue engineering, Adv. Drug Deliv. Rev., 59 (2007) 1366.

[15] A. Atala, D.J. Irvine, M. Moses, et al., Wound healing versus regeneration: role of the tissue environment in regenerative medicine, MRS Bull., 35 (2010) 597.

[16] A.J. Singer, R.A. Clark, Cutaneous wound healing, N. Engl. J. Med., 341 (1999) 738.

[17] E.R. Zielins, D.A. Atashroo, Z.N. Maan, et al., Wound healing: an update, Regen. Med., 9 (2014) 817.

[18] G.Y. Chen, G. Nuñez, Sterile inflammation: sensing and reacting to damage, Nat. Rev. Immunol., 10 (2010) 826.

[19] R. Shechter, M. Schwartz, CNS sterile injury: just another wound healing?, Trends Mol. Med., 19 (2013) 135.

[20] S.E. Hankinson, W.C. Willett, G.A. Colditz, et al., Circulating concentrations of insulin-like growth factor I and risk of breast cancer, Lancet, 351 (1998) 1393.

[21] G.L. Hortin, D. Sviridov, N.L. Anderson, High-abundance polypeptides of the human plasma proteome comprising the top 4 logs of polypeptide abundance, Clin. Chem., 54 (2008) 1608.

[22] M.H. Klinger, W. Jelkmann, Role of blood platelets in infection and inflammation, J. Interferon Cytokine Res., 22 (2002) 913.

[23] M.R. Thomas, R.F. Storey, The role of platelets in inflammation, J. Thromb. Haemost., 114 (2015) 449.

[24] A.T. Nurden, Platelets, inflammation and tissue regeneration, Drug Deliv. Transl. Res., 105 (2011) S13.

[25] S. Barrientos, O. Stojadinovic, M.S. Golinko, et al., Growth factors and cytokines in wound healing, Wound Repair Regen., 16 (2008) 585.

[26] A.T. Nurden, P. Nurden, M. Sanchez, et al., Platelets and wound healing, Front. Biosci., 13 (2008) 3532.

[27] E.M. Golebiewska, A.W. Poole, Platelet secretion: From haemostasis to wound healing and beyond, Blood Rev., 29 (2015) 153.

[28] P. Martin, S.J. Leibovich, Inflammatory cells during wound repair: the good, the bad and the ugly, Trends Cell Biol., 15 (2005) 599.

[29] D.M. Mosser, J.P. Edwards, Exploring the full spectrum of macrophage activation, Nat. Rev. Immunol., 8 (2008) 958.

[30] T.A. Wynn, A. Chawla, J.W. Pollard, Macrophage biology in development, homeostasis and disease, Nature, 496 (2013) 445.

[31] B. Behm, P. Babilas, M. Landthaler, et al., Cytokines, chemokines and growth factors in wound healing, J. Eur. Acad. Dermatol. Venereol., 26 (2012) 812.

[32] B. Hinz, S.H. Phan, V.J. Thannickal, et al., The myofibroblast: one function, multiple origins, J. Pathol., 170 (2007) 1807.

[33] T. Wynn, Cellular and molecular mechanisms of fibrosis, J. Pathol., 214 (2008) 199.

[34] T.A. Wynn, T.R. Ramalingam, Mechanisms of fibrosis: therapeutic translation for fibrotic disease, Nat. Med., 18 (2012) 1028.

[35] A. Page-McCaw, A.J. Ewald, Z. Werb, Matrix metalloproteinases and the regulation of tissue remodelling, Nat. Rev. Mol. Cell Biol., 8 (2007) 221.

[36] S. Levenson, E. Geever, L. Crowley, et al., Healing of rat skin wounds, Annals of Surgery, 161 (1965) 293.

[37] S.J. Forbes, N. Rosenthal, Preparing the ground for tissue regeneration: from mechanism to therapy, Nat. Med., 20 (2014) 857.

[38] L. Li, B. Yan, Y.-Q. Shi, et al., Live imaging reveals differing roles of macrophages and neutrophils during zebrafish tail fin regeneration, J. Biol. Chem., 287 (2012) 25353.

[39] H. Lu, D. Huang, N. Saederup, et al., Macrophages recruited via CCR2 produce insulin-like growth factor-1 to repair acute skeletal muscle injury, FASEB J., 25 (2011) 358.

[40] M. Saclier, H. Yacoub-Youssef, A.L. Mackey, et al., Differentially Activated Macrophages Orchestrate Myogenic Precursor Cell Fate During Human Skeletal Muscle Regeneration, STEM CELLS, 31 (2013) 384.

[41] S.A. Eming, T. Krieg, J.M. Davidson, Inflammation in wound repair: molecular and cellular mechanisms, J. Invest. Dermatol., 127 (2007) 514.

[42] A. Leask, D.J. Abraham, TGF-β signaling and the fibrotic response, FASEB J., 18 (2004) 816.

[43] R. Montesano, L. Orci, Transforming growth factor beta stimulates collagen-matrix contraction by fibroblasts: implications for wound healing, Proceedings of the National Academy of Sciences, 85 (1988) 4894.

[44] P.-J. Wipff, D.B. Rifkin, J.-J. Meister, et al., Myofibroblast contraction activates latent TGF-β1 from the extracellular matrix, J. Cell Biol., 179 (2007) 1311.

[45] K. Riedel, F. Riedel, U.R. Goessler, et al., TGF-β Antisense Therapy Increases Angiogenic Potential in Human Keratinocytes In Vitro, Arch. Med. Res., 38 (2007) 45.

[46] P.B. Saadeh, B.J. Mehrara, D.S. Steinbrech, et al., Transforming growth factor-β1 modulates the expression of vascular endothelial growth factor by osteoblasts, Am. J. Physiol., Cell Physiol., 277 (1999) C628.

[47] M. Shah, D.M. Foreman, M. Ferguson, Neutralisation of TGF-beta 1 and TGF-beta 2 or exogenous addition of TGF-beta 3 to cutaneous rat wounds reduces scarring, J. Cell. Sci., 108 (1995) 985.

[48] B.-S. Ding, D.J. Nolan, J.M. Butler, et al., Inductive angiocrine signals from sinusoidal endothelium are required for liver regeneration, Nature, 468 (2010) 310.

[49] C. Preeja, S. Arun, Platelet-rich fibrin: Its role in periodontal regeneration, Saudi J. Dent. Res., 5 (2014) 117.

[50] E. Anitua, M. Sanchez, A.T. Nurden, et al., New insights into and novel applications for platelet-rich fibrin therapies, Trends Biotechnol., 24 (2006) 227.

[51] E. Anitua, R. Prado, S. Padilla, et al., Platelet-rich plasma scaffolds for tissue engineering: more than just growth factors in three dimensions, Platelets, 26 (2015) 281.

[52] F.M. Chen, Y. An, R. Zhang, et al., New insights into and novel applications of release technology for periodontal reconstructive therapies, J. Control Release, 149 (2011) 92.

[53] R.E. Marx, Platelet-rich plasma: evidence to support its use, J. Oral Maxillofac. Surg., 62 (2004) 489.

[54] E. Anitua, R. Prado, M. Azkargorta, et al., High-throughput proteomic characterization of plasma rich in growth factors (PRGF-Endoret)-derived fibrin clot interactome, J. Tissue Eng. Regen. M., 9 (2015) E1.

[55] R.E. Marx, Platelet-rich plasma (PRP): what is PRP and what is not PRP?, Implant Dent., 10 (2001) 225.

[56] I.B. Copland, M.A. Garcia, E.K. Waller, et al., The effect of platelet lysate fibrinogen on the functionality of MSCs in immunotherapy, Biomaterials, 34 (2013) 7840.

[57] M.B. Zucker, M.W. Mosesson, M.J. Broekman, et al., Release of platelet fibronectin (cold-insoluble globulin) from alpha granules induced by thrombin or collagen; lack of requirement for plasma fibronectin in ADP-induced platelet aggregation, Blood, 54 (1979) 8.

[58] J.W. Weisel, R.I. Litvinov, Mechanisms of fibrin polymerization and clinical implications, Blood, 121 (2013) 1712.

[59] D.M. Dohan Ehrenfest, L. Rasmusson, T. Albrektsson, Classification of platelet concentrates: from pure platelet-rich plasma (P-PRP) to leucocyte- and platelet-rich fibrin (L-PRF), Trends Biotechnol., 27 (2009) 158.

[60] I. Andia, N. Maffulli, Platelet-rich plasma for managing pain and inflammation in osteoarthritis, Nat. Rev. Rheumatol. , 9 (2013) 721.

[61] E. Anitua, R. Alonso, C. Girbau, et al., Antibacterial effect of plasma rich in growth factors (PRGF(R)-Endoret(R)) against Staphylococcus aureus and Staphylococcus epidermidis strains, Clin. Exp. Dermatol., 37 (2012) 652.

[62] P.S. Babo, R.L. Pires, L. Santos, et al., Platelet Lysate-Loaded Photocrosslinkable Hyaluronic Acid Hydrogels for Periodontal Endogenous Regenerative Technology, ACS Biomater. Sci. Eng., (2016).

[63] T. Burnouf, M.L. Chou, Y.W. Wu, et al., Antimicrobial activity of platelet (PLT)-poor plasma, PLT-rich plasma, PLT gel, and solvent/detergent-treated PLT lysate biomaterials against wound bacteria, Transfusion, 53 (2013) 138.

[64] R.M.B. Yeaman, S. A., Antimicrobial peptides from platelets, Drug Resist. Updat., 2 (1999) 116.

[65] J. Krijgsveld, S.A. Zaat, J. Meeldijk, et al., Thrombocidins, microbicidal proteins from human blood platelets, are C-terminal deletion products of CXC chemokines, J. Biol. Chem., 275 (2000) 20374.

[66] F.W. Lam, K.V. Vijayan, R.E. Rumbaut, Platelets and their interactions with other immune cells, Compr. Physiol., 5 (2015) 1265.

[67] K. Krauel, C. Weber, S. Brandt, et al., Platelet factor 4 binding to lipid A of Gram-negative bacteria exposes PF4/heparin-like epitopes, Blood, 120 (2012) 3345.

[68] H. Hamzeh-Cognasse, P. Damien, A. Chabert, et al., Platelets and infections - complex interactions with bacteria, Front. Immunol., 6 (2015) 82.

[69] D. M Dohan Ehrenfest, T. Bielecki, R. Jimbo, et al., Do the fibrin architecture and leukocyte content influence the growth factor release of platelet concentrates? An evidence-based answer comparing a pure platelet-rich plasma (P-PRP) gel and a leukocyte-and platelet-rich fibrin (L-PRF), Curr. Pharm. Biotechnol., 13 (2012) 1145.

[70] M. Sánchez, E. Anitua, I. Andia, Poor standardization in platelet-rich therapies hampers advancement, Arthroscopy, 26 (2010) 725.

[71] G. Weibrich, W.K. Kleis, G. Hafner, et al., Growth factor levels in platelet-rich plasma and correlations with donor age, sex, and platelet count, J. Craniomaxillofac. Surg., 30 (2002) 97.

[72] D. Man, H. Plosker, J.E. Winland-Brown, The use of autologous platelet-rich plasma (platelet gel) and autologous platelet-poor plasma (fibrin glue) in cosmetic surgery, Plast. Reconstr. Surg., 107 (2001) 229.

[73] P.R. Amable, R.B. Carias, M.V. Teixeira, et al., Platelet-rich plasma preparation for regenerative medicine: optimization and quantification of cytokines and growth factors, Stem Cell Res. Ther., 4 (2013) 67.

[74] I. Hatakeyama, E. Marukawa, Y. Takahashi, et al., Effects of platelet-poor plasma, platelet-rich plasma, and platelet-rich fibrin on healing of extraction sockets with buccal dehiscence in dogs, Tissue Eng. Part A, 20 (2014) 874.

[75] D.M. Ranly, J. McMillan, T. Keller, et al., Platelet-derived growth factor inhibits demineralized bone matrix-induced intramuscular cartilage and bone formation. A study of immunocompromised mice, J. Bone Joint Surg. Am., 87 (2005) 2052.

[76] D.M. Dohan Ehrenfest, I. Andia, M.A. Zumstein, et al., Classification of platelet concentrates (Platelet-Rich Plasma-PRP, Platelet-Rich Fibrin-PRF) for topical and infiltrative use in orthopedic and sports medicine: current consensus, clinical implications and perspectives, Muscles Ligaments Tendons J., 4 (2014) 3.

[77] I. Martineau, E. Lacoste, G. Gagnon, Effects of calcium and thrombin on growth factor release from platelet concentrates: kinetics and regulation of endothelial cell proliferation, Biomaterials, 25 (2004) 4489.

[78] M.R. Messora, M.J. Nagata, R.C. Dornelles, et al., Bone healing in critical-size defects treated with platelet-rich plasma activated by two different methods. A histologic and histometric study in rat calvaria, J. Periodontal Res., 43 (2008) 723.

[79] G. Intini, S. Andreana, F.E. Intini, et al., Calcium sulfate and platelet-rich plasma make a novel osteoinductive biomaterial for bone regeneration, J. Transl. Med., 5 (2007) 13.

[80] M. Matsui, Y. Tabata, Enhanced angiogenesis by multiple release of platelet-rich plasma contents and basic fibroblast growth factor from gelatin hydrogels, Acta Biomater., 8 (2012) 1792.

[81] H.-L. Wang, G. Avila, Platelet Rich Plasma: Myth or Reality?, Eur. J. Dent., 1 (2007) 192.

[82] I. Pallotta, J.A. Kluge, J. Moreau, et al., Characteristics of platelet gels combined with silk, Biomaterials, 35 (2014) 3678.

[83] R. Crespo-Diaz, A. Behfar, G.W. Butler, et al., Platelet lysate consisting of a natural repair proteome supports human mesenchymal stem cell proliferation and chromosomal stability, Cell Transplant., 20 (2011) 797.

[84] N. Fekete, M. Gadelorge, D. Furst, et al., Platelet lysate from whole blood-derived pooled platelet concentrates and apheresis-derived platelet concentrates for the isolation and expansion of human bone marrow mesenchymal stromal cells: production process, content and identification of active components, Cytotherapy, 14 (2012) 540.

[85] J.M. DeLong, R.P. Russell, A.D. Mazzocca, Platelet-rich plasma: the PAW classification system, Arthroscopy, 28 (2012) 998.

[86] J. Magalon, O. Bausset, N. Serratrice, et al., Characterization and comparison of 5 platelet-rich plasma preparations in a single-donor model, Arthroscopy, 30 (2014) 629.

[87] G. Weibrich, T. Hansen, W. Kleis, et al., Effect of platelet concentration in platelet-rich plasma on peri-implant bone regeneration, Bone, 34 (2004) 665.

[88] P. Bajaj, A.R. Pradeep, E. Agarwal, et al., Comparative evaluation of autologous platelet-rich fibrin and platelet-rich plasma in the treatment of mandibular degree II furcation defects: a randomized controlled clinical trial, J. Periodontal Res., 48 (2013) 573.

[89] G. Weibrich, W.K. Kleis, W.E. Hitzler, et al., Comparison of the platelet concentrate collection system with the plasma-rich-in-growth-factors kit to produce platelet-rich plasma: a technical report, Int. J. Oral Maxillofac. Implants, 20 (2005) 118.

[90] P.A. Everts, J. Hoffmann, G. Weibrich, et al., Differences in platelet growth factor release and leucocyte kinetics during autologous platelet gel formation, Transfus. Med., 16 (2006) 363.

[91] C.F. Nathan, Secretory products of macrophages, J. Clin. Invest., 79 (1987) 319.

[92] G.A. Duque, A. Descoteaux, Macrophage cytokines: involvement in immunity and infectious diseases, Frontiers in immunology, 5 (2014).

[93] M. Lech, H.-J. Anders, Macrophages and fibrosis: How resident and infiltrating mononuclear phagocytes orchestrate all phases of tissue injury and repair, Biochim. Biophys. Acta, 1832 (2013) 989.

[94] E. Anitua, M.M. Zalduendo, M.H. Alkhraisat, et al., Release kinetics of platelet-derived and plasma-derived growth factors from autologous plasma rich in growth factors, Ann. Anat., 195 (2013) 461.

[95] W. Yin, X. Qi, Y. Zhang, et al., Advantages of pure platelet-rich plasma compared with leukocyte- and platelet-rich plasma in promoting repair of bone defects, J. Transl. Med., 14 (2016) 73.

[96] Y. Zhou, J. Zhang, H. Wu, et al., The differential effects of leukocyte-containing and pure platelet-rich plasma (PRP) on tendon stem/progenitor cells-implications of PRP application for the clinical treatment of tendon injuries, Stem Cell Res. Ther., 6 (2015) 173.

[97] M.M. Martino, P.S. Briquez, A. Ranga, et al., Heparin-binding domain of fibrin(ogen) binds growth factors and promotes tissue repair when incorporated within a synthetic matrix, Proc. Natl. Acad. Sci. U. S. A., 110 (2013) 4563.

[98] D. Fufa, B. Shealy, M. Jacobson, et al., Activation of platelet-rich plasma using soluble type I collagen, J. Oral Maxillofac. Surg., 66 (2008) 684.

[99] A. Kalén, O. Wahlström, C.H. Linder, et al., The content of bone morphogenetic proteins in platelets varies greatly between different platelet donors, Biochem. Biophys. Res. Commun., 375 (2008) 261.

[100] H.H. Luu, W.X. Song, X. Luo, et al., Distinct roles of bone morphogenetic proteins in osteogenic differentiation of mesenchymal stem cells, J. Orthop. Res., 25 (2007) 665.

[101] M. Beederman, J.D. Lamplot, G. Nan, et al., BMP signaling in mesenchymal stem cell differentiation and bone formation, J. Biomed. Sci. Eng., 6 (2013) 32.

[102] T.M. Fortunato, C. Beltrami, C. Emanueli, et al., Platelet lysate gel and endothelial progenitors stimulate microvascular network formation in vitro: tissue engineering implications, Sci. Rep., 6 (2016) 25326.

[103] M. Bernardi, F. Agostini, K. Chieregato, et al., The production method affects the efficacy of platelet derivatives to expand mesenchymal stromal cells in vitro, J. Transl. Med., 15 (2017) 90.

[104] V.E. Santo, M.E. Gomes, J.F. Mano, et al., Chitosan-chondroitin sulphate nanoparticles for controlled delivery of platelet lysates in bone regenerative medicine, J.Tissue Eng. Regen. Med., 6 (2012) s47.

[105] P.S. Babo, V.E. Santo, M.E. Gomes, et al., Development of an Injectable Calcium Phosphate/Hyaluronic Acid Microparticles System for Platelet Lysate Sustained Delivery Aiming Bone Regeneration, Macromol. Biosci., 16 (2016) 1662.

[106] P.S. Babo, X. Cai, A.S. Plachokova, et al., The Role of a Platelet Lysate-Based Compartmentalized System as a Carrier of Cells and Platelet-Origin Cytokines for Periodontal Tissue Regeneration, Tissue Eng. Part A, 22 (2016) 1164.

[107] T. Burnouf, D. Strunk, M.B.C. Koh, et al., Human platelet lysate: Replacing fetal bovine serum as a gold standard for human cell propagation?, Biomaterials, 76 (2016) 371.

[108] J. Choukroun, F. Adda, C. Schoeffer, et al., PRF: An opportunity in perio-implantology (in French), Implantodontie, 42 (2000) 55.

[109] D.M. Dohan, J. Choukroun, A. Diss, et al., Platelet-rich fibrin (PRF): a second-generation platelet concentrate. Part I: technological concepts and evolution, Oral Surg. Oral Med. Oral Pathol. Oral Radiol. Endod., 101 (2006) e37.

[110] S. Nishimoto, K. Fujita, Y. Sotsuka, et al., Growth Factor Measurement and Histological Analysis in Platelet Rich Fibrin: A Pilot Study, J. Maxillofac. Oral Surg., 14 (2015) 907.

[111] B. Chignon-Sicard, C.A. Georgiou, E. Fontas, et al., Efficacy of leukocyte- and platelet-rich fibrin in wound healing: a randomized controlled clinical trial, Plast. Reconstr. Surg., 130 (2012) 819e.

[112] W. Pluemsakunthai, S. Kuroda, H. Shimokawa, et al., A basic analysis of platelet-rich fibrin: distribution and release of platelet-derived growth factor-BB, Inflam. and Regen., 33 (2013) 164.

[113] E. Torreggiani, F. Perut, L. Roncuzzi, et al., Exosomes: novel effectors of human platelet lysate activity, Eur. Cell Mater., 28 (2014) 137.

[114] M.T. Aatonen, T. Ohman, T.A. Nyman, et al., Isolation and characterization of platelet-derived extracellular vesicles, J. Extracell. Vesicles, 3 (2014).

[115] S.C. Guo, S.C. Tao, W.J. Yin, et al., Exosomes derived from platelet-rich plasma promote the re-epithelization of chronic cutaneous wounds via activation of YAP in a diabetic rat model, Theranostics, 7 (2017) 81.

[116] N. Arraud, R. Linares, S. Tan, et al., Extracellular vesicles from blood plasma: determination of their morphology, size, phenotype and concentration, J. Thromb. Haemost., 12 (2014) 614.

[117] S.J. Kim, D.H. Song, J.W. Park, et al., Effect of Bone Marrow Aspirate Concentrate-Platelet-Rich Plasma on Tendon-Derived Stem Cells and Rotator Cuff Tendon Tear, Cell Transplant., 26 (2017) 867.

[118] O. Gidlof, M. van der Brug, J. Ohman, et al., Platelets activated during myocardial infarction release functional miRNA, which can be taken up by endothelial cells and regulate ICAM1 expression, Blood, 121 (2013) 3908.

[119] J. Li, M. Tan, Q. Xiang, et al., Thrombin-activated platelet-derived exosomes regulate endothelial cell expression of ICAM-1 via microRNA-223 during the thrombosis-inflammation response, Thromb. Res., 154 (2017) 96.

[120] I. Arbesu, M. Bucsaiova, M.B. Fischer, et al., Platelet-borne complement proteins and their role in platelet–bacteria interactions, J. Thromb. Haemost., 14 (2016) 2241.

[121] P. Harrison, E.M. Cramer, Platelet α-granules, Blood Rev., 7 (1993) 52.

[122] P. Blair, R. Flaumenhaft, Platelet α-granules: basic biology and clinical correlates, Blood Rev., 23 (2009) 177.

[123] A. McNicol, J.M. Gerrard, Post-receptor events associated with thrombin-induced platelet activation, Blood Coagul. Fibrinolysis, 4 (1993) 975.

[124] M. Aatonen, M. Grönholm, P.R.-M. Siljander, Platelet-derived microvesicles: multitalented participants in intercellular communication, in: First Platelet-derived microvesicles: multitalented participants in intercellular communication, Thieme Medical Publishers, 2012, pp. 102.

[125] E.J. Goetzl, L. Goetzl, J.S. Karliner, et al., Human plasma platelet-derived exosomes: effects of aspirin, FASEB J., 30 (2016) 2058.

[126] H.J. Huber, P. Holvoet, Exosomes: emerging roles in communication between blood cells and vascular tissues during atherosclerosis, Curr. Opin. Lipidol., 26 (2015) 412.

[127] V.A. Fadok, D.L. Bratton, A. Konowal, et al., Macrophages that have ingested apoptotic cells in vitro inhibit proinflammatory cytokine production through autocrine/paracrine mechanisms involving TGF-beta, PGE2, and PAF, J. Clin. Invest., 101 (1998) 890.

[128] S.G. Boswell, B.J. Cole, E.A. Sundman, et al., Platelet-rich plasma: a milieu of bioactive factors, Arthroscopy, 28 (2012) 429.

[129] M.O. Schär, J. Diaz-Romero, S. Kohl, et al., Platelet-rich concentrates differentially release growth factors and induce cell migration in vitro, Clin. Orthop. Relat. Res., 473 (2015) 1635.

[130] G.A. Duque, A. Descoteaux, Macrophage cytokines: involvement in immunity and infectious diseases, Front. Immunol., 5 (2014) 491.

[131] B.L. Eppley, J.E. Woodell, J. Higgins, Platelet Quantification and Growth Factor Analysis from Platelet-Rich Plasma: Implications for Wound Healing, Plast. Reconstr. Surg., 114 (2004) 1502.

[132] P. Hofbauer, S. Riedl, K. Witzeneder, et al., Human platelet lysate is a feasible candidate to replace fetal calf serum as medium supplement for blood vascular and lymphatic endothelial cells, Cytotherapy, 16 (2014) 1238.

[133] E. Anitua, I. Andí, M. Sanchez, et al., Autologous preparations rich in growth factors promote proliferation and induce VEGF and HGF production by human tendon cells in culture, J. Orthop. Res., 23 (2005) 281.

[134] M.P. Mojica-Henshaw, P. jacobson, J. Morris, et al., Serum-converted platelet lysate can substitute for fetal bovine serum in human mesenchymal stromal cell cultures, Cytotherapy, 15 (2013) 1458.

[135] H.S. Cho, I.H. Song, S.-Y. Park, et al., Individual Variation in Growth Factor Concentrations in Platelet-rich Plasma and Its Influence on Human Mesenchymal Stem Cells, Korean J. Lab. Med., 31 (2011) 212.

[136] H. El-Sharkawy, A. Kantarci, J. Deady, et al., Platelet-Rich Plasma: Growth Factors and Pro- and Anti-Inflammatory Properties, J. Periodontol., 78 (2007) 661.

[137] A. Roffi, G. Filardo, E. Assirelli, et al., Does platelet-rich plasma freeze-thawing influence growth factor release and their effects on chondrocytes and synoviocytes?, Biomed. Res. Int., 2014 (2014) 692913.

[138] J. Qiao, N. An, X. Ouyang, Quantification of growth factors in different platelet concentrates, Platelets, 28 (2017) 774.

[139] D.E. Roberts, A. McNicol, R. Bose, Mechanism of Collagen Activation in Human Platelets, J. Biol. Chem., 279 (2004) 19421.

[140] A.C. Brown, T.H. Barker, Fibrin-based biomaterials: Modulation of macroscopic properties through rational design at the molecular level, Acta Biomater., 10 (2014) 1502.

[141] J.J. Rice, M.M. Martino, L. De Laporte, et al., Engineering the regenerative microenvironment with biomaterials, Adv. Healthc. Mater., 2 (2013) 57.

[142] S. Reed, B. Wu, Sustained growth factor delivery in tissue engineering applications, Ann. Biomed. Eng., 42 (2014) 1528.

[143] K. Lee, E.A. Silva, D.J. Mooney, Growth factor delivery-based tissue engineering: general approaches and a review of recent developments, J. R. Soc. Interface, 8 (2011) 153.

[144] P. Tayalia, D.J. Mooney, Controlled growth factor delivery for tissue engineering, Adv. Mater., 21 (2009) 3269.

[145] L. Uebersax, H.P. Merkle, L. Meinel, Biopolymer-based growth factor delivery for tissue repair: from natural concepts to engineered systems, Tissue Eng. Part B Rev., 15 (2009) 263.

[146] A.C. Mitchell, P.S. Briquez, J.A. Hubbell, et al., Engineering growth factors for regenerative medicine applications, Acta Biomater., 30 (2016) 1.

[147] H.S. Azevedo, I. Pashkuleva, Biomimetic supramolecular designs for the controlled release of growth factors in bone regeneration, Adv. Drug Deliv. Rev., 94 (2015) 63.

[148] Y. Li, Y. Xiao, C. Liu, The horizon of materiobiology: A perspective on material-guided cell behaviors and tissue engineering, Chem. Rev., 117 (2017) 4376.

[149] S. Shanbhag, A. Stavropoulos, S. Suliman, et al., Efficacy of humanized mesenchymal stem cell cultures for bone tissue engineering: a systematic review with a focus on platelet-derivatives, Tissue Eng. Part B Rev., (2017).

[150] K. Bieback, Platelet lysate as replacement for fetal bovine serum in mesenchymal stromal cell cultures, Transfus. Med. Hemother., 40 (2013) 326.

[151] E.A. Masoudi, J. Ribas, G. Kaushik, et al., Platelet-rich blood derivatives for stem cell-based tissue engineering and regeneration, Stem Cell Reports, 2 (2016) 33.

[152] G. Gainza, S. Villullas, J.L. Pedraz, et al., Advances in drug delivery systems (DDSs) to release growth factors for wound healing and skin regeneration, Nanomedicine, 11 (2015) 1551.

[153] S. van Rijt, P. Habibovic, Enhancing regenerative approaches with nanoparticles, J. R. Soc. Interface, 14 (2017) 20170093.

[154] M.B. Oliveira, J.F. Mano, Polymer-based microparticles in tissue engineering and regenerative medicine, Biotechnol. Prog., 27 (2011) 897.

[155] E.-c. Shen, T.C. Chou, C.H. Gau, et al., Releasing growth factors from activated human platelets after chitosan stimulation: A possible bio-material for platelet-rich plasma preparation, Clin. Oral Implants Res., 17 (2006) 572.

[156] K. Kojima, Y. Okamoto, K. Kojima, et al., Effects of chitin and chitosan on collagen synthesis in wound healing, J. Vet. Med. Sci., 66 (2004) 1595.

[157] F.T. Bosman, I. Stamenkovic, Functional structure and composition of the extracellular matrix, J. Pathol., 200 (2003) 423.

[158] V.E. Santo, E.G. Popa, J.F. Mano, et al., Natural assembly of platelet lysate-loaded nanocarriers into enriched 3D hydrogels for cartilage regeneration, Acta Biomater., 19 (2015) 56.

[159] V.E. Santo, A.R.C. Duarte, E.G. Popa, et al., Enhancement of osteogenic differentiation of human adipose derived stem cells by the controlled release of platelet lysates from hybrid scaffolds produced by supercritical fluid foaming, J. Control. Rel., 162 (2012) 19.

[160] J.M. Burkhart, M. Vaudel, S. Gambaryan, et al., The first comprehensive and quantitative analysis of human platelet protein composition allows the comparative analysis of structural and functional pathways, Blood, 120 (2012) e73.

[161] D.Y. Arifin, L.Y. Lee, C.-H. Wang, Mathematical modeling and simulation of drug release from microspheres: implications to drug delivery systems, Adv. Drug Deliv. Rev., 58 (2006) 1274.

[162] M.M. Martino, P.S. Briquez, A. Ranga, et al., Heparin-binding domain of fibrin (ogen) binds growth factors and promotes tissue repair when incorporated within a synthetic matrix, Proc. Natl. Acad. Sci. U.S.A., 110 (2013) 4563.

[163] B. Kutlu, T. Aydın, R. Seda, et al., Platelet-rich plasma-loaded chitosan scaffolds: Preparation and growth factor release kinetics, J. Biomed. Mater. Res. B Appl. Biomater., 101 (2013) 28.

[164] M. Mori, S. Rossi, F. Ferrari, et al., Sponge-like dressings based on the association of chitosan and sericin for the treatment of chronic skin ulcers. II. Loading of the hemoderivative platelet lysate, J. Pharm. Sci. , 105 (2016) 1188.

[165] B.V. Slaughter, S.S. Khurshid, O.Z. Fisher, et al., Hydrogels in regenerative medicine, Adv. Mater., 21 (2009) 3307.

[166] Y.S. Zhang, A. Khademhosseini, Advances in engineering hydrogels, Science, 356 (2017) eaaf3627.

[167] X. Liu, Y. Yang, X. Niu, et al., An in situ photocrosslinkable platelet rich plasma–Complexed hydrogel glue with growth factor controlled release ability to promote cartilage defect repair, Acta Biomater., (2017) 179.

[168] T.E. Foster, B.L. Puskas, B.R. Mandelbaum, et al., Platelet-rich plasma: from basic science to clinical applications, Am. J. Sports Med., 37 (2009) 2259.

[169] A. Chevrier, V. Darras, G. Picard, et al., Injectable chitosan-platelet-rich plasma (PRP) implants to promote tissue regeneration: In vitro properties, in vivo residence, degradation, cell recruitment and vascularization, J. Tissue Eng. Regen. Med., (2017).

[170] S. Kuttappan, K.S. Keyan, M.B. Nair, Evaluation of osteoinductive and endothelial differentiation potential of Platelet-Rich Plasma incorporated Gelatin-Nanohydroxyapatite Fibrous Matrix, J. Biomed. Mater. Res. B Appl. Biomater., 104 (2016) 771.

[171] D.H.R. Kempen, L. Lu, A. Heijink, et al., Effect of local sequential VEGF and BMP-2 delivery on ectopic and orthotopic bone regeneration, Biomaterials, 30 (2009) 2816.

[172] J. Leijten, J. Seo, K. Yue, et al., Spatially and temporally controlled hydrogels for tissue engineering, Mater. Sci. Eng. R. Rep., 119 (2017) 1.

[173] J. Yao, C.W. Bastiaansen, T. Peijs, High strength and high modulus electrospun nanofibers, Fibers, 2 (2014) 158.

[174] S. Khorshidi, A. Solouk, H. Mirzadeh, et al., A review of key challenges of electrospun scaffolds for tissue-engineering applications, J. Tissue Eng. Regen. Med., 10 (2016) 715.

[175] S. Sahoo, L.T. Ang, J.C.H. Goh, et al., Growth factor delivery through electrospun nanofibers in scaffolds for tissue engineering applications, J. Biomed. Mater. Res. A, 93 (2010) 1539.

[176] J.S. Choi, H.S. Kim, H.S. Yoo, Electrospinning strategies of drug-incorporated nanofibrous mats for wound recovery, Drug Deliv. Transl. Res., 5 (2015) 137.

[177] V. Bertoncelj, J. Pelipenko, J. Kristl, et al., Development and bioevaluation of nanofibers with blood-derived growth factors for dermal wound healing, Eur. J. Pharm. Biopharm., 88 (2014) 64.

[178] J. Liu, H. Nie, Z. Xu, et al., Construction of PRP-containing nanofibrous scaffolds for controlled release and their application to cartilage regeneration, J. Mater. Chem., 3 (2015) 581.

[179] S.a. Guo, L.A. DiPietro, Factors affecting wound healing, J. Dent. Res., 89 (2010) 219.

[180] T. Nimal, G. Baranwal, M. Bavya, et al., Anti-staphylococcal Activity of Injectable Nano Tigecycline/Chitosan-PRP Composite Hydrogel Using Drosophila melanogaster Model for Infectious Wounds, ACS Appl. Mater. Interfaces, 8 (2016) 22074.

[181] Y.-H. Kim, H. Furuya, Y. Tabata, Enhancement of bone regeneration by dual release of a macrophage recruitment agent and platelet-rich plasma from gelatin hydrogels, Biomaterials, 35 (2014) 214.

[182] N.F. Huang, S. Li, Regulation of the matrix microenvironment for stem cell engineering and regenerative medicine, Ann. Biomed. Eng., 39 (2011) 1201.

[183] V.E. Santo, P. Babo, M. Amador, et al., Engineering Enriched Microenvironments with Gradients of Platelet Lysate in Hydrogel Fibers, Biomacromolecules, 17 (2016) 1985.

[184] J. Leotot, L. Coquelin, G. Bodivit, et al., Platelet lysate coating on scaffolds directly and indirectly enhances cell migration, improving bone and blood vessel formation, Acta Biomater., 9 (2013) 6630.

[185] B.D. Smith, D.A. Grande, The current state of scaffolds for musculoskeletal regenerative applications, Nat. Rev. Rheumatol. , 11 (2015) 213.

[186] J.-p. Seo, T. Tanabe, N. Tsuzuki, et al., Effects of bilayer gelatin/β-tricalcium phosphate sponges loaded with mesenchymal stem cells, chondrocytes, bone morphogenetic protein-2, and platelet rich plasma on osteochondral defects of the talus in horses, Res. Vet. Sci., 95 (2013) 1210.

[187] P.S. Babo, X. Cai, A.S. Plachokova, et al., Evaluation of a platelet lysate bi-layered system for periodontal regeneration in a rat intrabony 3-wall periodontal defect, J. Tissue Eng. Regen. Med.

[188] M.E. Gomes, M.T. Rodrigues, R.M. Domingues, et al., Tissue Engineering and Regenerative Medicine: New Trends and Directions—A Year in Review, Tissue Eng. Part B Rev., 23 (2017) 211.

[189] W. Kim, C.H. Jang, G. Kim, Optimally designed collagen/polycaprolactone biocomposites supplemented with controlled release of HA/TCP/rhBMP-2 and HA/TCP/PRP for hard tissue regeneration, Mater. Sci. Eng. C Mater. Biol. Appl., 78 (2017) 763.

[190] S.M. Oliveira, R.L. Reis, J.o.F. Mano, Assembling human platelet lysate into multiscale 3D scaffolds for bone tissue engineering, ACS Biomater. Sci. Eng., 1 (2014) 2.

[191] J. Folkman, Y. Shing, Control of angiogenesis by heparin and other sulfated polysaccharides, in: D.A. Lane, Björk, I., Lindahl, U. (Ed.) Heparin and related polysaccharides, Springer Science & Business Media., New York, 1992, pp. 355.

[192] I. Vlodavsky, H.-Q. Miao, B. Medalion, et al., Involvement of heparan sulfate and related molecules in sequestration and growth promoting activity of fibroblast growth factor, Cancer and Metastasis Rev., 15 (1996) 177.

[193] J.E. Babensee, L.V. McIntire, A.G. Mikos, Growth factor delivery for tissue engineering, Pharm. Res., 17 (2000) 497.

[194] W.G. La, H.S. Yang, Heparin-Conjugated Poly (Lactic-Co-Glycolic Acid) Nanospheres Enhance Large-Wound Healing by Delivering Growth Factors in Platelet-Rich Plasma, Artif. Organs, 39 (2015) 388.

[195] M. Klagsbrun, The affinity of fibroblast growth factors (FGFs) for heparin; FGF-heparan sulfate interactions in cells and extracellular matrix, Curr. Opin. Cell Biol., 2 (1990) 857.

[196] J.R. Bishop, M. Schuksz, J.D. Esko, Heparan sulphate proteoglycans fine-tune mammalian physiology, Nature, 446 (2007) 1030.

[197] J. Hirsh, T.E. Warkentin, S.G. Shaughnessy, et al., Heparin and low-molecular-weight heparin mechanisms of action, pharmacokinetics, dosing, monitoring, efficacy, and safety, Chest, 119 (2001) 64S.

[198] J. Valcarcel, R. Novoa-Carballal, R.I. Pérez-Martín, et al., Glycosaminoglycans from marine sources as therapeutic agents, Biotechnol. Adv., 35 (2017) 711.

[199] S.M. Oliveira, V.E. Santo, M.E. Gomes, et al., Layer-by-layer assembled cell instructive nanocoatings containing platelet lysate, Biomaterials, 48 (2015) 56.

[200] D.M. Ranly, C.H. Lohmann, D. Andreacchio, et al., Platelet-rich plasma inhibits demineralized bone matrix-induced bone formation in nude mice, JBJS, 89 (2007) 139.

[201] S.M. Oliveira, R.P. Pirraco, A.P. Marques, et al., Platelet lysate-based pro-angiogenic nanocoatings, Acta Biomater., 32 (2016) 129.

[202] C.A. Custódio, V.E. Santo, M.B. Oliveira, et al., Functionalized microparticles producing scaffolds in combination with cells, Adv. Funct. Mater., 24 (2014) 1391.

[203] C. Oliveira, A.R. Costa-Pinto, R.L. Reis, et al., Biofunctional nanofibrous substrate comprising immobilized antibodies and selective binding of autologous growth factors, Biomacromolecules, 15 (2014) 2196.

[204] J. Han, H. Meng, J. Tang, et al., The effect of different platelet-rich plasma concentrations on proliferation and differentiation of human periodontal ligament cells in vitro, Cell Prolif., 40 (2007) 241.

[205] R. Ito, N. Morimoto, L.H. Pham, et al., Efficacy of the controlled release of concentrated platelet lysate from a collagen/gelatin scaffold for dermis-like tissue regeneration, Tissue Eng. Part A, 19 (2013) 1398.

[206] D. Nakajima, Y. Tabata, S. Sato, Periodontal tissue regeneration with PRP incorporated gelatin hydrogel sponges, Biomed. Mater., 10 (2015) 055016.

[207] L.S. Neves, P.S. Babo, A.I. Gonçalves, et al., Injectable Hyaluronic Acid Hydrogels Enriched with Platelet Lysate as a Cryostable Off-the-Shelf System for Cell-Based Therapies, Regen. Eng. Transl. Med., 3 (2017) 53.

[208] E.D. Silva, P.S. Babo, R. Costa-Almeida, et al., Multifunctional magnetic-responsive hydrogels to engineer tendon-to-bone interface, Nanomedicine, (2017) 30108.

[209] S.A. Sell, J.J. Ericksen, T.W. Reis, et al., A case report on the use of sustained release platelet-rich plasma for the treatment of chronic pressure ulcers, J. Spinal Cord. Med., 34 (2011) 122.

[210] N. Morimoto, N. Kakudo, T. Ogura, et al., Easy-to-Use Preservation and Application of Platelet-Rich Plasma in Combination Wound Therapy With a Gelatin Sheet and Freeze-Dried Platelet-Rich Plasma: A Case Report, Eplasty, 16 (2016) e22.

[211] Y. Yamada, S. Nakamura, M. Ueda, et al., Papilla regeneration by injectable stem cell therapy with regenerative medicine: long-term clinical prognosis, J. Tissue Eng. Regen. Med., 9 (2015) 305.

[212] Osteoclast Impairment in Chronic Periodontitis by Regenerative Materials., in

https://clinicaltrials.gov/ct2/show/NCT03227367, Accessed date: 20 July 2017.

[213] Collplant Lda, in: http://www.collplant.com/products/orthobiologics/vergenixstr/, Accessed date: 27 July 2017.

[214] M.S. Shive, W.D. Stanish, R. McCormack, et al., BST-CarGel® treatment maintains cartilage repair superiority over microfracture at 5 years in a multicenter randomized controlled trial, Cartilage, 6 (2015) 62.

[215] J.C. Riboh, B.M. Saltzman, A.B. Yanke, et al., Effect of leukocyte concentration on the efficacy of platelet-rich plasma in the treatment of knee osteoarthritis, Am. J. Sports Med., 44 (2016) 792.

[216] L.P. Lai, T.P. Stitik, P.M. Foye, et al., Use of platelet-rich plasma in intra-articular knee injections for osteoarthritis: a systematic review, PM&R, 7 (2015) 637.

[217] G. Filardo, B. Di Matteo, E. Kon, et al., Platelet-rich plasma in tendon-related disorders: results and indications, Knee Surg. Sports Traumatol. Arthrosc., (2016) 1.

[218] A.L. Nelson, E. Dhimolea, J.M. Reichert, Development trends for human monoclonal antibody therapeutics, Nat. Rev. Drug Discov., 9 (2010) 767.

[219] M.I. Neves, M.E. Wechsler, M.E. Gomes, et al., Molecularly imprinted intelligent scaffolds for tissue engineering applications, Tissue Eng. Part B Rev., 23 (2017) 27.

[220] G. Vlatakis, L.I. Andersson, R. Muller, et al., Drug assay using antibody mimics made by molecular imprinting, Nature, 361 (1993) 645.

[221] B. Han, Z. Yang, J.Y. Fang, et al., The Effects of Heparin Binding Proteins in Platelet Releasate on Bone Formation, Tissue Eng. Part A, 20 (2014) 1263.

[222] J. Malda, J. Boere, C.H. Van De Lest, et al., Extracellular vesicles–new tool for joint repair and regeneration, Nat. Rev. Rheumatol. , 12 (2016) 243.

[223] G.D. Prestwich, S. Bhatia, C.K. Breuer, et al., What is the greatest regulatory challenge in the translation of biomaterials to the clinic?, Sci. Transl. Med., 4 (2012) 160cm14.

SECTION 2

EXPERIMENTAL MATERIALS AND METHODOLOGIES

Chapter II

Materials and Methods

Materials and Methods

The aim of this chapter is to describe the rationale behind the use of the experimental procedures used throughout this thesis. Moreover, although each thesis chapter contains a materials and experimental set-up description, herein it will be presented in detail the rational for the selection of biomaterials, processing and characterization techniques.

II-1. MATERIALS

This section aims at explaining the selection of the natural biomaterials that were used in this thesis, with a description of their functionality, inherent properties and processing techniques. Moreover, it will discuss their use in research and in a few clinical applications (when applicable), as well as how to overcome the biomaterials drawbacks in providing the adequate biological and physical cues, for the intended application that motivated the work performed under this thesis (Figure II-1).

II-1.1. Platelet lysate

Platelets contain thousands of proteins that with numerous post-translational modifications (e.g., mechanical disruption) results in over 1,500 protein-based bioactive factors (e.g., growth factors, cytokines, fibrinogen) [1, 2]. Platelet batches are obtained from a pool of platelet concentrates (PC) units, obtained from healthy, volunteer, regular blood donors and undergo standard testing for blood transfusion acceptance (negative for viral infections hepatitis B (HBs-Ag), hepatitis C (Anti-HCV), and HIV ½ (Anti-HIV ½)) compliant with the requisites stablished in annex II and III of directive 2004/33/CE and annex IV of directive 2002/98/CE [3].

PC units can be obtained from whole blood by two different methods: differential centrifugations or plateletapheresis [4-7]. In the first procedure, whole blood is centrifuged two times, which separates blood components and collects the platelet-rich plasma fraction (may contain white blood cells - buffy coat). In the second procedure, plateletapheresis, the donor's whole blood is passed through a medical device, which separates platelets from the other components of blood, collects the platelets, and returns the

remainder of the donor's blood. After collection, PC units are often submitted to gamma irradiation (minimum of 25 cGy) and 4 to 6 ABO-compatible PC units are combined [4]. PC batches (life span of 5 to 9 days) have been applied in clinic practice as fresh plasma (< 5 days old) or in research as expired plasma (> 5 days old). In clinical settings, the main indication for the transfusion of platelets is to prevent/treat bleeding in patients with platelets quantitative/qualitative defects (e.g, prophylaxis and treatment of hemorrhage in patients with thrombocytopenia or with primary or secondary functional disorders of platelets) [4, 8].

Unsurprisingly, platelet-based materials have been also extensively applied in clinical settings with the goal of promoting tissue regeneration (e.g., soft and hard tissue lesions) [7, 9]. For instance, platelet-rich blood derivatives formulations can positively influence wound healing and reduce the risk of infections [9, 10]. Among the different platelet-rich blood derivatives formulations, platelet lysate (PL) have a more reproducible preparation process based on platelet disruption instead of activation with calcium or/and thrombin (e.g. platelet-rich fibrin), and have shown comparatively lower batch-to-batch variability (when prepared from polls of donors) than other blood derivatives formulations [7, 9]. The surging demand for xeno-free materials has expanded the global human PL market, namely as a suitable alternative to FBS supplement for *in vitro* cell culture,[11] as previously discussed in ***Chapter 1***. On the other hand, the use of PL as a biomaterial displays serious constraints in TERM clinical strategies, mainly due to its limited mechanical properties, fast *in vitro/in vivo* biomolecules degradation, and short-term storage stability [7]. Thus, there is a definite need to improve PL-based biomaterial physicochemical and stability properties, while the best of PL-derived biomolecules therapeutic potential is maintained. Throughout this thesis, different processing techniques were performed using human PL to improve fibrin-based scaffolds stability and mechanical properties, to protect platelet-derived biomolecules from fast clearance and proteolytic degradation, and to hinder the shrinkage of the gel upon cells encapsulation [7].

In ***Chapter 3 to 6***, it was used human PL pools obtained from PC batches collected from whole blood differential centrifugations or plateletapheresis at Instituto Português do Sangue e Transplantação-IPST provided under an approved institutional board protocol. The harvesting, biological analysis and storage follows the guidelines of European Directive 2005/62/CE. The quality of PC batches was assured by the IPST, following the Portuguese national legislation (Decreto-Lei n. ° 267/2007) transcribed from European directive 2002/98/CE. In ***Chapter 7***, human PL formulations were purchased from Mill Creek Life Sciences (Minnesota, USA).

II-1.2. Cellulose nanocrystals

Cellulose is the most abundant polymer on earth, and it is a renewable source that have been incorporated into countless products and processes [12]. More recently, cellulose has been extensively explored for producing new nanoscale materials, including cellulose nanofibrils, bacterial nanocellulose, and cellulose nanocrystals (CNC). In particular, CNC are typically produced through a sulfuric acid hydrolysis process, in which the disordered (amorphous) regions of the raw material are degraded and the ordered (crystalline) regions with higher resistance to acid attack remain intact [13]. Rod-shaped nanocrystals can be extracted from different cellulose sources (e.g., tunicates, wood pulp or cotton) [14] and acid hydrolysis conditions (e.g., hydrolysis time, temperature and acid concentration) [15] that can greatly affect CNC behavior such as surface charge density, crystallinity and particle dimensions [16]. Interestingly, strong acid hydrolysis leaves sulfate half-ester groups on the CNC surface ($-OSO3^-$), conveying a stable colloid system in water and a negative surface charge that might potentially act as sulfated glycosaminoglycans (GAGs) [17, 18].

The scientific literature on CNC continues to grow exponentially, mainly due to their unique physical and chemical properties [12]. In addition to CNC strength and rigid structure (strength over 7 GPa, elastic modules of 150 GPa), CNC are able to self-assembled into chiral nematic liquid-crystalline phases and aligned in magnetic and electric fields [19, 20]. Concerning their chemical properties, they showed a reactive surface, an amphiphilic nature, high aspect ratio and large surface area enable several chemical modifications and their effective integration into different polymer matrices as crosslinkers or nanofillers (i.e., with no covalent attachment to the hydrogel) [13, 21-23]. Moreover, CNC have exhibited low cytotoxicity to a range of animal and human cell types [24], no acute adverse effects via ingestion or topical administration [25, 26], and a mild acute inflammatory responses *in vivo* with minimal bioaccumulation of CNC in any typical clearance organ biodistribution [26, 27].

Here, particular emphasis is given to aldehyde-modified CNC (a-CNC) that act as covalent protein crosslinkers to compensate PL mechanical, structural and cell supporting limitations. This nanoscale reinforcement greatly contributes to the development of promising novel functional nanomaterials, namely hydrogels and bioinks for stem cell three-dimensional (3D) microenvironment modulation (*Chapter 3 and 6*), cryogels for restoring hemostasis (*Chapter 4*) and nanostructured coatings for protein selective presentation (*Chapter 5*).

In this thesis, CNC were extracted from microcrystalline cellulose (MCC) powder (Sigma-Aldrich, USA) following the typical sulfuric acid hydrolysis according to Bondeson with minor modifications [15]. In brief, 42 g of MCC was mixed with 189 mL of deionized water (DI). DI/MCC suspension was then put in an ice bath and stirred using a mechanical agitator (500 rpm) for 10 minutes. 188.3 mL of concentrated sulfuric acid (95–98% from Sigma-Aldrich, USA) was added dropwise up to a final concentration of 64 wt.%. The suspension was heated to 44 °C while stirring at 500 rpm for 120 min. The reaction was stopped by diluting the suspension with cold water (5x) and left to decant at 4 °C. The supernatant was discarded, and the remaining suspension was centrifuged for 10 minutes at 9000 rpm and 5 °C. The supernatant was successively replaced with DI water and the suspension subjected to centrifugation cycles until the supernatant became turbid. The resulting suspension was collected and extensively dialyzed using cellulose dialysis membrane MWCO: 12-14 kDa (Sigma-Aldrich, USA) against DI water until neutral pH. After dialysis the content was sonicated three times (VCX-130PB-220, Sonics) for 10 minutes using an ultrasound probe at 60% of amplitude output, under ice cooling to prevent overheating. The cloudy suspension was centrifuged one last time to remove big particulates and the final supernatant containing the CNC was stored at 4 °C until further use. Then, a-CNC were produced by sodium periodate ($NaIO_4$) oxidation [28]. In a typical experiment, $NaIO_4$ (Sigma-Aldrich, USA) was added to CNC aqueous suspension (1.5 wt.%) in a 1:1 molar ratio ($NaIO_4$:CNC). The mixture was allowed to stir at room temperature (RT) for 12 hours preventing from light exposure. Unreacted periodate was quenched by the addition of excess of ethylene glycol (Sigma-Aldrich, USA). The mixture was transferred into a dialysis membrane (cellulose dialysis membrane MWCO: 12-14 kDa) and dialyzed against DI for 3 days with regular water replacement. The final working suspension of modified CNC was collected and stored at 4 °C.

II-1.3. Hyaluronic acid

Hyaluronic acid (HA) or hyaluronan is an anionic GAG component in the ECM, and the only GAG that does not contain any sulfate groups. HA is expressed throughout the body (e.g., vitreous humor and tendons) at a concentration and molecular weight that varies by tissue source or body location [29, 30]. In the ECM, HA interacts with matrix components (e.g. aggrecan) and resident cells (e.g., CD44 binding peptide), which provides physical and biological cues to maintain tissue homeostasis, and to modulate cellular signaling and matrix organization. Interestingly, HA biosynthesis and tissue turnover is regulated

by three synthases and several hyaluronidases that show differential activities in the HA fragment sizes they generate and can naturally catabolize HA with ranging from hours to days [31, 32].

The crucial role of HA in the structural properties and functions of ECM has been widely used in the design and development of engineered HA-based materials for regenerative medicine applications [33]. The unique native biofunctionality, the hydrophilic and viscoelastic HA nature produces a hydrated polymeric network with tunable physical and biochemical cues. Moreover, HA surface with carboxyl and hydroxyl groups allows new chemical modifications/compositions and the further combination with other polymers to fine-tune material properties. For example, HA gelation can be induced via covalent crosslinking through external triggers like light (e.g., thiol-ene click crosslinking), via supramolecular or non-covalent assembly [28, 34-36]. The positive outcomes of HA-based hydrogels contributed to the advanced clinical use in veterinary and human patients, particularly HA have been used as dermal fillers, and as intra-articular viscosupplements for corneal and dermal wound repair [37].

In this thesis, PL was incorporated into norbornene-modified hyaluronic acid (NorHA) microgels to modulate the physical and biochemical mesenchymal stem cell microenvironment (*Chapter 7*). Prior to NorHA synthesis, HA was converted to its tetrabutylammonium salt (HA-TBA) to be soluble in dimethyl sulfoxide (DMSO). First, NaHA was dissolved in DI H_2O at 2 wt% and the Dowex 50W proton exchange resin was added to the solution (3 g resin per 1 g NaHA) and allowed to exchange for 5 h. The resin was filtered off and the filtrate was titrated to a pH of 7.03 with TBA-OH (∼1.4 TBA per HA repeat unit). The resulting solution was frozen at −80 °C, lyophilized, and stored at −20 °C until used. Then, NorHA macromers were obtained by modifying the tetrabutylammonium salt of HA with 5-norbornene-2-carboxylic acid (Nor) via esterification through di-tert-butyl dicarbonate (Boc_2O) and 4-dimethylaminopyridine (DMAP), as previously described [35].

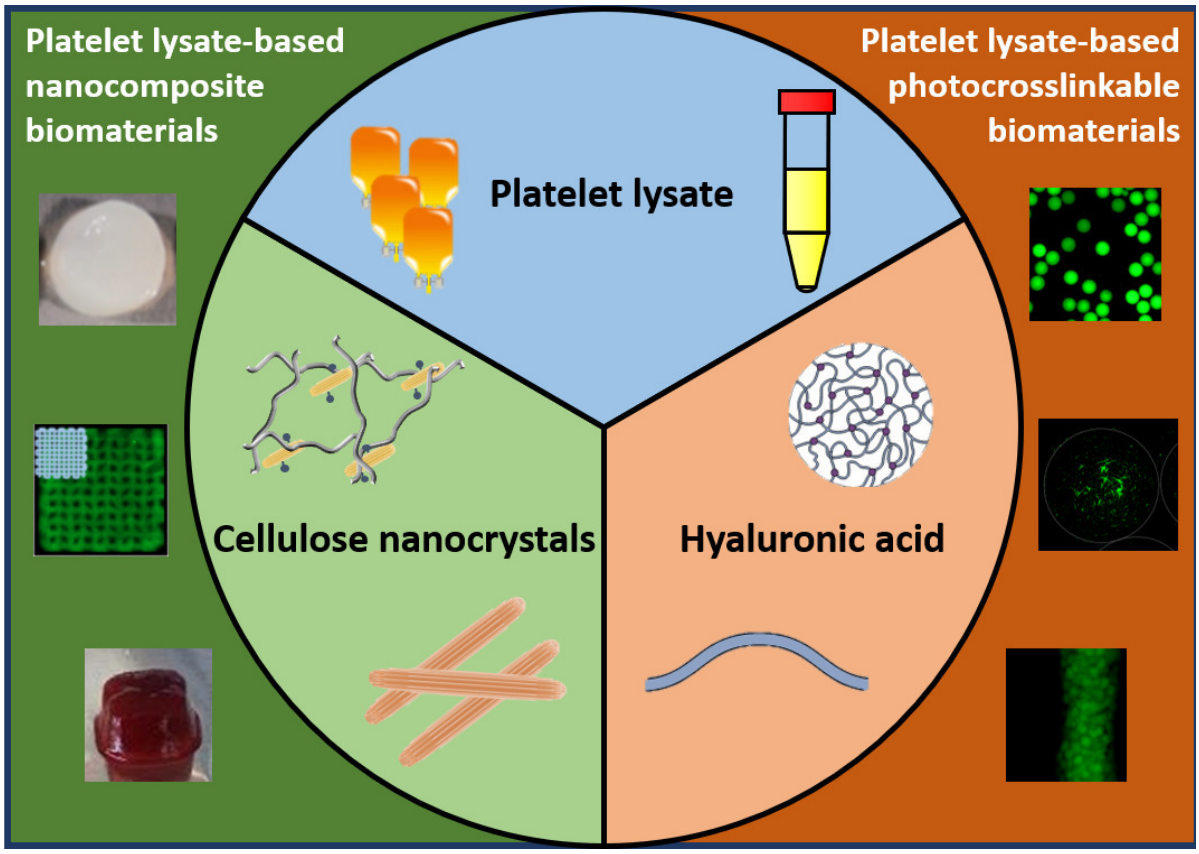

Figure II-1 Summary of the selected polymers/biomaterials and their further combination to produce PL-based systems with improved biophysical and biochemical properties.

II-2. PLATELET LYSATE-BASED COATINGS AND SCAFFOLDS PREPARATION

A plethora of biocompatible scaffolds have been developed along the years aiming at recreating the complex native environment [38]. Until now, the majority of these biomaterials have failed to provide adequate cell anchorage sites, mechanical stability and a dynamic mimetic network, which are crucial to support cell adhesion and proliferation, and to integrate the scaffold into the surrounding native tissue upon implantation [39, 40]. PL have long been known as an inexpensive milieu of GFs with multiple biological activities that can be explored to overcome the above-mentioned drawbacks. However, PL-based strategies are very soft gels that undergo fast degradation, limited structural integrity and extensive retraction upon cells encapsulation. Thus, we proposed different intrinsically bioactive systems to improve PL physical and biochemical properties through several processing techniques and methodologies. In this thesis, PL-based formulations were fabricated in 2D (*Chapter 5*) and in 3D (*Chapter 3, 4, 6 and 7*) systems namely in intrinsically bioactive injectable hydrogels (*Chapter 3*), cryogels (*Chapter 4*), advanced bioinks (*Chapter 6*) and jammed microgel inks (*Chapter 7*). The relevance of the proposed engineered

human-based systems that can find several applications in TERM is discussed in further detail in the following section.

II-2.1. Injectable hydrogels

Hydrogels are three-dimensional crosslinked polymer networks that possess high water content, and are able to mimic salient elements of native ECM (e.g., stiffness, viscoelasticity and microstructure) [39, 41]. Consequently, hydrogels have proven useful in a range of cell culture applications, mainly to modulate protein sequestration and cell behavior (e.g., cell expansion and differentiation) [42]. Particularly, injectable hydrogels have received significant attention in TERM due to their fast *in situ* polymerization, excellent ability in reaching the defects at any depth of tissue, ease administration with minimal surgical wounds, and cells and/or proteins can be easily incorporated before injection [43].

Throughout the last few decades, fibrin as the inherent temporally ECM matrix have been already successfully translated to the clinics as an injectable system (e.g. fibrin gel) [7]. However, the lack of standardization in the formulations preparation, a limited ability to retain and protect biomolecules from degradation and co-delivery of multifunctional molecules led to conflicting results in the therapeutic outcomes [44, 45]. To this end, PL-based fibrin network was reinforced with a-CNC (0 to 0.61 wt.%) to fine-tune the physical and biochemical microenvironment of PL gels, enabling their effective use as an injectable human-based fibrillar hydrogel, ***Chapter 3***. The nanocomposite hydrogel was extruded using a double-barrel syringe (ratio 1:1) to hinder needle clogging, mainly due to the fast polymerization (coagulation cascade induction).

II-2.2. Cryogels

Severe trauma results in the death of over 5 million people annually and is projected to surpass 8 million annually by the year 2020, specifically hemorrhage is responsible for 30 to 40% of trauma mortality [46]. Hence, it is crucial to develop an effective hemostatic agent capable of high blood absorption, concentrating clotting factors and cells and increasing clot formation. The clinical used hemostatic sponges are highly effective in stopping the hemorrhages, however they have a limited structural stability, shape memory, and biological functionality (e.g., antibacterial infection prevention, cell migration and/or proliferation) to induce an efficient regenerative healing after injury [47, 48]. Interestingly, cryogels have been extensively applied as hemostatic agents due to their unique physical

properties (e.g., interconnected macroporous structure, mechanical stability and elasticity), which plays a key role on their large water absorption capability and fast shape recovery [48, 49]. Besides to effective control the hemorrhage (i.e., physical process), it is crucial to envision the design of cryogels with intrinsically bioactive properties to modulate the *in vivo* microenvironment (i.e., biological process).

In ***chapter 4***, cryogels were developed by blending PL with a-CNC aqueous dispersions (1.22 to 2.44 wt.%) at a 1:1 volume ratio proportion. After casting into square molds, the cryogel precursors were frozen at -80°C and subsequently freeze-dried until full cryogelation.

II-2.3. Film coated coverslips

Upon introduction in the biological milieu environment, nanomaterials are rapidly covered with a layer of bioactive molecules (called the protein corona), which defines their biological identity and lifetime [50]. Conceptually, an initial corona is typically formed from the highly abundant proteins, consisting of a more loosely associated and rapidly exchanging layer of biomolecules (called the 'soft' corona) [50-52]. Over time, only the proteins with high nanoparticle affinity were maintained (called the 'hard' corona). Thus, it is expected that individual particles will show different biomolecular corona composition and binding dynamics that largely defines its chemical and biological functionality, for instance can affect the way cells recognize and process the nanosized material [51, 53].

GAGs are key structural and functional naturally-derived polysaccharides that can be distinguished by their sugar constituents, sulfation pattern and 3D conformation.[54, 55] GAGs are crucial to maintain hydrostatic pressure and hence resist compressive forces, covalent attach to proteoglycans to regulate biological functions and due to their negative charge, GAGs can interact with a wide range of positively charged proteins (e.g., growth factors (GFs), adhesion proteins, chemokines).[54-56] Thus, by playing a crucial role in the spatiotemporal bioavailability of these bioactive molecules (i.e., act as a co-factor to enhance signaling or inhibit it by sequestration), they can regulate numerous physiological and pathological processes such as embryogenesis, hemostasis, inflammation, and tumor formation and progression.[57-59] Until now, natural sulfate GAGs have few clinical applications, mainly due to their fast degradation rate, their isolation is costly and time consuming and often from animal sources (e.g., heparin from porcine mucosa), which further encourage the development of biomimetic GAGs for biomedical strategies.[59, 60]

In *chapter 5*, PL-derived bioactive molecules were presented in synergy with CNC with variable sulfation degree. In order to mimic the GFs interactions with ECM proteins (e.g., sulfated GAG's) for localized and low dose delivery with high efficiency to subsequently modulate stem cell behavior *in vitro*. To achieve this, CNC-PL film coated coverslips were fabricated by spin coating, which enables a similar surface density of CNC on glass-coated polyethylenimine regardless of the CNC sulfation degree and charge.

II-2.4. Bioinks

Biofabrication holds the promise to generate complex tissue constructs and fine designed constructs directly from a 3D computer model [61, 62]. Such printed constructs highlight the translational and personalized medicine potential to treat specific tissue defects with a precise control over composition, spatial distribution, and architecture of the printed constructs [61, 62].

Significant progress has been made in the bioink printability, namely in print fidelity and integrity, shear-thinning characteristics, and mechanical strength [61-63]. Although, current bioprinting systems achieved high print resolutions, those strategies suffer limitations on cell biocompatibility and biofunctionality [63]. In particular, the incorporation of cell-binding domains on bioink network is still limited, which is crucial to enhance cell-matrix interactions, and facilitate matrix remodeling and ECM synthesis [64]. Therefore, the previous injectable hydrogel concept (*Chapter 3*) was adjusted to develop a human-based bioink for the freeform biofabrication of hierarchically self-assembled and biologically-relevant 3D structures, *Chapter 6*. PL as a fibrinogen source can be used to mimic the hierarchical nano-to-macro fibrillary composition of native tissues. Moreover, CNC can be used to reinforce this weak fibrin matrix and improve the sustained delivery of the PL therapeutically-relevant bioactive molecules to significantly improve cell response (viability, migration and proliferation) without the use of serum proteins (typically from an animal source).[7]

First, a Creatr 3D printer (Leapfrog) thermoplastic extruder was customized to hold the double barrel syringe (ratio 1:1) coupled with a static mixer and a nozzle. Then, the 3D bioprinting was performed by depositing the biofunctional nanocomposite bioink within the agarose support bath, which sustains the bioprinted layers shape and hold their previously printed 3D structure.

II-2.5. Hydrogel microparticles

Over the past few decades, hydrogel microparticles (HMPs) or microgels have gain increasing relevance to engineer the structural and biochemical complex native microenvironment [65]. Conceptually, these dynamic building blocks are processed in the micro-scale range (10-1000 μm) by microfluidic technologies, which enables the incorporation of microgels with various composition (e.g., degradation, release profiles of encapsulated molecules or cell type) [66]. When HMPs are packed above a critical threshold to permit particle-particle interactions, it behaves as a solid. The cells in these granular hydrogels overcome gel enlacement and spread out fully into their natural morphology [65]. Also, it maximizes cell–cell interactions and synthesis of endogenous ECM, already at an early stage of the assembled constructs [66].

In *chapter 7*, PL in combination with norbornene-modified hyaluronic acid (NorHA) was processed via microfluidics and visible light exposure to obtain uniform building blocks microgels. The microgels were jammed into injectable inks to control the interconnected microporous environment, and to facilitate cell-matrix interactions and cell network formation.

II-3. PLATELET LYSATE-BASED MICRO/NANO-STRUCTURED SCAFFOLDS CHARACTERIZATION

II-3.1. PL-CNC interactions

Given the importance of nanomaterial surfaces on protein interactions and cellular behavior, there is a great need to study the nature of the adsorbed protein layer, or the protein (biomolecule) corona [67]. PL-CNC interactions were analyzed qualitatively and quantitatively by sodium dodecyl sulphate polyacrylic gel electrophoresis (SDS-PAGE) and nanoscale liquid chromatography coupled to tandem mass spectrometry (nano LC-MS/MS) analysis to determine whether the sulfate groups gradient on CNC surface would influence the composition of the PL-derived proteins corona (*Chapter 5).* Briefly, 'soft' corona and 'hard' corona of PL-CNC complexes were analyzed by SDS-PAGE that separates charged molecules in mixtures by their molecular sizes in an electric field [68]. Moreover, 'hard' corona formulations were processed for proteomics analysis following the solid-phase-enhanced sample-preparation (SP3) protocol as described in PMID30464214. Then, protein identification and quantitation was performed by LC-MS/MS. This equipment is composed by an Ultimate 3000 liquid chromatography

system coupled to a Q-Exactive Hybrid Quadrupole-Orbitrap mass spectrometer (Thermo Scientific, Bremen, Germany). Thus, it combines the physical separation capabilities of LC with the structural identity with high molecular specificity of MS [69]. The raw data was processed using Proteome Discoverer 2.4.0.305 software (Thermo Scientific) and searched against the UniProt database for the *Homo sapiens* Proteome 2019_09 and NIST Human Orbitrap HCD Spectral Library.

II-3.2. Microarchitecture

PL-based biomaterials aim at closely mimic the topography and hierarchical fibrillar structure of native ECM. Scanning electron microscopy (SEM), confocal microscopy, atomic force microscopy (AFM) and micro-computed tomography (micro-CT) were used to analyze individual fiber characteristics and scaffold interconnected porous structure. Briefly, SEM is used to analyze the sample's surface morphology (e.g., pore size and topography) by creating a beam of electrons and sweeping it over the specimen to produce an image (***Chapter 3 and 6***) [70] . The main limitation of this technique is the dehydration of the sample before analysis that can alters the native hydrogel structure, even with a prior fixation and a series of grading ethanol concentrations [39]. Hence, fluorescently labeled fibrinogen was added to PL solution to visualize the fiber network by confocal microscopy in a hydrated state (***Chapter 3 and 7***). The basic principle of confocal microscopy is to illuminate one spot of the sample through a pinhole in the detector system that eliminates out-of-focus (background) light [71]. In addition, AFM employs a cantilever-mounted tip to probe atomic details of PL-based hydrogel surface such as topography and young's modulus (***Chapter 3***). When the tip approaches a surface, the cantilever deflection is influenced by atomic interactions between the tip and sample [72].

Finally, PL-based cryogels (***Chapter 4***) were also analyzed by micro-CT to study scaffold anisotropy and microstructure properties (e.g., porosity, interconnectivity and trabecular separation). Micro-CT provides a high-resolution 3D construction of a sample, resulting from the digital projection of 2D trans-axial images of x-rays passing through a sample [73].

II-3.3. Polymerization kinetics and mechanical properties

Material´s physical cues, in particular mechanical properties, can be adjusted to direct the fate of stem cells towards specific lineages [74, 75]. Thus, the physical properties were assessed by AFM, rheology and universal mechanical testing machine. As previously described, AFM cantilever-mounted tip

was used to study the young's modulus of PL-derived fibrin fibers and PL-based hydrogel surface (*Chapter 3*) [72]. On the other hand, the rheometer quantifies the flow and deformation of matter, in which is applied a torque to the top plate that exerts a rotational shear stress on the material and the resulting strain or strain rate (shear rate) is measured to study parameters such as viscosity, storage and loss moduli (*Chapter 3, 6 and 7*) [76]. For example, in *Chapter 3*, rheology was a crucial technique to understand the impact of fibrinogen, thrombin, and calcium/salt concentrations over fibrin polymerization dynamics and the resulting PL-CNC hydrogel mechanical properties.

In addition, universal mechanical testing machine (INSTRON 5540) based on strain gauge load cells was used to record the deformation of PL-based cryogels under unidireccional and cyclic compression assays (*Chapter 4*).

II-3.4. Bioactive molecules delivery profile

PL contains an inexpensive enriched milieu of bioactive molecules (e.g., growth factors, cytokines, morphogens) and self-assembling scaffolding proteins (e.g., fibrinogen, fibronectin, vitronectin), which could modulate the three-dimensional (3D) cellular microenvironment [7]. Their release profile was studied by enzyme-linked immunosorbent assay (ELISA) and western blot, and bicinchoninic acid protein (BCA) assay with and without enzyme (e.g., hyaluronidase) presence. Briefly, ELISA was used to quantify specific antigens (e.g., PDGF-BB) in *Chapter 3*. The principle of this technique relies likewise on antigen-antibody binding, in which the antigen is quantified using a solid-phase enzyme immunoassay. At the end of the assay, the amount of PDGF-BB within the remaining hydrogels was qualitatively evaluated by western blot. Both methods were based on immunodetection, however ELISA generally detects a protein folded in its native form, whereas western blot detects proteins that is denatured during the process of SDS-PAGE [77]. Another technique used was BCA assay (*Chapter 3, 4 and 7*), which is a colorimetric assay that quantifies the total protein content in the sample supernatant. This assay is based in the reduction of Cu^{+2} to Cu^{+1} by protein in an alkaline environment and the chelation of Cu^{+1} by two molecules of BCA creates a purple color that is linear with increasing protein (albumin as protein model) concentrations.

II-3.5. Antibacterial activity

Platelets have shown to play a crucial role on antimicrobial host defence, mainly due to the release of antimicrobial peptides such as platelet factor-4, RANTES, connective tissue activating peptide 3, platelet basic protein, thymosin β-4, fibrinopeptide B, fibrinopeptide A and thrombocidins [7]. Thus, the antibacterial activity of the PL-based cryogels was tested against Gram-negative *Escherichia coli* and Gram-positive *Staphylococcus aureus* (***Chapter 4***).

II-3.6. Hemostatic properties

Once hemostatic agents are applied at the bleeding site, blood is the first component to interact with them [48]. Therefore, blood absorption capability, *in vitro* hemolysis ratio, blood cells adhesion and morphology of PL-based cryogels (***Chapter 4***) were studied.

II-3.7. Cell isolation and culture

PL-derived proteins have shown to influence the 3D cellular microenvironment, namely cell adhesion and proliferation [7, 44]. Moreover, fibrin contains binding sequences for integrins, which facilitate the *in vivo* adhesion of platelets, endothelial cells, smooth muscle cells, fibroblasts and leukocytes [78]. In this thesis, these biological properties were studied by using stem cells, namely human adipose-derived stem cells (hASCs) and human mesenchymal stromal cells (MSCs). These multipotent stem cells generally differentiate into mesodermal lineages such as osteocytes, adipocytes, and chondrocytes [79]. hASCs were obtained from lipoaspirate samples of the abdominal region of patients undergoing plastic surgery, under the scope of previously established protocols with Hospital da Prelada (Porto, Portugal) with the approval of the Hospital Ethics Committee. hASCs isolation and stemness characterization were performed using a previous optimized [80]. Briefly, the lipoaspirate samples were washed with PBS and 1% antibiotic/antimycotic solution until erythrocytes removal, and then digested with 0.05% collagenase Type I A in PBS for 60 minutes at 37 °C under gentle stirring. The digested tissue was filtered and centrifuged at 800xg for 10 minutes at 4°C and the supernatant removed. The heterogeneous cell pellet was resuspended in alpha-modified essential medium (α-MEM) medium supplemented (Thermo Fisher Scientific, USA) with 10% fetal bovine serum (FBS) (Thermo Fisher Scientific, USA), and 1% antibiotic/antimycotic solution (Thermo Fisher Scientific, USA). After 24 hours of incubation, the adherent

cells were washed (hASCs) and characterized by flow cytometry for the expression of mesenchymal stem cells markers (CD45, CD105 and CD90) as previously reported to define multipotent mesenchymal stromal cells [81-83]. Human MSCs were isolated from fresh unprocessed bone marrow from human donors (Lonza, USA) as previously described [84]. Briefly, diluted bone marrow (1:4 with PBS) was separated with Ficoll density gradient centrifugation (800 RCF, 20min). Mononuclear cells were collected from the liquid interface, plated on tissue culture plastic, cultured in α-MEM, 10% FBS, 1% penicillin/streptomycin, 5 ng. ml^{-1} basic fibroblast growth factor at 37 °C and 5% CO_2 until 80% confluency of the colonies and stored in liquid nitrogen (95% FBS, 5% dimethylsulfoxide).

II-3.8. *In vitro* cell culture studies

Stem cells were seeded or encapsulated in the PL-based systems, and then cell behavior was analyzed by cell viability, proliferation, migration, morphology, ECM production and cell differentiation (*Chapter 3 to 7*). Cell viability was assessed by Live/Dead assay, mostly this technique is based on the conversion of the cell permeant non-fluorescent calcein AM dye to the fluorescent calcein dye by intracellular esterase activity in live cells and also on propidium iodide (PI) that is a membrane impermeant, so does not enter in viable cells with intact membranes. The proliferation assays were assessed by cell proliferation using AlamarBlue® and PicoGreen® dsDNA assays. AlamarBlue® is based on resazurin compound, which upon entering living cells is reduced to resorufin and acquires a highly fluorescent and red color. PicoGreen® dsDNA quantification assay is a colorimetric assay that employs fluorescence to evaluate cellular proliferation through the binding to double-stranded DNA. In *chapter 4* (PL-based cryogels), a scratch assay was performed in a hASCs monolayer to mimic the *in vivo* wound healing process [85]. Briefly, the cell monolayer was supplemented with the releasates from PL-CNC cryogels and cell migration was monitored over 48 hours. Then, gene expression of fibrosis-associated mediators (α-smooth muscle actin, matrix metalloproteinase 9 and tissue inhibitor matrix metalloproteinase 1) was analyzed by real-time reverse transcriptase polymerase chain reaction (RT-PCR) analysis, that detects the exponential amplification of DNA sequences (PCR reaction products), removing the variability associated with conventional PCR [86].

Immunofluorescence provided more precise intracellular and extracellular localization of macromolecules. The specific binding of a primary antibody to an antigen, and the further binding of fluorescent-labeled secondary antibody enables the easy visualization of specific proteins under a

fluorescence microscope. For instance, in *chapter 3* was analyzed the collagen type III deposition by the encapsulated hASCs, which is deposited during the initial phases of wound healing [87]. *In chapter 6* was analyzed collagen type I and in *chapter 5* was studied aggrecan expression. Then, the cells were counterstained with Phalloidin-Tetramethylrhodamine B isothiocyanate (Phalloidin-TRITC), and 4,6-Diamidino-2-phenyindole dilactate (DAPI) or Hoechst 33342. Briefly, Phalloidin is a rigid bicyclic heptapeptide lethal toxin that binds and stabilizes actin filaments, whereas DAPI and Hoechst are nuclear and chromosome counterstain that emits fluorescence after binding preferentially to the adenine-thymine regions of DNA. In addition, on injectable hydrogels (*Chapter 3*) and nanostructured coatings (*Chapter 5*) studies, cell differentiation of hASCs was analyzed by RT-PCR (*Chapter 3*), alkaline phosphatase quantification (*Chapter 3*), alcian blue, alizarin red and oil red O staining (*Chapter 5*). In *chapter 3*, RT-PCR was performed for transcription factors related to distinct lineages (e.g., osteogenic, tenogenic, chondrogenic and adipogenic) as well as angiogenic related genes. Moreover, alkaline phosphatase activity was evaluated to assess the potential osteogenic commitment of the encapsulated hASCs. In *chapter 5*, several staining procedures were used, namely alcian blue is widely used as an indicator of the presence of acidic polysaccharides (e.g., sulfated glycosaminoglycans), alizarin red has been used to stain calcium deposits, and oil red O identifies the accumulation of intracellular lipids [88, 89].

II-3.9. *In vivo* studies

Animal protocols were conducted in accordance with Portuguese legislation (Portaria no1005/92) and international standards on animal welfare as defined by the EC Directive 2010/63/EU. Total of 16 Sprague-Dawley male rat of 7 weeks old and average weight of 185–210 g (Envigo, UK) were used in this study. In *chapter 4*, the hemostatic performance of PL-CNC 0.6 and 1.2 cryogels, and a commercial absorbable gelatin sponge (used as a control material), was evaluated on a standardized mouse liver trauma model by bleeding time and hemorrhage volume until hemostasis is achieved, as previously optimized [48]. Moreover, PL-CNC 0.6 and 1.2 formulations, saline solution, and a commercial absorbable gelatin sponge were implanted subcutaneous in mice to assess the in vivo degradation of the biomaterials and overall inflammatory tissue reactions. In each rat, four skin incisions (1 cm length) were made in the dorsal midline, two close to the head and the other two far from the head. At the end of the defined timepoints (7 and 14 days), the implanted materials were retrieved along with the surrounding tissue to standard histological tissue processing. The explants were fixed with 10 vol.% formalin, transferred to histological cassettes for paraffin-embedding, and then counterstained with hematoxylin

and eosin. Hematoxylin is a base that preferentially colors the acidic components (e.g., DNA and RNA, ribossomes) of the cell a bluish tint, whereas eosin is an acid that dyes the basic components of the cell with a pinkish color. The histological evaluation was crucial to assess the local biological effects after samples implantation, which includes fibrosis, necrosis and angiogenesis. This first assessment was determined by quantifying the number of inflammatory cells (e.g., lymphocytes, macrophages) and evaluating the degree of fibrosis and angiogenesis, according to ISO 10993-6, 2007 - biological evaluation of medical devices.

II-3.10. Statistical analysis

GraphPad PRISM version 7.0 was used to perform the statistical analysis. Shapiro-Wilk normality test, and one-way or two-way analysis of variance (ANOVA) was used to analyze experimental data, followed by the Tukey post hoc or Krustal-Wallis test for multiple comparisons. Statistical significance was set to *, $P < 0.05$ **, $P < 0.01$, ***, $P < 0.001$, ****, $P < 0.0001$. Results are presented as mean ± standard deviation.

II-4. REFERENCES

[1] V. Pavlovic, M. Ciric, V. Jovanovic, et al., Platelet Rich Plasma: a short overview of certain bioactive components, Open Med., 11 (2016) 242.

[2] S.G. Boswell, B.J. Cole, E.A. Sundman, et al., Platelet-Rich Plasma: A Milieu of Bioactive Factors, Arthroscopy, 28 (2012) 429.

[3] Ministério da Saúde, PORTARIA Nº 158, DE 04 DE FEVEREIRO DE 2016. Redefine o regulamento técnico de procedimentos hemoterápicos (2016) Portugal.

[4] Ministério da Saúde, Norma 010/2012: Utilização Clínica de Concentrados Plaquetários no Adulto, (2012) Portugal.

[5] J. Schwartz, A. Padmanabhan, N. Aqui, et al., Guidelines on the Use of Therapeutic Apheresis in Clinical Practice–Evidence-Based Approach from the Writing Committee of the American Society for Apheresis: The Seventh Special Issue, J. Clin. Apheresis, 31 (2016) 149.

[6] S.J. Slichter, Evidence-Based Platelet Transfusion Guidelines, Hematology Am. Soc. Hematol. Educ. Program, (2007) 172.

[7] B.B. Mendes, M. Gómez-Florit, P.S. Babo, et al., Blood derivatives awaken in regenerative medicine strategies to modulate wound healing, Adv. Drug Deliv. Rev., 129 (2018) 376.

[8] G. Liumbruno, F. Bennardello, A. Lattanzio, et al., Recommendations for the transfusion of plasma and platelets, Blood Transfus., 7 (2009) 132.

[9] U.D.S. Sekhon, A. Sen Gupta, Platelets and Platelet-Inspired Biomaterials Technologies in Wound Healing Applications, ACS Biomater. Sci. Eng., 4 (2018) 1176.

[10] D. Rainys, G. Samulėnas, M. Kievišas, et al., Platelet biology and the rationale of PRP therapy in chronic wounds, Eur. J. Plast. Surg., 40 (2017) 87.

[11] S. Kandoi, P.k. L, B. Patra, et al., Evaluation of platelet lysate as a substitute for FBS in explant and enzymatic isolation methods of human umbilical cord MSCs, Sci. Rep., 8 (2018) 12439.

[12] D. Klemm, E.D. Cranston, D. Fischer, et al., Nanocellulose as a natural source for groundbreaking applications in materials science: Today's state, Mater. Today, 21 (2018) 720.

[13] R.M. Domingues, M.E. Gomes, R.L. Reis, The potential of cellulose nanocrystals in tissue engineering strategies, Biomacromolecules, 15 (2014) 2327.

[14] M.S. Reid, M. Villalobos, E.D. Cranston, Benchmarking Cellulose Nanocrystals: From the Laboratory to Industrial Production, Langmuir, 33 (2017) 1583.

[15] D. Bondeson, A. Mathew, K. Oksman, Optimization of the isolation of nanocrystals from microcrystalline celluloseby acid hydrolysis, Cellulose, 13 (2006) 171.

[16] M. Jonoobi, R. Oladi, Y. Davoudpour, et al., Different preparation methods and properties of nanostructured cellulose from various natural resources and residues: a review, Cellulose, 22 (2015) 935.

[17] A.C. Mitchell, P.S. Briquez, J.A. Hubbell, et al., Engineering growth factors for regenerative medicine applications, Acta Biomater., 30 (2016) 1.

[18] P.S. Briquez, J.A. Hubbell, M.M. Martino, Extracellular Matrix-Inspired Growth Factor Delivery Systems for Skin Wound Healing, Adv. Wound Care, 4 (2015) 479.

[19] Y.F. Li, J.J.Y. Suen, E. Prince, et al., Colloidal cholesteric liquid crystal in spherical confinement, Nat. Commun., 7 (2016).

[20] S. Araújo-Custódio, M. Gomez-Florit, A.R. Tomás, et al., Injectable and Magnetic Responsive Hydrogels with Bioinspired Ordered Structures, ACS Biomater. Sci. Eng., 5 (2019) 1392.

[21] E. Lam, K.B. Male, J.H. Chong, et al., Applications of functionalized and nanoparticle-modified nanocrystalline cellulose, Trends Biotechnol., 30 (2012) 283.

[22] K.J. De France, T. Hoare, E.D. Cranston, Review of Hydrogels and Aerogels Containing Nanocellulose, Chem. Mater., 29 (2017) 4609.

[23] C.R. Silva, P.S. Babo, M. Gulino, et al., Injectable and tunable hyaluronic acid hydrogels releasing chemotactic and angiogenic growth factors for endodontic regeneration, Acta Biomater., 77 (2018) 155.

[24] Z. Hosseinidoust, M.N. Alam, G. Sim, et al., Cellulose nanocrystals with tunable surface charge for nanomedicine, Nanoscale, 7 (2015) 16647.

[25] B. O'Connor, R. Berry, R. Goguen, Commercialization of cellulose nanocrystal (NCC™) production: A business case focusing on the importance of proactive EHS management, in: Nanotechnology Environmental Health and Safety, Elsevier, 2014, pp. 225.

[26] M. Roman, Toxicity of Cellulose Nanocrystals: A Review, Ind. Biotechnol., 11 (2015) 25.

[27] K.J. De France, M. Badv, J. Dorogin, et al., Tissue Response and Biodistribution of Injectable Cellulose Nanocrystal Composite Hydrogels, ACS Biom. Sci. Eng., (2019).

[28] R.M.A. Domingues, M. Silva, P. Gershovich, et al., Development of Injectable Hyaluronic Acid/Cellulose Nanocrystals Bionanocomposite Hydrogels for Tissue Engineering Applications, Bioconjugate Chem., 26 (2015) 1571.

[29] B.P. Toole, Hyaluronan: from extracellular glue to pericellular cue, Nat. Rev. Cancer, 4 (2004) 528.

[30] J.A. Burdick, G.D. Prestwich, Hyaluronic Acid Hydrogels for Biomedical Applications, Adv. Mater., 23 (2011) H41.

[31] K.J. Wolf, S. Kumar, Hyaluronic Acid: Incorporating the Bio into the Material, ACS Biom. Sci. Eng., (2019).

[32] K.T. Dicker, L.A. Gurski, S. Pradhan-Bhatt, et al., Hyaluronan: A simple polysaccharide with diverse biological functions, Acta Biomater., 10 (2014) 1558.

[33] C.B. Highley, G.D. Prestwich, J.A. Burdick, Recent advances in hyaluronic acid hydrogels for biomedical applications, Curr. Opin. Biotechnol., 40 (2016) 35.

[34] C. Loebel, C.B. Rodell, M.H. Chen, et al., Shear-thinning and self-healing hydrogels as injectable therapeutics and for 3D-printing, Nat. Protoc., 12 (2017) 1521.

[35] W.M. Gramlich, I.L. Kim, J.A. Burdick, Synthesis and orthogonal photopatterning of hyaluronic acid hydrogels with thiol-norbornene chemistry, Biomaterials, 34 (2013) 9803.

[36] C.E. Schanté, G. Zuber, C. Herlin, et al., Chemical modifications of hyaluronic acid for the synthesis of derivatives for a broad range of biomedical applications, Carbohydr. Polym., 85 (2011) 469.

[37] N. Gallo, H. Nasser, L. Salvatore, et al., Hyaluronic acid for advanced therapies: Promises and challenges, Eur. Polym. J., 117 (2019) 134.

[38] M.P. Lutolf, J.A. Hubbell, Synthetic biomaterials as instructive extracellular microenvironments for morphogenesis in tissue engineering, Nat. Biotechnol., 23 (2005) 47.

[39] S.R. Caliari, J.A. Burdick, A practical guide to hydrogels for cell culture, Nat. Methods, 13 (2016) 405.

[40] M.E. Gomes, R.L. Reis, Biodegradable polymers and composites in biomedical applications: from catgut to tissue engineering. Part 2 Systems for temporary replacement and advanced tissue regeneration, Int. Mater. Rev., 49 (2004) 274.

[41] M.W. Tibbitt, K.S. Anseth, Hydrogels as extracellular matrix mimics for 3D cell culture, Biotechnol. Bioeng., 103 (2009) 655.

[42] C.M. Madl, S.C. Heilshorn, Engineering Hydrogel Microenvironments to Recapitulate the Stem Cell Niche, Annu. Rev. Biomed. Eng., 20 (2018) 21.

[43] L. Yu, J. Ding, Injectable hydrogels as unique biomedical materials, Chem. Soc. Rev., 37 (2008) 1473.

[44] T.M. Fortunato, C. Beltrami, C. Emanueli, et al., Platelet lysate gel and endothelial progenitors stimulate microvascular network formation in vitro: tissue engineering implications, Sci. Rep., 6 (2016) 1.

[45] R.E. Marx, Platelet-rich plasma: evidence to support its use, J. Oral Maxillofac. Surg., 62 (2004) 489.

[46] D.S. Kauvar, R. Lefering, C.E. Wade, Impact of hemorrhage on trauma outcome: an overview of epidemiology, clinical presentations, and therapeutic considerations, J. Trauma Acute Care Surg., 60 (2006) S3.

[47] T.L. Landsman, T. Touchet, S.M. Hasan, et al., A shape memory foam composite with enhanced fluid uptake and bactericidal properties as a hemostatic agent, Acta Biomater., 47 (2017) 91.

[48] X. Zhao, B. Guo, H. Wu, et al., Injectable antibacterial conductive nanocomposite cryogels with rapid shape recovery for noncompressible hemorrhage and wound healing, Nat. Comm., 9 (2018) 2784.

[49] A. Memic, T. Colombani, L.J. Eggermont, et al., Latest Advances in Cryogel Technology for Biomedical Applications, Adv. Ther., 2 (2019) 1800114.

[50] M.P. Monopoli, C. Åberg, A. Salvati, et al., Biomolecular coronas provide the biological identity of nanosized materials, Nat. Nanotech., 7 (2012) 779.

[51] I. Lynch, A. Salvati, K.A. Dawson, What does the cell see?, Nat. Nanotech., 4 (2009) 546.

[52] P.d. Pino, B. Pelaz, Q. Zhang, et al., Protein corona formation around nanoparticles – from the past to the future, MateR. Horiz., 1 (2014) 301.

[53] F. Bertoli, D. Garry, M.P. Monopoli, et al., The Intracellular Destiny of the Protein Corona: A Study on its Cellular Internalization and Evolution, ACS Nano, 10 (2016) 10471.

[54] N.S. Gandhi, R.L. Mancera, The Structure of Glycosaminoglycans and their Interactions with Proteins, Chem. Biol. Drug Des., 72 (2008) 455.

[55] T. Miller, M.C. Goude, T.C. McDevitt, et al., Molecular engineering of glycosaminoglycan chemistry for biomolecule delivery, Acta Biomater., 10 (2014) 1705.

[56] J.E. Scott, Structure and function in extracellular matrices depend on interactions between anionic glycosaminoglycans, Pathologie Biologie, 49 (2001) 284.

[57] L. Zhang, Glycosaminoglycan (GAG) Biosynthesis and GAG-Binding Proteins, in: L. Zhang (Ed.) Progress in Molecular Biology and Translational Science, Academic Press, 2010, pp. 1.

[58] U. Freudenberg, Y. Liang, K.L. Kiick, et al., Glycosaminoglycan-Based Biohybrid Hydrogels: A Sweet and Smart Choice for Multifunctional Biomaterials, Adv. Mater., 28 (2016) 8861.

[59] D. Hachim, T.E. Whittaker, H. Kim, et al., Glycosaminoglycan-based biomaterials for growth factor and cytokine delivery: Making the right choices, J. Control. Release, 313 (2019) 131.

[60] D.S.d. Costa, R.L. Reis, I. Pashkuleva, Sulfation of Glycosaminoglycans and Its Implications in Human Health and Disorders, Annu. Rev. Biomed. Eng., 19 (2017) 1.

[61] M.A. Heinrich, W. Liu, A. Jimenez, et al., 3D Bioprinting: from Benches to Translational Applications, Small, 15 (2019) 1805510.

[62] L. Moroni, J.A. Burdick, C. Highley, et al., Biofabrication strategies for 3D in vitro models and regenerative medicine, Nat. Rev. Mater., 3 (2018) 21.

[63] D. Chimene, K.K. Lennox, R.R. Kaunas, et al., Advanced Bioinks for 3D Printing: A Materials Science Perspective, Ann. Biomed. Eng., 44 (2016) 2090.

[64] J. Groll, J.A. Burdick, D.W. Cho, et al., A definition of bioinks and their distinction from biomaterial inks, Biofabrication, 11 (2018) 013001.

[65] L. Riley, L. Schirmer, T. Segura, Granular hydrogels: emergent properties of jammed hydrogel microparticles and their applications in tissue repair and regeneration, Curr. Opin. Biotechnol., 60 (2019) 1.

[66] M.D. Neto, M.B. Oliveira, J.F. Mano, Microparticles in Contact with Cells: From Carriers to Multifunctional Tissue Modulators, Trends Biotechnol., (2019).

[67] I. Lynch, K.A. Dawson, Protein-nanoparticle interactions, Nano Today, 3 (2008) 40.

[68] U.K. Laemmli, Cleavage of Structural Proteins during the Assembly of the Head of Bacteriophage T4, Nature, 227 (1970) 680.

[69] C.S. Hughes, S. Moggridge, T. Müller, et al., Single-pot, solid-phase-enhanced sample preparation for proteomics experiments, Nat. Protoc., 14 (2019) 68.

[70] C. Scheu, W.D. Kaplan, Introduction to Scanning Electron Microscopy, In-situ Electron Microscopy: Applications in Physics, Chem. Mater. Sci., (2012) 3.

[71] G.S. Kino, T.R. Corle, Confocal scanning optical microscopy and related imaging systems, Academic Press, 1996.

[72] G. Binnig, C.F. Quate, C. Gerber, Atomic Force Microscope, Phys. Rev. Lett., 56 (1986) 930.

[73] M.L. Bouxsein, S.K. Boyd, B.A. Christiansen, et al., Guidelines for assessment of bone microstructure in rodents using micro–computed tomography, J. Bone Miner. Res., 25 (2010) 1468.

[74] A.J. Engler, S. Sen, H.L. Sweeney, et al., Matrix Elasticity Directs Stem Cell Lineage Specification, Cell, 126 (2006) 677.

[75] A.W. Holle, J.L. Young, K.J. Van Vliet, et al., Cell-Extracellular Matrix Mechanobiology: Forceful Tools and Emerging Needs for Basic and Translational Research, Nano Letters, 18 (2018) 1.

[76] M.H. Chen, L.L. Wang, J.J. Chung, et al., Methods To Assess Shear-Thinning Hydrogels for Application As Injectable Biomaterials, ACS Biomat. Sci.Eng., 3 (2017) 3146.

[77] T. Mahmood, P.-C. Yang, Western blot: technique, theory, and trouble shooting, N. Am. J. Med. Sci., 4 (2012) 429.

[78] V.K. Lishko, N.P. Podolnikova, V.P. Yakubenko, et al., Multiple binding sites in fibrinogen for integrin alphaMbeta2 (Mac-1), J. Biol. Chem., 279 (2004) 44897.

[79] I. Ullah, R.B. Subbarao, G.J. Rho, Human mesenchymal stem cells - current trends and future prospective, Biosci. Rep., 35 (2015) e00191.

[80] P.P. Carvalho, X. Wu, G. Yu, et al., The effect of storage time on adipose-derived stem cell recovery from human lipoaspirates, Cells, tissues, organs, 194 (2011) 494.

[81] J.M. Gimble, F. Guilak, Differentiation potential of adipose derived adult stem (ADAS) cells, Curr. Top. Dev. Biol., 58 (2003) 137.

[82] J. Gimble, F. Guilak, Adipose-derived adult stem cells: isolation, characterization, and differentiation potential, Cytotherapy, 5 (2003) 362.

[83] M. Dominici, K. Le Blanc, I. Mueller, et al., Minimal criteria for defining multipotent mesenchymal stromal cells. The International Society for Cellular Therapy position statement, Cytotherapy, 8 (2006) 315.

[84] O.F.W. Gardner, M. Alini, M.J. Stoddart, Mesenchymal Stem Cells Derived from Human Bone Marrow, in: P.M. Doran (Ed.) Cartilage Tissue Engineering: Methods and Protocols, Springer New York, 2015, pp. 41.

[85] C.-C. Liang, A.Y. Park, J.-L. Guan, In vitro scratch assay: a convenient and inexpensive method for analysis of cell migration in vitro, Nat. Prot., 2 (2007) 329.

[86] M. Arya, I.S. Shergill, M. Williamson, et al., Basic principles of real-time quantitative PCR, Expert Rev. Mol. Diagn., 5 (2005) 209.

[87] G.C. Gurtner, S. Werner, Y. Barrandon, et al., Wound repair and regeneration, Nature, 453 (2008) 314.

[88] M.F. Pittenger, A.M. Mackay, S.C. Beck, et al., Multilineage Potential of Adult Human Mesenchymal Stem Cells, Science, 284 (1999) 143.

[89] J.-S. Cho, J.-H. Park, J.-H. Kang, et al., Isolation and characterization of multipotent mesenchymal stem cells in nasal polyps, Exp. Biol. Med. (Maywood), 240 (2015) 185.

SECTION 3

EXPERIMENTAL STUDIES

Chapter III

Human-based fibrillar nanocomposite hydrogel as bioinstructive matrices to tune stem cell behavior

Chapter III

Human-based fibrillar nanocomposite hydrogel as bioinstructive matrices to tune stem cell behavior

ABSTRACT

The extracellular matrix (ECM)-biomimetic fibrillar structure of platelet lysate (PL) gels along with their enriched milieu of biomolecules has drawn significant interest in regenerative medicine applications. However, PL-based gels have poor structural stability, which severely limits their performance as a bioinstructive biomaterial. Here, rod-shaped cellulose nanocrystals (CNC) are used as a novel approach to modulate the physical and biochemical microenvironment of PL gels enabling their effective use as injectable human-based cell scaffolds with a level of biomimicry that is difficult to recreate with synthetic biomaterials. The incorporation of CNC (0 to 0.61 wt. %) into the PL fibrillar network during the coagulation cascade leads to decreased fiber branching, increased interfiber porosity (from 66 to 83%) and modulates fiber (from 1.4 ± 0.7 to 27 ± 12 kPa) and bulk hydrogel (from 18 ± 4 to 1256 ± 82 Pa) mechanical properties. As a result of these physicochemical alterations, nanocomposite PL hydrogels resist the typical extensive clot retraction (from 76 ± 1 to 24 ± 3 at day 7) and show favored retention of PL bioactive molecules. The feedback of these cues on the fate of human adipose-derived stem cells is evaluated, showing how it can be explored to modulate the commitment of encapsulated stem cells toward different genetic phenotypes without the need for additional external biological stimuli. These fibrillar nanocomposite hydrogels allow therefore the exploration of the outstanding biological properties of human-based PL as an efficient engineered ECM which can be tailored to trigger specific regenerative pathways in minimal invasive strategies.

This chapter is based on the following publication: ***B. B Mendes***, *M. Gómez-Florit, R. M. A. Domingues, R. L. Reis, M. E. Gomes. Human-based fibrillar nanocomposite hydrogel as bioinstructive matrices to tune stem cell behavior. Nanoscale. 10 (36), 17388-17401. 2018.*

III-1. INTRODUCTION

Blood components orchestrate the highly complex microenvironment present in wound healing by providing a wide range of biological, chemical and scaffold-forming structural elements [1, 2]. In particular, platelet-rich blood derivatives contain an enriched milieu of growth factors (GFs), cytokines, and temporary extracellular matrix (ECM) precursors (e.g. fibrinogen and vitronectin) that have shown to influence stem cell behavior [3-6]. Among them, platelet lysate (PL) is particularly interesting because it shows a comparatively lower batch-to-batch variability due to its preparation method based on platelet disruption instead of activation with calcium or/and thrombin (e.g. platelet-rich fibrin), which clearly contributes to standardization of formulations [7-10], and because it hardly forms a spontaneous gel due to the removal of clot and platelet debris during its preparation that allows an easy further processing [10].

In clinical settings, the delivery of platelet-rich blood derivatives relies on their direct injection and further spontaneous platelet activation upon contact with the native collagen tissue [11, 12], or on the induction of the coagulation cascade prior to their injection by the addition of thrombin and/or calcium to be used as a fibrin-based scaffold [13]. Interestingly, the produced fibrin scaffold is organized into an ECM mimetic fibrillar network that contains key cell adhesion binding motifs, which promote an efficient tissue healing [14]. Despite their rapid translation into clinical applications for the treatment of numerous conditions, particularly of the musculoskeletal system [3], several pre-clinical studies and clinical trials have continuously shown contradictory therapeutic outcomes [15, 16]. Among the several limitations that can be identified to justify these results, there is the lack of well-designed clinical trials, the poor characterization of blood derivatives samples and the lack of control over the delivery mechanisms of multiple signaling biomolecules [10]. Moreover, current natural fibrillar gel scaffolds solely based on blood derivatives components exhibit limited ability to retain and protect biological active biomolecules from degradation [17], have extremely low mechanical properties and structural stability [18], and show a high contractile effect (~75% reduction in gel volume) upon cell encapsulation, severely limiting their potential as cell carriers and modulators of wound healing [19].

The reinforcement of low strength matrices generated by chemically or physically crosslinking natural and synthetic polymers with nanomaterials is being explored as tissue engineering and regenerative (TERM) strategies to produce a new generation of nanocomposite hydrogels with added functionalities (e.g. electrical or magnetic responsiveness) [20, 21], as well as to modulate their mechanical and/or biological properties, or to trigger specific cellular responses [22]. In this sense, we and others have been

using cellulose nanocrystals (CNC), i.e. rod-shaped nanoparticles produced from cellulose fibers, as natural-based nanofillers to improve the mechanical, structural and cell supporting properties of soft hydrogel matrices [23-25]. The outstanding strength and stiffness, high aspect ratio, convenient surface chemistry and high biocompatibility of CNC, are some of the properties that make them an appealing alternative to other typical reinforcing nanofillers. Additionally, the presence of sulfate groups on CNC surface resulting from their typical production method (based on sulfuric acid hydrolysis) might potentially allow an efficient binding of GFs through specific and reversible electrostatic interactions. This process would mimic the natural stabilization of GFs by sulfated glycosaminoglycans (GAGs) present in the ECM that are known to regulate their spatio-temporal presentation and signaling mechanisms in native tissues [26, 27]. In fact, it has been demonstrated that soluble cellulose sulfate derivatives with structural similarities to heparin, an highly sulfated GAG, establish specific interactions with growth factors, namely bone morphogenic protein 2 (BMP-2) and basic fibroblast GF (FGF-2) [28-30], suggesting that the sulfate groups on CNC surface might play a relevant role on the active modulations of the hydrogel biological microenvironment. In addition, CNC reinforcement might additionally enable to tune the mechanical properties of fibrin network at the fiber level in order to stabilize the natural fibrillar nature of blood derivatives and to use them as injectable biomimetic scaffolding biomaterials.

In this work, we developed an injectable and multifunctional nanocomposite fibrillar hydrogel based on the induction of PL coagulation cascade while incorporating CNC modified with surface aldehyde groups (Supplementary Figure III-1). Conceptually, CNC will be entrapped in the fibrils' structure and simultaneously crosslinked through reversible Schiff base bonds established with the amine groups of PL proteins. Thus, it is anticipated that this simple one-pot polymerization and crosslinking method potentiates its fast in situ gelation and structural stabilization after extrusion while allowing their administration using minimal invasive strategies. We hypothesize that the incorporation of CNC will not only have a positive impact on the microstructural and mechanical properties of the fibrillar structure but will also enable to modulate the biochemical microenvironment generated within the hydrogel. It is expected that these dynamic alterations on the physicochemical properties of PL-based fibrillar hydrogels

can influence the biological behavior of encapsulated stem cells and enable their use in a wide range of TERM applications.

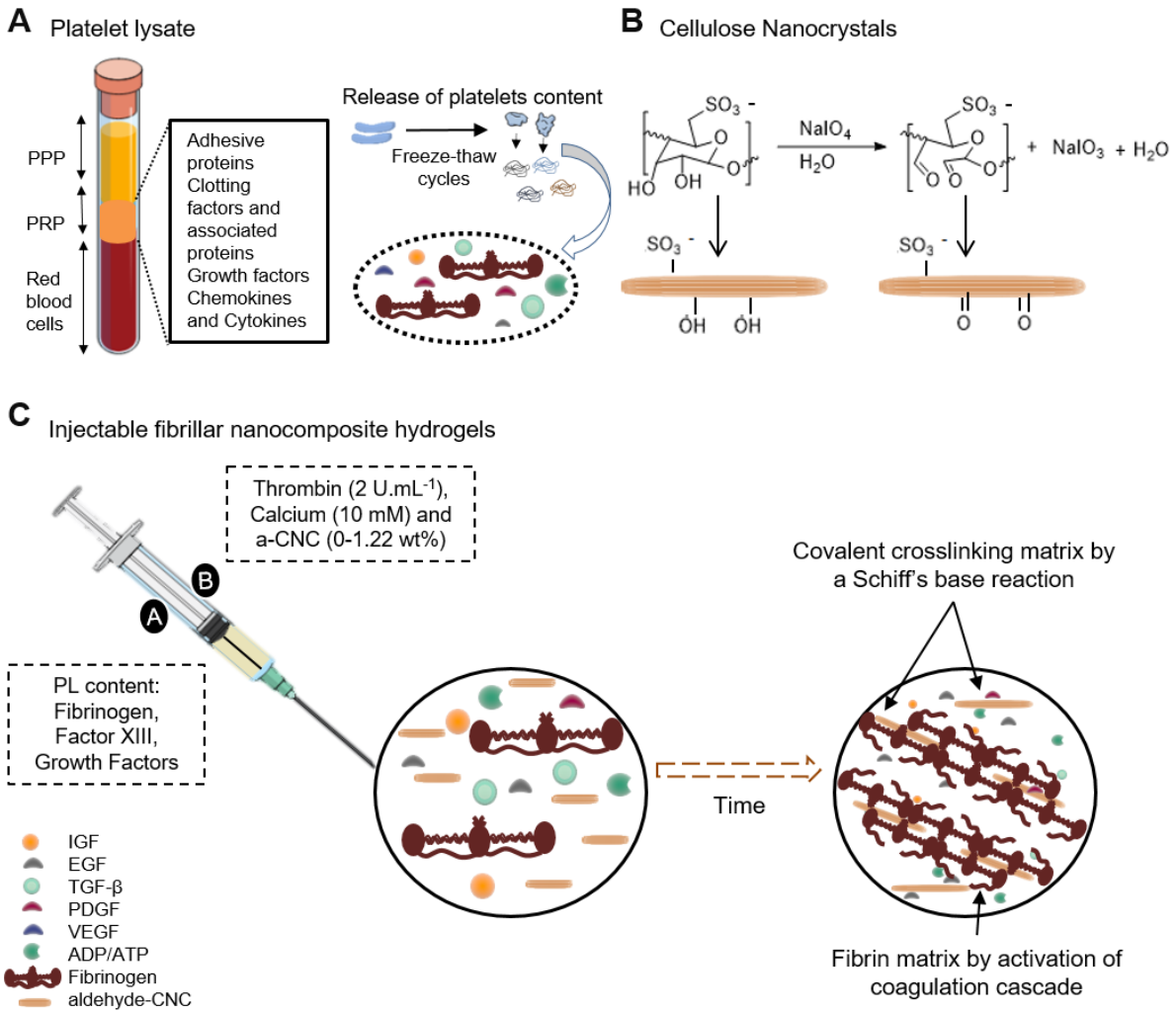

Scheme III-1 Schematic representation of the preparation of natural fibrillar nanocomposite hydrogels (PL-CNC 0-0.61). PL was obtained by freeze-thaw cycles which allowed the release of platelets content (A). CNC were modified with aldehyde groups by periodate oxidation (B). Injectable fibrillar nanocomposite hydrogels were prepared using fibrin polymerization (coagulation cascade induction) and covalent crosslinking between aldehydes on CNC surface and amine groups of PL proteins (Schiff's base reaction) (C).

III-2. MATERIALS AND METHODS

III-2.1. Hydrogel preparation

Stock solutions of PL and a-CNC were produced and fully characterized (for details on the preparation and characterization, see supporting information). Double-barrel syringe L-system (1:1 from Medmix,

Switzerland) with a static mixer tip (Medmix, Switzerland) was used to produce the hydrogels. Barrel A was filled with PL (67.6 mg mL^{-1} of total protein) composed of albumin, growth factors, cytokines and structural proteins (such as fibrinogen, vitronectin and fibronectin). Barrel B was composed of thrombin from human plasma (2 U mL^{-1}, Sigma-Aldrich, USA), calcium (10 mM, Sigma-Aldrich, USA) and a-CNC water dispersions corresponding to 0, 2.3, 4.5, 9 and 18 wt.% of PL total protein content. The precursor solutions were then hand extruded into cylindrical acrylic molds (10 mm diameter x 6 mm height). Finally, the samples were incubated during 2 hours at 37 °C to allow PL matrix polymerization and crosslinking. The final hydrogels were all composed of 50 vol.% of PL and were named according to their a-CNC concentrations: 0 wt.% (PL-CNC 0), 0.15 wt.% (PL-CNC 0.15), 0.31 wt.% (PL-CNC 0.31), 0.45 wt.% (PL-CNC 0.45), and 0.61 wt.% (PL-CNC 0.61).

III-2.2. Hydrogel characterization

III-2.2.1. Characterization of nanocomposite hydrogel microstructure

Hydrogels were produced as described above and then fixed in 2% glutaraldehyde (Merck, Germany) for 2 hours. After fixation, samples were solvent exchanged from water to ethanol (ethanol gradient from 25, 50, 75 and 99.9 vol.%) for 4 hours and then critical point dried with CO2. After immersion in liquid nitrogen, the samples were freeze-fractured to expose their inner structures, and sputter coated (30 seconds at 20 mA, Cressington) with gold prior observation in a scanning electron microscope (JSM-6010LV, JEOL, Japan). Based on the typical fibrinogen concentration range in PL (454 ± 75 µg mL^{-1}) [31], 9 µg of Alexa Fluor® 488 conjugated fibrinogen from human plasma (Thermo Fisher Scientific, USA) were added to each 1 mL of PL solution (barrel A) for visualization of the fibrin network by confocal microscopy. For this analysis, PL-CNC hydrogels were produced in PDMS molds (9 mm diameter x 2 mm height) on a glass coverslip and observed on a laser scanning confocal TCS SP8 (Leica Microsystems, Germany) with a 63x immersion objective. Twenty micrometer thick Z-stacks were imaged at every 0.2 µm beginning 5 µm above the coverslip surface. PL-CNC hydrogels porosity was calculated using ImageJ software (National Institutes of Health, USA). Z-stacks obtained from confocal fluorescence were subdivided into 4 µm Z-stacks (20 frames) and the corresponding projected images were filtered with Gaussian Blur filter (Sigma radius 1), background subtracted (pixel 15) and sharpen. From these filtered images, a thresholding mask was set to the mean pixel intensity of the image and the image was inverted

to determine the percent area that was not considered as a fiber. Then, the porosity area was determined indirectly.

III-2.2.2. Polymerization kinetics and mechanical properties of nanocomposite hydrogels

A Kinexus Prot Rheometer (Malvern Instruments, United Kingdom) with a parallel-plate geometry and a hood for temperature control (37 °C) was used to measure the viscoelastic properties of PL-CNC hydrogels. Time-sweep tests were applied to study polymerization kinetics of the different formulations. Immediately after dispensing 320 µL of extruded solution on the bottom plate, a 20 mm diameter top plate was lowered to a final gap of 1 mm (parallel plate set up). A thin film of mineral oil was poured over the exposed surface to reduce water evaporation. This time point was defined as the starting time (t=0). Time-sweep assays were performed at a strain amplitude of 1% and frequency of 1 Hz, and storage modulus values were monitored continuously at 10 seconds intervals. In strain and frequency-sweeps tests, hydrogels were formulated as described above and an 8 mm top plate was used (parallel plate set up). A fixed frequency of 1 Hz was applied with a strain amplitude from 0.01 to 100% to establish the linear region. At a fixed strain amplitude value (0.5%) selected within linear viscoelastic region, frequency sweeps from 0.1 to 10 Hz were performed to obtain the frequency dependence of the storage modulus (G') and loss modulus (G''). All measurements were performed in triplicate. Nanomechanical properties of the fibrillary hydrogels were assessed by atomic force microscopy (AFM, NanoWizard 3, JPK Instruments, Germany). Hydrogels were prepared on a coverslip sample holder (JPK Instruments) and kept hydrated in phosphate buffered saline (PBS). Cantilevers (Bruker, MSNL-10-C, nominal k = 0.01 N m-1) was pre-calibrated in PBS using a contact-based method (on a glass surface). Height and moduli images (256x256 pixels) were acquired over a 100 μm^2 square area of the hydrogel. Moduli were calculated by fitting the results to the Sneddon Model using a Poisson ratio of 0.5. At each acquired point it was used an indentation depth between 0.5-1.0 µm. JPK SPM Data Processing (JPK Instruments) were used to determine hydrogel (n=4) and fiber (n=20) rigidity.

III-2.2.3. Hydrogel degradation

For degradation assays, hydrogels were produced in a circular polypropylene support (9 mm diameter x 4 mm height). Each support was pre-weighted, and their weight was subtracted to the total weight of the support with hydrogel to obtain the hydrogel initial mass (M_i). After 2 hours of incubation at

37 °C to allow hydrogel polymerization and crosslinking, each hydrogel was incubated in 1.5 mL of PBS pH=7.4 at 37 °C and successively weighted at different time points to obtain the final mass (M_f). The weight loss was calculated according to the following Equation 1. The results are an average of three measurements obtained per formulation (n=4).

$$\text{Weight loss } (\%) = \frac{\text{Mi} - \text{Mf}}{\text{Mi}} \text{ x } 100$$

Equation III-1 Quantification of hydrogel weight loss.

III-2.2.4. Growth factor release

Hydrogels were produced in circular supports (V=0.4 mL) as described above for hydrogel degradation assay and incubated in 0.7 mL of cell culture medium at 37 °C. At different time points (6 h, 1, 2, 4, 5 days), the supernatant was collected and replaced with fresh cell culture medium. Platelet-Derived Growth Factor-BB (PDGF-BB) content in the supernatant of PL-CNC 0, 0.31 and 0.61 (n=5) was quantified using human PDGF-BB enzyme-linked immunosorbent assay (ELISA) Development kit (Peprotech, USA) according to the manufacturer's instructions. Furthermore, on day 5, remaining hydrogels were disrupted using a tissue grinder (Nippon Genetics, Japan) and 5 seconds of sonication using a sonication probe. After centrifugation, the pellet was used to detect PDGF-BB by sodium dodecyl sulfate–polyacrylamide gel electrophoresis (SDS-PAGE) and Western Blot. Laemmli sample buffer was mixed with standard PDGF-BB (Peprotech, USA) at 1:1 ratio, and with hydrogels pellet and PL at 9:1 ratio. All formulations were heated at 95 °C for 5 minutes and subjected to SDS-PAGE using 3% stacking and 12.5% separation polyacrylamide gels prepared according to manufacturer's protocol (SDS Gel Preparation kit, Sigma Aldrich, USA). Electrophoresis was carried out at 75 V for 15 min and then at 150 V for 1 h (BioRad, USA). The SDS-PAGE and polyvinylidene difluoride membrane were overlapped and proteins transferred at 70 V and 350 mA for 15 min (Pierce Power station, Thermo Fisher Scientific, USA). 5% milk powder solution was used for membrane blocking for 30 min at RT. The membrane was then incubated with 1:100 dilution rabbit anti-PDGF-BB (Peprotech, USA) primary antibody under mild mixing at 4 °C overnight. The membrane was washed with TBS-T solution for 5 min (3x) then incubated with a 1:1000 dilution of goat anti-rabbit IgG – alkaline phosphatase (Vector laboratories, USA) mixed at RT for 30 minutes, before washing the membrane as described above. The alkaline phosphatase

conjugate substrate (Thermo Fisher Scientific, USA) was added to the polyvinylidene difluoride membrane until color development, and after water washing, membranes were scanned.

III-2.3. Cell isolation and encapsulation in the hydrogels

Human adipose-derived stem cells (hASCs) were obtained from lipoaspirate samples of the abdominal region of patients undergoing plastic surgery, under the scope of previously established protocols with Hospital da Prelada (Porto, Portugal) with the approval of the Hospital Ethics Committee. The hASCs isolation and stemness characterization were performed using a previous optimized [32] Briefly, the lipoaspirate samples were washed with PBS and 1% antibiotic/antimycotic solution until erythrocytes removal, and then digested with 0.05% collagenase Type I A in PBS for 60 minutes at 37 °C under gentle stirring. The digested tissue was filtered and centrifuged at 800xg for 10 minutes at 4°C and the supernatant removed. The heterogeneous cell pellet was resuspended in α-MEM medium supplemented (Thermo Fisher Scientific, USA) with 10% fetal bovine serum (FBS) (Thermo Fisher Scientific, USA), and 1% antibiotic/antimycotic solution (Thermo Fisher Scientific, USA). After 24 hours of incubation, the adherent cells were washed (hASCs) and characterized by flow cytometry for the expression of mesenchymal stem cells markers (CD45, CD105 and CD90), Figure S4, as previously reported to define multipotent mesenchymal stromal cells [33-35]. hASCs were maintained in α-MEM supplemented with 10% FBS, and 1% antibiotic/antimicotic solution at 37 °C, 5% CO2. hASCs were loaded to PL solution (barrel B) at a density of 2x106 cells per 1 mL of PL (1x106 cells per 1 mL of final hydrogel), then hydrogels were produced as described above. All cell culture assays of hASCs encapsulated in hydrogels were performed using culture media without FBS.

III-2.4. *In vitro* cell culture studies

III-2.4.1. Cellular viability and proliferation studies

Cellular viability was assessed using 1:500 vol.% Calcein AM (Thermo Fisher Scientific, USA) and 1:1000 vol.% propidium iodide (Thermo Fisher Scientific, USA) for 15 min at 37 °C to stain live and dead cells, respectively. Samples were washed with PBS to reduce background fluorescence and visualized using confocal microscope TCS SP8 (Leica Microsystems, Germany). The metabolic activity of encapsulated hASCs was evaluated at 1, 4 and 7 days using Alamar Blue assay (Bio-Rad, USA).

Fluorescence readings of Alamar Blue were normalized to the deoxyribonucleic acid (DNA) content. For DNA quantification, hydrogels were sonicated three times for 10 s using an ultrasound probe at 40% of amplitude output. Released DNA was quantified using Quant-iT PicoGreen dsDNA assay kit (Thermo Fisher Scientific, USA) following manufacturer's instructions.

III-2.4.2. Cell morphology and matrix production

hASCs encapsulated in all PL-CNC hydrogels were cultured up to 8 days. Additionally, to analyze cell morphology within the fibrillar network, some hydrogel formulations were supplemented with fibrinogen-FITC, as described above for the analysis of the hydrogel microstructure. Hydrogels were washed with PBS and then fixed in 10 vol.% formalin (Thermo Fisher Scientific, USA) for 15 min at RT and permeabilized using 0.2 vol.% Triton-X100 (Sigma-Aldrich, USA). After washing, samples were incubated with 1:200 v/v rhodamine-conjugated phalloidin (Sigma-Aldrich, USA) for 10 minutes and 1:1000 v/v 4′, 6-diamidino-2-phenylindole (DAPI, Sigma-Aldrich, USA) for 20 minutes (dilutions in PBS). For collagen type III, samples were blocked using 3 w/v.% BSA and incubated with 1:100 v/v solution of specific primary antibody (ab7778, Abcam, UK). Then, samples were incubated with 1:200 v/v Alexa Fluor® 488 conjugated secondary antibody (Thermo Fisher Scientific, USA). The hydrogels were observed under a confocal microscope TCS SP8 (Leica Microsystems, Germany). The effect of CNC content on cell spreading area and cell axial ratio was characterized by analyzing their shape using Image J software object tools. Fluorescence confocal images were converted to binary images to identify individual cells and a mean threshold was used to quantify morphometric parameters. Aspect ratio and cell area were quantified at day 1 for all formulations (n=20) and at day 3 (n=20) for PL-CNC 0.61 formulation.

III-2.4.3. Ribonucleic acid (RNA) isolation and real-time polymerase chain reaction (PCR) analysis

After 1 and 7 days of cell culture, total RNA was isolated using Ribozol (Amresco, USA), according to manufacturer's protocol. Total RNA was quantified at 260 nm using a nanodrop spectrophotometer (Thermo Fisher Scientific, USA). The same amount of RNA (0.2 µg) was reverse transcribed to complementary DNA (cDNA) according to the protocol of the supplier (qScript cDNA Synthesis Kit, Quanta Biosciences, USA). Aliquots of each cDNA sample were frozen (-20 °C) until the PCR reactions were carried out. Real-time PCR was performed for two reference genes, glyceraldehyde-3-phosphate dehydrogenase (GAPDH) and β-Actin and target genes (Supplementary Table III-1). Real-time PCR was

performed in a thermocycler (Realplex, Eppendorf, Germany) using SYBR green detection (Quanta Biosciences, USA). Each reaction contained 7 µl of master mix (Perfecta SYBR Green FastMix, Quanta Biosciences, USA), the sense and the antisense specific primers (0.5 µM) and cDNA sample (3 µl) in a final volume of 10 µl. The amplification program consisted of a pre-incubation step for denaturation of the template cDNA (5 minutes 95 °C), followed by 45 cycles consisting of a denaturation step (10 seconds 95 °C), an annealing step (10 seconds 60 °C) and an extension step (10 seconds 72 °C). After each cycle, fluorescence was measured at 72 °C. A negative control without cDNA template was run in each assay. All samples were normalized by the geometric mean of the expression levels of β-Actin and GAPDH and fold changes were related to the control groups using the equation 2 adapted from [36]. Stability of reference genes was calculated using a statistical tool (BestKeeper software, Technical University of Munich, Weihenstephan, Germany) [37].

$$ratio = \frac{E_{\text{target}}^{\Delta \text{Cp target (mean control – sample)}}}{E_{\text{reference}}^{\Delta \text{Cp reference (mean control – sample)}}}$$

Equation III-2 Normalization of the experimental gene expression results. Where Cp is the crossing point of the reaction amplification curve and E is the efficiency from the given slopes using serial dilutions

III-2.4.4. Alkaline phosphatase activity

After 9 days of culture, hydrogels were washed with PBS and cells were lysed in water using two freeze-thaw cycles, mechanical disruption and ultrasounds. ALP activity from 25 µl of sample was quantified by measuring the cleavage of 100 µl of p-Nitrophenyl phosphate (pNPP; Sigma-Aldrich, USA) in a soluble yellow end product that absorbs at 405 nm. In parallel, a standard curve with calf intestinal ALP (Roche, Germany) was constructed. Readings were normalized to the DNA content, as previously described.

III-2.5. Statistical Analysis

The statistical analysis of data was performed using GraphPad PRISM v 7.0. One-way or two-way analysis of variance (ANOVA) was used to analyze experimental data, followed by Tukey post-hoc test for multiple comparisons. Statistical significance was set to $p < 0.05$. Results are presented as mean ± standard deviation.

III-3. RESULTS AND DISCUSSION

III-3.1. CNC content tuned the microstructural and physicochemical properties of fibrillar nanocomposite hydrogels

Fibrin gels result from the self-assembly of fibrinogen induced by thrombin and/or calcium ions, being widely explored as a multifunctional framework for cell adhesion, proliferation and differentiation [13]. In our study, the nanocomposite hydrogel was extruded using a double-barrel syringe (ratio 1:1). Barrel A was filled with PL (67.6 mg. mL^{-1} of total protein content) and barrel B was composed of thrombin, calcium ($CaCl_2$) and a-CNC water dispersions. Herein, the concentrations of thrombin and calcium were pre-optimized to maximize the hydrogel mechanical properties and stability (Supplementary Figure III-2). The final concentration of 1 $U.mL^{-1}$ thrombin and 5 mM $CaCl_2$ produced relatively fast gelling and stable PL gel clots and was therefore chosen as the control condition (PL-CNC 0). CNC were then incorporated at varying concentrations (0.31-1.22 wt.%) to obtain nanocomposite fibrillar hydrogels with the final concentration of 0.15-0.61 wt.% (PL-CNC 0.15-0.61) (Scheme III-1).

The impact of CNC on individual fiber characteristics and hydrogel network microstructure were analyzed by confocal and scanning electron microscopy (SEM), Figure III-1. For confocal microscopy analysis, 9 µg of fluorescently labeled fibrinogen was added to 1 mL of PL solution in order to enable the observation of the fiber structure. Similarly to the previously reported characteristic of other PL based hydrogel [31], PL-CNC 0 exhibited a dense meshwork of highly branched and randomly oriented fibrin fibers with low interfiber space (Figure III-1A and D). The incorporation of CNC led to an overall decrease of fiber branching and gradual increase of interfiber porosity from 66% in PL-CNC 0 up to 83% in PL-CNC 0.61 (Figure III-1B). Interestingly, the same trend is also observed in fiber diameter, with PL-CNC 0 having relatively thin fibers (152 ± 54 nm) that gradually become thicker with increasing CNC incorporation in nanocomposite hydrogels (259 ± 85 nm in PL-CNC 0.61), Figure III-1C.

Under physiological conditions, fibrin central domains interact non-covalently with complementary sites at the end domains of other fibrin molecules and assemble into two-stranded protofibrils. Upon growing to a sufficient length, protofibrils start to laterally associate [38-40]. In our study, the observed physical differences demonstrate that CNC have an impact on the fibrinogen self-assembly and fibrin network architecture mechanisms. Considering CNC dimensions (3.5 ± 1.3 nm of height and 168 ± 60 nm of length, determined by atomic force microscopy), it is plausible that CNC might get entrapped along

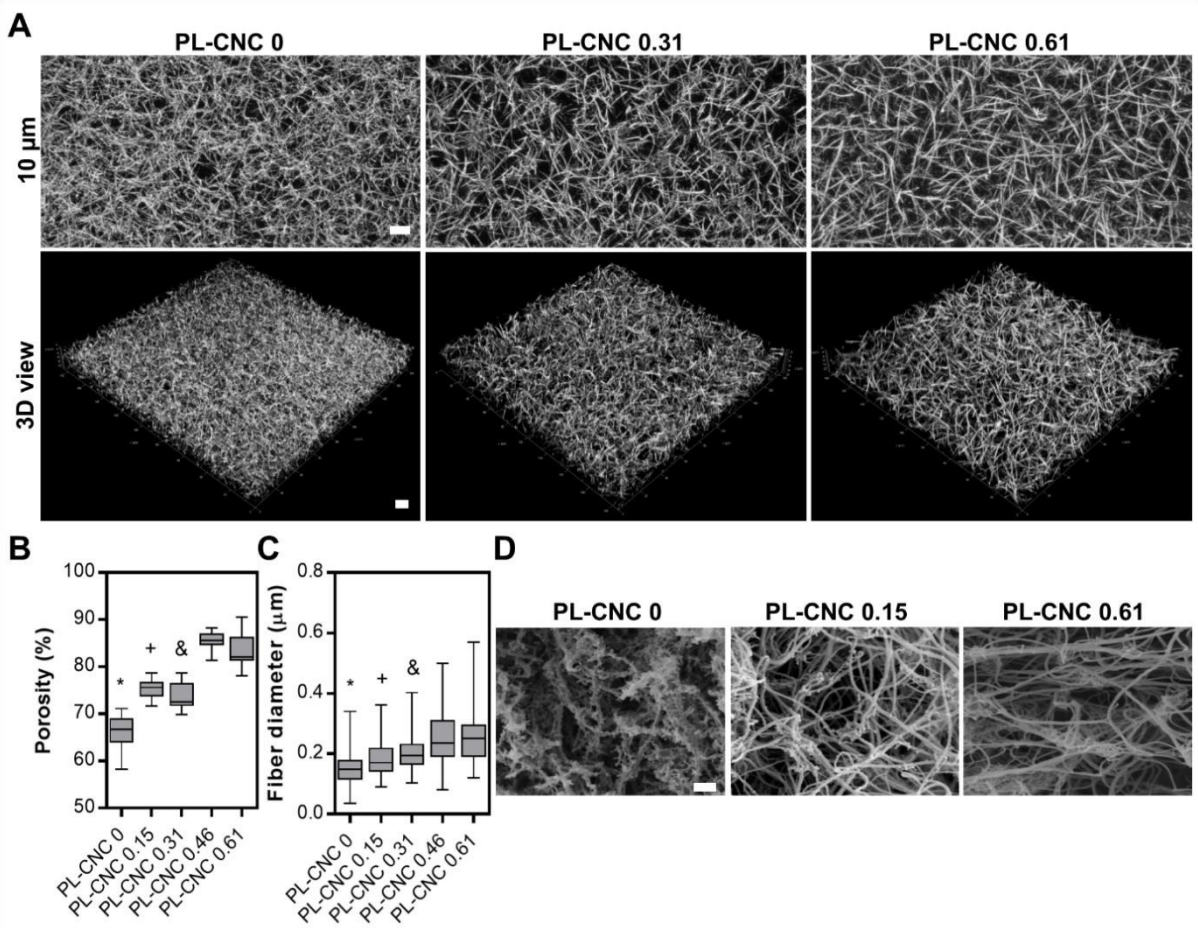

Figure III-1 Microstructure of PL and nanocomposite fibrillar hydrogels. Maximum intensity projection (10 µm height stack) and 3D view of Alexa Fluor 488 conjugated fibrinogen showing fibrin polymerized network (A). Percent of porosity of a 4 µm thick section of fluorescent confocal images (B). Fiber diameter determined from SEM images (C). Microstructural analysis by SEM (D). Statistical differences: $P < 0.05$, * PL-CNC 0 vs PL-CNC (0.15-0.61); + PL-CNC 0.15 vs PL-CNC (0.46-0.61) and & PL-CNC 0.31 vs PL-CNC (0.46-0.61). Scale bar: 10 µm (A) and 1 µm (D).

the fibers during the lateral aggregation of fibrin protofibrils, and at the same time introduce intermolecular covalent bonds that might further promote this process. Since the aldehyde groups on CNC's surface allow them to act as covalent protein crosslinkers, it potentiates the natural fiber packing, playing a similar role as Factor XIIIa, which forms crosslinks between the protofibrils within each fiber and later complete the maturation of the network structure [41, 42]. Consequently, fibers gradually become more densely packed with increasing CNC content, ultimately resulting in thicker and straighter fibers as observed in the nanocomposite hydrogels.

The structural differences induced by the incorporation of CNC in PL hydrogels led to significant changes in their physical properties. Figure III-2 shows the mechanical properties at different length scales (bulk and nanoscale), degradation behavior and platelet-derived GF-BB (PDGF-BB) release profile of hydrogels prepared with different CNC concentrations (0 to 0.61 wt.%). Concerning the bulk mechanical

behavior, no significant differences could be detected for gelation time, with all formulations showing a solid-like behavior (G´ > G´´) right after extrusion (t=0) rather than behaving as a fluid (Figure III-2A). Nevertheless, increasing CNC loadings gradually increased the storage modulus (G') plateau, although at the highest CNC content it could be noticed a slower progression that did not fully cease after 1.5 hour. This behavior finds some parallelism with the slow increase of stiffness observed in blood clots along the time, a process governed by Factor XIIIa [41], supporting our hypothesis on the effect of CNC over the mechanisms of fiber formation. In general, all formulations showed a relatively fast polymerization and crosslinking, reaching a near G' plateau within 5 to 10 min of incubation, demonstrating therefore its potential to be used as an injectable and in situ crosslinkable formulation.

Measurements within the hydrogel linear viscoelastic region demonstrated that bulk hydrogel stiffness significantly increased compared to the neat PL matrix, even at the low CNC loadings used here (Figure III-2B). While PL-CNC 0 had a low storage modulus (18 ± 4 Pa), confirming the soft nature of these gels also reported in other studies (G' lower than 10 Pa for similar PL formulations) [31], for formulations containing CNC, G' increases by up to an impressive two orders of magnitude (1256 ± 82 Pa in PL-CNC 0.61). We next explored the nanoscale mechanical properties of the nanocomposite hydrogels to better understand and anticipate the possible interactions with cells at this size scale (Figure III-2C and D). High CNC loadings increased hydrogel rigidity, as observed in the bulk rheological characterization (Figure III-2C). Strikingly, PL-CNC 0, 0.31 and 0.61 fibers achieved elasticity values (Young's modulus) close to brain (0.1-1 kPa), muscle (8-17 kPa) and collagenous bone (25-40 kPa) tissues, respectively [43, 44], Figure III-2D. However, whereas the rigidity of PL-CNC 0 hydrogel (1.8 ± 0.03 kPa) was similar to the values obtained along its fibers (1.4 ± 0.7 kPa) as demonstrated by the homogeneous elastic modulus along these samples (Figure III-2C), increase of CNC loadings is accompanied by an increase of fiber thickness (topography images) and sample heterogeneity (moduli images), showing significant difference between fiber (27 ± 12 kPa) and hydrogel moduli (12 ± 7 kPa). Interestingly, it has been previously demonstrated that the fiber elastic modulus strongly decreases with increasing fiber diameter in either plasma or purified fibrinogen clots [39]. It has been suggested that this negative diameter dependence of the modulus is correlated with a decrease of cross-sectional density of bonds within fibrin fibers with larger diameters. Moreover, it has also been demonstrated that clots with thinner fibers have higher whole-clot moduli due to the increased modulus of the single fibers and network branch points [39, 45]. Remarkably, the mechanical properties of our nanocomposite hydrogels show a reverse trend. Increasing CNC loadings leads to 1) thicker fibers with higher stiffness; 2) hydrogels with

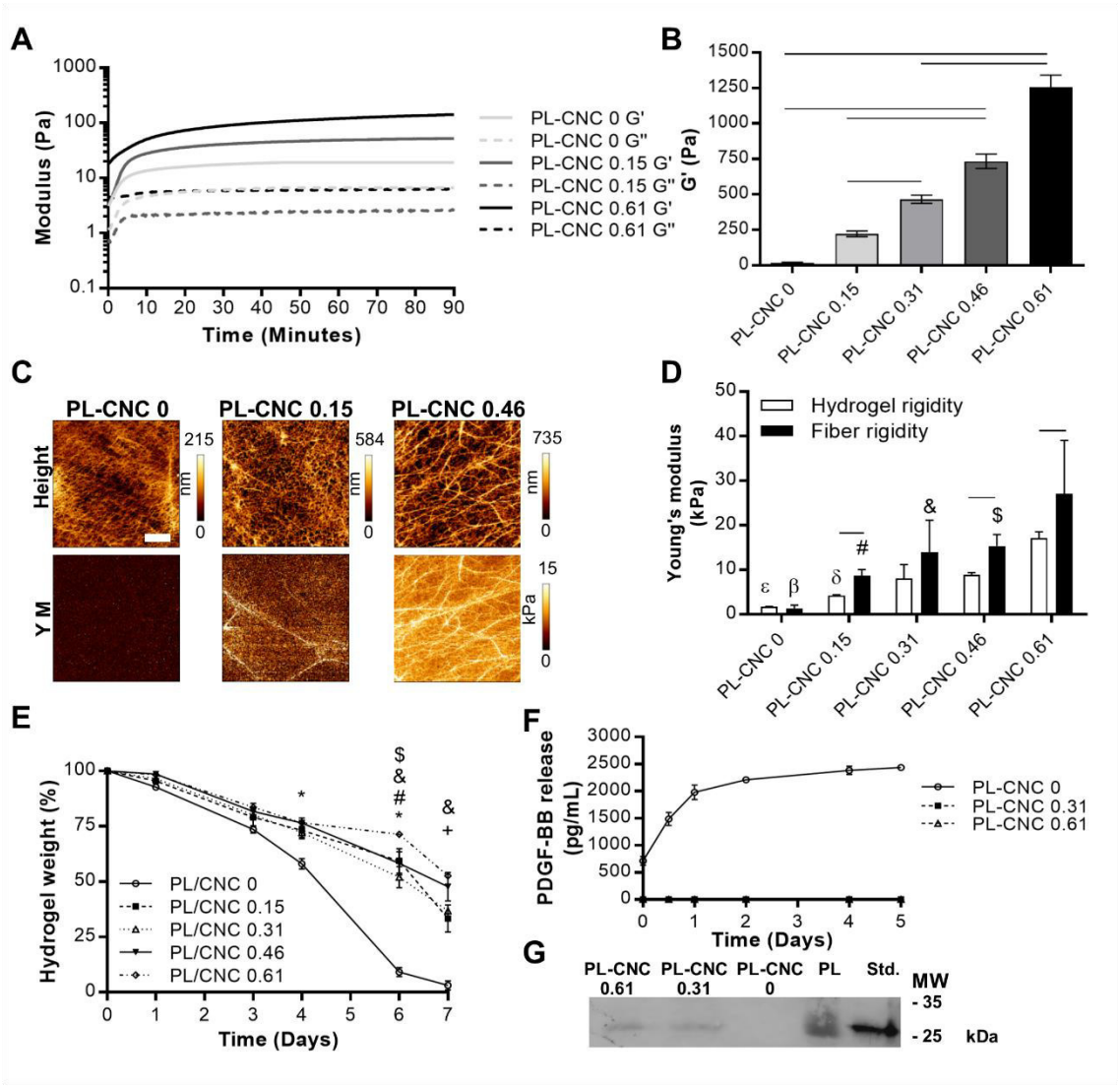

Figure III-2 Physical characterization of nanocomposite hydrogels. Storage modulus (G') versus polymerization and crosslinking time at 1% strain and frequency of 1 Hz (A). Storage modulus (G') of PL/CNC hydrogels averaged from the frequency-sweep measurements between 0.1 to 1 Hz at 0.5% strain (B). Representative images of AFM-generated height (top) and Young's modulus (YM) (bottom) for PL-CNC hydrogels conditions (C) and Average Young's modulus for hydrogels (all image) and fibrils in each PL-CNC formulation (D). Weight loss over 7 days immersed in PBS (E). Cumulative concentration release of PDGF-BB in cell culture medium (F). Western Blot of PDGF-BB within natural fibrillar hydrogels at day 5 in cell culture medium (G). Statistical differences: $P < 0.05$, ___ between selected conditions, * PL-CNC 0 vs PL-CNC (0.15-0.61); + PL-CNC 0.15 vs PL-CNC (0.46-0.61); # PL-CNC 0.15 vs PL-CNC 0.61; & PL-CNC 0.31 vs PL-CNC 0.61; $ PL-CNC 0.46 vs PL-CNC 0.61. Hydrogel rigidity: ε PL-CNC 0 vs PL-CNC 0.61; δ PL-CNC 0.15 vs PL-CNC 0.61; Fiber rigidity: β PL-CNC 0 vs PL-CNC 0.61; # PL-CNC 0.15 vs PL-CNC 0.61; & PL-CNC 0.31 vs PL-CNC 0.61; $ PL-CNC 0.46 vs PL-CNC 0.61. Scale bar: 2 µm (C).

higher interfiber space (porosity), and thus lower branch points, with higher bulk stiffness. Therefore, these results further support the hypothesis that CNC might indeed increase the crosslinking density among protofibrils within the fibrin fiber in a process that also promotes the effective stress transfer from the protein matrix to the stiff reinforcing nanofiller. All these effects synergistically contribute to increase

the fiber and hydrogel stiffness with high CNC content, demonstrating how the proposed strategy might be used to control the physical properties of PL hydrogels as biomaterials for TERM applications.

III-3.2. Fibrillar nanocomposite hydrogels modulated matrix degradation and the proteins release profile

Besides poor mechanical properties, the use of fibrin-based gels has been challenging due to their low *in vitro/in vivo* stability [13]. The use of fibrinolysis inhibitors such as aprotinin has been applied to mitigate this problem [31] [46]. However, it has been recently shown that aprotinin impaired vascular network formation in *in vitro* co-cultures of human umbilical vascular endothelial cells and hASCs encapsulated in fibrin gels [47], suggesting that its use might have negative implications in general tissue engineering strategies. Herein we did not use protease inhibitors, and therefore PL-CNC 0 hydrogels showed a markedly higher weight loss (95 ± 4%) in comparison with PL-CNC 0.61 (51 ± 7%) after 7 days of degradation in PBS (Figure III-2E) and the same trend was observed on total protein release (Supplementary Figure III-3). PL-CNC 0 was almost completely degraded over time, whereas PL-CNC 0.61 maintained 61% of the hydrogel protein at the end of the assay, demonstrating that CNC incorporation hinders the inherent proteolytic degradation of PL hydrogels and could therefore be an interesting alternative to the use of aprotinin.

Another important drawback associated with PL-based gels is the lack of control over dose and spatio-temporal delivery of specific platelet-derived biomolecules due to the low stability of the gel fibrillar matrix [9, 10]. In an *in vivo* scenario, fibrin(ogen) is known for its ability to bind GFs through its heparin-binding domain and uses this affinity-based mechanism to control the sequestering and subsequent release of signaling biomolecules [48]. For example, whereas FGF-2 has high binding affinity to fibrinogen and strong retention in the fibrin matrix, PDGF-BB, the major GF constituent of platelet releasate [49], has low binding affinity to fibrinogen and low retention in the fibrin matrix (> 80% released after one day from fibrin gels) [48]. Considering the low affinity of PDGF-BB to fibrin, we select it as a GF model to investigate the potential impact of CNC on the sequestering and release profile of signaling biomolecules from nanocomposite hydrogels. Strikingly, whereas PL-CNC 0 showed a burst release profile of PDGF-BB within the first day (Figure III-2F), a behavior also observed in other PL based gels [17], in the nanocomposite hydrogels its release was below the detection limit of the ELISA assay. To guarantee that PDGF-BB release from the nanocomposite hydrogels was not detected due to experimental inaccuracies,

we qualitatively evaluated by western blot the amount of PDGF-BB within the remaining hydrogels at the end of the assay (Figure III-2G). As expected, PDGF-BB was detectable in the nanocomposite formulations, indicating that this GF was sequestered within the hydrogel network, but not in PL-CNC 0. The electrostatic binding of PDGF-BB (isoelectric point at pH 9.39) on the negatively charged CNC surface certainly contributes to its significant retention within the nanocomposite hydrogels, although other binding mechanisms might justify these results. Upon contact with platelet-derived biomolecules, a "hard" corona composed by high affinity proteins will develop on CNC surface over time, which might be stabilized by imine bonding. In theory, the recruitment of specific biomolecules to the nanoparticle surface might be advantageously exploited to modulate the protein corona composition and consequently the biological identity of the nanocomposite hydrogel microenvironment [50]. This concept would find a parallelism with the events happening during wound healing, where signaling molecules are released from ECM through finely-orchestrated mechanisms regulated by its binding affinity to matrix components and on the action of proteases [27]. Sulfated GAGs in particular play important roles on the regulation of their spatio-temporal presentation within the wound microenvironment [51]. Considering that majority of CNC surface chemistry has high similarities with sulfated GAGs, it is plausible to hypothesize that it might favor the dynamic adsorption of biomolecules with high affinity to these polysaccharides [52], including, not only PDGF-BB, but several other platelet-derived GF that establish specific binding to sulfated GAGs [51]. However, in contrast to GAGs the soluble form of cellulose sulfate derivatives, which are relatively flexible and predominantly hydrophilic polymers, the surface chemistry of rigid CNC is not isotropic and contains hydrophilic but also exposed hydrophobic domains attributed to the (200)β/(220)α crystalline edge of the cellulosic crystals, conferring them an amphiphilic character [53]. The recent developments on the characterization of bio-nano interfaces [30, 50] suggests that such structural and chemical anisotropy will certainly have an important impact on the entity of the protein corona built on CNC surface in the complex PL environment. Therefore, the nature of the interactions establish between specific PL biomolecules of interest with the CNC surface should be systematically characterized in future studies.

It worth noting that the equilibrium established between the imine bond and its corresponding precursors in aqueous media, namely, carbonyls of CNC and amines of PL's proteins, has a dynamic nature. Imines can participate in multiple types of equilibrium-controlled reactions (hydrolysis, exchange or metathesis) influenced by several external factors (e.g. precursor's concentration, pH or temperature) [54, 55] which have been extensively explored in the development of controlled drug delivery systems [56-58]. Although the carbonyls of CNC will preferentially react with the higher concentrated proteins in the PL, e.g. albumin and fibrin(ogen) [10], it can also react with GFs, representing therefore an additional

level of control in the sequestration and release of these bioactive molecules from the nanocomposite hydrogel matrix. For example, it is known that the pH milieu in wounds can vary from acidic to basic depending on several factors, including the time course and wound-stage (acid in acute wounds and basic in chronic wounds) [59]. Therefore, it is likely that the shift of the imine reaction equilibrium toward the precursors or the products in acute or chronic wounds, respectively, will result in different GF release profiles from the nanocomposite hydrogel matrix.

III-3.3. Stem cells were able to sense and respond to fibrillar hydrogels stiffness

As mentioned above, CNC incorporation improved PL hydrogel mechanical properties and stability due to the inherent CNC stiffness and the increased crosslinking density of the fibrillar hydrogel network. Having fiber diameters close to collagen fibrils (100-200 nm), these biomaterials closely mimic the topography and hierarchical structure of native ECM, characteristics that are not present in the typical polymer hydrogel systems used in TERM applications [60]. The geometrical properties (e.g. porosity, fiber like-architecture) of PL-CNC nanocomposites are crucial not only to allow sufficient nutrient and waste product transport [61] and consequently enable cell survival, but also affect other important cell behaviors such as migration [62, 63]. Acknowledging that dynamic changes in ECM microenvironment (e.g. mechanical cues and remodeling) have been shown to regulate cell functions [44, 64], we analyzed the impact of hydrogel features on stem cell supportive properties using hASCs. These cells are harvested from adipose tissue in large numbers and have been studied as an excellent and widely available autologous multipotent cell source [65]. The facile crosslinking process allowed hASCs encapsulation within the hydrogel network, showing high viability immediately after extrusion that was maintained in the following 7 days of culture (Figure III-3A). Although a higher cell density was visible on PL-CNC 0, the decrease of normalized metabolic activity indicates that this cell number is due to the extensive retraction of fibrin network leading the high cellular concentration in the gel volume (Figure III-3B). Upon hASCs encapsulation, PL-CNC 0 had a manifold densification of the fibrin network, referred to as clot retraction, which led to a dramatic 75% reduction in hydrogel diameter (Figure III-3C and D). *In vivo*, it is assumed that clot retraction plays a role in approximating the edges of a tissue defect and in concentrating the clot in the injured area [66]. However, this high contractile effect is undesirable for hydrogels to be applied in space filling of wounded sites. With CNC incorporation, the hydrogels showed a lower clot retraction accompanied by a higher proliferative capacity. The produced fibrin fiber network recapitulating the

cellular-ECM interactions complexity and supporting cell adhesion and remodeling [14] is clearly favored by CNC reinforcement.

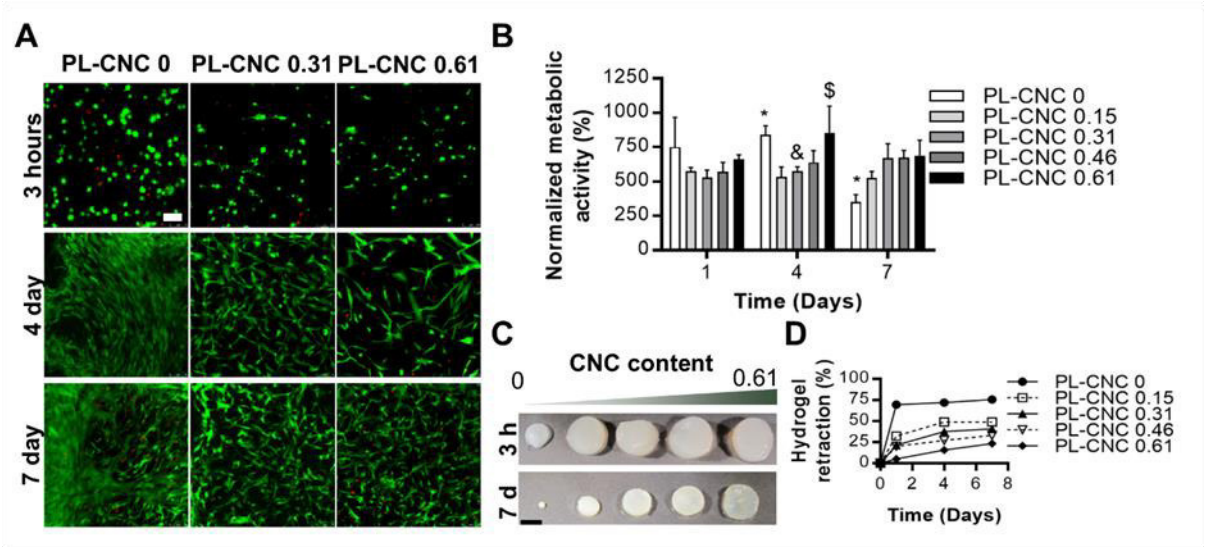

Figure III-3 In vitro evaluation of cell supportive properties and hydrogels retraction upon cell encapsulation. Live/Dead staining with Calcein AM/PI (green: live cell; red: dead cell) of hASCs encapsulated in PL/CNC hydrogels (A). Metabolic activity normalized by total DNA content (B). Photographs of PL-CNC hydrogels after 3 hours and 7 days in culture (C). Hydrogels diameter retraction in percentage at 1, 4 and 7 days – statistically differences in all formulations, except PL-CNC 0.31 vs PL-CNC 0.46 at time point 1 (D). Statistical differences: P < 0.05, * PL-CNC 0 vs PL-CNC (0.15-0.61); & PL-CNC 0.31 vs PL-CNC 0.61 and $ PL-CNC 0.61 vs PL-CNC 0.15. Scale bar: 75 µm (A) and 4 mm (C).

Material´s biophysical cues, namely topography and mechanical properties, are key parameters in the regulation of stem cell behavior [44, 63]. Regarding mechanical properties in particular, there is an increasing body of evidence supporting the concept that mesenchymal stem cells are extremely sensitive to tissue-level elasticity and that these physical cues are transduced into lineage specification [43, 67]. Therefore, considering the significantly different physicochemical properties of the developed nanocomposite hydrogels, we evaluated its impact on cell cytoskeleton organization, spreading and gene expression as a preliminary indication of stem cell preferential differentiation pathways.

In the soft PL gels, actin filaments were not well developed and visible, but these progressively became longer and organized on the stiffer nanocomposite hydrogels (Figure III-4-A). 24 hours upon encapsulation, the majority of hASCs in PL-CNC 0 showed a round morphology that was even more evident at day 3 (Figure III-4C), mainly due to the contraction of the fibrin network in response to the pulling forces exerted by cells during culture (Figure III-4A). Conversely, PL-CNC 0.31 and 0.46 formulations showed high cell spreading area and cell axial ratio (Figure III-4B), demonstrating that the nanocomposite fibrillar network can counteract cell puling forces without undergoing extensive retraction. In PL-CNC 0.61 it was even possible to quantify these cellular parameters at a later time point (day 3)

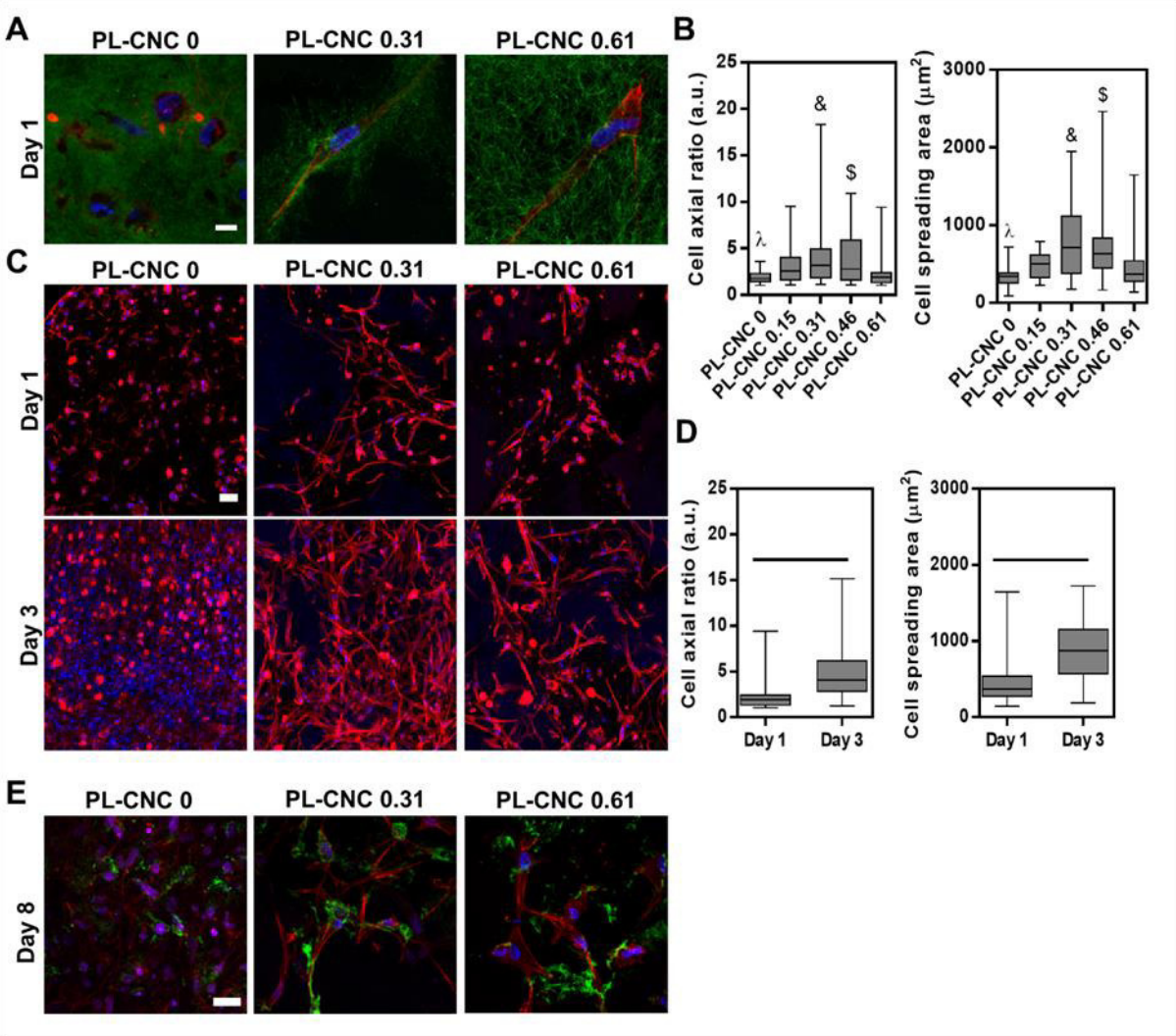

Figure III-4 In vitro evaluation of cellular differentiation in PL and PL-CNC hydrogels. Fluorescence microscopy images showing cytoskeleton organization in the fibrin matrix after 1 day in culture (A). Cell axial ratio and cell spreading area after 1 day of culture were quantified for all conditions (B). Fluorescence microscopy images showing cytoskeleton organization after 1 and 3 days in culture (C). Cell axial ratio and cell spreading area after 1 and 3 days of culture were quantified for PL-CNC 0.61 (D). Collagen Type III deposition after 8 days in culture. Staining fibrinogen (green) (A), collagen Type III (green) (E), actin (red) and nuclei (blue) (A, C and E). Statistical differences: $P < 0.05$, ___ between selected conditions; λ PL-CNC 0 vs PL -CNC (0.15-0.46); & PL-CNC 0.31 vs PL -CNC 0.61 and $ PL-CNC 0.46 vs PL -CNC 0.61. Scale bar: 10 μm (A) and 50 μm (C).

due to the minimal cellular overlap, showing that as cells continue to proliferate, they undergo high cytoskeleton elongation and present extended cell spreading area (Figure III-4D). This trend was confirmed by histological analysis for longer culture periods (14 days), demonstrating that whereas PL-CNC 0 show a highly compact cellularized structure due to the extensive hydrogel retraction, CNC-loaded hydrogels promote cell spreading and the formation of well-developed cellular networks (Supplementary Figure III-5). To evaluate the impact of these different cellular behaviors on ECM synthesis, we further analyzed the deposition of collagen type III by encapsulated hASCs, which is deposited during the initial

phases of wound healing to provide a provisional cell supportive matrix [2], being remodeled to other collagen types in later stages of wound repair. Interestingly, cell encapsulated in CNC-loaded hydrogels showed higher deposition of collagen type III and with a more fibrillar-like appearance than PL-CNC 0 hydrogels (Figure III-4E), suggesting that those formulations favor the progressive remodeling of the hydrogel 3D space with newly synthesized cell-origin ECM, a factor that might contribute to the increased hydrogel structural stability observed during cell culture. The marked differences observed in cell morphology also feedback the role of the hydrogel biophysical cues on the cells mechanotransduction process, since the stiffer fibrillar nanocomposite hydrogels promoted molecular mechanosensing mechanisms mediated by integrins which are transduced into actin polymerization and focal adhesion maturation [63]. Ultimately, the traction forces between hydrogel matrix and cells can alter gene expression, and therefore induce cell commitment toward different phenotypes [68]. In fact, gene expression analysis revealed that on one hand, hASCs laden on the softest PL CNC 0 hydrogels (2.2 kPa) showed an upregulation of transcription factors related to distinct lineages osteogenic [69], tenogenic [70], chondrogenic [71] and adipogenic [72]), and PDGF-BB, an anti-morphogenic marker (Figure III-5A). These results are in agreement with the increasing use of PL as a prevailing supplement for cell culture in replacement of animal serum, being capable of faster *in vitro* stem cell expansion while maintaining their stemness [73-75], therefore suggesting its potential to repress cell differentiation into specific lineages. The presence of multiple cytokines and chemokines with opposite biological signaling roles in PL formulations might contribute to explain these results and highlight one of main difficulties generally associated with the use of blood derivatives in regenerative medicine: the establishment of rational cell stimuli protocols and consequently, therapeutic strategies [10]. On the other hand, hASCs cultured on CNC-loaded hydrogels exhibited distinct genetic profiles, showing an upregulation osteogenic and chondrogenic related markers along with downregulation of lipoprotein lipase (LPL), an adipogenic marker, indicating potential cell commitment toward different lineages depending on CNC content [76, 77]. In the stiffer PL-CNC 0.61 hydrogels, the levels of Runt-related transcription factor 2 (RUNX2) increased over time (from 11 ± 1.1% at day 1 to 20 ± 3.6 % at day 7), while the expression of all the other studied transcription factors decreased. Furthermore, cells on this hydrogel formulation showed around 10-fold upregulation of ALP expression, confirmed by increased ALP activity (Figure III-5B), indicating potential osteogenic commitment. Differently, on moderately stiff PL-CNC 0.31 hydrogels, from day 1 to day 7, hASCs show an increased expression of two chondrogenic related markers namely, cartilage oligomeric matrix protein (COMP) and SRY-box 9 (SOX9). Remarkably, although the use of PL-based gels has attracted significant interest in the promotion of vascularization in regenerative strategies due to their

contents in angiogenic GFs that favor mesenchymal stem cells invasion and endothelial sprouting [17, 31], we observed that the expression of angiogenic related genes such as vascular endothelial GF (VEGF) declined more than one-fold at day 7 in PL-CNC 0 (Figure III-4A). In contrast, in the moderately stiff matrices PL-CNC 0.31, the expression of this gene increased to the levels of control group (PL-CNC 0 at day 1). These findings suggest that, as in native ECM [78], an adequate physical and chemical environment capable of sequestering and presenting angiogens to cell receptors might be needed to

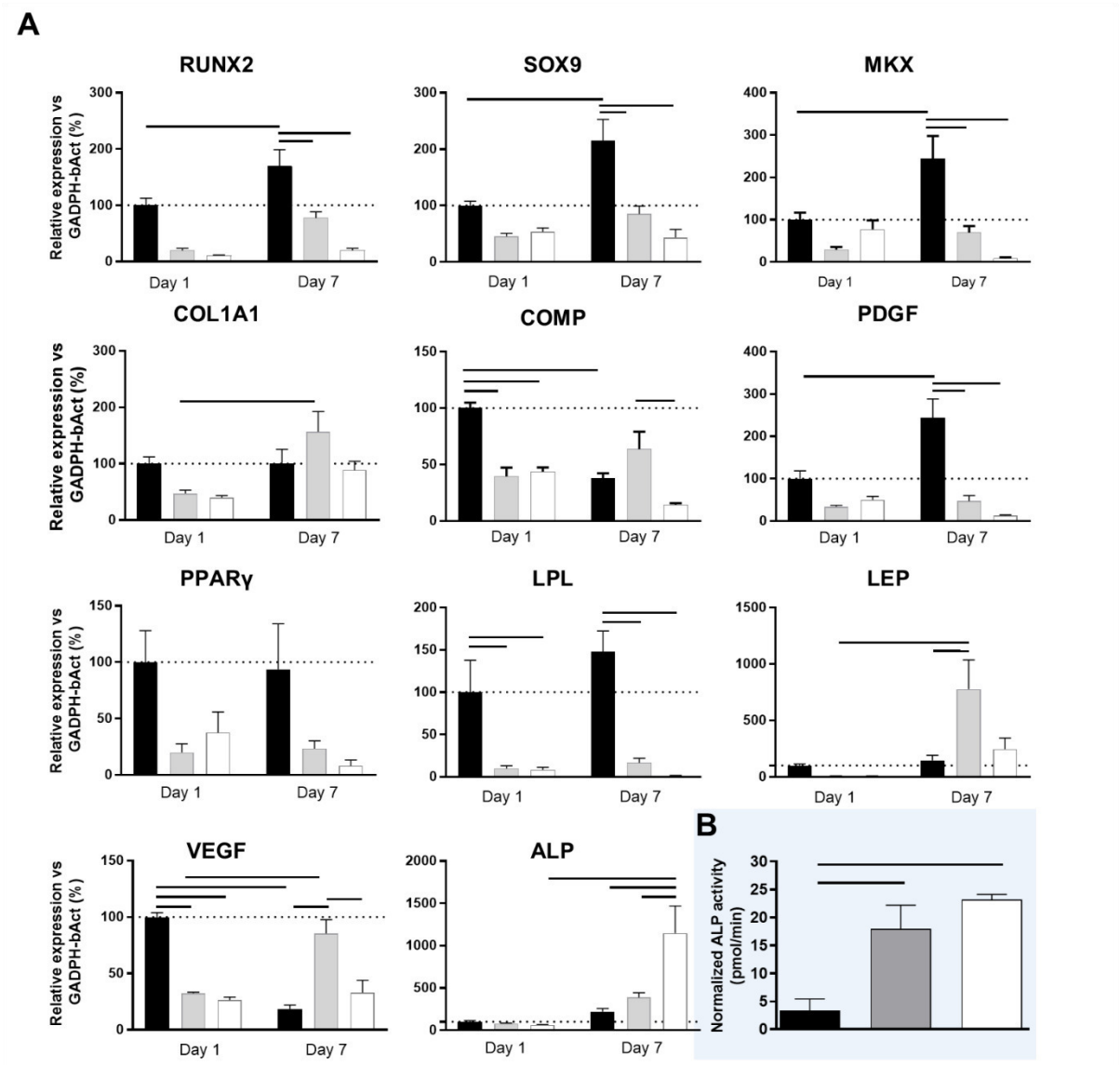

Figure III-5 hASCs were assessed for the expression of chondrogenic (SOX-9 and COMP), osteogenic (RUNX2, COLA1 and ALP), adipogenic (LPL and PPAR γ), tenogenic (MKX), anti-morphogenic (PDGF) and angiogenic markers (VEGF) (A). ALP activity was quantified after 9 days in culture (B). Abbreviations: Runt-related transcription factor 2 (RUNX2), SRY-box 9 (SOX9), Mohawk (MKX), collagen type I alpha 1 chain (COLA1), cartilage oligomeric matrix protein (COMP), platelet-derived growth factor-B (PDGF), peroxisome proliferator-activated receptor γ (PPAR γ), lipoprotein lipase (LPL), leptin (LEP), vascular endothelial growth factor (VEGFA) and alkaline phosphatase (ALP), and leptin (LEP). Statistical differences: $P < 0.05$, ___ between selected conditions.

sustain the angiogenic potential of PL over time. Therefore, the interaction between angiogens and nanocomposite hydrogel matrix and how these synergies can potentiate vascularization processes deserve further study.

In summary, we developed a method to create injectable fibrillar nanocomposite hydrogels based on PL combined with CNC as a platform that allowed the use of this blood derivative not only as a source of signaling biomolecules involved in wound healing, but also as an injectable cell carrier biomaterial with tunable biophysical and biochemical cues for cell delivery in TERM strategies. We have demonstrated that by increasing CNC loading in natural fibrillar PL hydrogels it is possible to increase fiber diameter, stiffness, interfibrillar porosity, hinder the typical fast clot degradation, and improve bioactive molecules sequestering, enabling therefore its use as effective ECM-mimetic biomaterials in which we can control the 3D cell microenvironment (Scheme III-2). The physical changes occurring in the fibrillar network stemming from CNC load and crosslinking led to hydrogels that do not compromise the outstanding cytocompatibility of PL gels, can resist extensive retraction upon 3D cell culture and have a marked impact on determining cell behavior. We have shown that cell cytoskeletal organization can be easily manipulated by controlling CNC loadings and these effects might be adjusted to direct the fate of encapsulated hASCs toward specific lineages.

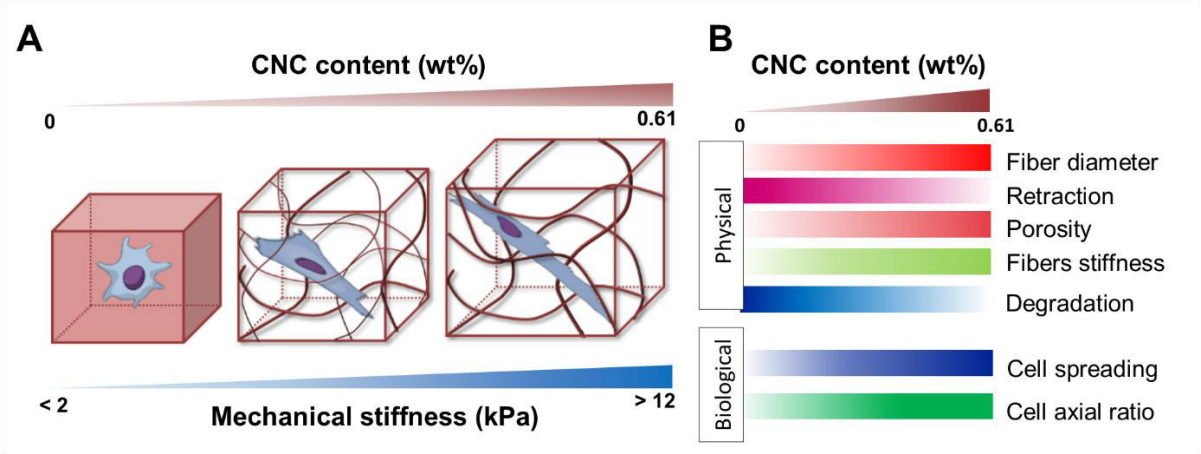

Scheme III-2 Schematic representation of the cytoskeletal organization of encapsulated hASCs in function of PL nanocomposite hydrogel composition and stiffness (A). Influence of each studied parameter in the hydrogel physical properties and cell behavior (B).

III-4. CONCLUSIONS

We have developed in this study injectable PL nanocomposite fibrillar hydrogels that are biochemically, mechanically and structurally tunable, enabling the modulation of multiple parameters of

the 3D cell microenvironment in ways that are poorly achieved with other traditional polymer-based strategies. It is anticipated that this natural-based hydrogel platform will find multiple applications as a bioactive cell carrier matrix capable of harnessing the regenerative potential of platelets content and promote regenerative wound healing outcomes in tissue engineering strategies.

III-5. SUPPLEMENTARY INFORMATION

III-5.1. Supplementary material and methods

III-5.1.1. Preparation of Platelet Lysate

Platelet concentrates were obtained from different platelet collections performed at Serviço de Imunohematologia do Centro Hospitalar de São João (CHSJ, Porto, Portugal), under a previously established cooperation protocol. All the platelet products were biologically qualified according to the Portuguese legislation. The platelet count was performed at the IPS using the COULTER® LH 750 Hematology Analyzer and the sample volume adjusted to 1 million platelet μL^{-1}. PL were prepared according to a previously established protocol [79]. Briefly, the collected platelet concentrate samples were subject to three repeated temperature cycles (frozen with liquid nitrogen at −196 °C and heated at 37 °C water bath), in order to promote platelets lysing and the release of their corresponding protein content. Aliquots of PL were stored at −80 °C. Prior to use, the lysate was centrifuged at 4000 G for 5 minutes and filtered through a 0.45 µm pore filter to remove the platelet membrane fragments.

III-5.1.2. Total Protein content quantification

Total protein content was quantified by Bicinchoninic Acid Assay (Thermo Fisher Scientific, USA). Briefly, a calibration curve in the range of 25-2000 $\mu g\ mL^{-1}$ and PL concentrates at different dilutions were measured at 562 nm on a plate reader according to Pierce BCA Protein Assay Kit instructions.

III-5.1.3. CNC production

CNC were extracted from microcrystalline cellulose (MCC) powder (Sigma-Aldrich, USA) following the typical sulfuric acid hydrolysis according to Bondeson with minor modifications [80]. In brief, 42 g of MCC was mixed with 189 mL of deionized water (DI). DI/MCC suspension was then put in an ice bath and stirred using a mechanical agitator (500 rpm) for 10 minutes. 188.3 mL of concentrated sulfuric acid (95–98% from Sigma-Aldrich, USA) was added dropwise up to a final concentration of 64 wt.%. The suspension was heated to 44 °C while stirring at 500 rpm for 120 min. The reaction was stopped by diluting the suspension with cold water (5x) and left to decant at 4 °C. The supernatant was discarded, and the remaining suspension was centrifuged for 10 minutes at 9000 rpm and 5 °C. The supernatant was successively replaced with DI water and the suspension subjected to centrifugation cycles until the supernatant became turbid. The resulting suspension was collected and extensively dialyzed using cellulose dialysis membrane MWCO: 12-14 kDa (Sigma-Aldrich, USA) against DI water until neutral pH. After dialysis the content was sonicated three times (VCX-130PB-220, Sonics) for 10 minutes using an ultrasound probe at 60% of amplitude output, under ice cooling to prevent overheating. The cloudy suspension was centrifuged one last time to remove big particulates and the final supernatant containing the CNC was stored at 4 °C until further use.

III-5.1.4. Oxidation of CNC

Aldehyde CNC (a-CNC) were produced by sodium periodate ($NaIO_4$) oxidation [24]. In a typical experiment, $NaIO_4$ (Sigma-Aldrich, USA) was added to CNC aqueous suspension (1.5 wt.%) in a 1:1 molar ratio ($NaIO_4$:CNC). The mixture was allowed to stir at room temperature (RT) for 12 hours preventing from light exposure. Unreacted periodate was quenched by the addition of excess of ethylene glycol (Sigma-Aldrich, USA). The mixture was transferred into a dialysis membrane (cellulose dialysis membrane MWCO: 12-14 kDa) and dialyzed against DI for 3 days with regular water replacement. The final working suspension of modified CNC was collected and stored at 4 °C. The desired concentration of the working suspension was adjusted by diluting or concentrating it against poly(ethylene glycol) (average MW 20,000 kDa, Sigma-Aldrich, USA) using benzoylated cellulose dialysis membranes (2000 Da NMWCO, Sigma-Aldrich, USA).

III-5.1.5. Analysis of chemical modification of CNC

Fourier transform infrared spectroscopy (FTIR) was used to evaluate the chemical modification of CNC in a Shimadzu spectrometer. Before FTIR analysis, freeze-dried CNC and a-CNC were oven-dried at 105 °C for 30 minutes preventing from air exposure to avoid water resorption and pelleted in potassium bromide (Sigma-Aldrich, USA). Spectral data were acquired between 4400 and 400 cm^{-1} from 128 averaged scans at a resolution of 4 cm^{-1}.

III-5.1.6. Morphological characterization of CNC

CNC morphology was analyzed by AFM. Drops of the diluted modified CNC suspension (0.0015 wt. %) were deposited on freshly cleaved mica discs (9.9 mm diam. 0.27 thick). The suspension was left to adsorb for 15 minutes and the excess liquid was removed. The disc was washed two times with ultrapure water (Milli-Q, 18.2 M Ω cm^{-1}) and allowed to dry overnight. The samples were imaged in tapping mode with a MultiMode AFM (Bruker, USA) and the particle size distribution was determined with Gwyddion software (n=50).

III-5.1.7. Quantification of CNC carbonyl content

The carbonyl group content of the oxidized a-CNC was determined by conductometric titration [24]. In a typical run, 3.6 mL of a-CNC aqueous suspension (1.39 wt.%, 0.050 g) and 0.025 g (0.62 mmol) of NaOH were dispersed in a final volume of 10 mL of ultra-pure water. 0.193 g of silver (I) oxide (Sigma-Aldrich, USA) were added to the solution, which was allowed to stir overnight and selectively oxidize the aldehyde groups to carboxylic acids. 5 mL of the oxidized reaction mixture were diluted with 80 mL of ultra-pure water and the pH was adjusted to c.a. 3.5 with hydrochloric acid (Thermo Fisher Scientific, USA). Finally, the solution was titrated using 0.01M sodium hydroxide (Thermo Fisher Scientific, USA). The total amount of carboxyl groups corresponding to the carbonyl content or degree of oxidation (DO) was calculated from Supplementary Equation III-1:

$$DO = \frac{162C(V_2 - V_1)}{w - 36C(V_2 - V_1)}$$

Supplementary Equation III-1 Quantification of the degree of oxidation. Where C is the NaOH concentration (mol. L^{-1}), V_1 and V_2 are the amount of NaOH as shown in conductimetric titration curves (Fig S1D), and w (g) is the weight of a-CNC.

III-5.1.8. Quantification of CNC sulfation degree

The CNC sulfate content was determined following the CNC pre-treatment steps and conductometric titration according to Beck, S. et [81] al with minor modifications. First, CNC suspension was fed from the top of the column that contains a bed of dowex marathon C hydrogen form strong acid cation (Sigma Aldrich, USA) to fully protonate CNC sulfate half-ester groups. Then, sulfate half-ester content was determined via conductometric titration (113 mg of CNC in 200 mL of 1 mM NaCl aqueous solution and 10 mM NaOH as titrant), and sulfate half-ester groups content and the sulfur content (%) [82] was calculated using Supplementary Equation III-2 and III-3, respectively:

$$mmol/kg = \frac{V_{NaOH}\, C_{NaOH}}{m_{CNC}}$$

Supplementary Equation III-2 Quantification of the sulfate half-ester content. Where VNaOH is the inset equivalence point determined from conductometric titration curve, CNaOH is the concentration of titration used and mcnc is the mass of the CNC suspension.

$$\%S = \frac{V_{NaOH}\, C_{NaOH}\, M_W(S)}{m_{susp}\, C_{susp}}\ x\ 100$$

Supplementary Equation III-3 Quantification of the sulfur content. Where m_{susp} and C_{susp} are the mass and concentration (mass %) of the CNC suspension and M_w (S) is the atomic mass of sulfur

III-5.1.9. Hydrogel Degradation

For quantification of total protein release, at different time points the supernatant was collected and replaced with fresh PBS. Total protein content was quantified by bicinchoninic acid assay (Thermo Fisher Scientific, USA). Briefly, a calibration curve in the range 25-2000 µg mL^{-1} and the protein released from PL-CNC hydrogels were measured at 562 nm on a plate reader according to Pierce BCA Protein Assay Kit instructions. The results are an average of three measurements obtained per formulation (n=4).

III-5.1.10. Hematoxylin and eosin (H&E) staining

After 14 days of culture, PL-CNC 0, 0.31 and 0.61 formulations were washed with PBS and then fixed in 10 vol.% formalin (Thermo Fisher Scientific, USA) for 30 min at RT. The samples were embedded in Histogel specimen processing gel (Thermo Fisher Scientific, USA), dehydrated through graded ethanol solutions and embedded in paraffin for further sectioning using a microtome (HM355S, Microm, Thermo Scientific). Sections of 5 μm thickness were prepared and stained with hematoxylin and eosin (H&E) for histological evaluation of cell distribution and hydrogel retraction. Sections were observed under a transmitted light Microscope (Zeiss, Germany).

Supplementary Table III-1 List of genes under evaluation, forward (F) and reverse (R) primers used in the gene expression analysis of encapsulated hASCs in PL-CNC hydrogels over 1 and 7 days in culture.

Gene	*Sequence (5'-3')*
β-Actin	*F:CTGGAACGGTGAAGGTGACA*
	R:AAGGGACTTCCTGTAACAA
GAPDH	*F:GGGAGCCAAAAGGGTCATCA*
	R:GCATGGACTGTGGTCATGAGT
SOX9	*F:TTCATGAAGATGACCGACGC*
	R:GTCCAGTCGTAGCCCTTGAG
RUNX2	*F:TTCCAGACCAGCAGCACTC*
	R:CAGCGTCAACACCATCATTC
COL1A1	*F:CCCCAGCCACAAAGAGTCTAC*
	R:TTGGTGGGATGTCTTCGTCT
MKX	*F: TCGCACAGACACTCTGGAAAA*
	R: TGTTAAGGCCATAGCTGCGT
ALP	*F:GAAGGAAAAGCCAAGCAGGC*
	R:GGGGGCCAGACCAAAGATAG
PDGFB	*F:CCCCACACTCCACTCTGATT*
	R:GCCCTGGCCTCTAGTCTTCT
VEGFA	*F:CCATCCAATCGAGACCCTGG*
	R:TCCGCATAATCTGCATGGTG
LEP	*F:CTCAGGGATCTTGCATTCCC*

	R:CCATGCATTTGGCTGTTCAG
LPL	*F: ACTTGGAGAGGGACGAAGAA*
	R: ATGATGCAGGCCAATGGTAG
COMP	*F: AGGATGGAGACGGACATCAG*
	R: TCTGCATCAAAGTCGTCCTG
PPARγ	*F: TGGGTGAAACTCTGGGAGAT*
	R: GCGATCTCTGTGTCAACCAT

Abbreviations: Glyceraldehyde-3-phosphate dehydrogenase (GAPDH), SRY-box 9 (SOX9), runt-related transcription factor 2 (RUNX2), collagen type I alpha 1 chain (COLA1), Mohawk (MKX), alkaline phosphatase (ALP), platelet-derived growth factor-B (PDGF-B), vascular endothelial growth factor (VEGFA), leptin (LEP), lipoprotein lipase (LPL), cartilage oligomeric matrix protein (COMP) and peroxisome proliferator-activated receptor γ (PPARγ).

III-5.2. Supplementary results and discussion

III-5.2.1. Morphological and chemical characterization of modified CNC

CNC were extracted from commercial MCC by the common sulfuric acid hydrolysis procedure [80]. In this reaction, sulfuric acid reacts with the surface hydroxyl groups via an esterification process allowing the grafting of anionic sulfate ester groups that are the basis of their high stability in aqueous solutions. Then, vicinal hydroxyl groups on CNC's surface were converted to carbonyls by periodate oxidation for 12 hours. CNC morphology and dimensions were evaluated by AFM (Supplementary Figure III-1A and B). They exhibit a typical rod-like shape morphology with averaged height of 3.5 ± 1.3 nm and length of 168 ± 60 nm, similar to previous works [24,80]. The effective aldehyde functionalization of CNC was confirmed by FTIR (Supplementary Figure III-1C), demonstrated by the characteristic C=O stretching vibration band at 1740 cm^{-1} from the aldehyde groups visible on modified CNC and not in initial CNC formulation. Conductometric titration was performed to quantify the corresponding degree of oxidation (Supplementary Figure III-1D). It was estimated that 9.1 ± 0.95 carbonyl groups per 100 anhydroglucose units have been oxidatively introduced. The degree of chemical modification achieved guarantee sufficient reactivity while preserving the integrity of crystalline structure of CNC, since higher degrees of oxidation showed to affect its' original crystalline properties [83]. Conductometric titration was also used to determine the charged sulfate half-ester groups at the CNC surface (Supplementary Figure III-1E). The estimated content of sulfate groups in CNC is 296.78 ± 10.62 $mmol.kg^{-1}$ (0.95 ± 0.03 % S). These results

are in agreement with those reported for CNC isolated from different cellulose sources by sulfuric acid hydrolysis that typically contains 80-350 mmol.kg^{-1} of anionic sulfate half-esters introduced at some of the surface hydroxyl groups [84].

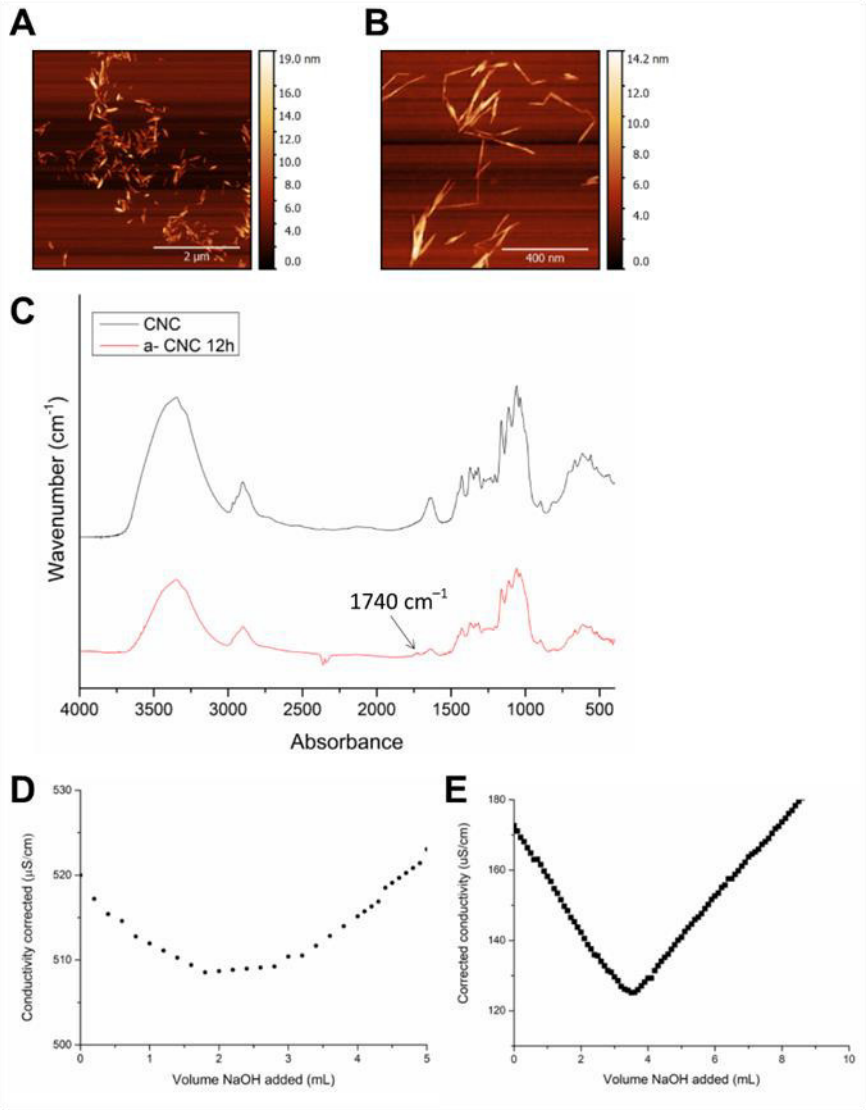

Supplementary Figure III-1 Morphological and chemical characterization of CNC and modified CNC. AFM images of modified CNC at 5x5 µm (A) and 0.5x0.5 µm (B). FTIR analysis of CNC and modified CNC (C). Conductometric titration curve of modified CNC to calculate the oxidation (D) and sulfation degree (E).

III-5.2.2. Physical characterization of hydrogels

The impact of clotting factors in fibrin network formation was performed using different concentrations of thrombin (low, L - 1 U.mL^{-1} and high, H - 2 U.mL^{-1}) and calcium (L – 2.5 mM and H - 5

mM), (HH, HL and HH formulations – thrombin and calcium), Supplementary Figure III-2A. According to the rheological analysis, LH formulation led to faster polymerization and superior storage modulus (G') in comparison with HH and HL formulations. These results are consistent with previous studies reporting that softer clots are obtained at higher thrombin and lower calcium levels [45]. The incorporation of CNC (at 0.61 wt.% concentration) did not hamper PL matrix polymerization and resulted in an increase of G' in all formulations (HH, HL and LH). Based on these results, we developed PL-CNC hydrogels using 1 $U.mL^{-1}$ of thrombin, 5 mM of $CaCl_2$ and variable CNC concentration (0 – 0.61 wt.%).

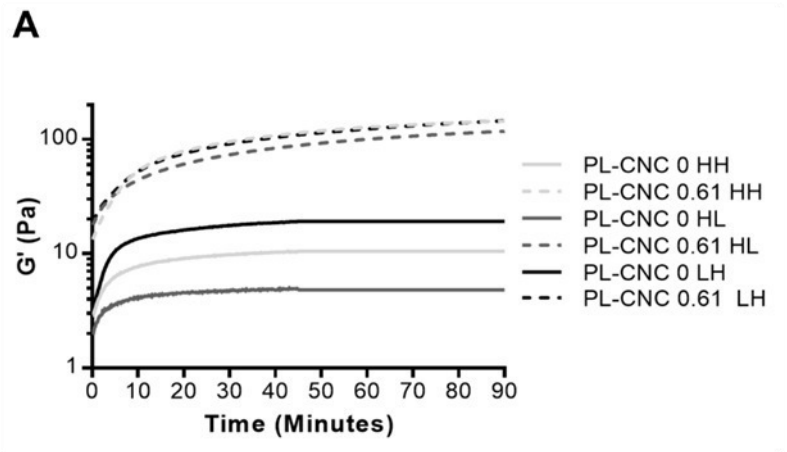

Supplementary Figure III-2 Characterization of hydrogel polymerization kinetics. Storage modulus (G') versus polymerization and crosslinking time at 1% strain and frequency of 1 Hz for fibrillar hydrogels with different concentrations of thrombin and calcium (HH, HL and HH formulations), and without (PL-CNC 0) or with (PL-CNC 0.61) CNC incorporation (A).

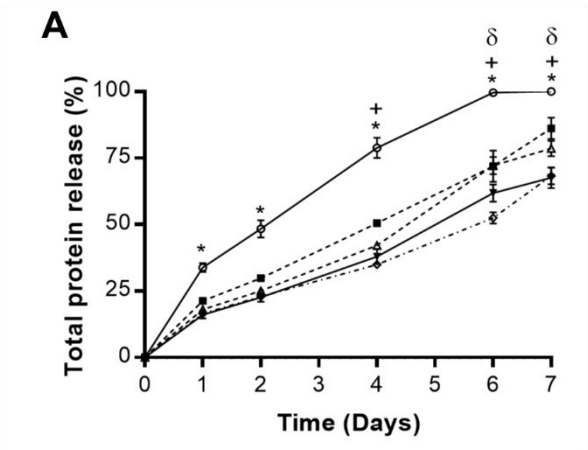

Supplementary Figure III-3 Characterization of hydrogel degradation. Percent of total protein release from PL-CNC hydrogels over 7 days immersed in PBS (A). Statistical differences: $P < 0.05$, * PL-CNC 0 vs PL-CNC (0.15-0.65); + PL-CNC 0.15 vs PL-CNC (0.46-0.61) and δ PL-CNC 0.31 vs PL-CNC (0.46-0.61).

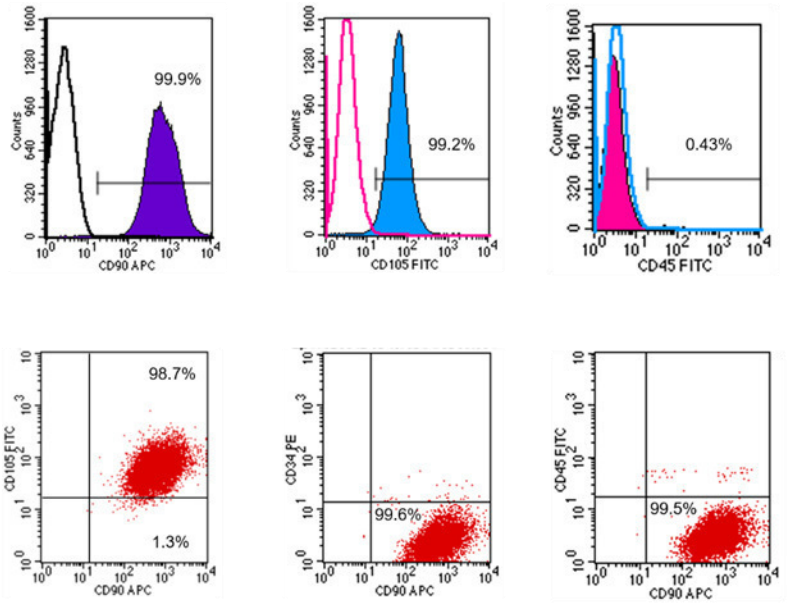

	%
CD90+	99.9%
CD105+	99.2%
CD45-	0.43%
CD90+/CD105+	98.7%
CD45-/CD90+	99.5%

Supplementary Figure III-4 Flow cytometry analysis of stemness markers, CD45 (≤2%), CD90 (≥95%) and CD105 (≥95%).

III-5.2.3. Hematoxylin and eosin (H&E) staining

Eosin stains extracellular and intracellular proteins while hematoxylin stains cell nuclei and some carbohydrates. Eosin is more intense in PL-CNC 0 hydrogels than in CNC-loaded hydrogels, indicating the shrinkage of these hydrogels (Supplementary Figure III-5B). Furthermore, cells are tightly packed in PL-CNC 0 while cells on hydrogels with CNC are spread and form well-developed cellular networks.

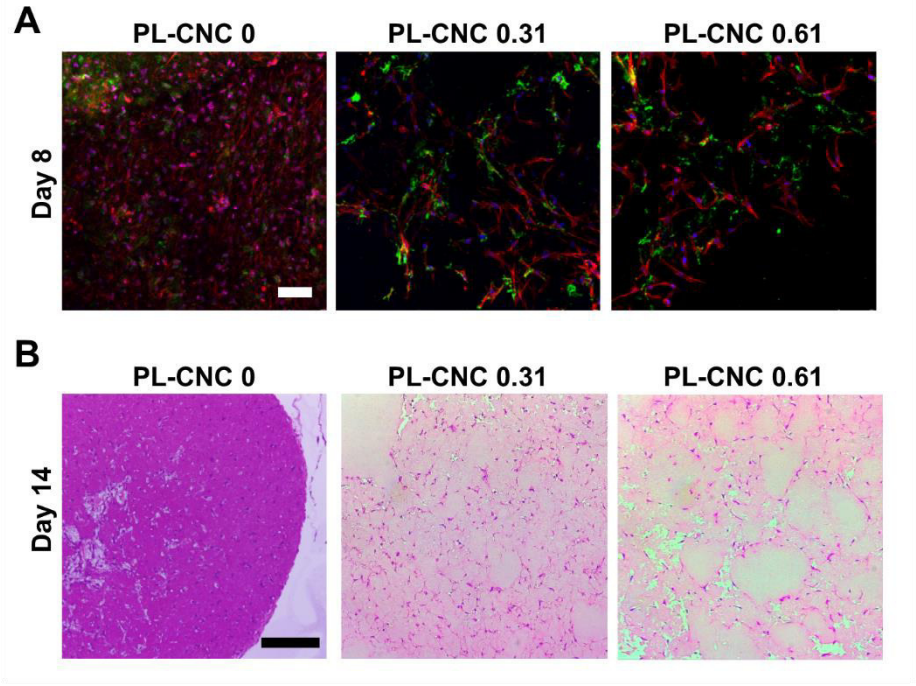

Supplementary Figure III-5 *In vitro* evaluation of matrix production, cell morphology and hydrogels retraction upon cell encapsulation. Fluorescence microscopy images showing cytoskeleton organization and matrix production after 8 days in culture (A). H&E staining after 14 days in culture showing cellular distribution and (B). Staining collagen III (green), actin (red) and nuclei (blue) (A). Cell nuclei and some carbohydrates (purple) and extracellular and intracellular proteins (pink) (B). Scale bar: 75 µm (A) and 200 µm (C).

III-6. REFERENCES

[1] S.A. Eming, P. Martin, M. Tomic-Canic, Wound repair and regeneration: mechanisms, signaling, and translation, Sci. Transl. Med., 6 (2014) 265.

[2] G.C. Gurtner, S. Werner, Y. Barrandon, et al., Wound repair and regeneration, Nature, 453 (2008) 314.

[3] S. Padilla, M. Sánchez, G. Orive, et al., Human-Based Biological and Biomimetic Autologous Therapies for Musculoskeletal Tissue Regeneration, Trends Biotechnol., 35 (2017) 192.

[4] D.M. Dohan Ehrenfest, L. Rasmusson, T. Albrektsson, Classification of platelet concentrates: from pure platelet-rich plasma (P-PRP) to leucocyte- and platelet-rich fibrin (L-PRF), Trends Biotechnol., 27 (2009) 158.

[5] T. Burnouf, H.A. Goubran, T.-M. Chen, et al., Blood-derived biomaterials and platelet growth factors in regenerative medicine, Blood Rev., 27 (2013) 77.

[6] Y. Qian, Q. Han, W. Chen, et al., Platelet-Rich Plasma Derived Growth Factors Contribute to Stem Cell Differentiation in Musculoskeletal Regeneration, Front. Chem., 5 (2017) 1.

[7] R. Crespo-Diaz, A. Behfar, G.W. Butler, et al., Platelet Lysate Consisting of a Natural Repair Proteome Supports Human Mesenchymal Stem Cell Proliferation and Chromosomal Stability, Cell Transplant., 20 (2011) 797.

[8] N. Fekete, M. Gadelorge, D. Fürst, et al., Platelet lysate from whole blood-derived pooled platelet concentrates and apheresis-derived platelet concentrates for the isolation and expansion of human bone marrow mesenchymal stromal cells: production process, content and identification of active components, Cytotherapy, 14 (2012) 540.

[9] P.S. Babo, R.L. Reis, M.E. Gomes, Periodontal tissue engineering: current strategies and the role of platelet rich hemoderivatives, J. Mater. Chem. B, 5 (2017) 3617.

[10] B.B. Mendes, M. Gomez-Florit, P.S. Babo, et al., Blood derivatives awaken in regenerative medicine strategies to modulate wound healing, Adv. Drug Del. Rev., (2017).

[11] D.E. Roberts, A. McNicol, R. Bose, Mechanism of Collagen Activation in Human Platelets, J. Biol. Chem., 279 (2004) 19421.

[12] J.M. Pachence, Collagen-based devices for soft tissue repair, J. Biomed. Mater. Res. A, 33 (1996) 35.

[13] A.C. Brown, T.H. Barker, Fibrin-based biomaterials: Modulation of macroscopic properties through rational design at the molecular level, Acta Biomater., 10 (2014) 1502.

[14] A.M. Rosales, K.S. Anseth, The design of reversible hydrogels to capture extracellular matrix dynamics, Nature Rev. Mater., 1 (2016) 1.

[15] H.-L. Wang, G. Avila, Platelet Rich Plasma: Myth or Reality?, Eur. J. Dent., 1 (2007) 192.

[16] M.P. Hall, J.P. Ward, D.A. Cardone, Platelet rich placebo? Evidence for platelet rich plasma in the treatment of tendinopathy and augmentation of tendon repair, Bull. Hosp. Joint Dis., 71 (2013) 54.

[17] T.M. Fortunato, C. Beltrami, C. Emanueli, et al., Platelet lysate gel and endothelial progenitors stimulate microvascular network formation in vitro: tissue engineering implications, Sci. Rep., 6 (2016) 1.

[18] M. Sadeghi-Ataabadi, Z. Mostafavi-pour, Z. Vojdani, et al., Fabrication and characterization of platelet-rich plasma scaffolds for tissue engineering applications, Mater. Sci. Eng., C, 71 (2017) 372.

[19] S.T. Robinson, L.P. Brewster, Platelet Lysate to Promote Angiogenic Cell Therapies, in: D. Simionescu, A. Simionescu (Eds.) Physiologic and Pathologic Angiogenesis - Signaling Mechanisms and Targeted Therapy, InTech, Rijeka, 2017, pp. 365.

[20] A. Motealleh, N.S. Kehr, Nanocomposite Hydrogels and Their Applications in Tissue Engineering, Adv. Healthc. Mater., 6 (2017) 1.

[21] P. Schexnailder, G. Schmidt, Nanocomposite polymer hydrogels, Colloid. Polym. Sci., 287 (2009) 1.

[22] M. Adnan, A.A. Hani, M.A. Hussain, et al., Hydrogels 2.0: improved properties with nanomaterial composites for biomedical applications, Biomed. Mater., 11 (2016) 1.

[23] R.M.A. Domingues, M.E. Gomes, R.L. Reis, The Potential of Cellulose Nanocrystals in Tissue Engineering Strategies, Biomacromolecules, 15 (2014) 2327.

[24] R.M.A. Domingues, M. Silva, P. Gershovich, et al., Development of Injectable Hyaluronic Acid/Cellulose Nanocrystals Bionanocomposite Hydrogels for Tissue Engineering Applications, Bioconjugate Chem., 26 (2015) 1571.

[25] K.J. De France, T. Hoare, E.D. Cranston, Review of Hydrogels and Aerogels Containing Nanocellulose, Chem. Mater., 29 (2017) 4609.

[26] A.C. Mitchell, P.S. Briquez, J.A. Hubbell, et al., Engineering growth factors for regenerative medicine applications, Acta Biomater., 30 (2016) 1.

[27] P.S. Briquez, J.A. Hubbell, M.M. Martino, Extracellular Matrix-Inspired Growth Factor Delivery Systems for Skin Wound Healing, Adv. Wound Care, 4 (2015) 479.

[28] Z. Kai, P. Dieter, B. Erica, et al., Synthesis and Bioactivity of Cellulose Derivatives, Macromol. Symp., 280 (2009) 28.

[29] D. Peschel, K. Zhang, N. Aggarwal, et al., Synthesis of novel celluloses derivatives and investigation of their mitogenic activity in the presence and absence of FGF2, Acta Biomater., 6 (2010) 2116.

[30] D. Peschel, K. Zhang, S. Fischer, et al., Modulation of osteogenic activity of BMP-2 by cellulose and chitosan derivatives, Acta Biomater., 8 (2012) 183.

[31] S.T. Robinson, A.M. Douglas, T. Chadid, et al., A novel platelet lysate hydrogel for endothelial cell and mesenchymal stem cell-directed neovascularization, Acta Biomater., 36 (2016) 86.

[32] P.P. Carvalho, X. Wu, G. Yu, et al., The effect of storage time on adipose-derived stem cell recovery from human lipoaspirates, Cells Tissues Organs, 194 (2011) 494.

[33] J.M. Gimble, F. Guilak, Differentiation potential of adipose derived adult stem (ADAS) cells, Curr. Top. Dev. Biol., 58 (2003) 137.

[34] J. Gimble, F. Guilak, Adipose-derived adult stem cells: isolation, characterization, and differentiation potential, Cytotherapy, 5 (2003) 362.

[35] M. Dominici, K. Le Blanc, I. Mueller, et al., Minimal criteria for defining multipotent mesenchymal stromal cells. The International Society for Cellular Therapy position statement, Cytotherapy, 8 (2006) 315.

[36] M.W. Pfaffl, A new mathematical model for relative quantification in real-time RT–PCR, Nucleic Acids Res., 29 (2001) e45.

[37] M.W. Pfaffl, A. Tichopad, C. Prgomet, et al., Determination of stable housekeeping genes, differentially regulated target genes and sample integrity: BestKeeper–Excel-based tool using pair-wise correlations, Biotechnol. Lett, 26 (2004) 509.

[38] L. Huang, J.P.-L. Hsiao, C. Powierza, et al., Does Topology Drive Fiber Polymerization?, Biochemistry (Mosc.), 53 (2014) 7824.

[39] W. Li, J. Sigley, M. Pieters, et al., Fibrin Fiber Stiffness Is Strongly Affected by Fiber Diameter, but Not by Fibrinogen Glycation, Biophys. J., 110 (2016) 1400.

[40] M. De Spirito, G. Arcovito, M. Papi, et al., Small- and wide-angle elastic light scattering study of fibrin structure, J. Appl. Crystallogr., 36 (2003) 636.

[41] N.A. Kurniawan, J. Grimbergen, J. Koopman, et al., Factor XIII stiffens fibrin clots by causing fiber compaction, Thromb. Haemost., 12 (2014) 1687.

[42] C. Duval, P. Allan, S.D. Connell, et al., Roles of fibrin alpha- and gamma-chain specific cross-linking by FXIIIa in fibrin structure and function, Thromb. Haemost., 111 (2014) 842.

[43] A.J. Engler, S. Sen, H.L. Sweeney, et al., Matrix Elasticity Directs Stem Cell Lineage Specification, Cell, 126 (2006) 677.

[44] K.H. Vining, D.J. Mooney, Mechanical forces direct stem cell behaviour in development and regeneration, Nat. Rev. Mol. Cell Biol., 18 (2017) 728.

[45] E.A. Ryan, L.F. Mockros, J.W. Weisel, et al., Structural origins of fibrin clot rheology, Biophys. J., 77 (1999) 2813.

[46] P.S. Briquez, K.M. Lorentz, H.M. Larsson, et al., Human Kunitz-type protease inhibitor engineered for enhanced matrix retention extends longevity of fibrin biomaterials, Biomaterials, 135 (2017) 1.

[47] S. Muhleder, K. Pill, M. Schaupper, et al., The role of fibrinolysis inhibition in engineered vascular networks derived from endothelial cells and adipose-derived stem cells, Stem cell research & therapy, 9 (2018) 1.

[48] M.M. Martino, P.S. Briquez, A. Ranga, et al., Heparin-binding domain of fibrin(ogen) binds growth factors and promotes tissue repair when incorporated within a synthetic matrix, Proc. Natl. Acad. Sci. U. S. A., 110 (2013) 4563.

[49] P.R. Amable, R.B. Carias, M.V. Teixeira, et al., Platelet-rich plasma preparation for regenerative medicine: optimization and quantification of cytokines and growth factors, Stem cell Res. Ther., 4 (2013) 1.

[50] M.P. Monopoli, C. Aberg, A. Salvati, et al., Biomolecular coronas provide the biological identity of nanosized materials, Nat. Nanotechnol., 7 (2012) 779.

[51] I. Capila, R.J. Linhardt, Heparin-protein interactions, Angew. Chem. Int. Ed. Engl., 41 (2002) 391.

[52] P.C. Ke, S. Lin, W.J. Parak, et al., A Decade of the Protein Corona, ACS Nano, 11 (2017) 11773.

[53] I. Kalashnikova, H. Bizot, B. Cathala, et al., Modulation of cellulose nanocrystals amphiphilic properties to stabilize oil/water interface, Biomacromolecules, 13 (2012) 267.

[54] R.W. Layer, The Chemistry of Imines, Chem. Rev., 63 (1963) 489.

[55] M.E. Belowich, J.F. Stoddart, Dynamic imine chemistry, Chem. Soc. Rev., 41 (2012) 2003.

[56] Y. Tao, S. Liu, Y. Zhang, et al., A pH-responsive polymer based on dynamic imine bonds as a drug delivery material with pseudo target release behavior, Polym. Chem., 9 (2018) 878.

[57] A. Seoane, R.J. Brea, A. Fuertes, et al., Biomimetic Generation and Remodeling of Phospholipid Membranes by Dynamic Imine Chemistry, J. Am. Chem. Soc., 140 (2018) 8388.

[58] G. Zhao, L. Long, L. Zhang, et al., Smart pH-sensitive nanoassemblies with cleavable PEGylation for tumor targeted drug delivery, Sci. Rep., 7 (2017) 3383.

[59] L.A. Schneider, A. Korber, S. Grabbe, et al., Influence of pH on wound-healing: a new perspective for wound-therapy?, Arch. Dermatol. Res., 298 (2007) 413.

[60] T. Ushiki, Collagen fibers, reticular fibers and elastic fibers. A comprehensive understanding from a morphological viewpoint, Arch. Histol. Cytol., 65 (2002) 109.

[61] Q.L. Loh, C. Choong, Three-dimensional scaffolds for tissue engineering applications: role of porosity and pore size, Tissue Eng. Part B Rev., 19 (2013) 485.

[62] J. Demol, D. Lambrechts, L. Geris, et al., Towards a quantitative understanding of oxygen tension and cell density evolution in fibrin hydrogels, Biomaterials, 32 (2011) 107.

[63] Y. Li, Y. Xiao, C. Liu, The Horizon of Materiobiology: A Perspective on Material-Guided Cell Behaviors and Tissue Engineering, Chem. Rev., 117 (2017) 4376.

[64] W.L. Murphy, T.C. McDevitt, A.J. Engler, Materials as stem cell regulators, Nat. Mater., 13 (2014) 547.

[65] T. Rada, R.L. Reis, M.E. Gomes, Adipose tissue-derived stem cells and their application in bone and cartilage tissue engineering, Tissue Eng. Part B Rev., 15 (2009) 113.

[66] M.E. Carr, Jr., S.L. Carr, Fibrin structure and concentration alter clot elastic modulus but do not alter platelet mediated force development, Blood Coagul. Fibrinolysis, 6 (1995) 79.

[67] A.W. Holle, J.L. Young, K.J. Van Vliet, et al., Cell-Extracellular Matrix Mechanobiology: Forceful Tools and Emerging Needs for Basic and Translational Research, Nano Lett., 18 (2018) 1.

[68] Enateri V. Alakpa, V. Jayawarna, A. Lampel, et al., Tunable Supramolecular Hydrogels for Selection of Lineage-Guiding Metabolites in Stem Cell Cultures, Chem, 1 (2016) 298.

[69] T. Komori, Regulation of bone development and maintenance by Runx2, Front. Biosci., 13 (2008) 898.

[70] L. Gaut, D. Duprez, Tendon development and diseases, Wiley Interdiscip. Rev. Dev. Biol., 5 (2016) 5.

[71] C. Healy, D. Uwanogho, P.T. Sharpe, Regulation and role of Sox9 in cartilage formation, Dev. Dyn., 215 (1999) 69.

[72] E.D. Rosen, C.-H. Hsu, X. Wang, et al., C/EBPα induces adipogenesis through PPARγ: a unified pathway, Genes Dev., 16 (2002) 22.

[73] E. Fernandez-Rebollo, B. Mentrup, R. Ebert, et al., Human Platelet Lysate versus Fetal Calf Serum: These Supplements Do Not Select for Different Mesenchymal Stromal Cells, Sci. Rep., 7 (2017) 5132.

[74] T. Burnouf, D. Strunk, M.B.C. Koh, et al., Human platelet lysate: Replacing fetal bovine serum as a gold standard for human cell propagation?, Biomaterials, 76 (2016) 371.

[75] S.M. Jonsdottir-Buch, R. Lieder, O.E. Sigurjonsson, Platelet Lysates Produced from Expired Platelet Concentrates Support Growth and Osteogenic Differentiation of Mesenchymal Stem Cells, PLoS ONE, 8 (2013) e68984.

[76] J. Upadhyay, O.M. Farr, C.S. Mantzoros, The role of leptin in regulating bone metabolism, Metabolism, 64 (2015) 105.

[77] C. Granéli, A. Thorfve, U. Ruetschi, et al., Novel markers of osteogenic and adipogenic differentiation of human bone marrow stromal cells identified using a quantitative proteomics approach, Stem Cell Res., 12 (2014) 153.

[78] V. Vogel, Unraveling the Mechanobiology of Extracellular Matrix, Annu. Rev. Physiol., 80 (2018) 353.

[79] V. E. Santo, M. E. Gomes, J. F. Mano, et al., Chitosan–chondroitin sulphate nanoparticles for controlled delivery of platelet lysates in bone regenerative medicine, J. Tissue Eng. Regen. Med., 6 (2012) 47.

[80] D. Bondeson, A. Mathew, K. Oksman, Optimization of the isolation of nanocrystals from microcrystalline cellulose by acid hydrolysis, Cellulose, 13 (2006) 171.

[81] S. Beck, M. Méthot and J. Bouchard, General procedure for determining cellulose nanocrystal sulfate half-ester content by conductometric titration, Cellulose, 22 (2015) 101.

[82] T. Abitbol, E. Kloser and D. G. Gray, Estimation of the surface sulfur content of cellulose nanocrystals prepared by sulfuric acid hydrolysis, Cellulose, 20 (2013) 785.

[83] E. E. Brown, D. Hu, N. Abu Lail, et al, Potential of nanocrystalline cellulose–fibrin nanocomposites for artificial vascular graft applications, Biomacromolecules, 14 (2013) 1063.

[84] E. J. Foster, R. J. Moon, U. P. Agarwal, et al, Current characterization methods for cellulose nanomaterials, Chemical Society Rev., 47 (2018) 2609.

Chapter IV

Intrinsically bioactive cryogels based on platelet lysate nanocomposites for hemostasis and wound regeneration applications

Chapter IV

Intrinsically bioactive cryogels based on platelet lysate nanocomposites for hemostasis and wound regeneration applications

ABSTRACT

The currently used hemostatic agents are highly effective in stopping hemorrhages but have a limited role in the modulation of the wound healing environment to promote regeneration. Herein, we propose an intrinsically bioactive hemostatic cryogel with potential regenerative properties based on platelet lysate (PL) and aldehyde-functionalized cellulose nanocrystals (a-CNC). PL have attracted great attention as an inexpensive milieu of therapeutically-relevant proteins, however its application as hemostatic agent exhibits serious constraints (e.g., structural integrity and short shelf-life). The incorporation of a-CNC showed to reinforce the low strength PL matrix by covalent cross-link its amine groups that exhibits an elastic interconnected porous network after full cryogelation. Upon blood immersion, the PL-CNC cryogels absorbed higher volumes of blood at a faster rate than commercial hemostatic porcine gelatin sponges. Simultaneously, the cryogels increased stem cell proliferation, metabolic activity and migration as well as downregulated expression of markers of the fibrinolytic process. In a *in vivo* liver defect model, PL-CNC cryogels showed similar hemostatic performance in comparison with gelatin sponges and normal material-induced tissue response upon subcutaneous implantation. Overall, owing to its structure and bioactive composition, the proposed PL-CNC cryogels provide an alternative off-the-shelf hemostatic biomaterial with the potential to promote wound regeneration for clinical applications.

This chapter is based on the following publication: **B. B Mendes,** *M. Gómez-Florit, Ana C. Araújo, J. Prada, P. Babo, R. M. A. Domingues, R. L. Reis, M. E. Gomes. Intrinsically bioactive cryogels based on platelet lysate nanocomposites for hemostasis and wound regeneration applications. (Submitted)*

IV-1. INTRODUCTION

Wound healing is a complex process orchestrated by the blood coagulation cascade and the cellular components of the immune system, which releases multiple cytokines, and induces crucial cellular and inflammatory pathways [1, 2]. Immediately after an injury occurs, it is of utmost importance to prevent excessive bleeding, as well as bacterial infection [3]. In healthy individuals, natural clotting process is relatively fast (within few minutes) and effective, even though severe bleeding accounts for approximately one third of total deaths in hospitals that occur due to traumatic injury events [3-6]. Thus, a prompt arrest of hemorrhage is essential for initial survival and for an optimal recovery in civilian and military trauma emergencies [7, 8]. Although the currently used polymeric and inorganic hemostatic formulations display good hemostatic capability, they still present several limitations [9]. For example, QuikClot® generates heat that might induce a thermal injury, whereas fibrin dressings have shown xenotoxicity due to the use of bovine origin products (e.g., thrombin) [10, 11]. In addition, despite the versatility of the available hemostatic systems, the continued refinement of their composition should lead to formulations enabling not only effectively control hemorrhage and bacterial infection, but also promote tissue regeneration.

Cryogels can be defined as a class of hydrogels that introduced a new set of unique physical properties in the field of biomedical research [12]. Cryogels formation based on the freeze-drying process is much easier (one step process) and eco-friendly than other macro-pore forming methods, avoiding the need for porogen removal (e.g., acid/base, high temperature or solvent leaching) [13]. Interestingly, cryogels physical properties (e.g, interconnected macroporous structure, mechanical stability and elasticity) play a key role on their large water absorption capability and fast shape recovery, which are crucial features for their application as hemostatic agents. For example, carbon nanotubes reinforced chitosan cryogels demonstrated ability to quick expand and mitigate bleeding *in vivo* [14]. Nevertheless, besides their rapid expansion to effectively control the hemorrhage (i.e., physical process), it is important to envision the design of cryogels with intrinsically bioactive properties to modulate the *in vivo* microenvironment towards wound regeneration (i.e., biological process).

Platelets contain thousands of proteins that, with numerous post-translational modifications, results in over 1,500 identified protein-based bioactive factors [15, 16]. Among the different platelet-rich blood derivatives formulations, platelet lysate (PL) has a more reproducible preparation process and have shown comparatively lower batch-to-batch variability (when prepared from pools of samples/donors) than other blood derivatives formulations [17, 18]. Although the well-known biological role of platelet-derived

molecules during the wound healing process, up to now, there are no previous reports on the use of PL on the development of hemostatic agents. This is most likely related with the limited PL structural integrity that is necessary for a fast blood uptake and blood cells entrapment; short-term storage stability that restricts the maintenance of PL biofunctionality in a ready-to-use off-the-shelf product; and low retention and protection of the PL biomolecules from degradation that are crucial to produce a fibrin clot and promote cell recruitment to the bleeding site [7, 17].

Recent attention has been paid to the use of nanomaterials as crosslinkers to effectively improve hydrogels mechanical strength [19, 20]. In this field, rod-shaped cellulose nanocrystals (CNC), known as the 'nature' carbon nanotubes, have been extensively applied in tissue engineering and regenerative medicine due to their mechanical strength, biocompatibility and high surface area [20]. Interestingly, it has been previously shown that aldehyde-modified CNC reinforced PL-based hydrogel network, fine-tuned hydrogel physical and biochemical microenvironment, and thus positively modulated the behavior of encapsulated stem cell [21]. Although these strategy demonstrated the outstanding biological properties of PL as an efficient engineered extracellular matrix (ECM) to promote regenerative wound healing outcomes, PL-CNC hydrogels approach do not exhibit a fast enough gelation nor the blood absorption capacity to be applied on the control of hemorrhages [12].

In this study, we aim to mimic the *in vivo* wound healing process through the creation of an off-the-shelf intrinsically bioactive hemostatic PL-CNC cryogel. It is envisioned that the proposed hemostatic agent acts as a stable three-dimensional (3D) network to promote blood cells and blood-clotting factors entrapment while locally delivering the therapeutically-relevant PL-derived proteins, Scheme IV-1. The physical and microstructural properties of isotropic and anisotropic PL-CNC cryogels are characterized. Then, the protein release from PL-CNC cryogels, as well as their antibacterial efficacy is evaluated. The impact of bioactive molecules released from PL-CNC cryogels on stem cell proliferation, migration and gene expression was assessed. Furthermore, the cryogels hemostatic potential was analyzed both *in vitro* and *in vivo* along with the evaluation of the tissue inflammatory response. We anticipate that this strategy will introduce a new approach to manipulate the structural properties of blood-derived hemostatic materials, while potentiating the therapeutic effect of their biomolecules for promoting wound healing and regeneration.

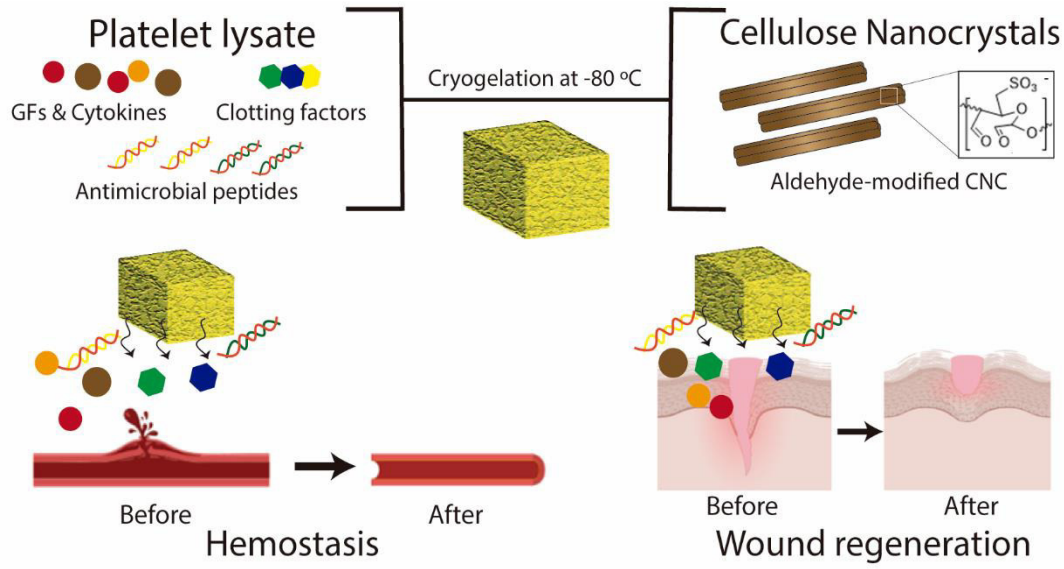

Scheme IV-1 Schematic representation of the preparation of natural fibrillar nanocomposite Cryogels for hemostasis restore and wound regeneration.

IV-2. MATERIALS AND METHODS

IV-2.1. Precursors and cryogels preparation

IV-2.1.1. Preparation of PL

Platelet concentrate collections, obtained from volunteer donation from healthy donors as by 2005/62/CE, were performed at Serviço de Imuno-Hemoterapia – Centro Hospitalar de São João (Portugal) provided under an approved institutional board protocol (ethical commission of CHSJ/FMUP approved at 18/13/2018). A pool of twelve platelet concentrate batches were subject to three freeze/ thaw cycles (−196 °C and 37 °C), and stored at −80 °C. Just before use, PL was thaw at room temperature (RT), centrifuged at 4000 x g for 5 minutes and filtered through a 0.45 µm pore filter to remove any cell debris or clots.

IV-2.1.2. Preparation and characterization of a-CNC

CNC were extracted from microcrystalline cellulose powder (Sigma-Aldrich, USA) by sulfuric acid hydrolysis according to Bondeson et al. with minor modifications, as previously described [21, 22]. Then, vicinal hydroxyl groups on CNC's surface were converted to carbonyls by adding sodium periodate ($NaIO_4$) at a 1:1 molar ratio for 12 hours [23]. The chemical modification on a-CNC was confirmed by FTIR and CNC morphology was imaged by atomic force microscopy (AFM), as previously described [21]. The desired concentration of the working suspension was adjusted by concentrating it against poly(ethylene glycol) (average MW 20,000 kDa, Sigma-Aldrich, USA) using benzoylated cellulose dialysis membranes (2000 Da NMWCO, Sigma-Aldrich, USA).

IV-2.1.3. PL-CNC cryogels preparation

PL-CNC cryogels were prepared blending PL with a-CNC at 1:1 volume ratio. A double-barrel syringe L-system (1:1 from Medmix, Switzerland) with a static mixer tip (Medmix, Switzerland) was used to homogenously extrude the cryogels into squared molds. Barrel 1 was filled with PL and barrel 2 with a-CNC aqueous dispersions (1.2 to 2.4 wt.%). After casting into the molds, the cryogel precursors were frozen at -80°C and subsequently freeze-dried until full cryogelation. Anisotropic structured cryogels were also prepared (described in supplementary information). Cryogels formulations were named according to their final a-CNC concentrations: 0 wt.% (PL-CNC 0), 0.6 wt.% (PL-CNC 0.6) and 1.2 wt.% (PL-CNC 1.2).

IV-2.2. Cryogels characterization

IV-2.2.1. Microstructure

PL-CNC cryogels were freeze-fractured in liquid nitrogen to expose their inner structures, and then sputter coated (30 seconds at 20 mA, Cressington) with gold prior observation in a SEM (JSM-6010LV, JEOL, Japan). Isotropic and anisotropic PL-CNC formulations (7 x 7 x 5 mm, n=5) were also scanned using X-ray scan micrograph (micro-CT; SkyScan 1272; Bruecker, Kontich, Belgium), at a resolution of 10 µm, reconstructed using the software NRecon (Version: 1.6.6.0, Skyscan), and analyzed on CT analyzer (Version: 1.17.0.0, Skyscan) (for more information please see supplementary information).

IV-2.2.2. Mechanical characterization

Universal Mechanical Testing Machine (Instron 5540) equipped with a load cell of 1 kN was used to conduct unidirectional compression tests. The hydrated (2 hours in PBS) anisotropic and isotropic PL-CNC specimens (7 x 7 x 5 mm, n=5) were set on the lower plate and compressed by moving the upper plate at a compression rate of 1 mm per minute at RT. For cyclic tests, isotropic PL-CNC 1.2 formulation was subjected to three successive loading and unloading cycles at a compression rate of 1 mm per minute and ε = 50%. The obtained stress-strain curves were used to calculate the Young's modulus (i.e. the average slope of the stress-strain curve in the initial linear region) in order to study cryogels structural integrity and their capacity for recovery.

IV-2.2.3. Weight loss

Isotropic and anisotropic PL-CNC cryogels were incubated in 1.5 mL of phosphate buffered saline (PBS) pH=7.4 at 37 °C for 2 hours. After removing the excess of PBS, the initial mass of the cryogel was measured (M_i) and successively weighted at different time points (M_f) to determine the weight loss (%), according to Equation IV-1. The results are expressed as an average of five samples.

$$\text{Weight loss} = \frac{\text{Mi} - \text{Mf}}{\text{Mi}} \text{ x } 100$$

Equation IV-1 Quantification of hydrogel weight loss

IV-2.2.4. Protein release from cryogels

PL-CNC cryogels were incubated in 1 mL of α-MEM with 1% antibiotic/antimycotic solution (i.e., without serum supplementation) at 37 °C. At different time points (5 minutes, 6 hours, 1, 3, 5 and 7 days of incubation), the supernatant was collected and replaced with fresh cell culture medium. The timepoints were named as follows: D0 (5 minutes), 6H (6 hours), D1 (1 day), D3 (3 days), D5 (5 day) and D7 (7 days). After 1 week, PL-CNC cryogels were digested in 200 U. mL^{-1} *Trichoderma sp.* Cellulase (Sigma-Aldrich, USA) (3-10 U. mg^{-1} solid). Total protein content in the diluted supernatant of PL-CNC formulations (n=3) was quantified according to the manufacturer's instructions using Coomassie (Bradford) protein assay kit (Thermo Scientific, USA).

IV-2.3. Antibacterial activity

IV-2.3.1. Escherichia coli and Staphylococcus aureus reduction analysis

The antibacterial activity of the cryogels was tested against *Escherichia coli* (*E. coli*; ATCC 25922 Gram negative bacteria) and *Staphylococcus aureus* (*S. aureus; ATCC 25923*, Gram positive bacteria), as previously described [24]. Bacterial cultures were grown in Tryptic Soy Broth medium at 37 °C overnight with agitation (150 rpm). Bacterial cells were centrifuged at 9000 x g for 5 minutes at 4 °C and washed twice with sterile PBS. Then, 10 µL of 1-2 x 10^6 CFU. mL^{-1} bacterial suspension in PBS was added onto PL-CNC cryogels surface and incubated for 2 hours at 37 °C. Afterwards, 1 mL of PBS was added to each well and 10 µL of the suspension was plated on the Tryptic Soy Agar plates. CFUs were counted after 24 h of incubation at 37 °C. 10 µL of bacterial suspension in PBS (1-2 x10^6 CFU. mL^{-1}) was used as a negative control. Tests were repeated three times for each group and the results were expressed as bacterial reduction (%), see Equation IV-2.

$$\text{Bacterial reduction} = \frac{\text{colonies count of control} - \text{survivor count on sample}}{\textit{colonies count of control}} \text{ x } 100$$

Equation IV-2 Quantification of the bacterial reduction.

IV-2.4. Hemostatic properties

IV-2.4.1. Whole blood collection

Human blood samples were drawn from healthy donors at *Serviço de Imuno-Hemoterapia – Centro Hospitalar de São João* (Portugal) provided under an approved institutional board protocol (ethical commission of CHSJ/FMUP approved at 18/13/2018). It was collected in sterile BD Vacutainer® tubes (BD-Plymouth, UK), which contains 0.129 M sodium citrate at 9:1 ratio. The collected whole blood was stored at RT.

IV-2.4.2. Blood absorption rate

PL-CNC cryogels and commercial hemostatic porcine gelatin sponge (Gelita-Spon® Standard, Gelita® Medical, Germany) were weighted (M_d), and incubated with whole blood for 5, 30, 60 and 180 seconds. The samples were immediately transferred to the clean gauze for 10 s to remove the unabsorbed blood and weighed (M_w). The adsorption rate (%) was calculated using Equation IV-3. Images of the samples after 180 seconds of incubation in whole blood were taken.

$$\text{Blood absorption rate} = \frac{\text{Mw} - \text{Md}}{\text{Md}} \text{ x } 100$$

Equation IV-3 Quantification of the blood absorption rate.

IV-2.4.3. Hemolytic activity assay

Whole blood was centrifuged at 116 x g for 10 minutes, washed three times with PBS, and then the obtained erythrocytes were diluted to a final concentration of 5 vol.% as previously reported [14, 25]. Afterwards, 10 mg of each sample was added to 500 µL of erythrocyte suspension. PBS buffer (0% lysis) and 0.1 vol.% Triton X-100 (100% lysis) were also added to the erythrocyte suspension, and served as the negative and positive control, respectively. After incubation for 1 hour at 37 °C in a shaking incubator chamber, the mixture was centrifuged at 120 x g for 10 minutes. 100 µL of the obtained supernatants were transferred into a 96-well clear plate, and the absorbance was measured at 540 nm to determine the hemolytic ratio (%), see Equation IV-4.

$$\text{Hemolytic ratio} = \frac{\text{Test sample} - \text{Negative control}}{\text{Positive control} - \text{Negative control}} \text{ x } 100$$

Equation IV-4 Quantification of hemolytic ratio.

IV-2.4.4. Blood cells adhesion

Whole blood was added dropwise into PL-CNC cryogels and commercial absorbable gelatin sponge hemostat (7 x 7 x 3 mm), and then incubated for 5 minutes at 37 °C as described in the literature [14, 26]. In platelet adhesion studies, whole blood was centrifuged at 300 x g for 10 minutes and then the upper phase (i.e., platelet-rich plasma) was added dropwise to the sample and incubated for 1 hour

at 37 °C. All samples were washed three times with PBS to remove the non-adherent and loosely attached cells, and then fixed with 2.5 vol.% glutaraldehyde (Merck, Germany) for 2 hours. After fixation, samples were solvent exchanged from water to ethanol (ethanol gradient 25, 50, 75 and 99.9 vol.%) for 4 hours, and then dried overnight at RT. Finally, the samples were sputter coated (30 seconds at 20 mA, Cressington) with gold prior observation in a SEM.

IV-2.5. Cell isolation

Human adipose-derived stem cells (hASCs) were obtained from lipoaspirate samples of the abdominal region of healthy donors undergoing plastic surgery under the scope of an established protocol with Hospital da Prelada (Porto, Portugal), and with the approval of the Hospital Ethics Committee. The hASCs isolation were performed using a previously optimized protocol [27]. hASCs were maintained in α-MEM supplemented with 10% fetal bovine serum (FBS) and 1% antibiotic/antimycotic solution at 37 °C, 5% CO_2.

IV-2.6. *In vitro* cell culture studies

IV-2.6.1. Cell viability

$5x10^5$ hASCs were seeded on the cryogels surface. After 90 minutes, α-MEM with 1% antibiotic/antimycotic solution (i.e., without FBS supplementation) was added to the cryogel formulations and changed every two days. On days 3 and 7, cellular viability was assessed using 1:500 vol.% Calcein AM (Thermo Fisher Scientific, USA) and 1:1000 vol.% propidium iodide (Thermo Fisher Scientific, USA) staining for 15 minutes at 37 °C. PL-CNC cryogels formulations were washed twice with PBS and visualized using confocal microscope TCS SP8 (Leica Microsystems, Germany).

IV-2.6.2. Cell proliferation

1.66×10^4 hASCs per 1 cm^2 were seeded in 48-well plates for 24 hours in α-MEM supplemented with 10% FBS and 1% antibiotic/antimycotic solution. The medium was removed and replaced with 200 µL of PL-CNC cryogel and gelatin sponge releasates collected after D0, 6H, D1, D3, D5 and D7. After 24 hours, the metabolic activity and proliferation of hASCs were evaluated using Alamar Blue assay kit (Bio-

Rad, USA) and Quant-iT PicoGreen dsDNA assay kit (Thermo Fisher Scientific, USA), respectively. Briefly, hASCs were incubated with alamar blue solution for 4 hours at 37 °C. The alamar blue fluorescence was assayed at 535 (excitation) and 600 (emission) nm. After washing twice with PBS, ultrapure water was added to the cell culture plate and frozen at -80 °C. The released DNA was quantified following manufacturer's instructions (Thermo Fisher Scientific, USA).

IV-2.6.3. Scratch assay

hASCs at a density of 7.7×10^4 per 1 cm^2 were seeded on 96-well plates, as previously described [28]. After 24 hours, a confluent cell monolayer was formed, and the monolayer was scraped with a 0.1–10 μL sterile pipette tip (0.57 mm) in a straight line to create a scratch. The medium was removed, the wells were washed with PBS, and replaced with 100 μL of PL-CNC cryogel and gelatin sponge releasates collected at D0. Cell migration was imaged and monitored using an inverted phase-contrast microscope for 48 hours. The images were quantitatively analyzed using Tscratch software to calculate open wound area (%), see Equation IV-5.

$$\text{Open wound area} = \frac{100 \text{ x open wound area at 48 hours}}{\text{open wound area at 0 hours}}$$

Equation IV-5 Quantification of the open wound area.

IV-2.6.4. Gene expression analysis

After scratch assay analysis, the releasates were removed, and hASCs were washed with PBS. Then, total ribonucleic acid (RNA) was isolated using TriReagent® (Sigma-Aldrich, USA), according to the manufacturer's protocol. Total RNA was quantified at 260 nm using a NanoDrop spectrophotometer (Thermo Fisher Scientific, USA). The same amount of RNA (225 ng) was reverse transcribed to complementary DNA (cDNA) according to the protocol of the supplier (qScript cDNA Synthesis Kit, Quanta Biosciences, USA). Aliquots of each cDNA sample were frozen until the PCR reactions were carried out. Real-time PCR was performed for two reference genes, glyceraldehyde-3-phosphate dehydrogenase (GAPDH) and β-actin and target genes (Supplementary Table VI-1), as previously described [21]. All samples were normalized by the geometric mean of the expression levels of β-actin and GAPDH as

explained in [29]. Finally, fold changes were expressed relative to the expression in the gelatin sponge control group.

IV-2.7. *In vivo* studies

IV-2.7.1. Housing and maintenance of animals

All animal procedures were based upon the ''3Rs" policy (Replacement, Reduction and Refinement) and were carried out after approval by the Ethics Committee of University of Minho and Portuguese Licensing Authority (DGAV). Total of 16 Sprague-Dawley male rat of 7 weeks old and average weight of 185–210 g (Envigo, UK) were used in this study. Each rat was anesthetized by intraperitoneal injection: Domitor INJ 1 mg. mL^{-1} (Medetomidine 1 mg. kg^{-1}, Novavet, Braga, Portugal) and Imalgene 1000 INJ 100 mg. mL^{-1} (Ketamine 75 mg. kg^{-1}, Novavet, Braga, Portugal).

IV-2.7.2. Hemostatic test on a standardized rat liver trauma model

The liver of the rat was exposed by abdominal incision. A pre-weighted filter paper on a paraffin film was placed beneath the liver and the liver bleeding was induced using an 18 G needle. Immediately after the injury, PL-CNC 0.6 and 1.2 cryogels, and a commercial absorbable gelatin sponge (n=6) were applied on the site of lesion until bleeding stopped. The weight of the filter paper with absorbed blood (blood loss) was measured, as well as the time to restore hemostasis (hemostasis time). The rats were euthanized by intracardiac injection of excess Eutasil 200 mg. mL-1 (pentobarbital sodium, Novavet, Braga, Portugal). Samples were fixed with 2.5 % glutaraldehyde (Merck, Germany) for 2 hours. After fixation, samples were solvent exchanged from water to ethanol (ethanol gradient 25, 50, 75 and 99.9 vol.%) for 4 hours and then dried overnight at RT. Finally, the samples were sputter coated (30 seconds at 20 mA, Cressington) with gold prior observation in a SEM.

IV-2.7.3. Host response evaluation

The rat hair was shaved at the implantation area, followed by disinfection with 70% ethanol and iodine. In each rat, four skin incisions (1 cm length) were made in the dorsal midline, two close to the head and the other two far from the head. PL-CNC 0.6 and 1.2 formulations, saline solution, and a

commercial absorbable gelatin sponge were implanted into the respective pockets, followed by skin suturing. The rats were euthanized 7 and 14 days postsurgery by intracardiac injection of excess Eutasil 200 mg. mL-1 (pentobarbital sodium, Novavet, Braga, Portugal) and the implanted materials were retrieved along with the surrounding tissue to histological analysis. The explants were fixed with 10 vol.% formalin and transferred to histological cassettes for paraffin-embedding. Samples were then serially sectioned using a microtome and stained with hematoxylin & eosin (H&E) to further microscopic examination.

IV-2.7.4. Local biological effects assessment after samples implantation

The evaluation of fibrosis, necrosis and angiogenesis was performed according to ISO 10993-6, 2007 biological evaluation of medical devices. The results were expressed in ordinal scale units.

IV-2.8. Statistical analysis

The statistical analysis of data was performed using GraphPad PRISM v 7.0. Shapiro-Wilk normality test and one-way analysis of variance (ANOVA) was used to analyze experimental data, followed by the Tukey post hoc or Krustal-Wallis test for multiple comparisons. Results are presented as mean ± standard deviation.

IV-3. RESULTS AND DISCUSSION

An ideal hemostatic agent should allow a high blood uptake capacity, a rapid blood triggered shape recovery and absorption speed, inherent antibacterial ability, robust mechanical strength, as well as, it should be biocompatible, ready and easy to use, lightweight, stable, and inexpensive [7]. In order to explore the full potential of PL-based cryogels for hemostatic applications, it is fundamental to improve their structural integrity and to extend their shelf life while preserving the therapeutic potential of PL-derived biomolecules such as cytokines, antimicrobial peptides, soluble adhesion molecules and coagulation factors [30]. It is known that cryogels production methods have impact on the material porous structure and lamella densification, and these properties directly affect their blood adsorption capability [31]. Thus, to evaluate the impact of different microstructures on the functional material performance,

cryogels with isotropic or anisotropic pore organization were produced by applying uniform or unidirectional temperature gradient during the cryogelation process, respectively.

IV-3.1. Preparation and physical characterization of PL nanocomposite cryogels

During gelation at subzero temperatures, the aqueous component freezes and forms ice crystals that act as pore-forming agents, excluding solute (i.e., PL proteins and a-CNC) from the ice lattice into the space between the growing ice crystals [32]. The application of non-directional or unidirectional temperature gradients, has been used to determine the anisotropy degree of the resulting porous structure upon freeze-drying [33]. Herein, PL and a-CNC were homogeneously extruded into a square mold in equal parts and submitted to non-directional and unidirectional freeze-casting at −80 °C, and then PL-CNC formulations were freeze-dried, obtaining isotropic and anisotropic PL-CNC cryogels respectively. First, to assess the stability of PL-CNC 0, 0.6 and 1.2 wt.% cryogels, the formulations were immersed in PBS and the changes in the shape of cryogels were recorded (Figure IV-1A and Supplementary Figure IV-1A). The cryogel solely based on PL showed a fast solubilization, losing the preformed 3D structure (Figure IV-1A), whereas PL-CNC formulations composed of 0.6 and 1.2 wt.% CNC content maintained their structure and showed a high mold fidelity (Figure IV-1A and Supplementary Figure IV-1A). These findings suggest that upon cryogel hydration, the chemical covalent cross-linking between a-CNC and the amine groups of PL proteins through reversible Schiff base bonds along with their densification of a-CNC nanomaterials and PL-proteins (i.e., polymers) in the pore walls during ice crystals growth, are pivotal factors to provide cryogels structural integrity and to prevent their disintegration.

PL-CNC cryogels structure was evaluated by micro-computed tomography (μ-CT) and SEM (Figure IV-1 and Supplementary Figure IV-1). In line with previous cryogelation studies, isotropic PL-CNC cryogels revealed a disordered pore structure (Figure IV-1B), with a mean pore diameter around 110 μm (Supplementary Table IV-2), whereas anisotropic PL-CNC cryogels exhibited longer and narrower (around 35 μm; Supplementary Table IV-3) aligned pores along the freezing direction (Supplementary Figure IV-1B and IV-1Ci and ii), and a honeycomb-like structure in the XY-plane perpendicular to the ice-growth direction (Supplementary Figure IV-1CIII and IV) [33]. In addition, anisotropic PL-CNC cryogels showed markedly smaller pore diameter (around 35 μm), and a lower pore interconnectivity (around 4%) in comparison with isotropic PL-CNC cryogels (around 110 μm of pore size and 95% of interconnectivity respectively) (Table S2 and S3) as a result of the fast unidirectional freezing of the grown ice crystals, as previously demonstrated in other studies with cryogels [33-35].

CNC have been used as biocompatible reinforcement nanofillers in low strength matrices due to its high stiffness (200-220 GPa) and axial elastic modulus (110 to 220 GPa) [19, 20]. To confirm the effect of CNC incorporation in the mechanical properties of PL-CNC cryogels were evaluated on swollen conditions (Figure IV-1C to E). While it was impossible to determine Young's modulus of PL-CNC 0 due to its fast solubilization (Figure IV-1A), PL-CNC 1.2 modulus (4.42 ± 1.07 kPa) was almost the double of the modulus of PL-CNC 0.6 (2.29 ± 0.33 kPa). As expected, at higher concentration of a-CNC, there is an increase of total cryogel crosslinking density, which results in stiffer cryogels [36]. The anisotropy of cryogels also influences their mechanical behavior (Supplementary Figure IV-1D) as anisotropic PL-CNC 1.2 (6.07 ± 1.55 kPa) exhibited a higher modulus in the Z-direction than isotropic PL-CNC 1.2 (4.42 ± 1.07 kPa). Most likely, the thin pore walls with high CNC alignment in the freezing direction are generated due to the high CNC aspect ratios, which leads to this mechanical robustness, as previously observed in other CNC-based formulations [34].

Since blood absorption capacity is crucial to accelerate blood cells entrapment to form a blood clot, the water uptake was evaluated in isotropic and anisotropic cryogels [14, 37]. Regarding the ability to adsorb liquids, isotropic PL-CNC cryogels exhibited a faster water uptake capability (Supplementary Figure IV-1F). Most likely, it is a direct consequence of the above reported larger pore size and highly interconnected structure of the isotropic formulations. Therefore, isotropic PL-CNC cryogels were selected for further physical and biological characterization to be applied as a potential hemostatic agent.

Strikingly, PL-CNC 1.2 cryogels could be compressed up to 50% strain level without being mechanically or structurally damaged (Figure IV-1DI and E). Upon load removal, the elastically deformed cryogels recovered their original shape as the surrounding water was reabsorbed, exhibiting a fast deformation reversion (~on the order of seconds), Figure IV-1E. Then, PL-CNC 1.2 cryogels were subjected to three successive compression cycles with a deformation speed of 1 mm per minute (Figure IV-1DI). Even though the cryogel exhibited hysteresis loops comprising the loading and unloading phases that indicates energy dissipation, there is an overlap of the cyclic stress-strain curves with comparable and reproducible compressive strength values. These results confirmed that PL-CNC cryogels possess a good mechanical strength and high compression resilience under continuous and dynamic compression as well as withstand extensive deformations without being destroyed. These findings are in agreement with previous results where the incorporation of high aspect ratio and high stiffness nanoparticles such as carbon nanotubes in cryogels composition led to nanocomposite materials displaying similar unique

mechanical characteristics [12, 14]. Remarkably, after 6-month of storage at RT, cryogels high elastic behavior was still evident, demonstrating its structural resilience to long-term storage (Figure IV-1DII).

The most recent hemostatic studies have shown the importance to locally deliver these agents in a minimally invasive strategy (i.e., as injectable systems) [24, 38]. Remarkably, after PL-CNC cryogels syringe extrusion, they showed an immediately water absorption, while its strength and easy handling is maintained. These findings demonstrate the versatile properties of PL-CNC cryogels, envisioning their potential application in deep and irregular shape wounds, as well as in noncompressible areas.

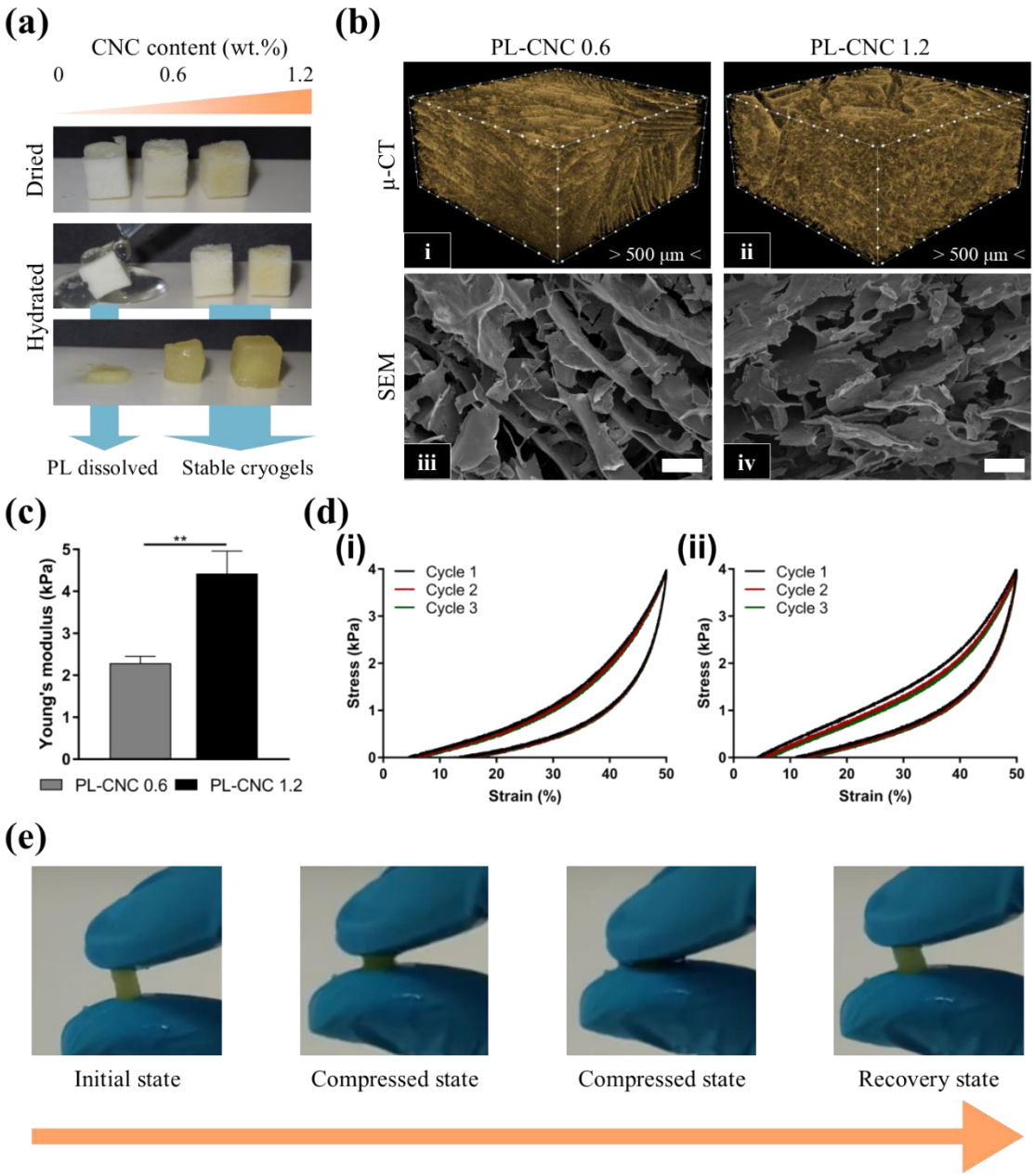

Figure IV-1 Physical properties of the cryogels formulations. (a) Cryogels stability after immersion in PBS. (b) Microstructure evaluation by SEM (i-ii) and μ-CT (iii-iv). (c) Young's modulus from the uniaxial compression stress–strain curves. (d) Three

successive loading and unloading cycles of PL-CNC 1.2 at ε = 50% in fresh (i) and 6 months stored samples (ii). (e) Photographs representing the shape memory property and rapid recovery speed of PL-CNC 1.2 cryogels after absorbing water. Statistical significance: **, P < 0.01. Scale bar: 50 μm (b-iii and iv).

IV-3.2. Protein release from PL-CNC cryogels

Wound healing is a complex process that involves the interplay of multiple cell populations and soluble mediators in a highly organized and orchestrated manner [1, 2]. Generally, upon injury, platelets in wound site suffer degranulation through the activation by any thrombogenic agent, which induce morphological changes and the release of bioactive factors from their α- and dense granules, and lysosomes into the local wound environment [39]. These factors include clotting agents (e.g., thrombin, von Willebrand factor), cytokines/chemokines (e.g., IL4, IL8), structural proteins (e.g., fibrinogen, fibronectin), microbicidal proteins (e.g., β-lysin, complement proteins), ions (e.g., calcium), membrane proteins (e.g., CD63) and GFs (e.g., platelet-derived GF, vascular endothelial GF, transforming GF) mediate several wound healing stages [17, 40]. Besides the recruitment of immune cells and the initiation of the clot formation during hemostasis, platelet-derived biomolecules have also been shown to be crucial mediators in several further wound healing stages, for example immunomodulatory processes, antibacterial activity, inflammatory response, and tissue repair and regeneration [17]. In a biomimetic approach, platelet concentrate units were mechanically disrupted to promote the release of these biomolecules milieu in a reproducible large scale and cost-effective manufacturing. Upon full cryogelation, a-CNC act as crosslinkers of PL proteins to produce a scaffold that close resembles fibrin network physical support.

Once PL-CNC cryogels are applied in the wound site, it is crucial the adequate maintenance of its mechanical strength and porosity, blood cells infiltration and local delivery of PL-derived proteins at the bleeding site [7, 41]. Thus, the structural integrity of PL-CNC cryogels over 7 days was evaluated by measuring the weight loss and total protein content release assays, Figure IV-2A. First, weight losses were monitored as a measure of cryogels degradation (Figure IV-2AI). Both formulations undergo weight decrease over the time, though PL-CNC 0.6 showed a markedly higher weight loss (45.13 ± 6.24 %) in comparison with PL-CNC 1.2 (19.37 ± 2.65 %). As previously anticipated, the formulation with high precursor content (1.2 wt.%) led to an increase of crosslinking degree between the a-CNC and amine groups of PL-derived proteins (i.e., chemical crosslinking) as well as to a more tightly packed structure that increased nanomaterial/protein interactions (i.e., physical crosslinking), which is sufficient to maintain its initial structural integrity.

Most proteins are only marginally stable, thus the processing and storage conditions (e.g., temperature and pH changes) are often detrimental to maintain their structure and biological activity [42]. Interestingly, previous studies have tested several platelets and PL storage conditions for its shelf-life extension and bioactivity preservation [43-45]. One study demonstrated that higher concentrations of GFs (e.g., platelet-derived GF-BB and vascular endothelial GF) were detected in cryopreserved PL groups than in freeze-dried PL by enzyme-linked immunosorbent assay (perhaps due to potential proteins denaturation during this process) [43]. Nevertheless, both formulations showed to have similar bioactivity *in vitro* and *in vivo*. The release of the protein cryogels content was quantified to evaluate the potential of cryogels as biomolecules delivery systems (Figure IV-2AII). Upon incubation for 5 minutes (D0), both conditions exhibited an initial burst release, followed by an apparent "plateau" profile. This protein release profile can be explained by the simple diffusion of the proteins non-bound to the cryogel at the first minutes, as previously demonstrated in other PL crosslinked scaffolds [46, 47]. At the end of the experiment, PL-CNC 0.6 cryogel released 73.89 ± 11.30 wt. % of total protein content whereas PL-CNC 1.2 delivered 85.42 ± 5.94 wt. % of total protein content. Considering the low amount of CNC used and the open macroporous cryogel structure, this initial burst release of biomolecules into the solution was expectable. It is worth to mention that the weight assay was conducted after 2 hours of incubation in PBS, thus considering the burst proteins release and the remained water, it is expected a difference on cryogels weight and protein release assays. Accordingly, this material should not be infused into an aqueous solution prior to use, since it exhibited an initial burst release of the bioactive molecules, envisioning improved functionalities when applied dry.

IV-3.3. Antibacterial properties

Conferring antibacterial properties to hemostatic sponges might bring several benefits since the continued presence of a high bacterial load in wounds increases inflammation and delays the healing process [2]. Interestingly, platelets have a significant and direct role in the antimicrobial host defense, mainly due to the release of a wide variety of antimicrobial peptides (also called host defense peptides) in response to injury, namely platelet factor-4, RANTES, connective tissue activating peptide 3, platelet basic protein, thymosin β-4, fibrinopeptide B, fibrinopeptide A and thrombocidins, which are able to kill

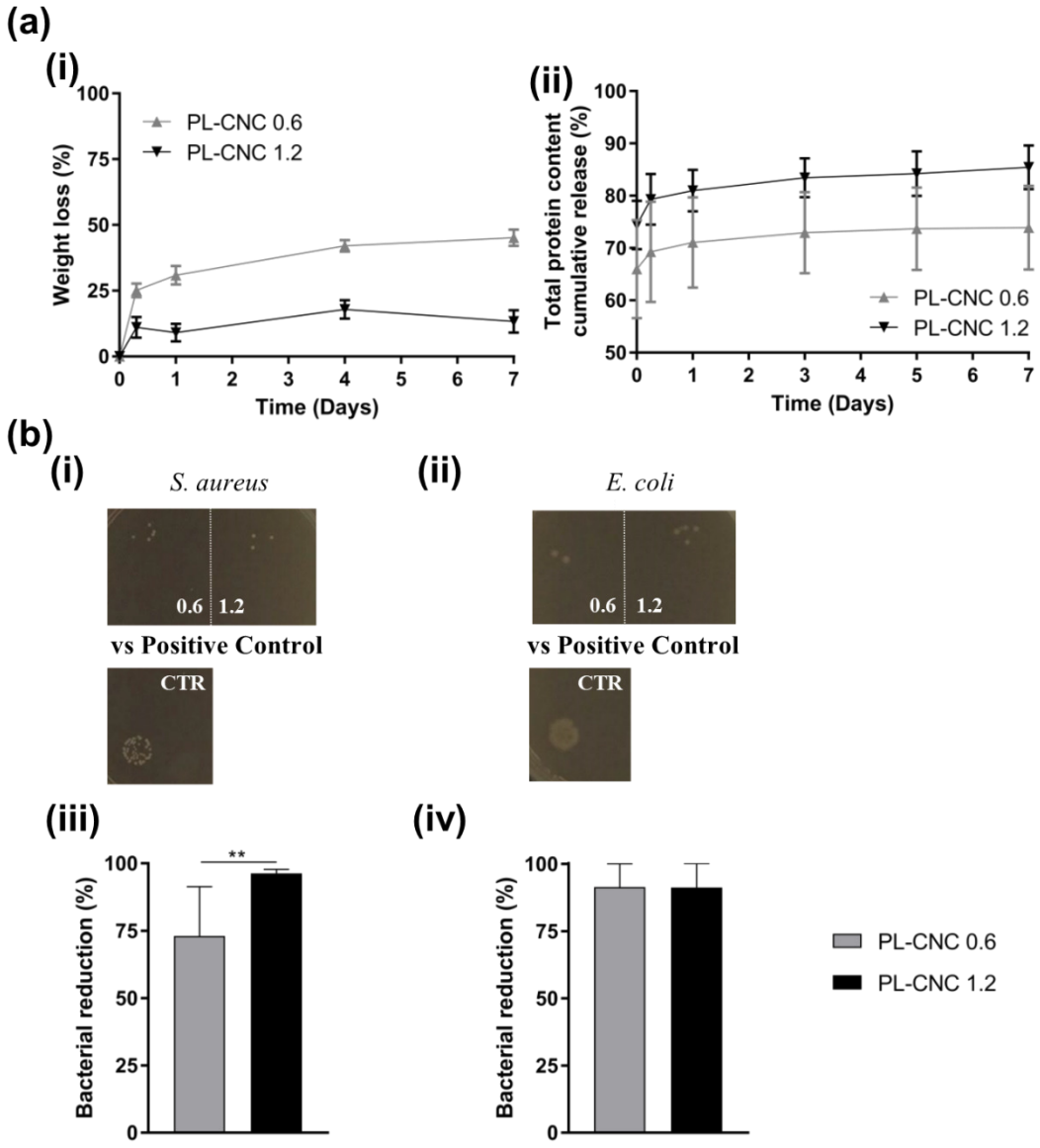

Figure IV-2 Release of bioactive molecules from PL-CNC cryogels. (a) Weigh loss (i) and release kinetics of bioactive proteins from PL-CNC cryogels over 7 days (ii). (b) Antibacterial activity of the PL-CNC 0.6 (0.6), PL-CNC 1.2 (1.2) and 10 µL of bacterial suspension in PBS (CTR) against S. aureus (i-iii) and E. coli (ii-iv), photographs of agar plates (i and ii) and bacterial reduction quantification (iii and iv) (b). Statistical significance: **, $P < 0.01$.

bacteria by cytoplasmatic membrane permeation and cell lysis [48-50]. Moreover, our group has previously demonstrated that genipin-crosslinked PL patches exhibited an antibacterial effect by preventing the adhesion, proliferation and biofilm formation by *S. aureus*, which can be related to PL proteins presence [51]. Therefore, the antibacterial activity of the cryogels developed in this study was assessed against Gram positive *S. aureus* and Gram negative *E. coli* bacteria (Figure IV-2B). Remarkably, PL-CNC cryogels showed significant reduction of *S. aureus* and *E. coli* survival. The reduction of *S. aureus* survival in the presence of PL-CNC was 73.08 ± 16.38 % (PL-CNC 0.6) and 96.30 ± 1.33 % (PL-CNC

1.2), Figure IV-2BI and iii. Moreover, the inhibitory effect of PL-CNC cryogels against *E. coli* bacteria was found to be similar between PL-CNC 0.6 (91.4 ± 7.94 %) and PL-CNC 1.2 (91.24 ± 8.22 %) groups, Figure IV-2BII and IV. Thus, we hypothesize that PL-CNC cryogels can be potent prophylactic agents to impede bacterial infection, although further investigation is needed to fully understand the underlying their mechanisms of action.

IV-3.4. *In vitro* hemostatic potential

In order to manage an uncontrolled post-traumatic hemorrhage, it is critical a rapid blood absorption to accumulate blood cells and to activate coagulation factors, which, ultimately, will effectively control an *in vivo* hemorrhage [7]. Hence, the hemostatic properties of PL-CNC cryogels *in vitro* were studied and compared with a commercial hemostatic porcine gelatin sponge (Gelita-Spon® Standard, Gelita® Medical, Germany). Gelatin-based hemostatic agents are obtained from the denaturation and subsequent purification of animal-based collagen, typically from bovine or porcine origin [52]. Due to their availability, easy handling, relative low cost and effective hemostatic action, gelatin sponges have been extensively applied as topical hemostatic agent in surgery [52]. Although the hemostatic mechanism of gelatin is still not fully understood, it is hypothesized that the close contact of the platelets when entrapped in the porous sponge network promotes platelets aggregation and the formation of a stable blood clot [52].

As a first screening for hemostatic potential, both PL-CNC cryogel and gelatin sponge control formulations were immersed in whole blood. PL-CNC cryogels revealed a homogeneous absorption and maintenance of initial shape integrity (Figure IV-3A). On the other hand, commercial gelatin sponges of the same size (7 x 7 x 3 mm) exhibited a structural collapse without the recovery of its original shape that was exacerbated when gelatin samples were handled. As previously observed in water absorption test, it seems that the interconnectivity of PL-CNC cryogels is adequate to promote blood cells infiltration. During the first 5 seconds, gelatin sponges showed the lowest absorption potential, reaching a maximum of 354.5 ± 77.1 %, which was significantly lower than the cryogels absorption capacity. PL-CNC 0.6 cryogels showed a faster blood absorption than PL-CNC 1.2 cryogels, and after 30 seconds they reached a blood absorption plateau at 1158.2 ± 156.7 wt. % and 1260.6 ± 40.8 wt. % of their initial dry weight, respectively (Figure IV-3B). It is worth mentioning the importance of the large surface area, macroporous morphology and high pore interconnectivity in the obtained swelling capacity of the control and test samples, which are undoubtedly much higher than those of traditional hydrogels [12]. Moreover, PL-CNC groups exhibited

higher blood absorption capacity than other hemostatic agents, for example mesoporous chitosan sponge [25]. Remarkably, the macrostructural integrity of PL-CNC cryogels is decisive to obtain a higher blood uptake than the water-soluble gelatin sponge.

Once hemostatic agents are applied at the bleeding site, blood is the first component to interact with them. The material-to-blood direct contact can promote the loss of red blood cells (RBC) membrane integrity (hemolysis) leading to the leakage of hemoglobin into blood plasma, which can trigger specific pathophysiologies [53]. Thus, the hemocompatibility of materials was evaluated by *in vitro* hemolysis ratio (Figure IV-3C) as well as RBC (Figure IV-3D) and platelets (Figure IV-3E) adhesion and morphology on the different cryogel formulations. Upon incubation with a RBC suspension, hemolysis ratios of PL-CNC cryogels, gelatin sponge, PBS (positive control) and Triton X-100 (negative control) were determined (Figure IV-3C). PL-CNC cryogels and gelatin sponge supernatants exhibited a light yellow color similar to PBS, whereas Triton-X was bright red due to the release of hemoglobin into the liquid (Figure IV-3CI). For the quantitative hemolysis ratio, gelatin sponge showed the lowest value of 1.9 ± 0.5 %, but not statistically significant to PL-CNC 0.6 (3.7 ± 2.0 %) and PL-CNC 1.2 (2.5 ± 0.6 %) groups (Figure IV-3CII), indicating that these are non-harmful for RBC. The obtained hemolysis ratios values are comparable with previously reported hemostatic materials, thus confirming cryogels hemocompatibility [14].

The three groups showed a large number of blood cells (i.e. RBC and platelets) adhering to their surfaces (Figure IV-3D and E). High-magnification SEM images of blood cells clearly display two type of cells: (1) round cells with an indented center and biconcave disc shape (normal RBC) that tend to form aggregates (“rouleaux”) [54] and (2) spherical cells covered with abundant fine uniform crenations (echinocytes or altered RBC), Figure IV-3DIII, VI and IX. The presence of echinocytes can be explained by the exposure to anticoagulants or staining techniques, but RBC are able to recover their discoid shape when re-introduced into fresh plasma [55]. Concerning platelet adhesion on hemostats surface, PL-CNC cryogels and gelatin sponge were incubated for 1 hour with PRP (Figure IV-3E). Platelets of 2-3 µm diameter adhered to the material’s surface and exhibit a flattened morphology with projections of pseudopodia and lamellipodia, which is an indicator of platelet activation [14, 26, 56]. The adhesive interactions mediated platelet to platelet aggregation that produced a tenaciously adherent mass of platelets, being more evident on PL-CNC 0.6 cryogel formulation (Figure IV-3EII). Altogether, the results indicate that PL-CNC cryogels have a higher uptake of blood than the control, which enhances blood cells

adhesion, platelets activation and aggregation, and possible release of coagulation factors that will clearly contribute to their *in vivo* blood-clotting capability [30].

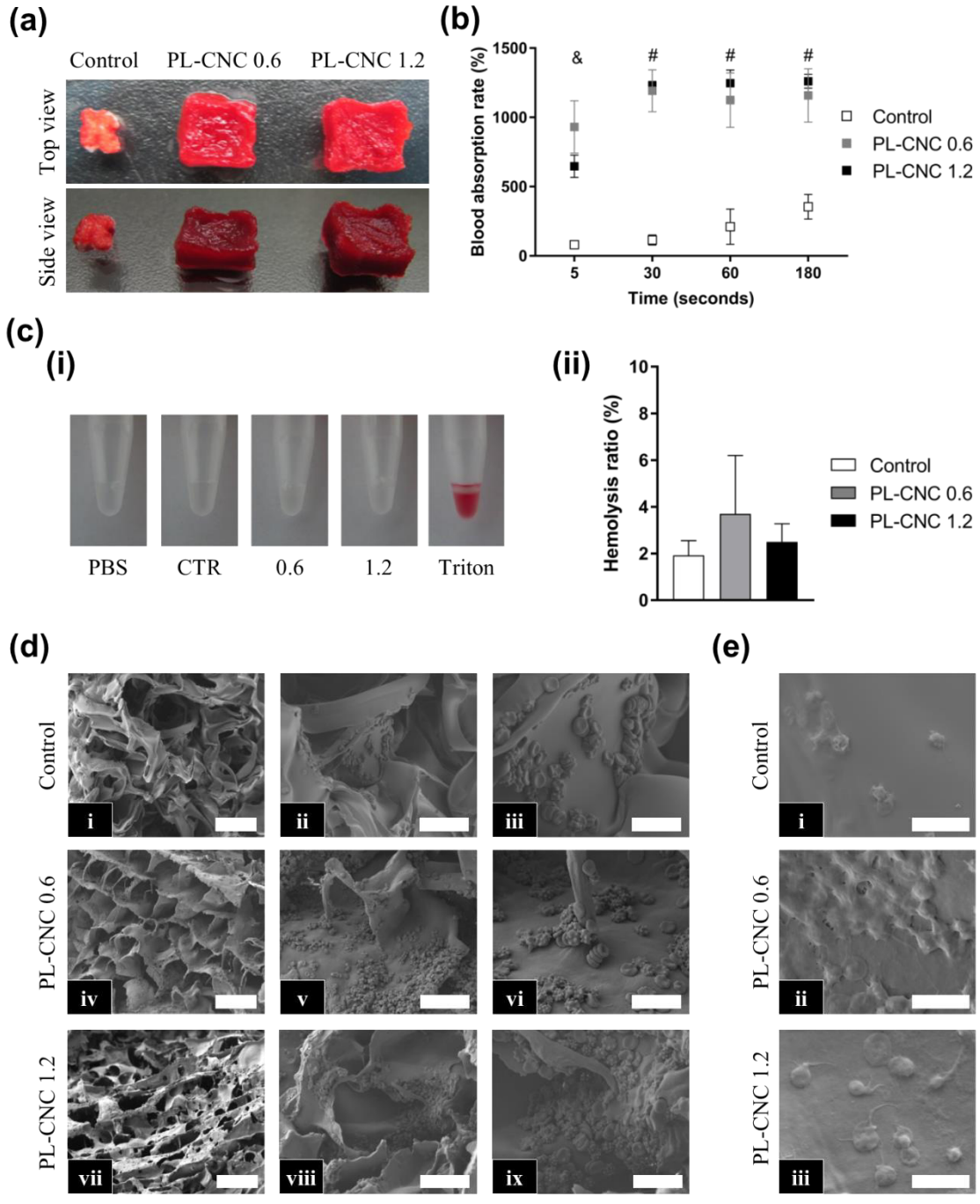

Figure IV-3 *In vitro* hemostatic capacity evaluation of PL-CNC cryogels compared to commercial gelatin-based hemostatic sponges (control). After 3 minutes immersion in whole blood, (a) structural shape maintenance and (b) blood absorption rate were evaluated. (c) Photographs from hemolytic activity assay (i) and hemolysis ratio (ii) of the tested formulations. SEM images of (d) adhesion and morphology of blood cells and (e) platelets on the cryogels and commercial gelatin sponge surface. Statistical significance: &, $P < 0.01$, Control vs PL CNC 0.6 and #, $P < 0.0001$, Control vs PL CNC 0.6-1.2. Scale bar: 100 µm (d-i, iv and vii), 50 µm (d-ii, v and viii), 10 µm (d-iii, vi and ix) and 5 µm (e).

IV-3.5. *In vitro* cell behavior

The response of hASCs to PL-CNC cryogels and to their leachable compounds was evaluated to assess their cytocompatibility (Figure IV-4A and B). For this purpose, hASCs were seeded/cultured onto the cryogels without serum supplementation (i.e., FBS), Figure IV- 4A. Three days after seeding, live/dead assay results showed a high cell viability (> 90 %) in both PL-CNC groups, which is maintained until the end of the experiment (7 days). Moreover, hASCs presented a spindle-like morphology and were distributed within the entire cryogel network, mainly due to the structural support of PL-CNC cryogels for hASCs attachment. After 21 days in culture, hASCs exhibited high cytoskeleton elongation and extended cell spreading area, showing that the cryogels enabled an appropriate microenvironment for cells that led to well-developed cellular networks formation (Supplementary Figure IV-2).

hASCs were also challenged with supernatants obtained from PL-CNC 0.6, PL-CNC 1.2 and commercial gelatin formulations for 24 hours, Figure IV-4B. The obtained results indicated that PL-CNC cryogel releasates collected from D0 (5 min of incubation), D0–6H and 6H–D1 significantly enhanced cell proliferation in comparison with gelatin sponge group releasates (Figure IV-4BI). Moreover, cells cultured with PL-CNC cryogels supernatants at D0 exhibited a lower metabolic activity per cell in comparison with gelatin sponge (control) releasates at D0, values that are leveled for the cultures performed with the releasates of the subsequent time points, Figure IV-4BII. At an early time interval (D0), 65.99 ± 13.25 % (PL-CNC 0.6) and 74.42 ± 6.57 % (PL-CNC 1.2) of PL protein content was released (Figure IV-2AII), which likely contains relevant GFs (e.g., mitogenic platelet-derived GF) that are able to induce cell proliferation [57]. At the subsequent time points, lower amounts of protein were released from the cryogels, resulting in minimal cell proliferation when compared with the cultures using the initial PL-CNC cryogels releasates. The unique open porous structure and structural stability of PL-CNC cryogels along with bioactive cues (e.g., GFs and cytokines) presence are crucial to their excellent cytocompatibility and biofunctionality.

The effect of the soluble factors in cryogel releasates on stem cell migration and gene expression was evaluated using a scratch assay (Figure IV-4C). Interactions among endogenous stem cells, tissue-resident cells and immune cells are essential factors for wound healing and regulation of the regenerative processes [58]. Endogenous stem cells enable the regeneration or repair of every human tissue, they can be activated in the local environment, recruited from circulation or undergo transdifferentiation. Thus, the recruitment of stem cells to the wound side can potentially regulate site-specific repair/regeneration processes. First, a scratch was performed in a hASCs monolayer to mimic the *in vivo* wound healing

process, and subsequently the cells were treated for 48 hours with the releasates collected at D0 (Figure IV-4CI and Supplementary Figure IV-3). hASCs migrated faster in the presence of PL-CNC 0.6 releasates (open wound area of 0 %) when compared to hASCs in PL-CNC 1.2 (14.80 ± 29.6 %) and gelatin sponge (32.53 ± 37.59 %) releasates. We hypothesize that hASCs migrated faster in PL-CNC cryogels formulations possibly influenced by soluble PL-derived GFs that are known to promote an efficient wound closure (e.g., platelet-derived GF or stromal cell–derived factor 1α) [17, 59, 60].

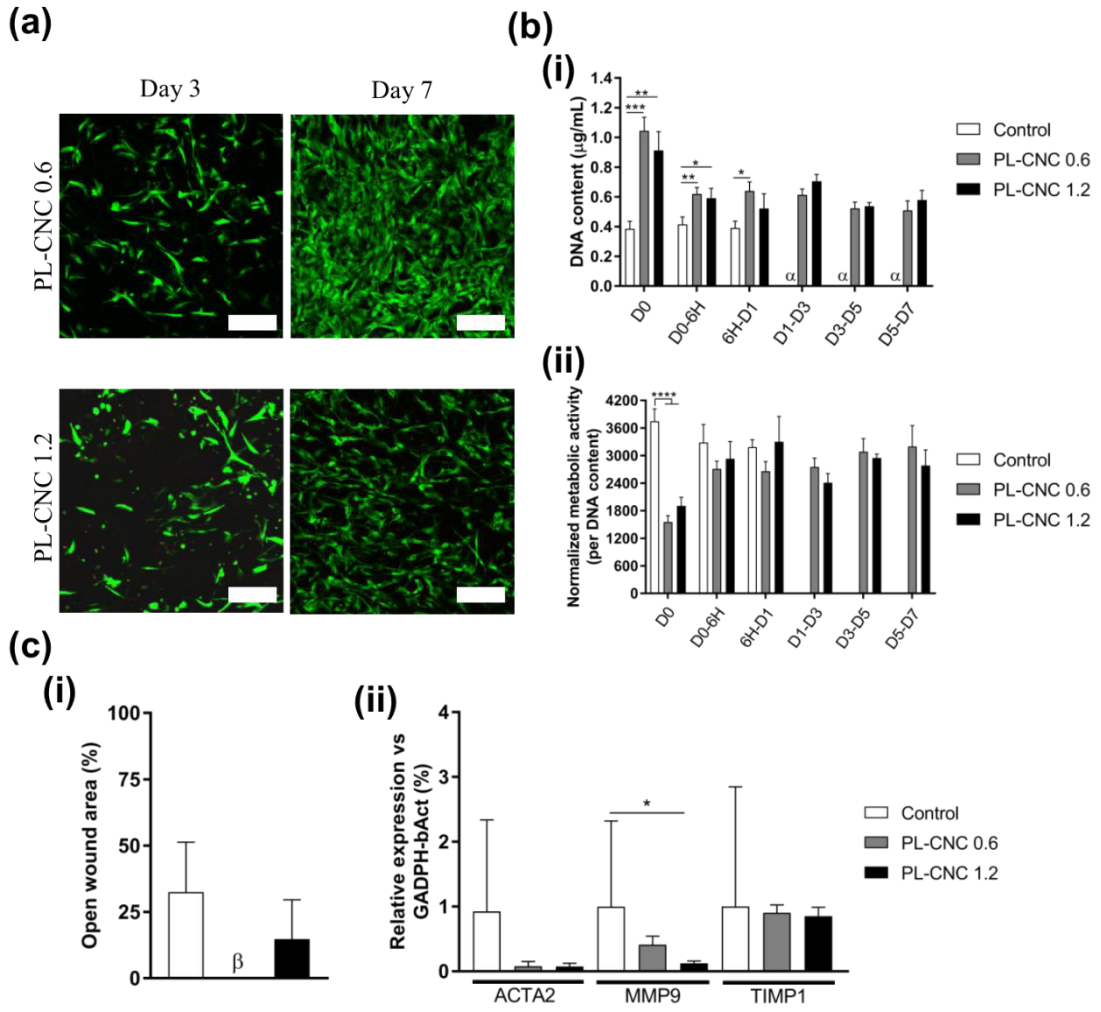

Figure IV-4 *In vitro* evaluation of cell supportive properties. (a) Live/Dead staining with Calcein AM and propidium iodide (green: live cells; red: dead cells) of hASCs seeded in PL-CNC cryogels after 3 and 7 days in culture. (b) DNA content (i) and metabolic activity fluorescence normalized by total DNA content (ii) of hASCs cultured with releasates of PL-CNC cryogel and gelatin sponge control (α - gelatin sponge group degraded after one day). (c) Wound healing photographs after 48 hours in culture (β - PL-CNC 0.6 formulation (n=3) showed an open wound area of 0%) (i) and gene expression of hASCs on the different formulations (ii). α-smooth muscle actin (ACTA2), matrix metalloproteinase 9 (MMP9) and tissue inhibitor matrix metalloproteinase 1 (TIMP1). Statistical significance: *, P < 0.1, **, P < 0.01 and ***, P < 0.001. Scale bar: 200 µm (a) and 250 µm (b).

The precise regulation of the wound healing response is determinant for the heathy new tissue formation [1, 61]. The process requires an adequate and controlled transition from repair to regeneration in order to avoid abnormal production of inflammatory mediators, fibrosis and ultimately promote tissue repair [58]. To evaluate the potential of our cryogels to modulate this response, the expression of α-smooth muscle actin (ACTA2), matrix metalloproteinase 9 (MMP9) and tissue inhibitor matrix metalloproteinase 1 (TIMP1) was evaluated. These makers were selected due to their importance on the degradation and turnover of the ECM that is tightly regulated by MMPs and their inhibitors (TIMPs) [62]. Moreover, ACTA2 marker is associated with myofibroblast differentiation and fibrogenic conditions [63]. The gene expression results revealed that PL-CNC cryogels groups showed a downregulation of scarring markers compared with gelatin group including ACTA2 and MMP9, and similar mRNA expression of TIMP1. Thus, the gene levels of the fibrosis-associated mediators ACTA2 and MMP9 decreased for hASCs cells and TIMP1 is maintained, which suggests a more-regenerative and less-scarring response.

IV-3.6. *In vivo* hemostatic performance

The hemostatic performance of PL-CNC cryogels and gelatin sponge was evaluated by bleeding time and hemorrhage volume until hemostasis was achieved (Figure IV-5). Liver exhibits an extremely abundant blood supply and it is susceptible to severe traumatic hemorrhaging, thus a defect in the rat lobe liver was induced [64], and then treated with the tested formulations (Figure IV-5AI and Supplementary Figure IV-3). The bleeding was controlled in 102.9 ± 31.2, 84.5 ± 58.9 and 113.6 ± 28.6 seconds after gelatin, PL-CNC 0.6 and PL-CNC 1.2 groups application, respectively (Figure IV-5AII). Until hemorrhage control, there was a blood loss of 115.8 ± 182.0 mg, 93.6 ± 38.9 mg and 65.6 ± 34.8 mg in gelatin, PL-CNC 0.6 and PL-CNC 1.2 groups, respectively (Figure IV-5AIII). Besides the non-statistically significant differences between the commercial gelatin sponge and the PL-CNC cryogels groups, the tested formulations demonstrated an excellent hemostatic effect with comparable or better outcomes than other previously proposed hemostatic agents, such as thrombin-receptor-agonist-peptide-immobilized onto starch/polyethylene glycol sponge (hemostatic time of 44 seconds and blood loss of 81 mg) [65], and quaternized chitosan-g-polyaniline-based hydrogel (blood loss of 214.7 mg) [24].

The formulations were successfully removed from the treated injuries without rebleeding and then the adsorbed blood cells and clotting factors were analyzed (Figure IV-5B). As previously observed in the *in vitro* hemocompatibility studies, a large number of RBC and platelets are rapidly recruited to the site of

injury and adhered to the material surface. It is worth noticing that a fibrin network was formed in all the three formulations, which clearly enhanced blood cells absorption, platelet aggregation and effectively controlled the *in vivo* hemorrhage. The hemostatic mechanism of PL-CNC cryogels is mainly mediated by two key material features. First, human-based nanocomposite cryogels contain an enriched milieu of platelet-derived clotting molecules that trigger platelet activation, and quickly induce blood cells adhesion, accumulation and agglomeration at the bleeding site. Moreover, PL-CNC cryogels showed a burst delivery of proteins (~70% of their initial protein content is released upon 5 minutes of incubation in an aqueous solution) containing relevant biological factors that play a significant role in antimicrobial activity and intracellular communications, thereby strengthening the blood clotting process [17]. Remarkably, cellulose-based products have been widely applied in post-traumatic bleedings, specifically non-regenerated oxidized cellulose (e.g., Oxycel®) or regenerated oxidized cellulose (e.g., Surgicel®) gauzes [66, 67]. In this study, by combining nanocellulose with PL-derived proteins, we are able to reproduce the strength of such materials to stop hemorrhage. Upon full cryogelation, minor CNC amounts showed to reinforce the low strength PL network, and then producing a stable 3D porous and interconnected structure that enables the entrapment of aggregated RBC and circulating platelets in a dense fibrin meshwork. Thus, the developed multicomponent material properties promote a rapid blood absorption rate, blood-concentrating effect and blood cells adhesion, which produce a fibrin clot and contribute to the excellent hemostasis capability of PL-CNC nanocomposite cryogels.

IV-3.7. *In vivo* host response

When hemostatic agents are applied in the injury site, they can leave residues in the wound that can induce a severe foreign-body reaction leading to inflammation or/and thrombus [7]. PL-CNC 0.6, PL-CNC 1.2 and commercial gelatin groups were subcutaneously implanted in rats for 7 and 14 days to evaluate their *in vivo* biological response (saline solution was used as control), namely cellular infiltration and degradation behavior (Figure IV-5C and D, and Supplementary Figure IV-4 and 5). At the end of the defined timepoints, the implanted conditions and surrounding tissue were excised for histologic evaluation (Figure IV-5C). After implantation for 1 week, gelatin sponges were completely absorbed, although its life-time was specified to be less than 4 weeks. Due to fast degradation, the *in vivo* response of gelatin sponge was comparable to the saline control group, thus only PL-CNC cryogels local biological effect was evaluated (Figure IV-5D). Histologic evaluation showed that both PL-CNC formulations induced inflammatory tissue reactions with different magnitudes. At day 7, the tissue reaction to the PL-CNC 0.6

formulation included a narrow band of fibrosis without fatty infiltrate (Figure IV-5DI), groups of 4-7 capillaries with supporting fibroblastic structures (Figure IV-5DII) and moderate necrosis (Figure IV-5III). In contrast, the formulation with the highest CNC content induced a tissue reaction involving a moderately thick band of fibrosis without fatty infiltrate (Figure IV-5DI), minimal vascularization of its implant beds (Figure IV-5DII) and a more severe necrosis (Figure IV-5DIII). After 14 days of implantation, both formulations showed a minimal local inflammatory response in the subcutaneous space (Figure IV-5D). Interestingly, both formulations showed a low fibrosis degree, and a very low number of foreign body giant cells and neutrophils, then the overall tissue inflammatory response was significantly diminished. Our findings are in agreement with previous studies showing that CNC exhibited a mild acute inflammatory response *in vivo* [68, 69]. Although the host response was the result of the normal material-induced inflammatory tissue reaction, the observed initial inflammatory response might also be potentially caused by human PL-derived proteins. In summary, these results indicated that PL-CNC cryogels could be used as biocompatible hemostatic agents for *in vivo* application.

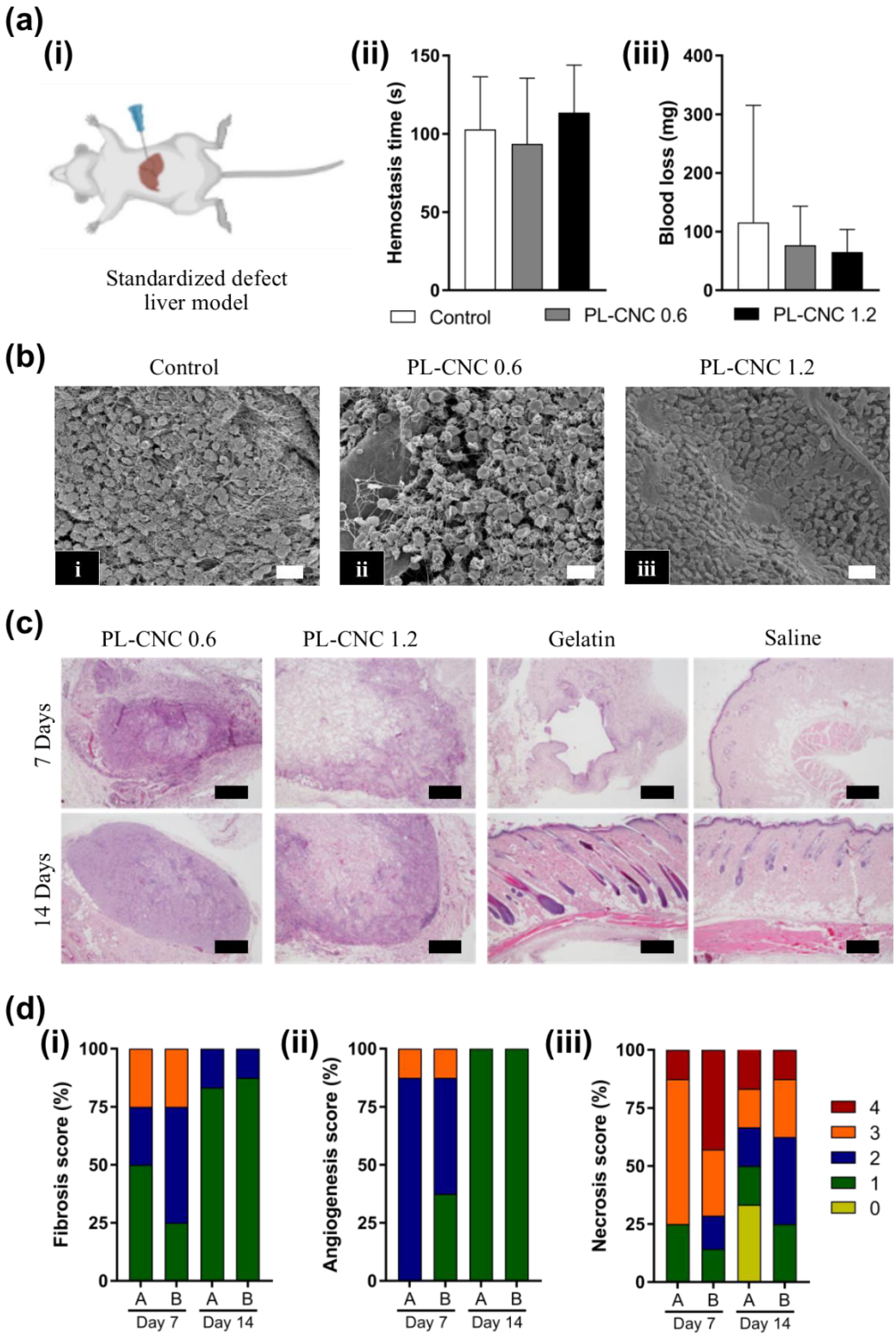

Figure IV-5 *In vivo* hemostatic capacity and host response evaluation of the cryogels compared to commercial gelatin hemostatic sponges and saline solution. (a) Scheme representation of the rat defect liver model (i), blood loss (ii) and hemostatic time (ii) in the standardized liver defect model. (b) SEM images of surface adhesion of blood cells at the bleeding site. (c) H&E staining results of PL-CNC 0.6 and PL-CNC 1.2 cryogels, gelatin sponge and saline solution on day 7 and 14. (d) Frequency distribution of the fibrosis (i), angiogenesis (ii) and necrosis (iii) score of PL-CNC 0.6 (A) and PL-CNC 1.2 (B) groups on day 7 and 14. Scale bar: 500 µm (b) and (c).

IV-4. CONCLUSION

The incorporation of rod-shaped CNC enabled the reinforcement of the low strength PL-based network, resulting in cryogels with improved mechanical properties and favoring PL-CNC cryogels blood uptake capability and handling. Interestingly, PL-CNC cryogels porosity and structural integrity together with the ability to deliver PL-derived bioactive molecules enabled cells adhesion, increased cells migration and proliferation, respectively. The hASCs behavior upon exposure to PL-CNC cryogels releasates indicated a likely more-regenerative and less-scarring response. In a standardized liver defect model, nanocomposite cryogels showed similar hemostatic performance compared to commercial products and a normal material-induced inflammatory tissue response *in vivo*. PL-CNC cryogels composed of small amounts of nanocellulose were not completely degraded *in vivo* due to the lack of cellulase enzymes in mammalians, but it can be incorporated in the formulations as a bioorthogonal strategy to modulate their degradation profiles. In summary, the proposed PL-CNC cryogels allow the use of PL not only as a source of signaling biological factors involved in wound healing, but also as a user-friendly off-the-shelf hemostatic biomaterial with potential to promote regenerative wound healing outcomes.

IV-5. SUPPLEMENTARY INFORMATION

IV-5.1. Supplementary materials and methods

IV-5.1.1. Anisotropic PL-CNC cryogels production

Double-barrel syringe L-system (1:1 from Medmix, Switzerland) with a static mixer tip (Medmix, Switzerland) was used to produce the cryogels. PL-CNC cryogels were prepared blending PL with a-CNC at 1:1 volume ratio. Barrel 1 was filled with PL and a-CNC aqueous dispersions (1.2 to 2.4 wt.%) were loaded in barrel 2. To create anisotropic structures, the previous solution was casted into square molds covered with a custom-made styrofoam mold all around except the bottom, where a brass plate at –80 °C was directly placed overnight. Then, the scaffolds were freeze-dried until full cryogelation. The final anisotropic cryogels were named according to their final a-CNC concentrations: 0 wt.% (PL-CNC 0), 0.6 wt.% (PL-CNC 0.6) and 1.2 wt.% (PL-CNC 1.2).

IV-5.1.2. Microstructure

Series of two-dimensional projections, with a resolution of 10 μm were acquired over a rotation range of 180°, at a rotation step of 0.45°, by cone-beam acquisition. The data was reconstructed using the software NRecon (Version: 1.6.6.0, Skyscan), and analyzed on CT analyzer (Version: 1.17.0.0, Skyscan). The region of interest (ROI) was defined as a 6 x 6 mm square centered over the specimen. By auto-interpolation the manually-defined ROI was yielded a representative 6 mm thick cobblestone-shaped volume of interest (VOI), which was the essential basis for the quantitative analyses. For the 3D morphological analysis, the Batman tool of CT analyzer software was used. The object was automatically defined (Ridler-Calvard method) to produce binarised projections, and the total porosity (Po.V (tot); vol. %), structure thickness (Tb.Th; μm), and pore size (Tb.Sp; μm) were calculated. The interconnectivity (InterConn) of the pores present in each sample was calculated according to Supplementary Equation IV-1.

$$\mathrm{InterConn} = 1 - \frac{\mathrm{TV.2px} - \mathrm{Obj.V.2px}}{\mathrm{TV} - \mathrm{Obj.V}}$$

Supplementary Equation IV-1 Quantification of interconnectivity of the pores present in each sample. TV.2px is the total VOI volume; Obj.V.2px is the object volume after shrink over holes with a diameter of 4 voxels (40 μm²), defined as the lower dimensions for an interconnective pore; TV is the total VOI volume, and Obj.V is the object volume. The 3D reconstructions were produced using the CTVOX software.

IV-5.1.3. Water uptake

Isotropic and anisotropic PL-CNC cryogels were weighted (M_i) and immersed in water 30 seconds. The samples were immediately weighed (M_f) and water uptake (mg/mg sample) was calculated using Supplementary Equation IV-2.

$$\text{Water uptake} = \frac{\text{Mf} - \text{Mi}}{\text{Mi}}$$

Supplementary Equation IV-2 Quantification of water uptake.

IV-5.1.4. Cell morphology

hASCs seeded in PL-CNC cryogels were cultured for up to 21 days. Cryogels were washed twice with PBS and then fixed in 10 vol.% formalin (Thermo Fisher Scientific, USA) for 15 min at RT and permeabilized using 0.2 vol.% Triton-X100 (Sigma-Aldrich, USA). After washing, the samples were incubated with 1:200 v/v rhodamine- conjugated phalloidin (Sigma-Aldrich, USA) for 30 minutes and 1:1000 v/v 4′,6-diamidino-2-phenylindole (DAPI, Sigma-Aldrich, USA) for 10 minutes (dilutions in PBS). PL-CNC cryogels formulations were washed twice with PBS and visualized using confocal microscope TCS SP8 (Leica Microsystems, Germany).

Supplementary Table IV-1 List of genes under evaluation, forward (F) and reverse (R) primers used in the gene expression analysis of hASCs.

Gene	*Sequence (5'-3')*
β-Actin	*F: CTGGAACGGTGAAGGTGACA*
	R: AAGGGACTTCCTGTAACAA
GAPDH	*F: GGGAGCCAAAAGGGTCATCA*
	R: GCATGGACTGTGGTCATGAGT
ACTA2	*F: AAAGCAAGTCCTCCAGCGTT*
	R: TTAGTCCCGGGGATAGGCAA
MMP9	*F: CTTTGAGTCCGGTGGACGAT*
	R: TCGCCAGTACTTCCCATCCT
TIMP1	*F: CATCCGGTTCGTCTACACCC*
	R: GGATAAACAGGGAAACACTGTGC

Abbreviations: Glyceraldehyde-3-phosphate dehydrogenase (GAPDH), α-smooth muscle actin (ACTA2), matrix metalloproteinase 9 (MMP9) and tissue inhibitor matrix metalloproteinase 1 (TIMP1).

IV-5.2. Supplementary results

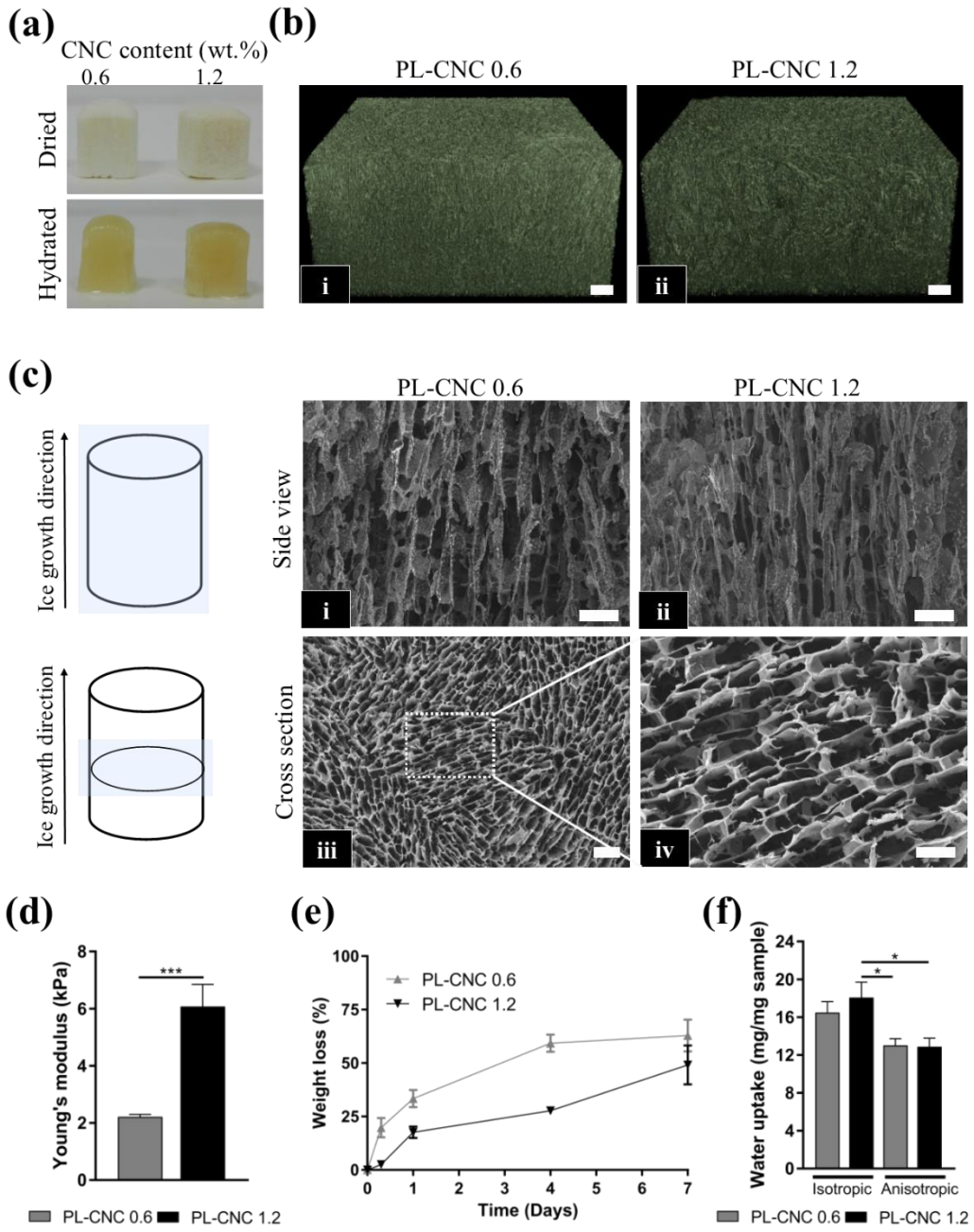

Supplementary Figure IV-1 Physical properties of the anisotropic cryogels. (a) Photographs of cryogels before and after immersion in PBS. Microstructure evaluation by (b) SEM and (c) μ-CT images of the cross-section of the cryogels in the Z-plane parallel to the ice-growth direction (c-i and ii) and XY-plane perpendicular to the ice-growth direction (c-iii and iv). (d) Young's modulus from the uniaxial compression stress–strain curves of the cryogels formulations. (e) Weigh loss of PL-CNC anisotropic cryogels over 7 days. (f) After 30 seconds immersed in water, water uptake was determined. Scale bar: 500 μm (b), 100 μm (c – ii) and 50 μm (c – i, ii and iv). Statistical significance: *, $P < 0.1$, ***, $P < 0.001$.

Supplementary Table IV-2 Analysis of μ-CT parameters and results of isotropic PL-CNC cryogels are presented as mean ± standard deviation.

	PL-CNC 0.6	PL-CNC 1.2
Porosity (vol.%)	87.63 ± 2.98	88.87 ± 1.48
Structure (trabecula) thickness (μm)	22.61 ± 10.30	18.3 ± 3.08
Structure separation (pore diameter) (μm)	112.30 ± 51.28	105.60 ± 13.17
Interconnectivity (%)	91.96 ± 5.69	96.88 ± 2.51

Supplementary Table IV-3 Analysis of anisotropic cryogels parameters and results of anisotropic PL-CNC cryogels are presented as mean.

	PL-CNC 0.6	PL-CNC 1.2
Porosity (vol.%)	70.93	75.43
Structure (trabecula) thickness (μm)	20.60	20.50
Structure separation (pore diameter) (μm)	33.37	39.38
Interconnectivity (%)	1.47	6.73

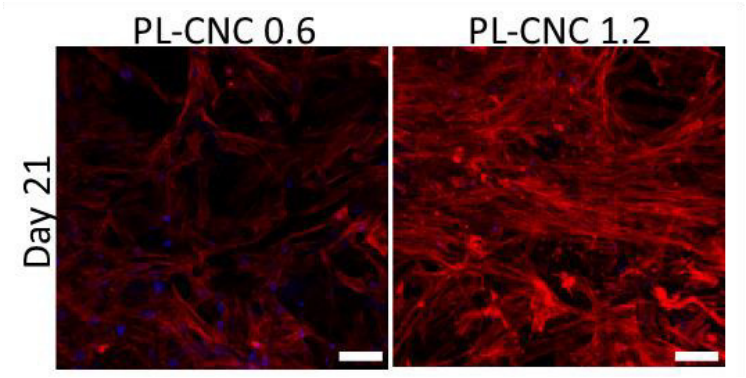

Supplementary Figure IV-2 Fluorescence microscopy images showing cytoskeleton organization in the cryogels formulations after 21 days in culture. Scale bar: 75 μm.

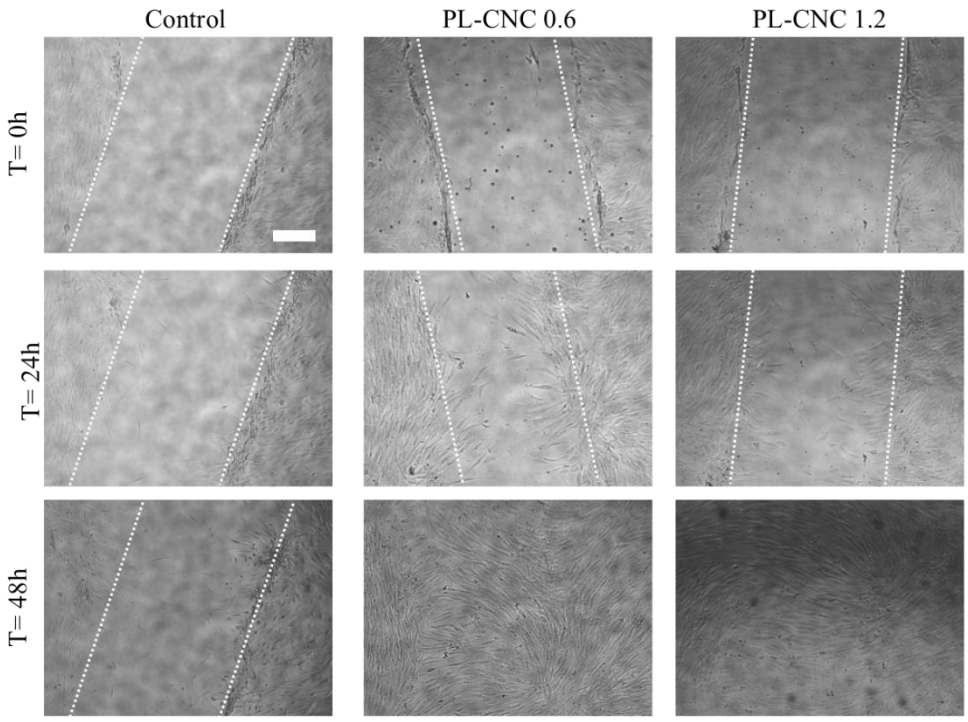

Supplementary Figure IV-3 Wound healing photographs after (a) PL-CNC 0.6, PL-CNC 1.2 and commercial gelatin control (b) and after 48 hours in culture. Scale bar: 75 µm.

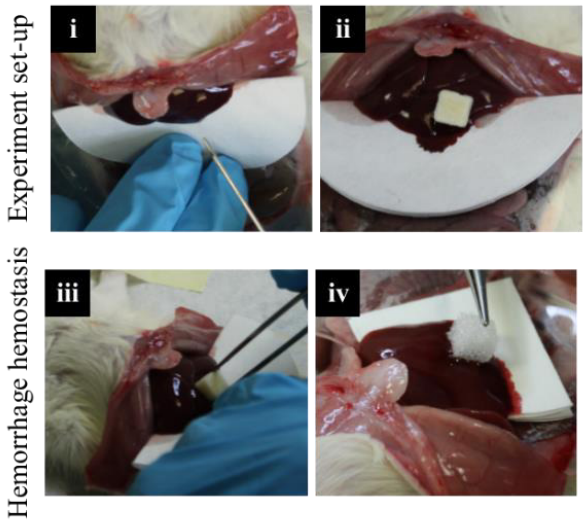

Supplementary Figure IV-4 *In vivo* hemostatic capacity of PL-CNC cryogels and commercial gelatin control. A standardized rat liver defect model was used by inducing a liver bleeding with a 18G needle (i). The formulations were applied in the hemorrhage (ii), namely PL-CNC cryogels (iii) and gelatin-based sponge (iv) until hemostasis was achieved.

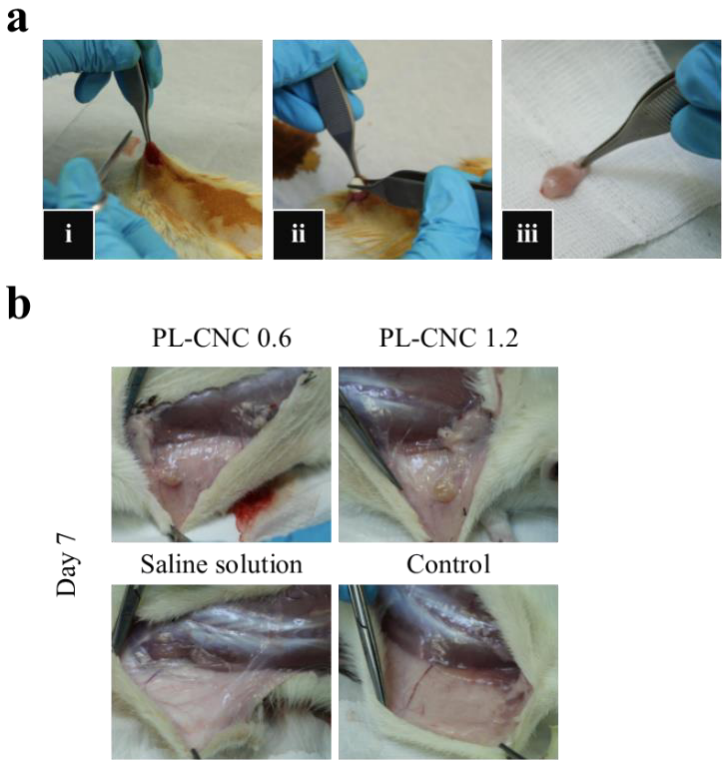

Supplementary Figure IV-5 In vivo subcutaneous assay procedure. (a) After the rat model was anesthetized (a-i), subcutaneous tissue was spread to create a pocket for formulations delivery (a-ii), that were removed after 7 (a-iiii and b) and 14 days.

IV-6. REFERENCES

[1] G.C. Gurtner, S. Werner, Y. Barrandon, et al., Wound repair and regeneration, Nature, 453 (2008) 314.

[2] S.A. Eming, P. Martin, M. Tomic-Canic, Wound repair and regeneration: mechanisms, signaling, and translation, Sci. Transl. Med., 6 (2014) 265sr6.

[3] M. Tomaiuolo, L.F. Brass, T.J. Stalker, Regulation of Platelet Activation and Coagulation and Its Role in Vascular Injury and Arterial Thrombosis, Interv. Cardiol. Clin., 6 (2017) 1.

[4] J.W. Weisel, R.I. Litvinov, Mechanisms of fibrin polymerization and clinical implications, Blood, 121 (2013) 1712.

[5] A. Sauaia, F.A. Moore, E.E. Moore, et al., Epidemiology of Trauma Deaths: A Reassessment, J. Trauma and Acute Care Surg., 38 (1995) 185.

[6] D.S. Kauvar, R. Lefering, C.E. Wade, Impact of hemorrhage on trauma outcome: an overview of epidemiology, clinical presentations, and therapeutic considerations, J. Trauma and Acute Care Surg., 60 (2006) S3.

[7] H. Khoshmohabat, S. Paydar, H.M. Kazemi, et al., Overview of Agents Used for Emergency Hemostasis, Trauma Mon., 21 (2016) e26023.

[8] C.A. Morrison, The prehospital treatment of the bleeding patient:Dare to dream, J. Surg. Res., 180 (2013) 246.

[9] J.J. Devlin, S. Kircher, B.G. Kozen, et al., Comparison of ChitoFlex®, CELOX™, and QuikClot® in Control of Hemorrhage, J. Emerg. Med., 41 (2011) 237.

[10] P. Rhee, C. Brown, M. Martin, et al., QuikClot Use in Trauma for Hemorrhage Control: Case Series of 103 Documented Uses, J. Trauma and Acute Care Surg., 64 (2008) 1093.

[11] R.F. Reiss, M.C. Oz, Autologous fibrin glue: Production and clinical use, Transfus. Med. Rev., 10 (1996) 85.

[12] A. Memic, T. Colombani, L.J. Eggermont, et al., Latest Advances in Cryogel Technology for Biomedical Applications, Adv. Ther., 2 (2019) 1800114.

[13] T.M.A. Henderson, K. Ladewig, D.N. Haylock, et al., Cryogels for biomedical applications, J. Mater. Chem. B, 1 (2013) 2682.

[14] X. Zhao, B. Guo, H. Wu, et al., Injectable antibacterial conductive nanocomposite cryogels with rapid shape recovery for noncompressible hemorrhage and wound healing, Nat. Commun., 9 (2018) 2784.

[15] V. Pavlovic, M. Ciric, V. Jovanovic, et al., Platelet Rich Plasma: a short overview of certain bioactive components, Open Med., 11 (2016) 242.

[16] S.G. Boswell, B.J. Cole, E.A. Sundman, et al., Platelet-Rich Plasma: A Milieu of Bioactive Factors, Arthroscopy, 28 (2012) 429.

[17] B.B. Mendes, M. Gómez-Florit, P.S. Babo, et al., Blood derivatives awaken in regenerative medicine strategies to modulate wound healing, Adv. Drug Deliv. Rev., 129 (2018) 376.

[18] U.D.S. Sekhon, A. Sen Gupta, Platelets and Platelet-Inspired Biomaterials Technologies in Wound Healing Applications, ACS Biomater. Sci. Eng., 4 (2018) 1176.

[19] R.M.A. Domingues, M.E. Gomes, R.L. Reis, The Potential of Cellulose Nanocrystals in Tissue Engineering Strategies, Biomacromolecules, 15 (2014) 2327.

[20] E.J. Foster, R.J. Moon, U.P. Agarwal, et al., Current characterization methods for cellulose nanomaterials, Chem. Soc. Rev., 47 (2018) 2609.

[21] B.B. Mendes, M. Gómez-Florit, R.A. Pires, et al., Human-based fibrillar nanocomposite hydrogels as bioinstructive matrices to tune stem cell behavior, Nanoscale, 10 (2018) 17388.

[22] D. Bondeson, A. Mathew, K. Oksman, Optimization of the isolation of nanocrystals from microcrystalline celluloseby acid hydrolysis, Cellulose, 13 (2006) 171.

[23] R.M.A. Domingues, M. Silva, P. Gershovich, et al., Development of Injectable Hyaluronic Acid/Cellulose Nanocrystals Bionanocomposite Hydrogels for Tissue Engineering Applications, Bioconjugate Chem., 26 (2015) 1571.

[24] X. Zhao, H. Wu, B. Guo, et al., Antibacterial anti-oxidant electroactive injectable hydrogel as self-healing wound dressing with hemostasis and adhesiveness for cutaneous wound healing, Biomaterials, 122 (2017) 34.

[25] Z. Chen, L. Han, C. Liu, et al., A rapid hemostatic sponge based on large, mesoporous silica nanoparticles and N-alkylated chitosan, Nanoscale, 10 (2018) 20234.

[26] F. Cheng, C. Liu, X. Wei, et al., Preparation and Characterization of 2,2,6,6-Tetramethylpiperidine-1-oxyl (TEMPO)-Oxidized Cellulose Nanocrystal/Alginate Biodegradable Composite Dressing for Hemostasis Applications, ACS Sustain. Chem. Eng., 5 (2017) 3819.

[27] P.P. Carvalho, X. Wu, G. Yu, et al., The effect of storage time on adipose-derived stem cell recovery from human lipoaspirates, Cells Tissues Organs, 194 (2011) 494.

[28] C.-C. Liang, A.Y. Park, J.-L. Guan, In vitro scratch assay: a convenient and inexpensive method for analysis of cell migration in vitro, Nat. Protoc., 2 (2007) 329.

[29] S.C. Taylor, K. Nadeau, M. Abbasi, et al., The Ultimate qPCR Experiment: Producing Publication Quality, Reproducible Data the First Time, Trends Biotechnol., 37 (2019) 761.

[30] S. Viau, A. Lagrange, L. Chabrand, et al., A highly standardized and characterized human platelet lysate for efficient and reproducible expansion of human bone marrow mesenchymal stromal cells, Cytotherapy, 21 (2019) 738.

[31] J. Wu, Q. Zhao, J. Sun, et al., Preparation of poly(ethylene glycol) aligned porous cryogels using a unidirectional freezing technique, Soft Matter, 8 (2012) 3620.

[32] V.I. Lozinsky, I.Y. Galaev, F.M. Plieva, et al., Polymeric cryogels as promising materials of biotechnological interest, Trends Biotechnol., 21 (2003) 445.

[33] M. Chau, K.J. De France, B. Kopera, et al., Composite Hydrogels with Tunable Anisotropic Morphologies and Mechanical Properties, Chem. Mater., 28 (2016) 3406.

[34] P. Munier, K. Gordeyeva, L. Bergström, et al., Directional Freezing of Nanocellulose Dispersions Aligns the Rod-Like Particles and Produces Low-Density and Robust Particle Networks, Biomacromolecules, 17 (2016) 1875.

[35] B. Yetiskin, O. Okay, High-strength silk fibroin scaffolds with anisotropic mechanical properties, Polymer, 112 (2017) 61.

[36] R. Dash, M. Foston, A.J. Ragauskas, Improving the mechanical and thermal properties of gelatin hydrogels cross-linked by cellulose nanowhiskers, Carbohydr. Polym., 91 (2013) 638.

[37] S.A. Bencherif, R. Warren Sands, O.A. Ali, et al., Injectable cryogel-based whole-cell cancer vaccines, Nat. Commun., 6 (2015) 7556.

[38] J. Hoque, R.G. Prakash, K. Paramanandham, et al., Biocompatible Injectable Hydrogel with Potent Wound Healing and Antibacterial Properties, Mol. Pharm., 14 (2017) 1218.

[39] S. Sorrentino, J.-D. Studt, O. Medalia, et al., Roll, adhere, spread and contract: Structural mechanics of platelet function, Eur. J. Cell Biol., 94 (2015) 129.

[40] R. Flaumenhaft, Chapter 18 - Platelet Secretion, in: A.D. Michelson (Ed.) Platelets (Third Edition), Academic Press, 2013, pp. 343.

[41] D.J. Neveleff, Optimizing Hemostatic Practices: Matching the Appropriate Hemostat to the Clinical Situation, AORN J., 96 (2012) S1.

[42] T. Arakawa, S.J. Prestrelski, W.C. Kenney, et al., Factors affecting short-term and long-term stabilities of proteins, Adv. Drug Deliv. Rev., 46 (2001) 307.

[43] S.C. Notodihardjo, N. Morimoto, N. Kakudo, et al., Comparison of the efficacy of cryopreserved human platelet lysate and refrigerated lyophilized human platelet lysate for wound healing, Regen. Ther., 10 (2019) 1.

[44] A. Muraglia, C. Ottonello, R. Spanò, et al., Biological activity of a standardized freeze-dried platelet derivative to be used as cell culture medium supplement, Platelets, 25 (2014) 211.

[45] M. Mori, S. Rossi, F. Ferrari, et al., Sponge-Like Dressings Based on the Association of Chitosan and Sericin for the Treatment of Chronic Skin Ulcers. II. Loading of the Hemoderivative Platelet Lysate, J. Pharm. Sci., 105 (2016) 1188.

[46] P.S. Babo, V.E. Santo, M.E. Gomes, et al., Development of an Injectable Calcium Phosphate/Hyaluronic Acid Microparticles System for Platelet Lysate Sustained Delivery Aiming Bone Regeneration, Macromol. Biosci., 16 (2016) 1662.

[47] D.Y. Arifin, L.Y. Lee, C.-H. Wang, Mathematical modeling and simulation of drug release from microspheres: Implications to drug delivery systems, Adv. Drug Deliv. Rev., 58 (2006) 1274.

[48] M.R. Yeaman, Platelets in defense against bacterial pathogens, Cell Mol. Life Sci., 67 (2010) 525.

[49] Y.-Q. Tang, M.R. Yeaman, M.E. Selsted, Antimicrobial peptides from human platelets, Infect. Immun., 70 (2002) 6524.

[50] P.Y. Chung, R. Khanum, Antimicrobial peptides as potential anti-biofilm agents against multidrug-resistant bacteria, J. Microbiol. Immunol. Infect., 50 (2017) 405.

[51] R. Costa-Almeida, A.R. Franco, T. Pesqueira, et al., The effects of platelet lysate patches on the activity of tendon-derived cells, Acta Biomater., 68 (2018) 29.

[52] B.M. Pereira, J.B. Bortoto, G.P. Fraga, Agentes hemostáticos tópicos em cirurgia: revisão e perspectivas, Rev. Col. Bras. Cir., 45 (2018).

[53] D.J. Schaer, P.W. Buehler, A.I. Alayash, et al., Hemolysis and free hemoglobin revisited: exploring hemoglobin and hemin scavengers as a novel class of therapeutic proteins, Blood, 121 (2013) 1276.

[54] C. Wagner, P. Steffen, S. Svetina, Aggregation of red blood cells: From rouleaux to clot formation, C. R. Phys., 14 (2013) 459.

[55] M. Bessis, Red Cell Shapes. An Illustrated Classification and its Rationale, in: M. Bessis, R.I. Weed, P.F. Leblond (Eds.) First Red Cell Shapes. An Illustrated Classification and its Rationale, Springer Berlin Heidelberg, Berlin, Heidelberg, 1973, pp. 1.

[56] S.-H. Yun, E.-H. Sim, R.-Y. Goh, et al., Platelet Activation: The Mechanisms and Potential Biomarkers, Biomed. Res. Int., (2016) 9060143.

[57] F. Lai, N. Kakudo, N. Morimoto, et al., Platelet-rich plasma enhances the proliferation of human adipose stem cells through multiple signaling pathways, Stem Cell Res. Ther., 9 (2018) 107.

[58] H. Xia, X. Li, W. Gao, et al., Tissue repair and regeneration with endogenous stem cells, Nat. Rev. Mater., 3 (2018) 174.

[59] E. Ranzato, L. Mazzucco, M. Patrone, et al., Platelet lysate promotes in vitro wound scratch closure of human dermal fibroblasts: different roles of cell calcium, P38, ERK and PI3K/AKT, J. Cell. Mol. Med., 13 (2009) 2030.

[60] S. Massberg, I. Konrad, K. Schürzinger, et al., Platelets secrete stromal cell-derived factor 1alpha and recruit bone marrow-derived progenitor cells to arterial thrombi in vivo, J. Exp. Med., 203 (2006) 1221.

[61] S.J. Forbes, N. Rosenthal, Preparing the ground for tissue regeneration: from mechanism to therapy, Nat. Med., 20 (2014) 857.

[62] S. O'Sullivan, J.F. Gilmer, C. Medina, Matrix metalloproteinases in inflammatory bowel disease: an update, Mediators Inflamm., 2015 (2015) 964131.

[63] B. Hinz, S.H. Phan, V.J. Thannickal, et al., The myofibroblast: one function, multiple origins, Am. J. Pathol., 170 (2007) 1807.

[64] N. Ahmed, J.J. Vernick, Management of liver trauma in adults, J. Emerg. Trauma Shock, 4 (2011) 114.

[65] X. Yang, W. Liu, Y. Shi, et al., Peptide-immobilized starch/PEG sponge with rapid shape recovery and dual-function for both uncontrolled and noncompressible hemorrhage, Acta Biomater., 99 (2019) 220.

[66] K.M. Lewis, D. Spazierer, M.D. Urban, et al., Comparison of regenerated and non-regenerated oxidized cellulose hemostatic agents, Eur. Surg., 45 (2013) 213.

[67] X. Yang, W. Liu, N. Li, et al., Design and development of polysaccharide hemostatic materials and their hemostatic mechanism, Biomater. Sci., 5 (2017) 2357.

[68] K.J. De France, M. Badv, J. Dorogin, et al., Tissue Response and Biodistribution of Injectable Cellulose Nanocrystal Composite Hydrogels, ACS Biomater. Sci. Eng., (2019).

[69] M. Roman, Toxicity of Cellulose Nanocrystals: A Review, Ind. Biotechnol., 11 (2015) 25.

Chapter V

Cellulose nanocrystals of variable sulfation degree can sequester specific platelet lysate-derived biomolecules to modulate stem cells response

Chapter V

Cellulose nanocrystals of variable sulfation degree can sequester specific platelet lysate-derived biomolecules to modulate stem cells response

ABSTRACT

The surface chemistry of cellulose nanocrystals was engineered to show variable sulfation degree, which was exploited to modulate platelet lysate-derived biomolecules sequestration and presentation. The protein coronas developed on CNC surface were characterized and it was demonstrated how it promotes different signaling effects on human adipose-derived stem cells behavior.

This chapter is based on the following publication: *B. B Mendes, M. Gómez-Florit, H. Osório, A. Vilaça, R. M. A. Domingues, R. L. Reis, M. E. Gomes. Cellulose nanocrystals of variable sulfation degree can sequester specific platelet lysate-derived biomolecules to modulate stem cells response. 2020. Chemical Communications. DOI: 10.1039/D0CC01850C.*

V-1. INTRODUCTION

Cellullose nanocrystals (CNC) have been increasingly used for multiple tissue engineering (TE) applications due to their outstanding mechanical properties, easy surface functionalization, complex rheological behavior and minimal toxicity [1]. A representative example of these strategies is our recently developed injectable platelet lysate (PL) based hydrogels reinforced with CNC [2]. In this nanocomposite biomaterial, was used as an inexpensive human-based source of supra-physiological doses of multiple signaling molecules known to modulate different cell functions, including adhesion, proliferation and differentiation [3]. It was demonstrated that the increase of CNC content had a positive impact on the biomaterial cell supportive potential due to the improvement of their physical properties. It was also suggested that these positive effects may be correlated with the possible sequestration and solid phase presentation of PL signaling proteins anchored onto CNC's surface, emulating a biomimetic mechanism, which is increasingly recognized to increase the half-life and boost the bioactivity of signaling molecules such as growth factors (GFs). However, the nature and extent of these CNC-PL protein interactions and how it can be leveraged to guide cell fate has not been demonstrated.

It is well known that upon introduction in the complex biological fluid (e.g., human blood plasma contains more than 3700 proteins), nanomaterials are rapidly covered by a layer of proteins know as protein corona [4, 5]. Conceptually, an initial corona is typically formed from the highly abundant proteins, consisting of a more loosely associated and rapidly exchanging layer of biomolecules (called the 'soft' corona) [4-6]. Those biomacromolecules are in rapid exchange with the biological environment, being displaced over time from the nanomaterial surface by proteins with higher binding affinity and slower exchange rate (called the 'hard' corona) [4-6]. In an *in vivo* scenario, nanomaterials interact with thousands of different types of proteins that defines their lifetime, physicochemical properties (e.g., protein conformation, hydrodynamic size, surface charge), and subsequently their biological identity (e.g., cytotoxicity, biodistribution, and endocytosis into specific cells) [7].

The surface chemistry of nanomaterials is among the most determinant factors on the amount and composition of the hard corona [7]. Tuning the protein corona by tailoring the chemical composition of nanoparticles has been widely explored in nanomedicine to adjust their functionality as e.g. drug carriers or abiotic protein affinity reagents [8, 9]. Remarkably, it has been demonstrated that the more abundantly associated proteins are not necessarily responsible for the most significative effect at cell-nanomaterial interfaces, since a less abundant protein with high specificity for a particular receptor could trigger a crucial biological process [5, 7]. Therefore, our hypothesis is that by modulating the surface chemistry of

CNC to recruit specific signaling biomolecules from PL to the nanoparticles surface, it would be possible to tune the composition of their protein corona. In the development of PL-CNC biomaterials, this strategy would provide a new tool to define the biological identity of cells microenvironment and thus control their fate in TE strategies based on this xeno-free cell matrix.

The most typical production method of CNC, which was also adopted in this study, is based on sulfuric acid hydrolysis [10, 11]. During this process, CNC are simultaneously grafted with anionic sulfate ester groups on their surface, which are responsible for their colloidal stability in aqueous solutions. Interestingly, in mammalian tissues, protein binding by membrane or extracellular matrix sulfated glycosaminoglycans (GAGs), such as heparin and heparan sulfate, is known to play key roles in potentiating protein cell signaling and in protecting them from proteolytic degradation [12]. This GAG mediated presentation and stabilization of a wide range of proteins (e.g., GFs, adhesion proteins, chemokines) is dominated by electrostatic interactions but also includes the contribution of hydrogen-bonding, van der Waal, and hydrophobic interactions [13-15]. Numerous functional GAGs mimetic biomaterials have been developed, including supramolecular nanostructures displaying on their surfaces different sulfated monosaccharide motifs, which could regulate GFs bioactivity *in vitro* and *in vivo* in a sulfation pattern dependent manner [16]. Inspired on these functional nanostructures as GAGs analogs, in this work we produced CNC with variable sulfation degrees in the surface glucose units to modulate the sequestering of PL-derived proteins (Squeme V-1).

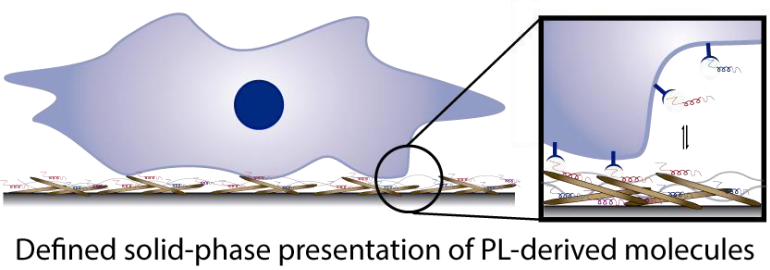

Scheme V-1 Schematic representation of the defined solid-phase presentation of PL-derived molecules. CNC can bind different patterns of PL-derived protein in a surface sulfation dependent manner. Thus, this bioinstructive platform were explored to direct stem cell fate by solid-phase presentation of defined protein coronas.

V-2. MATERIALS AND METHODS

V-2.1. Precursors preparation

V-2.1.1. Preparation of PL

Platelet concentrate collections, obtained from volunteer donation from healthy donors as by 2005/62/CE, were performed at *Serviço de Imuno-Hemoterapia – Centro Hospitalar de São João* (Portugal) provided under an approved institutional board protocol (ethical commission of CHSJ/FMUP approved at 18/13/2018). Platelet batches are obtained from a pool of donors of platelet concentrates from whole blood differential centrifugations or platelet apheresis [3, 17-19]. Then, PL was prepared in-house from a pool of twelve platelet concentrates that were subjected to three temperature cycles (-196 °C and 37 °C), and stored at -80 °C. Just before use, PL was thawed at RT, centrifuged at 4000 x g for 5 minutes and filtered through a 0.45 µm pore filter to remove any cell debris or clots.

V-2.1.2. Preparation of CNC of variable surface sulfation degrees

CNC were extracted from microcrystalline cellulose (MCC) powder (Sigma-Aldrich, USA) by sulfuric acid hydrolysis according to Bondeson with minor modifications [10]. In brief, 42 g of MCC was mixed with 189 mL of deionized water (DI). DI/MCC suspension was then put in an ice bath and stirred using a mechanical agitator (500 rpm) for 10 minutes. 188.3 mL of concentrated sulfuric acid (95–98% from Sigma-Aldrich, USA) was added dropwise up to a final concentration of 64 wt.%. The suspension was heated to 44 °C while stirring at 500 rpm for 120 min. The reaction was stopped by diluting the suspension with cold water (5x) and left to decant at 4 °C. The supernatant was discarded, and the remaining suspension was centrifuged for 10 minutes at 9000 rpm and 5 °C. The supernatant was successively replaced with DI water and the suspension subjected to centrifugation cycles until the supernatant became turbid. The resulting suspension was collected and extensively dialyzed using cellulose dialysis membrane MWCO: 12-14 kDa (Sigma-Aldrich, USA) against DI water until neutral pH. After dialysis the content was sonicated three times (VCX-130PB-220, Sonics) for 10 minutes using an ultrasound probe at 60% of amplitude output, under ice cooling to prevent overheating. The cloudy

suspension was centrifuged one last time to remove big particulates and the final supernatant containing the CNC (high -SO_3H content, High) was stored at 4 °C until further use.

V-2.1.3. Preparation of CNC of variable surface sulfation degrees

Custom-made stainless steel autoclaves of height 12 cm and diameter 6 cm (Neves & Neves Metalomecânica, Portugal) were used during hydrothermal treatment of aqueous CNC suspensions. Briefly, an aqueous suspension of CNC (90 mL, 1 wt. %) was added to a glass flask, while the autoclave was sealed and heated to 120 °C for 30 min. Then, the glass flask was placed inside the autoclave for 3 h (medium -SO_3H content, Medium) or 6 h (low -SO_3H content, Low) at 120 °C in a self-pressurizing environment. After cooling the autoclave to RT for 1 hour, the resulting CNC suspension was collected and extensively dialyzed using cellulose dialysis membrane MWCO: 12-14 kDa (Sigma-Aldrich, USA) against DI water until neutral pH to remove the sulfuric acid product from CNC solution. The final suspension was stored at 4 °C until further characterization was performed.

V-2.1.4. Preparation of a-CNC

Vicinal hydroxyl groups on CNC's surface were converted to carbonyls by adding sodium periodate ($NaIO_4$) in a 1:1 molar ratio for 12 hours [20]. In a typical experiment, $NaIO_4$ (Sigma-Aldrich, USA) was added to CNC aqueous suspension (1 wt.%) in a 1:1 molar ratio ($NaIO_4$:CNC). The mixture was allowed to stir at RT for 12 hours preventing from light exposure. Unreacted periodate was quenched by the addition of excess of ethylene glycol (Sigma-Aldrich, USA). The mixture was transferred into a dialysis membrane (cellulose dialysis membrane MWCO: 12-14 kDa) and dialyzed against DI water for 3 days with regular water replacement. The final working suspension of modified CNC was collected and stored at 4 °C.

V-2.2. Precursors characterization

V-2.2.1. Morphological characterization of CNC

CNC morphology was analyzed by Atomic Force Microscopy (AFM). One drop of each diluted solution of 0.0015 wt. % CNC in DI water was dropped on freshly cleaved mica discs (9.9 mm diam. and 0.27 thick). The suspension was left to adsorb for 15 min and the excess liquid was removed. The disc was washed two times with ultrapure water (Milli-Q, 18.2 M Ω.cm^{-1}) to remove particles excess and allowed to dry overnight at RT. The samples were imaged in tapping mode with a MultiMode atomic force microscopy (AFM, Bruker, USA). The obtained images were treated and analyzed using Gwyddion software (version 2.53) to measure the length and height of CNC formulations. At least 50 particles were randomly selected from different AFM images.

V-2.2.2. Quantification of CNC sulfation degree

The CNC sulfate content was determined following the ion-exchange resin treatment and conductometric titration of CNC according to Beck, S. et al. [21] Dowex marathon C hydrogen from strong acid action exchange resin (Sigma-Aldrich, USA) that fully protonates CNC sulfate half-ester groups was immersed in ultrapure water for 30 min and poured into glass Econo-Column® chromatography columns (2.5 × 30 cm, Bio-Rad Laboratories, USA) with a porous polymer bed support at the bottom. CNC suspensions (100 mL, 0.5 wt.%) was fed from the top of the column at 3-4 mL.min^{-1}, and the initial 1-2 bed volumes were discarded to avoid excessive sample dilution. The resin-to-CNC mass ratios was approximately 20.8 (0.5 g of CNC to 10.4 g of resin). Then, sulfate half-ester content was determined via conductometric titration. Briefly, 113 mg of resin-treated CNC and 0.0117g (1 mM NaCl aqueous solution) were dispersed in a final volume of 200 mL of ultrapure water. Samples were treated with 10 mM NaOH (Sigma-Aldrich, USA) added in 0.1 mL increments. Titration conductivity values were corrected for dilution effects and sulfate half-ester groups content (mmol.kg^{-1} CNC) was calculated using Equation V-1.

$$R - OSO_3H = \frac{V_{NaOH}\, C_{NaOH}}{m_{CNC}}$$

Equation V-1 Quantification of the sulfate half-ester content. Where V_{NaOH} (mL) is the inset equivalence point determined from conductometric titration curve, C_{NaOH} (mol. L^{-1}) is the concentration of titration used and m_{cnc} (g) is the mass of the CNC suspension.

V-2.2.3. Surface charge

Zeta potential of the different a-CNC formulations at concentration of 1 mg. mL^{-1} in water was determined (n=3) using a zetasizer (Nano ZS, Malvern Instruments)

V-2.3. Protein corona characterization

V-2.3.1. Incubation of CNC with PL-derived proteins

Prior to corona preparation, a-CNC solutions (High, Medium and Low) were diluted with ultrapure water to a final concentration of 2 mg. mL^{-1}. Afterwards, 1900 µL of CNC dispersions (containing 3.8 mg of CNC) were incubated with 1900 µL PL solution (containing 128.44 mg of total protein content) for 90 min at 37 °C under constant agitation (200 rpm) for a final CNC concentration of 1 mg. mL^{-1}. CNC were separated from the supernatant by centrifugation at 15000 × g for 30 min. The particle pellet was resuspended in phosphate-buffered saline (PBS) and washed by three centrifugation steps at 15000 × g for 30 min, and subsequently re-dispersed in 60 µL of ultrapure water and freeze until further analysis. The proteins adsorbed on CNC surface after the first centrifugation are called as 'soft' corona, whereas CNC-PL complexes that were successively washed to remove the unbound or loosely bound proteins ('soft' corona) are called as 'hard' corona.

V-2.3.2. Sodium dodecyl sulphate polyacrylic gel electrophoresis

20 µl of non-reducing sodium dodecyl sulphate (SDS) sample buffer, which was prepared using 4% w/v SDS, 20% v/v glycerol, 10% w/v 2-mercaptoethanol, 0.05% w/v bromophenol blue, 125 mM TRIS-HCl to pH 6.8, was added to the 'soft' and 'hard' corona PL-CNC complexes. Pellet was dispersed

by vortexing and heating for 5 min at 95 °C. PL-protein complexes were thus shattered, and CNC were removed by centrifugation at 12300 × g for 15 min. Aliquots of adsorbed proteins (10 µL) were loaded on SDS-polyacrylamide gel using 3 vol.% stacking and 12.5 vol.% separation polyacrylamide gels prepared according to manufacturer's protocol (SDS Gel Preparation kit, Sigma Aldrich, USA) in SDS running buffer (0.1 % w/v SDS, 25 mM TRIS base, 192 mM glycine). Electrophoresis was carried out at 75 V for 15 min and then at 150 V for 1 h (BioRad, USA). After electrophoresis, the gels were stained with Coomassie Brilliant blue staining (1 g Commassie Brillant Blue, 500 mL methanol, 100 mL glacial acetic acid in 1 L of DI water) for 1 h, de-stain I solution (80 mL methanol, 20 mL acetic acid in 200 mL of DI water) for 45 min and then de-stain II solution (12.5 mL methanol, 17.5 mL acetic acid in 220 mL of DI water) for 45 min. The molecular weight of PL-CNC proteins complexes was calculated by analyzing their area using FIJI software gel analysis tools [22].

V-2.3.3. Mass spectrometry

Proteins were solubilized with 100 mM Tris pH 8.5, 1% sodium deoxycholate, 10 mM tris(2-carboxyethyl)phosphine (TCEP), 40 mM chloroacetamide and protease inhibitors for 10 minutes at 95°C at 1000 rpm (Thermomixer, Eppendorf). Each sample was processed for proteomics analysis following the solid-phase-enhanced sample-preparation (SP3) protocol as described in PMID30464214. Enzymatic digestion was performed with Trypsin/LysC (2 micrograms) overnight at 37°C at 1000 rpm.

Protein identification and quantitation was performed by nanoLC-MS/MS. This equipment is composed by an Ultimate 3000 liquid chromatography system coupled to a Q-Exactive Hybrid Quadrupole-Orbitrap mass spectrometer (Thermo Scientific, Bremen, Germany). Samples were loaded onto a trapping cartridge (Acclaim PepMap C18 100Å, 5 mm x 300 µm i.d., 160454, Thermo Scientific) in a mobile phase of 2% ACN, 0.1% FA at 10 µL/min. After 3 min loading, the trap column was switched in-line to a 50 cm by 75µm inner diameter EASY-Spray column (ES803, PepMap RSLC, C18, 2 µm, Thermo Scientific, Bremen, Germany) at 250 nL/min. Separation was generated by mixing A: 0.1% FA, and B: 80% ACN, with the following gradient: 5 min (2.5% B to 10% B), 120 min (10% B to 30% B), 20 min (30% B to 50% B), 5 min (50% B to 99% B) and 10 min (hold 99% B). Subsequently, the column was equilibrated with 2.5% B for 17 min. Data acquisition was controlled by Xcalibur 4.0 and Tune 2.9 software (Thermo Scientific, Bremen, Germany).

The mass spectrometer was operated in data-dependent (dd) positive acquisition mode alternating between a full scan (*m/z* 380-1580) and subsequent HCD MS/MS of the 10 most intense peaks from full scan (normalized collision energy of 27%). ESI spray voltage was 1.9 kV. Global settings: use lock masses best (*m/z* 445.12003), lock mass injection Full MS, chrom. peak width (FWHM) 15s. Full scan settings: 70k resolution (*m/z* 200), AGC target 3e6, maximum injection time 120 ms. dd settings: minimum AGC target 8e3, intensity threshold 7.3e4, charge exclusion: unassigned, 1, 8, >8, peptide match preferred, exclude isotopes on, dynamic exclusion 45s. MS2 settings: microscans 1, resolution 35k (*m/z* 200), AGC target 2e5, maximum injection time 110 ms, isolation window 2.0 *m/z*, isolation offset 0.0 m/z, spectrum data type profile.

The raw data was processed using Proteome Discoverer 2.4.0.305 software (Thermo Scientific) and searched against the UniProt database for the *Homo sapiens* Proteome 2019_09 and NIST Human Orbitrap HCD Spectral Library. The Sequest HT search engine was used to identify tryptic peptides. The ion mass tolerance was 10 ppm for precursor ions and 0.02 Da for fragment ions. Maximum allowed missing cleavage sites was set 2. Cysteine carbamidomethylation was defined as constant modification. Methionine oxidation and protein N-terminus acetylation were defined as variable modifications. Peptide confidence was set to high. The processing node Percolator was enabled with the following settings: maximum delta Cn 0.05; decoy database search target FDR 1%, validation based on q-value. Protein label free quantitation was performed with the Minora feature detector node at the processing step. Precursor ions quantification was performing at the processing step with the following parameters: unique plus razor peptides were considered, precursor abundance was based on intensity, normalization mode was based on total peptide amount, pairwise protein ratio calculation, hypothesis test was based on t-test (background based).

UniProt entries were converted to gene name using the UniProt tool (https://www.uniprot.org/uploadlists/). The common or exclusively identified proteins were analyzed using the Venny tool (https://bioinfogp.cnb.csic.es/tools/venny/, version 2.1.0). Proteins have been grouped with regard to the biological process involved using the categories of the Panther Biological process (http://www.pantherdb.org/, version 15.0). The relative abundance of the 30 main components and selected signaling molecules were classified as Panther protein class and heat maps were done using the GraphPad PRISM v 7.0. Average presence was set to 100 (white) and red color denotes counts higher

and blue denotes lower than groups average. Finally, the isoelectric point (*pI*) of the 30 main components of CNC formulations was estimated using Isoelectric Point Calculator [23].

V-2.4. *In vitro* cell culture studies

V-2.4.1. CNC film coating preparation

Circular glass coverslips of 13 mm diameter and 1 mm thickness (Agar Scientific, UK) were first cleaned in 5:1:1 solution of H_2O:NH_3:H_2O_2 at 75 °C for 5 minutes, washed with ultrapure water, dried gently with nitrogen and finally UV/ozone treated (Vilber-lourmat, France) for 10 min. Then, 200 µL of polyethyleneimine (PEI, Sigma-Aldrich, USA, high molecular weight and branched, 20 mM in 0.5 M KCl) was spin coated (Laurell technologies, USA) for 30 s at 2000 rpm to confer a positive charge, and subsequently washed two times with ultrapure water at 500 rpm for 10 s. Afterwards, the samples were dried gently under a steady nitrogen stream, followed by adsorption of the CNC suspensions (200 µL, 1 wt. %) at stationary state for 10 s, and then at 2000 rpm for 30 s. The so-coated CNC samples were dried overnight at 60 °C, washed two times with ultrapure water to desorb loosely bound species. AFM images were obtained in tapping mode with a MultiMode AFM (Bruker, USA), and the data analysis was performed using the freeware Gwyddion 2.26. For cells experiment, the coverslips samples were rinsed with ethanol and dried in a laminar flow with sterile air.

V-2.4.2. Incubation with relevant bioactive molecules

The CNC coated coverslips were incubated with PL for 1 hour at 37 °C under constant agitation (200 rpm), and subsequently washed three times with sterile PBS.

V-2.4.3. Cell isolation and expansion

Human adipose-derived stem cells (hASCs) were obtained from lipoaspirate samples of the abdominal region of patients undergoing plastic surgery under the scope of an established protocol with Hospital da Prelada (Porto, Portugal), and with the approval of the Hospital and University of Minho Ethics Committee. The hASCs isolation was performed using a previous optimized protocol [24]. hASCs were

maintained in α-MEM supplemented with 10% FBS and 1% antibiotic/antimycotic solution at 37 °C, 5% CO2. hASCs were seeded onto coverslip surfaces at a density of 4000 cells per 1 cm2. The first 2 h (initial cell adhesion) were in the culture media without serum, and then all cell culture assays of hASCs seeded onto coverslip surfaces were performed using α-MEM supplemented with 1% FBS and 1% antibiotic/antimycotic solution.

V-2.4.4. Immunofluorescence

After 2, 7 or 28 days of culture, the coverslips were washed with PBS and then fixed in 10 vol.% formalin (Thermo Fisher Scientific, USA) for 15 min at RT and permeabilized using 0.2 vol.% Triton-X 100 (Sigma-Aldrich, USA). After washing, samples were blocked using 3% w/v BSA and incubated with 1:50 v/v solution of specific aggrecan primary antibody (MA316888, Thermo Fisher Scientific, USA) or 1:100 v/v solution of specific collagen type II primary antibody (MAB1330, Millipore, USA). Then, samples were incubated with 1:200 v/v Alexa Fluor® 488 conjugated secondary antibody (Thermo Fisher Scientific, USA). After washing, samples were incubated with 1:200 v/v rhodamine-conjugated phalloidin (Sigma-Aldrich, USA) for 10 min and 1:1000 v/v 4′, 6-diamidino-2-phenylindole (DAPI, Sigma-Aldrich, USA) for 20 min (dilutions in PBS). After washing, the samples were mounted in an fluoromount aqueous mounting medium (Sigma-Aldrich, USA) and observed under a confocal microscope TCS SP8 (Leica Microsystems, Germany). The expression levels of aggrecan was assessed by calculating the mean fluorescence intensity of obtained confocal images ($n > 5$) using Fiji software. Briefly, images were thresholded to separate the signal from the background, and the mean fluorescence values were calculated and normalized by the number of nucleus (per cell). Cell proliferation was evaluated measuring cell nuclei per area using Image J software.

V-2.4.5. Staining procedures

After 28 days of culture, PL-CNC coated coverslips were washed with PBS and then fixed in 10% formalin (Thermo Fisher Scientific, USA) for 30 min at RT. The samples were stained with alcian blue (1% w/v alcian blue solution in 3 vol.% acetic acid) for h. For alizarin red staining (2% v/v alizarin solution at pH 4.1-4.3), the samples were immersed for 5 min. Finally, the samples were also stained with oil red O staining (0.5 vol.% oil red in isopropanol, and then dilute 3 mL of the stock solution in 2 mL of water) for

25 min. All formulations were washed three times with PBS and then mounted in an fluoromount aqueous mounting medium (Sigma-Aldrich, USA). The transmitted light microscope (Zeiss, Germany) was used to observe the stained formulations. The Alcian Blue coverage area was calculated using Fiji software (n > 10). Briefly, images were thresholded to separate the signal from the background, and the area fraction was determined.

V-2.5. Statistical analysis

The statistical analysis of data was performed using GraphPad PRISM v 7.0. Shapiro-Wilk normality test and one-way or two-way analysis of variance (ANOVA) was used to analyze experimental data, followed by Tukey posthoc test for multiple comparisons. Statistical significance was set to *, $P < 0.05$; **, $P < 0.01$; $^{\alpha\alpha\alpha}$, $P < 0.001$; **** and $^{\alpha\alpha\alpha\alpha}$, $P < 0.0001$. Results are presented as mean ± standard deviation.

V-3. RESULTS & DISCUSSION

CNC were produced from microcrystalline cellulose resulting in the typical rod-shaped and negatively charged nanoparticles (Figure V-1A) [10, 11]. Afterwards, this CNC suspension with a high sulfation degree (H-CNC) were hydrothermally treated in an autoclave [25]. At high temperatures, in situ acid autocatalyzed desulfation reaction occurs, promoting the hydrolysis of sulfate half-ester groups and their conversion to hydroxyl groups [25]. We hydrothermally treated the original H-CNC (292 ± 5 mmol.kg-1) suspension for 3 or 6 hours at 120 °C to obtain CNC with medium (M-CNC, 233 ± 4 mmol.kg-1) and low (L-CNC, 88.6 ± 0.4 mmol.kg-1) sulfation degree, respectively (Supplementary Figure V-1A and B), as confirmed by conductometric titration measurements (Figure V-1C). To maintain the possibility of reacting with the PL proteins through reversible Schiff base bonds and following the concept that we have previously proposed for PL-CNC hydrogels, [2] the three CNC formulations with different sulfation degrees were then aldehyde-modified (a-CNC) by sodium periodate oxidation and their surface charge analyzed by zeta potential (Supplementary Figure V-1C). CNC morphology confirms a non-significant variability of nanoparticle dimensions, and thus of their surface area, between formulations (Figure V-1B).

Previous studies on as GAGs mimetic polymers have shown that it can establish favorable interactions with GFs and thus boost their bioactivities namely, increase cell proliferation (induced by fibroblast growth factor-2) or osteogenic differentiation potential (induced by bone morphogenic protein-2) [26, 27]. In contrast to cellulose sulfate derivatives that are relatively flexible and have an excellent water solubility, CNC are stiff solid particles and exhibits an amphiphilic character. This character stems from the cellulose chain packing that, besides the hydroxyl and sulfate hydrophilic groups, also results in a hydrophobic crystalline plane for which axial CH moieties are exposed at the surface of the nanocrystals [28, 29]. These physical and chemical properties of CNC, much different from soluble cellulose sulfate derivatives, will certainly contribute to the entity of the protein corona built on the materials surface, as well as on their release kinetics and further presentation in the cellular microenvironment [5].

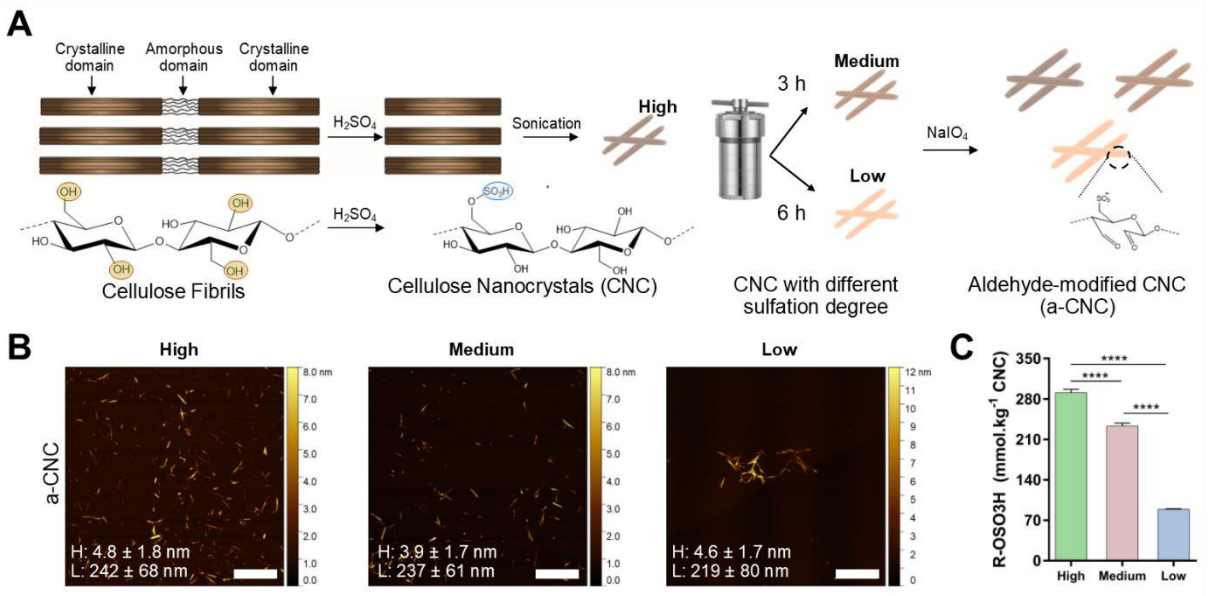

Figure V-1 (A) Schematic representation of CNC production starting from microcrystalline cellulose and the typical sulfuric acid hydrolysis process that introduces sulfate groups on their surface. CNC suspension (high sulfate groups content on CNC surface) hydrothermally treated undergo desulfation to obtain CNC with different sulfation degree (medium and low sulfate groups content on CNC surface), which are further aldehyde-modified by sodium periodate oxidation. (B) AFM images of aldehyde-modified CNC. (C) Sulfate groups quantification determined by conductometric titration. Scale bar: 1 µm (B). H: height and L: length.

CNC with different sulfation degrees were incubated with PL solution to investigate the impact on the composition of the protein corona (Figure V-2). First, we studied the protein composition of the 'soft' and 'hard' corona according their molecular weight by SDS-PAGE (Figure V-2A). Increasing surface charge density led to an increase in protein adsorption and in PL-CNC complexes pellet size, as reflected in the intensity of the bands present in the gel that is more evident in low sulfated CNC group [30]. In the three

formulations evaluated, the 'soft' corona was characterized by the predominance of highly abundant PL proteins namely, serum albumin (≈41% of total PL proteins [20]), as reflected in the expanded spot at ≈67 kDa. Differences among formulations were also observed on the profiles of the gel separated proteins, namely in the intensity of the band at ≈55 kDa and ≈35 kDa, which can be attributed to fibrinogen gamma and apoliprotein A-I, respectively [31]. In particular, the band at ≈35 kDa has higher intensity in M-CNC than in H-CNC and is barely seen in L-CNC. Next, PL-CNC complexes were extensively washed to remove loosely bound proteins and to analyze the proteins with high nanoparticle binding affinity. The band profile of gel lanes show differences in the 'hard' corona of the different CNC groups in terms of both proteins composition and relative quantity, particularly for the lower molecular weight bands like that at ≈15 kDa, which corresponds to the molecular weight of several GF monomers [32]. The protein composition of the different 'hard' coronas were then evaluated in detail by proteomic analysis (Figure V-2B). The total number of identified proteins was similar for H-CNC (n=702) and M-CNC (n=638) groups, whereas it was lower for L-CNC formulations (n=491). The common and unique proteins in each formulation are represented as a Venn diagram. The homology between the coronas was ≈53%, ≈58% and ≈76% for H-CNC, M-CNC and L-CNC formulations, respectively. On the other hand, H-CNC have a higher fraction (≈18%) of unique proteins than M-CNC (≈10%) and L-CNC (≈13%). The identified proteins were then classified according to categories of biological response. Although their distribution is in line with previous PL proteomic profiles [33], differences are observed not only for the total number of protein related processes but also for the relative weight of each category (Figure V-2BI). These differences are more evident when performing this analysis only on the unique proteins of each formulation. H-CNC show the higher fraction of proteins related with metabolic process (organic substance and cellular metabolic process), (Figure V-2BII). Proteins related with biological regulation (biological process and molecular function) are more represented in M-CNC, whereas L-CNC corona is richer in proteins related with processes of immune system (leukocyte activation and immune effector process), Figure V-2BII.

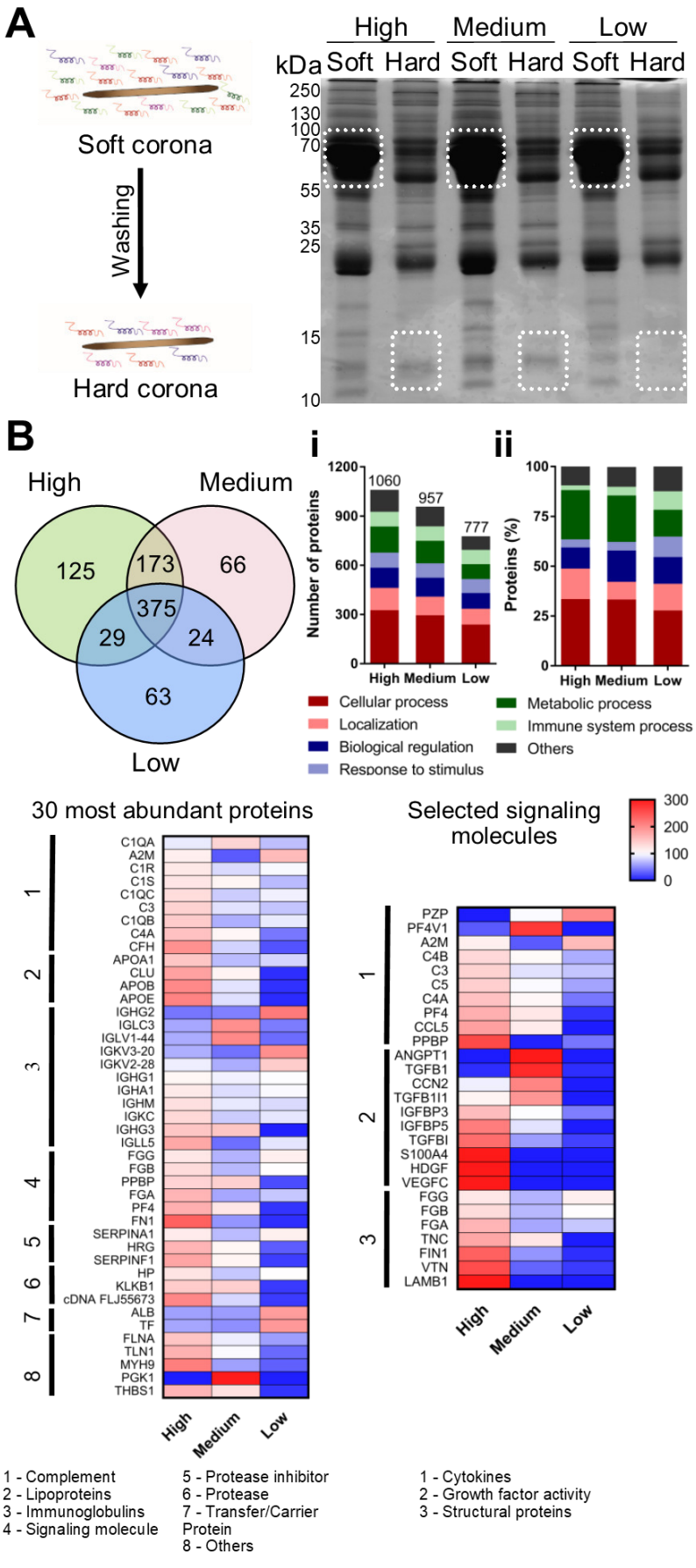
A
Soft corona
Washing
Hard corona
High
Medium
Low
kDa
Soft
Hard
250
130
100
70
55
35
25
15
10
B
High
Medium
Low
125
173
66
375
29
24
63
i
ii
Number of proteins
Proteins (%)
1060
957
777
Cellular process
Localization
Biological regulation
Response to stimulus
Metabolic process
Immune system process
Others
30 most abundant proteins
Selected signaling molecules
C1QA
A2M
C1R
C1S
C1QC
C3
C1QB
C4A
CFH
APOA1
CLU
APOB
APOE
IGHG2
IGLC3
IGLV1-44
IGKV3-20
IGKV2-28
IGHG1
IGHA1
IGHM
IGKC
IGHG3
IGLL5
FGG
FGB
PPBP
FGA
PF4
FN1
SERPINA1
HRG
SERPINF1
HP
KLKB1
cDNA FLJ55673
ALB
TF
FLNA
TLN1
MYH9
PGK1
THBS1
PZP
PF4V1
A2M
C4B
C3
C5
C4A
PF4
CCL5
PPBP
ANGPT1
TGFB1
CCN2
TGFB1I1
IGFBP3
IGFBP5
TGFBI
S100A4
HDGF
VEGFC
FGG
FGB
FGA
TNC
FIN1
VTN
LAMB1
1 - Complement
2 - Lipoproteins
3 - Immunoglobulins
4 - Signaling molecule
5 - Protease inhibitor
6 - Protease
7 - Transfer/Carrier Protein
8 - Others
1 - Cytokines
2 - Growth factor activity
3 - Structural proteins

Figure V-2 Upon incubation with PL, (A) initial CNC was decorated with a 'soft' corona that over time only the strong bind proteins were maintained as analysed by the protein profile in SDS-PAGE gel. (B) Analysis of 'hard' corona, Venn diagram of identified proteins. Proteins were classified by their biological process displayed as (i) number of proteins considering all identified proteins and (ii) protein (%) considering only the exclusively proteins of each group. Main components (30) found in 'hard' corona and selected signaling molecules by their relative abundance and classified as Panther protein class. Red colour denotes counts higher and blue denotes lower than groups average (set to 100, white).

Interestingly, the top 30 most abundant proteins accounted for over 80% of the total protein content in the nanoparticles with the three different chemistries (Supplementary Table V-1). The H-CNC corona has a strong enrichment in apolipoproteins ApoA1 and ApoE. L-CNC was highly enriched in transfer/carrier proteins as albumin (zinc, calcium and magnesium transporter) and serotransferrin (ferrous iron transporter), which may have a further role in stimulating cell growth and proliferation [34, 35]. Collectively, detailed analysis of these results further suggests that electrostatic interactions are not the main driving mechanism in the development of CNC 'hard' corona (Supplementary Table V-2 and Supplementary Figure V-2). Figure V-2B also highlights the different signaling molecules adsorption pattern on the individual biomolecular corona, where is evident the presence or completely absence of certain proteins depending on the sulfation degree of CNC. For instance, hepatoma-derived GF and vascular endothelial GF-C (VEGF-C) were only found in H-CNC, whereas angiopoietin-1, which regulates angiogenesis,[36] and transforming growth factor beta-1 (TGF-β1) were only found in M-CNC. Moreover, H-CNC showed higher affinity for different structural proteins such as fibronectin and fibrinogen that have in their structure different peptide motifs involved in cell adhesion and regulation of GF signaling [37, 38]. In addition, to explore collective functions of the exclusive proteins identified in each formulation, we reconstructed network models describing the interactions among these proteins. Notably, it can be observed that, for example, in the M-CNC corona there is an enrichment of proteins involved in hypoxia inducible factor-1 and VEGF signaling pathways (Supplementary Figure V-4). Overall, these results confirm that the 'hard' biomolecular corona adsorbed from PL on CNC is surface chemistry dependent, and therefore might be able to entirely change the *in vitro* biological response of PL-CNC biomaterials. To test this hypothesis, thin films of the different CNC were spin-coated on cell culture glass coverslips (Supplementary Figure V-6), incubated with PL solutions and then washed to remove the 'soft' biomolecular corona.

hASCs were seeded on these substrates and cultured *in vitro* to evaluate their biological behavior. Overall, cells proliferated faster on M-CNC and L-CNC than in H-CNC, although cell numbers tended to level by day 28 (Supplementary Figure V-7A). Cell morphology and cell spreading area was also evidently

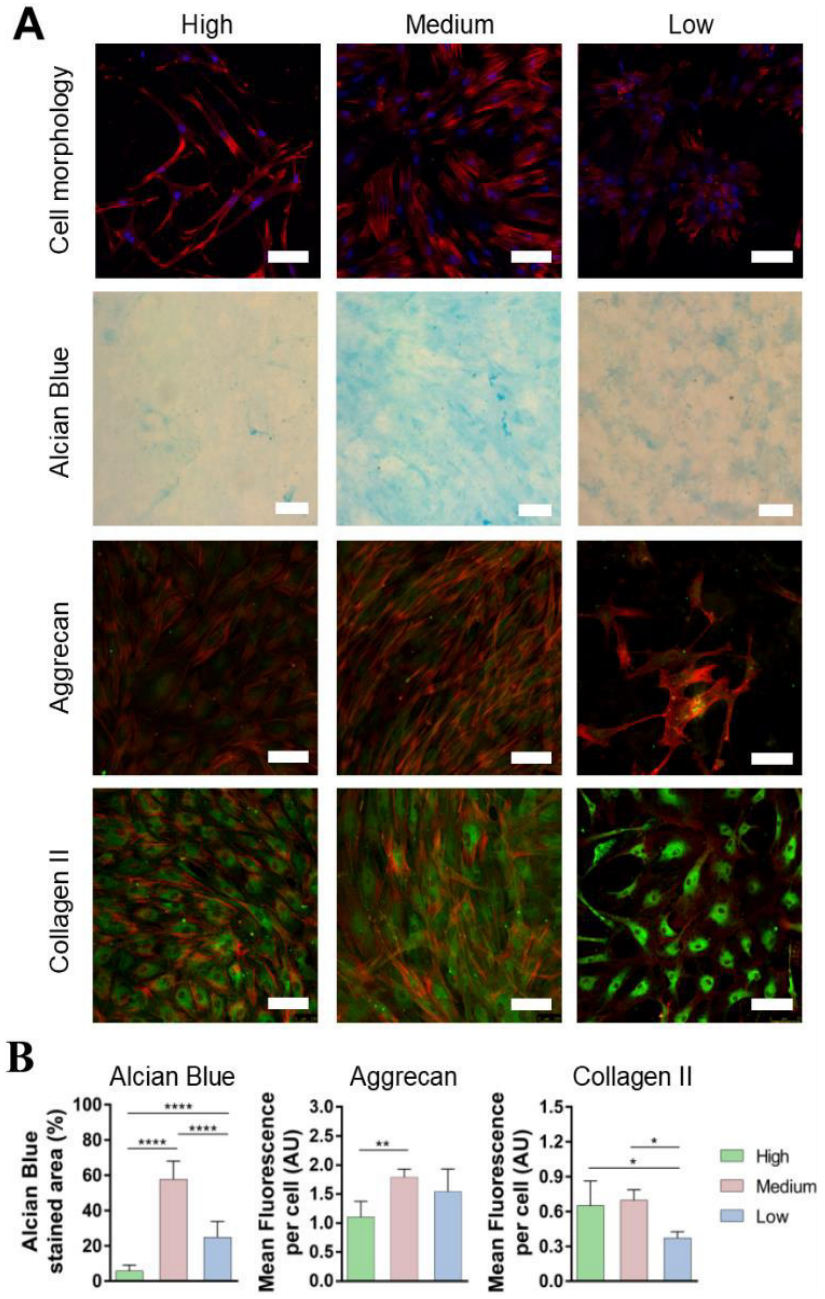

Figure V-3 (A) In vitro evaluation of hASCs behavior. Fluorescence microscopy images showing cell morphology at day 7, alcian blue, aggrecan and collagen type II expression at day 28. (B) Quantification of mean fluorescence intensity of alcian blue staining by coverage staining area, aggrecan and collagen II by cell nuclei. Staining actin (red), nuclei (blue), aggrecan and collagen type II (green). Scale bar: 100 µm (cell morphology, aggrecan, collagen type II), 50 µm (Alcian Blue).

different among groups (Figure-V3A and Supplementary Figure V-7B). Histological stainings were used as a first screening to evaluate the effect of the different CNC on the potential cell commitment to three common mesenchymal lineages (chondrogenic, osteogenic and adipogenic). While all groups stained negative to Oil red O and Alizarin red (Supplementary Figure V-7), hASCs seeded onto M-CNC stained positive for Alcian Blue, indicating an increased content of sulfated GAGs in the newly cell deposited ECM,

Figure V-3. Considering that positive staining for this marker, which is usually related with the chondrogenic commitment of stem cells, we then evaluated the expression of other markers related with this lineage namely, aggrecan and collagen type II, by immunochemistry. Consistent with the histological staining, M-CNC group also revealed an increased expression of these cartilaginous markers. Although this cell behavior might result from the synergistic effect of several signaling biomolecules, it is interesting to notice that e.g. TGF-β1 and CCN family member 2, two GFs known to stimulate cell adhesion and proliferation as well as to induce chondrogenic differentiation of stem cells, were upregulated in M-CNC group (Figure V-2) [39, 40].

V-4. CONCLUSIONS

These results demonstrate that the different CNC surface chemistries led to different corona compositions of PL protein. The sequestering and presentation of tailored protein coronas to cell receptors can activate different cell signaling pathways and guide cell fate decisions. The novel concept here proposed has thus the potential to enable the development of a portfolio of PL-CNC engineered biomaterials with tissue specific bioactivity that could find broad application as artificial ECMs in organotypic TE strategies.

V-5. SUPPLEMENTARY INFORMATION

V-5.1. Supplementary results and discussion

V-5.1.1. Morphological and chemical characterization of modified CNC

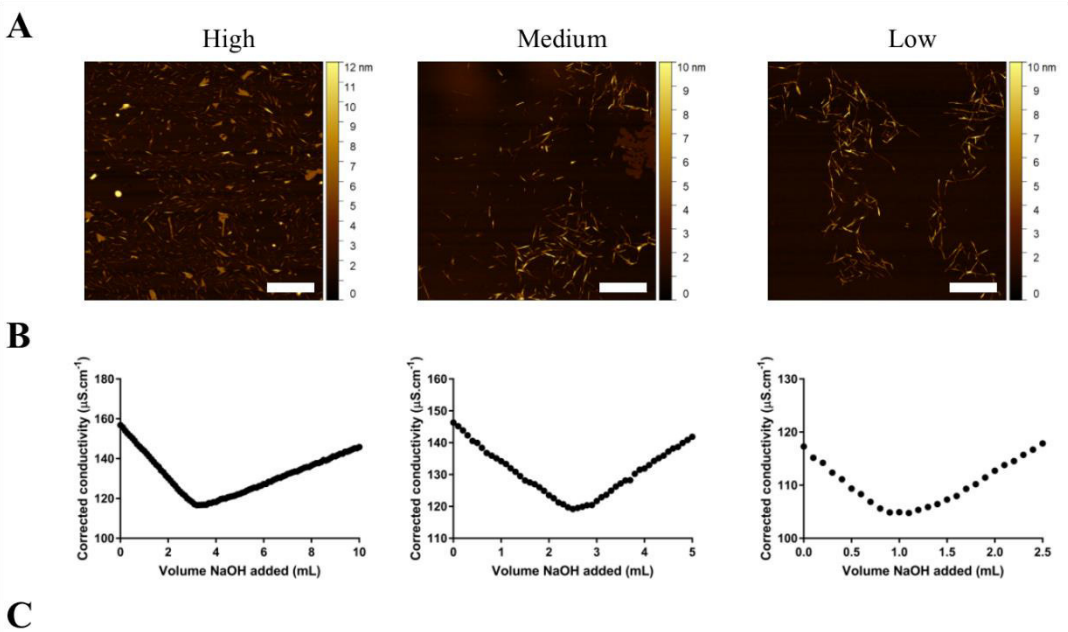

C

High	Medium	Low
- 43.9 ± 3.44 mV	- 27.7 ± 2.17 mV	- 16.2 ± 1.10 mV

Supplementary Figure V-1 Morphological and chemical characterization of CNC with different sulfation degrees (High, Medium and Low). (A) AFM images of modified CNC at 5x5 µm. (B) Conductometric titration curve of modified CNC to calculate sulfation degree. (C) Surface charge of the different a-CNC formulations. Scale bar: 1 µm (A).

V-5.1.2. Protein corona characterization

The 30 most abundant proteins identified in CNC coronas (Supplementary Table V-1) were grouped in negatively charged (pI<7), neutral (7<pI<8) and positively charged (pI>8) proteins, Table S2.

The sum of protein abundances for each group is shown in Supplementary Figure V-2. H-CNC hard corona is richer in negatively charged proteins than M-CNC and L-CNC. Negatively charged proteins

derived from human serum (main components of PL) such as complement protein C3 (*pI*=5.77), fibrinogen alpha chain (*pI*=5.49) or serum albumin (*pI*=5.57) are among the most abundant in the hard corona of H-CNC. On the other hand, all CNC formulations show considerably (one to two orders of magnitude) lower contents of positively charged than of negatively charged or neutral proteins in the hard corona. Moreover, similar contents of positively charged proteins are observed in the different CNC formulations, irrespective of their sulfation degrees.

Remarkably, these patterns of corona composition diverge from what would be expected in a system were electrostatic forces dominate the protein-nanoparticle interactions. Although they certainly have a relevant contribution for the development of CNC hard coronas, these results suggest that electrostatic interactions are not the main driving mechanism of this process, supporting the hypothesis that nanoparticle surface chemistry might have a more determinate role on their composition.

Supplementary Table V-1 Main components found in high, medium and low sulfated 'hard' corona formulations by mass spectrometry analysis, listed according to their relative abundance.

N	High	Medium	Low
1	Apolipoprotein B-100	Immunoglobulin heavy constant gamma 1	Serum albumin
2	Immunoglobulin heavy constant gamma 1	Complement C3	Immunoglobulin heavy constant gamma 1
3	Complement C3	Apolipoprotein B-100	Complement C3
4	Immunoglobulin kappa constant	Serum albumin	Immunoglobulin kappa constant
5	Fibrinogen alpha chain	Immunoglobulin kappa constant	Immunoglobulin heavy constant um
6	Complement C4-A	Complement C4-A	Fibrinogen alpha chain
7	Immunoglobulin heavy constant mu	Immunoglobulin heavy constant mu	Immunoglobulin heavy constant gamma 2

8	Serum albumin	Fibrinogen alpha chain	Fibrinogen beta chain
9	Apolipoprotein E	Immunoglobulin heavy constant gamma 3	Complement C4-A
10	Myosin-9	Talin-1	Fibrinogen gamma chain
11	Talin-1	Apolipoprotein E	Immunoglobulin heavy constant alpha 1
12	Filamin-A	Filamin-A	Immunoglobulin lambda-like polypeptide 5
13	Fibronectin	Immunoglobulin lambda constant 3	Filamin-A
14	Immunoglobulin heavy constant gamma 3	Myosin-9	Complement C1q subcomponent subunit C
15	cDNA FLJ55673, highly similar to Complement factor B	Clusterin	Serotransferrin
16	Immunoglobulin lambda-like polypeptide 5	Complement C1s subcomponent	Talin-1
17	Complement factor H	Fibrinogen beta chain	Complement C1s subcomponent
18	Fibrinogen beta chain	Immunoglobulin heavy constant alpha 1	Apolipoprotein A-I
19	Clusterin	cDNA FLJ55673, highly similar to Complement factor B	Myosin-9
20	Fibrinogen gamma chain	Complement factor H	Complement C1q subcomponent subunit B
21	Complement C1q subcomponent subunit C	Complement C1q subcomponent subunit C	Apolipoprotein B-100
22	Immunoglobulin heavy constant alpha 1	Thrombospondin-1	Immunoglobulin kappa variable 3-20

23	Complement C1s subcomponent 1	Plasma kallikrein	Complement C1q subcomponent subunit A
24	Apolipoprotein A-I	Fibrinogen gamma chain	Immunoglobulin lambda constant 3
25	Thrombospondin-1	Immunoglobulin lambda variable 1-44	Alpha-1-antitrypsin
26	Platelet factor 4	Complement C1q subcomponent subunit A	Complement C1r subcomponent
27	Complement C1q subcomponent subunit B	Platelet basic protein	Complement factor H
28	Plasma kallikrein	Platelet factor 4	Immunoglobulin kappa variable 2-28
29	Histidine-rich glycoprotein	Phosphoglycerate kinase 1	Haptoglobin
30	Pigment epithelium-derived factor	Fibronectin	Alpha-2-macroglobulin

Supplementary Table V-2 Collective list of the thirty most abundant proteins detected in the hard coronas of each of the CNC with different sulfation degree and their respective molecular weight (Mw), isoelectric point (*pI*) and relative abundance values obtained by mass spectrometry. Proteins are sorted by ascending pI. (AU – arbitrary units).

UNIPROT Accession	Description	Mw (kDa)	*pI*	Protein abundance (mean values, AU)		
				High	Medium	Low
TSP1_HUMAN	Thrombospondin-1	129,3	4,51	1,49E+09	1,14E+09	9,38E+07
C1S_HUMAN	Complement C1s subcomponent	76,6	4,76	1,60E+09	1,42E+09	9,09E+08
KV320_HUMAN	Immunoglobulin kappa variable 3-20	12,5	4,77	1,85E+08	1,08E+08	5,67E+08
LV144_HUMAN	Immunoglobulin lambda variable 1-44	12,2	4,8	2,96E+08	9,55E+08	1,65E+08

A1AT_HUMAN	Alpha-1-antitrypsin	46,7	5,11	4,54E+08	2,70E+08	4,38E+08
FINC_HUMAN	Fibronectin	272,2	5,16	3,67E+09	8,18E+08	1,22E+08
FIBG_HUMAN	Fibrinogen gamma chain	51,5	5,2	2,00E+09	1,10E+09	1,88E+09
MYH9_HUMAN	Myosin-9	226,4	5,39	5,48E+09	1,49E+09	7,68E+08
APOA1_HUMAN	Apolipoprotein A-I	30,8	5,41	1,57E+09	7,32E+08	8,47E+08
KV228_HUMAN	Immunoglobulin kappa variable 2-28	12,9	5,43	2,25E+08	1,56E+08	3,53E+08
FLNA_HUMAN	Filamin-A	280,6	5,48	3,76E+09	2,29E+09	1,43E+09
FIBA_HUMAN	Fibrinogen alpha chain	94,9	5,49	9,23E+09	3,42E+09	4,22E+09
APOE_HUMAN	Apolipoprotein E	36,1	5,55	5,73E+09	2,36E+09	1,80E+08
C1R_HUMAN	Complement C1r subcomponent	81,8	5,57	4,72E+08	3,28E+08	3,81E+08
TLN1_HUMAN	Talin-1	269,6	5,58	4,98E+09	2,90E+09	1,01E+09
CLUS_HUMAN	Clusterin	52,5	5,65	2,45E+09	1,48E+09	1,05E+08
ALBU_HUMAN	Serum albumin	69,3	5,67	6,09E+09	5,90E+09	1,95E+10
PEDF_HUMAN	Pigment epithelium-derived factor	46,3	5,73	9,45E+08	5,73E+08	7,51E+07
A2MG_HUMAN	Alpha-2-macroglobulin	163,2	5,76	2,22E+08	5,33E+07	3,13E+08
CO3_HUMAN	Complement C3	187	5,77	1,20E+10	7,54E+09	6,40E+09
IGHA1_HUMAN	Immunoglobulin heavy constant alpha 1	37,6	5,77	1,91E+09	1,37E+09	1,56E+09
HPT_HUMAN	Haptoglobin	45,2	5,83	4,09E+08	2,49E+08	3,38E+08
IGKC_HUMAN	Immunoglobulin kappa constant	11,8	5,85	9,46E+09	5,46E+09	6,26E+09
CFAH_HUMAN	Complement factor H	139	5,88	2,91E+09	1,20E+09	3,55E+08

IGHM_HUMAN	Immunoglobulin heavy constant mu	49,4	6,02	6,89E+09	4,86E+09	4,52E+09
APOB_HUMAN	Apolipoprotein B-100	515,3	6,27	1,42E+10	6,08E+09	6,42E+08
CO4A_HUMAN	Complement C4-A	192,7	6,29	7,52E+09	5,24E+09	1,95E+09
B4E1Z4	cDNA FLJ55673, highly similar to Complement factor B	140,9	6,35	3,23E+09	1,30E+09	2,14E+08
TF_HUMAN	Serotransferrin	77	6,41	3,75E+08	3,12E+08	1,17E+09
IGLC3_HUMAN	Immunoglobulin lambda constant 3	11,3	6,53	6,58E+08	2,13E+09	4,53E+08
HRG_HUMAN	Histidine-rich glycoprotein	59,5	6,66	1,04E+09	6,80E+08	1,78E+08
IGHG2_HUMAN	Immunoglobulin heavy constant gamma 2	35,9	6,76	6,99E+08	7,87E+08	3,83E+09
A0A4W9A917	Immunoglobulin heavy constant gamma 3	41,3	7,03	3,37E+09	3,37E+09	3,70E+07
PGK1_HUMAN	Phosphoglycerate kinase 1	44,6	7,28	3,39E+05	8,46E+08	4,71E+06
KLKB1_HUMAN	Plasma kallikrein	71,3	7,32	1,16E+09	1,14E+09	1,04E+08
IGHG1_HUMAN	Immunoglobulin heavy constant gamma 1	36,1	7,38	1,28E+10	1,12E+10	1,18E+10
FIBB_HUMAN	Fibrinogen beta chain	55,9	7,45	2,65E+09	1,39E+09	2,07E+09
C1QC_HUMAN	Complement C1q subcomponent subunit C	25,8	7,75	1,92E+09	1,15E+09	1,38E+09
PLF4_HUMAN	Platelet factor 4	10,8	7,89	1,19E+09	8,48E+08	7,23E+07
C1QB_HUMAN	Complement C1q subcomponent subunit B	26,7	7,95	1,16E+09	5,17E+08	7,25E+08
CXCL7_HUMAN	Platelet basic protein	13,9	8,04	8,59E+08	8,76E+08	1,31E+08
IGLL5_HUMAN	Immunoglobulin lambda-like polypeptide 5	23,1	8,13	3,03E+09	6,18E+08	1,52E+09
C1QA_HUMAN	Complement C1q subcomponent subunit A	26	8,44	6,25E+08	9,43E+08	4,91E+08

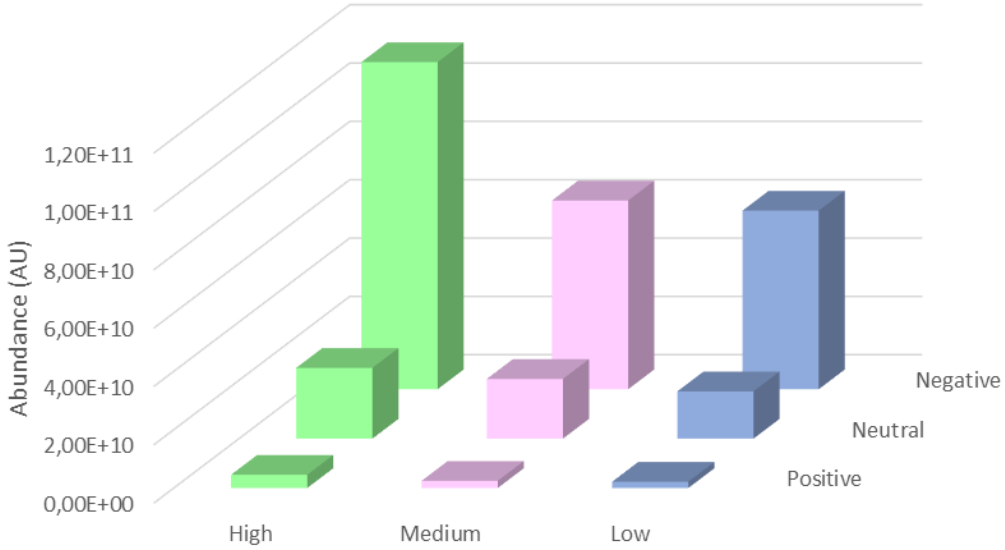

Supplementary Figure V-2 Sum of negatively charged (pI<7), neutral (7<pI<8) and positively charged (pI>8) proteins in high, medium and low sulfated 'hard' corona formulations (AU – arbitrary units).

A

Pathway description	N° protein IDs	FDR	UNIPROT IDs of matching proteins in the network
AGE-RAGE signaling pathway in diabetic complications	6	0,0124	MAPK1,MMP2,PLCB2,PRKCD,STAT5B,VEGFC
Endocytosis	8	0,0244	AP2A1,CAPZB,CHMP1B,CLTA,PDCD6IP,SH3GL1,SNX6,WAS
Necroptosis	6	0,0443	CHMP1B,EIF2AK2,H2AFV,HIST1H2AC,HIST2H2AC,STAT5B
Synaptic vesicle cycle	4	0,0443	AP2A1,ATP6V1B2,ATP6V1E1,CLTA

B

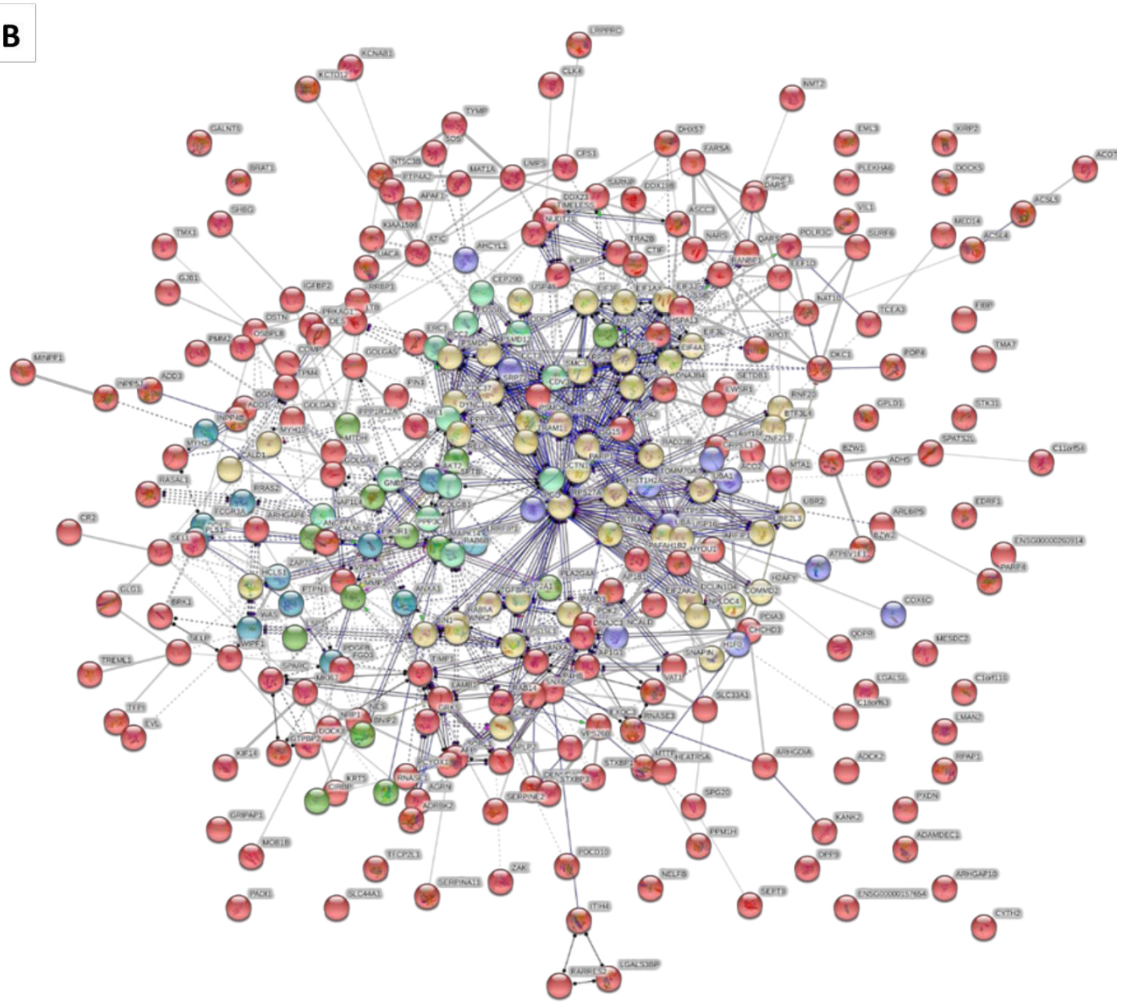

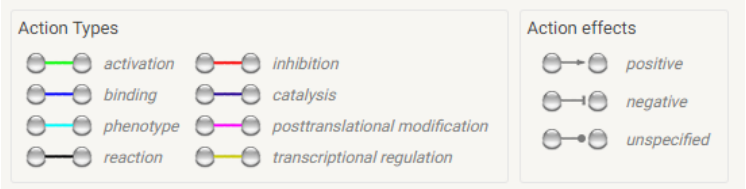

Supplementary Figure V-3 Enrichment in KEGG pathways (A) and networks (B) based on STRING annotation tool applied on the list of exclusively H-CNC proteins. Network edges are based on molecular action (Kmeans clustering n=6). FDR= False Discovery Rate.

A

Pathway description	N° protein IDs	FDR	UNIPROT IDs of matching proteins in the network
Non-small cell lung cancer	7	0,0045	EML4,ERBB2,MAPK3,PIK3R2,PLCG2,PRKCA,STAT5A
ErbB signaling pathway	7	0,0088	ABL1,ERBB2,MAPK3,PIK3R2,PLCG2,PRKCA,STAT5A
Ribosome	8	0,0141	RPL8,RPLP0,RPLP2,RPS15,RPS15A,RPS20,RPS3A,RPS8
Fc epsilon RI signaling pathway	6	0,0141	BTK,MAP2K3,MAPK3,PIK3R2,PLCG2,PRKCA
EGFR tyrosine kinase inhibitor resistance	6	0,0183	ERBB2,MAPK3,PDGFD,PIK3R2,PLCG2,PRKCA
Gap junction	6	0,0262	GNAQ,GUCY1A3,MAPK3,PDGFD,PRKCA,TUBA1B
VEGF signaling pathway	5	0,0264	MAPK3,MAPKAPK3,PIK3R2,PLCG2,PRKCA
HIF-1 signaling pathway	6	0,0352	ANGPT1,ERBB2,MAPK3,PIK3R2,PLCG2,PRKCA
Choline metabolism in cancer	6	0,0352	DGKA,LYPLA1,MAPK3,PDGFD,PIK3R2,PRKCA
Ras signaling pathway	9	0,0383	AB-L1,ANGPT1,GNB1,MAPK3,PDGFD,PIK3R2,PLCG2,PRKCA,RAB5C
Adherens junction	5	0,0383	CSNK2A2,CSNK2B,ERBB2,LMO7,MAPK3

B

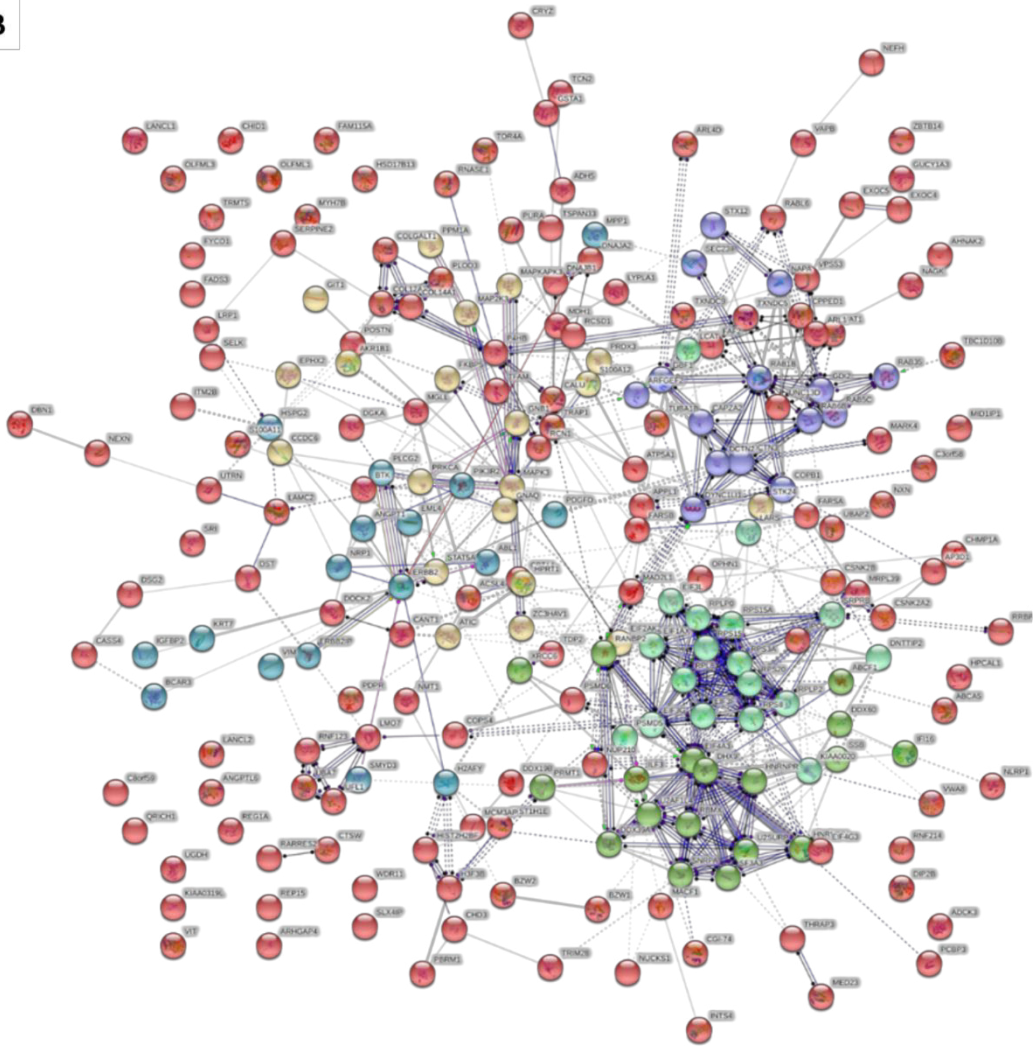

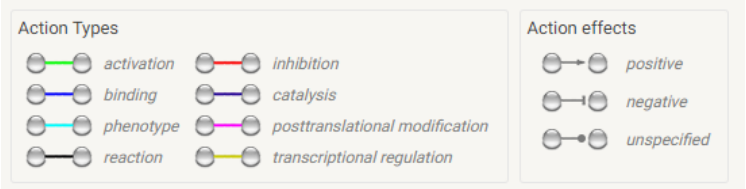

Supplementary Figure V-4 Enrichment in KEGG pathways (A) and networks (B) based on STRING annotation tool applied on the list of exclusively M-CNC proteins. Network edges are based on molecular action (Kmeans clustering n=6). FDR= False Discovery Rate.

A

Pathway description	N° protein IDs	FDR	UNIPROT IDs of matching proteins in the network
Proteasome	6	0,0023	PSMA3,PSMB1,PSMD11,PSMD8,PSME2,PSME3
Metabolic pathways	28	0,0129	ACO-T8,AK1,ALDOC,ALOX12,AMY1A,ANPEP,ATP5B,ATP5F1,BLVRA,CBR1,CNDP2,ECHS1,FAH,GNPDA1,GPT,HSD17B4,LTA4H,MAN1A1,MDH1,NT5C,PGD,PNP,PRPS2,PTGS1,PYGL,RPN2,TALDO1,UQCRC1
Pentose phosphate pathway	4	0,0202	ALDOC,PGD,PRPS2,TALDO1
Arachidonic acid metabolism	5	0,0202	ALOX12,CBR1,GPX3,LTA4H,PTGS1
Carbon metabolism	7	0,0202	ALDOC,ECHS1,GPT,MDH1,PGD,PRPS2,TALDO1
Endocytosis	10	0,0202	AR-F3,ARPC4,DAB2,DNM2,FAM21A,HSPA8,IST1,RAB5B,SH3KBP1,VPS35
Tight junction	8	0,0202	ACTN4,CLDN5,JAM3,LLGL2,MYH14,MYH8,MYL6,TUBA8
Phospholipase D signaling pathway	7	0,0269	DNM2,FCER1G,GNAS,GRB2,GRM7,NRAS,RRAS
Thyroid hormone synthesis	5	0,0299	ALB,GNAS,GPX3,SERPINA7,TG
Aminoacyl-tRNA biosynthesis	4	0,0317	DARS,GARS,HARS,MARS
Regulation of actin cytoskeleton	8	0,0323	AC-TN4,ARPC4,IQGAP2,MYH14,NRAS,PPP1CA,PPP1R12B,RRAS
Glutathione metabolism	4	0,039	ANPEP,GPX3,GSTP1,PGD
Platelet activation	6	0,039	COL1A1,FCER1G,GNAS,PPP1CA,PTGS1,STIM1

B

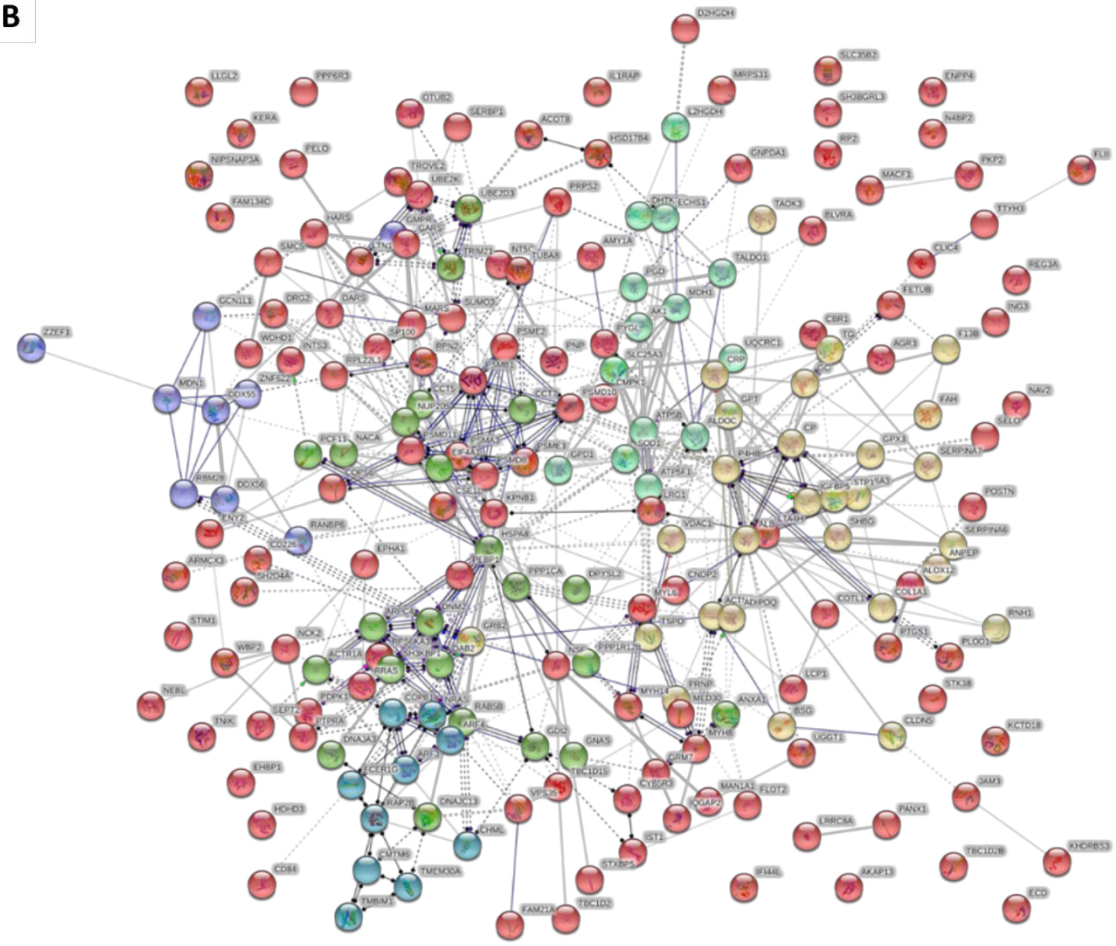

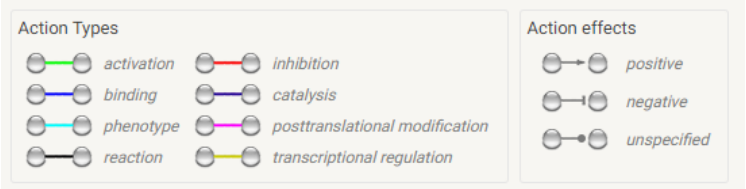

Supplementary Figure V-5 Enrichment in KEGG pathways (A) and networks (B) based on STRING annotation tool applied on the list of the exclusively L-CNC proteins. Network edges are based on molecular action (Kmeans clustering n=6). FDR= False Discovery Rate.

V-5.1.3. Characterization of CNC film coated coverslips

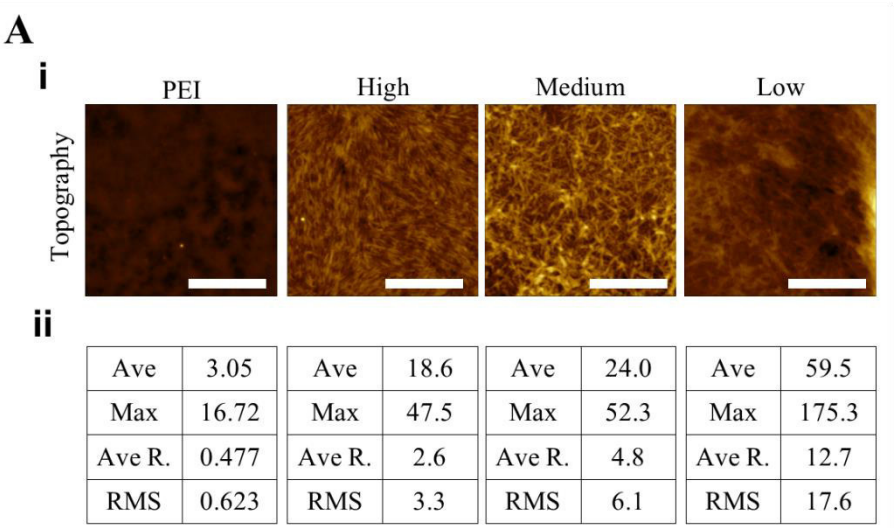

Ave	3.05	Ave	18.6	Ave	24.0	Ave	59.5
Max	16.72	Max	47.5	Max	52.3	Max	175.3
Ave R.	0.477	Ave R.	2.6	Ave R.	4.8	Ave R.	12.7
RMS	0.623	RMS	3.3	RMS	6.1	RMS	17.6

Supplementary Figure V-6 (A)AFM topographies of PEI and 1 wt.% CNC films (i) and roughness parameters (ii): average height (AVE); maximum height (Max); average roughness (Ra); root mean square roughness (RMS). Scale bar: 1 µm.

V-5.1.4. hASCs behavior on CNC coated coverslips after PL incubation

At day 2, cells seeded on CNC film coatings pre-incubated with PL showed similar proliferation rate in all groups (Supplementary Figure V-7B). On the other hand, whereas H-CNC group did not exhibit significant cell proliferation from day 2 to day 7, cells seeded onto L-CNC and, in particular, M-CNC significantly increased proliferation. By day 28, all conditions increased the number of cells, but no significant differences could be observed among tested conditions. Interestingly, although hASCs morphology during the first few days (day 2) was also very similar, considerable differences between groups start to be noticed by day 7 (Supplementary Figure V-7A). Whereas hASCs cultured on H-CNC showed a highly elongated morphology, on M-CNC films they exhibited a spindle-like shape and on L-CNC

formulation they tended to form dense cell clusters. These morphological characteristics were maintained over the time in culture up to day 28 (Figure V-3A and Supplementary Figure V-7).

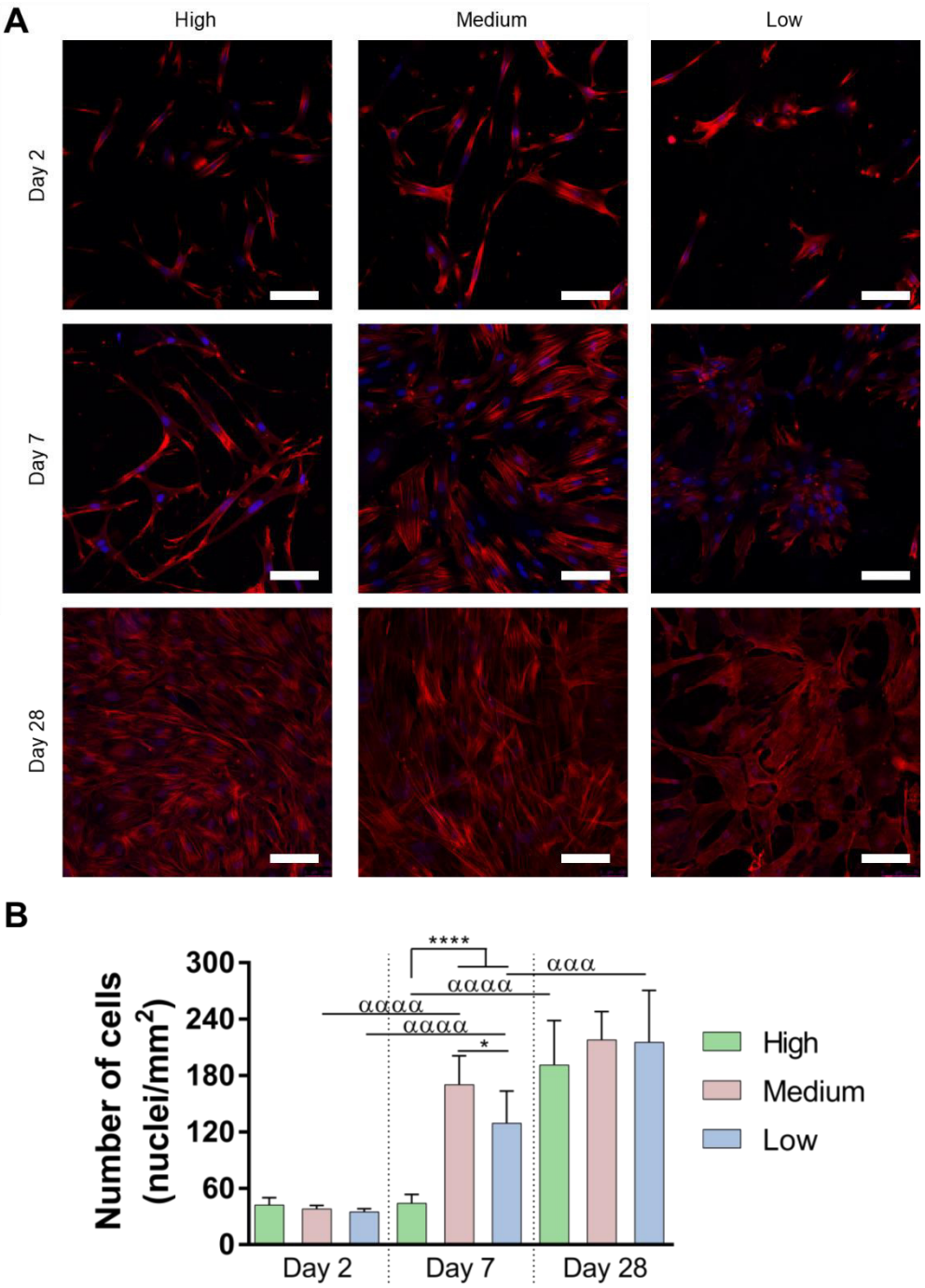

Supplementary Figure V-7 *In vitro* evaluation of hASCs behaviour. (A) Fluorescence microscopy images showing cell morphology after 2, 7 and 28 days in culture. Staining actin (red) and nuclei (blue). (B) Analysis of cell proliferation rate. Statistical significance: '*'- between formulations and 'α' - between timepoints. Scale bar: 100 µm.

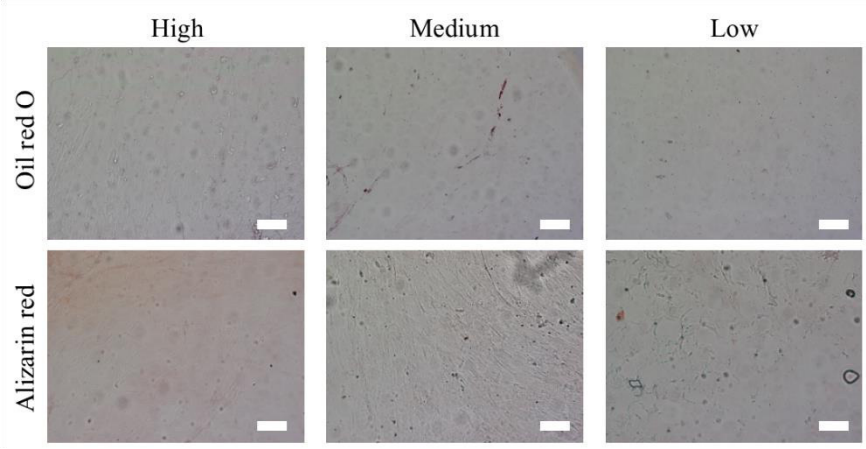

Supplementary Figure V-8 Analysis of hASCs commitment to the adipogenic (Oil red O staining) and osteogenic (Alizarin red staining) lineages. Potential adipogenesis would be indicated by the accumulation of neutral lipid vacuoles that stain with Oil red O (top) and osteogenesis would be indicated by the increase of calcium deposition (bottom). None of the different formulations analyzed stained for these markers. Scale: 50 µm.

V-6. REFERENCES

[1] D. Klemm, E.D. Cranston, D. Fischer, et al., Nanocellulose as a natural source for groundbreaking applications in materials science: Today's state, Mater. Today, 21 (2018) 720.

[2] B.B. Mendes, M. Gómez-Florit, R.A. Pires, et al., Human-based fibrillar nanocomposite hydrogels as bioinstructive matrices to tune stem cell behavior, Nanoscale, 10 (2018) 17388.

[3] B.B. Mendes, M. Gómez-Florit, P.S. Babo, et al., Blood derivatives awaken in regenerative medicine strategies to modulate wound healing, Adv. Drug Deliv. Rev., 129 (2018) 376.

[4] P.C. Ke, S. Lin, W.J. Parak, et al., A Decade of the Protein Corona, ACS Nano, 11 (2017) 11773.

[5] M.P. Monopoli, C. Åberg, A. Salvati, et al., Biomolecular coronas provide the biological identity of nanosized materials, Nat. Nanotechnol., 7 (2012) 779.

[6] C. Corbo, R. Molinaro, A. Parodi, et al., The impact of nanoparticle protein corona on cytotoxicity, immunotoxicity and target drug delivery, Nanomedicine, 11 (2015) 81.

[7] M. Mahmoudi, I. Lynch, M.R. Ejtehadi, et al., Protein–Nanoparticle Interactions: Opportunities and Challenges, Chem. Rev., 111 (2011) 5610.

[8] S. Schöttler, K. Landfester, V. Mailänder, Controlling the Stealth Effect of Nanocarriers through Understanding the Protein Corona, Angew. Chem. Int. Ed., 55 (2016) 8806.

[9] J. O'Brien, K.J. Shea, Tuning the Protein Corona of Hydrogel Nanoparticles: The Synthesis of Abiotic Protein and Peptide Affinity Reagents, Acc. Chem. Res., 49 (2016) 1200.

[10] D. Bondeson, A. Mathew, K. Oksman, Optimization of the isolation of nanocrystals from microcrystalline celluloseby acid hydrolysis, Cellulose, 13 (2006) 171.

[11] M.S. Reid, M. Villalobos, E.D. Cranston, Benchmarking Cellulose Nanocrystals: From the Laboratory to Industrial Production, Langmuir, 33 (2017) 1583.

[12] D. Xu, J.D. Esko, Demystifying Heparan Sulfate–Protein Interactions, Annu. Rev. Biochem., 83 (2014) 129.

[13] J.E. Scott, Structure and function in extracellular matrices depend on interactions between anionic glycosaminoglycans, Pathol. Biol., 49 (2001) 284.

[14] T. Miller, M.C. Goude, T.C. McDevitt, et al., Molecular engineering of glycosaminoglycan chemistry for biomolecule delivery, Acta Biomater., 10 (2014) 1705.

[15] N.S. Gandhi, R.L. Mancera, The Structure of Glycosaminoglycans and their Interactions with Proteins, Chem. Biol. Drug Des., 72 (2008) 455.

[16] S.S. Lee, T. Fyrner, F. Chen, et al., Sulfated glycopeptide nanostructures for multipotent protein activation, Nat. Nanotechnol., 12 (2017) 821.

[17] Direcção Geral da Saúde, Norma 010/2012: Utilização Clínica de Concentrados Plaquetários no Adulto, (2012) Portugal.

[18] J. Schwartz, A. Padmanabhan, N. Aqui, et al., Guidelines on the Use of Therapeutic Apheresis in Clinical Practice–Evidence-Based Approach from the Writing Committee of the American Society for Apheresis: The Seventh Special Issue, J. Clin. Apheresis, 31 (2016) 149.

[19] S.J. Slichter, Evidence-Based Platelet Transfusion Guidelines, Hematology Am. Soc. Hematol. Educ. Program, (2007) 172.

[20] R.M.A. Domingues, M. Silva, P. Gershovich, et al., Development of Injectable Hyaluronic Acid/Cellulose Nanocrystals Bionanocomposite Hydrogels for Tissue Engineering Applications, Bioconjugate Chem., 26 (2015) 1571.

[21] S. Beck, M. Méthot, J. Bouchard, General procedure for determining cellulose nanocrystal sulfate half-ester content by conductometric titration, Cellulose, 22 (2015) 101.

[22] J. Schindelin, I. Arganda-Carreras, E. Frise, et al., Fiji: an open-source platform for biological-image analysis, Nat. Methods, 9 (2012) 676.

[23] L.P. Kozlowski, IPC – Isoelectric Point Calculator, Biol. Direct, 11 (2016) 55.

[24] P.P. Carvalho, X. Wu, G. Yu, et al., The effect of storage time on adipose-derived stem cell recovery from human lipoaspirates, Cells Tissues Organs, 194 (2011) 494.

[25] L. Lewis, M. Derakhshandeh, S.G. Hatzikiriakos, et al., Hydrothermal Gelation of Aqueous Cellulose Nanocrystal Suspensions, Biomacromolecules, 17 (2016) 2747.

[26] D. Peschel, K. Zhang, N. Aggarwal, et al., Synthesis of novel celluloses derivatives and investigation of their mitogenic activity in the presence and absence of FGF2, Acta Biomater., 6 (2010) 2116.

[27] D. Peschel, K. Zhang, S. Fischer, et al., Modulation of osteogenic activity of BMP-2 by cellulose and chitosan derivatives, Acta Biomater., 8 (2012) 183.

[28] I. Kalashnikova, H. Bizot, B. Cathala, et al., Modulation of Cellulose Nanocrystals Amphiphilic Properties to Stabilize Oil/Water Interface, Biomacromolecules, 13 (2012) 267.

[29] C. Bruel, J.R. Tavares, P.J. Carreau, et al., The structural amphiphilicity of cellulose nanocrystals characterized from their cohesion parameters, Carbohydr. Polym., 205 (2019) 184.

[30] A. Gessner, A. Lieske, B.R. Paulke, et al., Influence of surface charge density on protein adsorption on polymeric nanoparticles: analysis by two-dimensional electrophoresis, Eur. J. Pharm. Biopharm., 54 (2002) 165.

[31] S. Kinzebach, L. Dietz, H. Klüter, et al., Functional and differential proteomic analyses to identify platelet derived factors affecting ex vivo expansion of mesenchymal stromal cells, BMC Cell Biology, 14 (2013) 48.

[32] P.-J. Yu, G. Ferrari, A.C. Galloway, et al., Basic fibroblast growth factor (FGF-2): The high molecular weight forms come of age, J. Cell. Biochem., 100 (2007) 1100.

[33] S. Viau, A. Lagrange, L. Chabrand, et al., A highly standardized and characterized human platelet lysate for efficient and reproducible expansion of human bone marrow mesenchymal stromal cells, Cytotherapy, 21 (2019) 738.

[34] A.W.M. Lee, P.S. Oates, D. Trinder, Effects of cell proliferation on the uptake of transferrin-bound iron by human hepatoma cells, Hepatology, 38 (2003) 967.

[35] G.L. Francis, Albumin and mammalian cell culture: implications for biotechnology applications, Cytotechnology, 62 (2010) 1.

[36] H.G. Augustin, G. Young Koh, G. Thurston, et al., Control of vascular morphogenesis and homeostasis through the angiopoietin–Tie system, Nat. Rev. Mol. Cell Biol., 10 (2009) 165.

[37] V. Llopis-Hernández, M. Cantini, C. González-García, et al., Material-driven fibronectin assembly for high-efficiency presentation of growth factors, Sci. Adv., 2 (2016) e1600188.

[38] M.M. Martino, P.S. Briquez, A. Ranga, et al., Heparin-binding domain of fibrin(ogen) binds growth factors and promotes tissue repair when incorporated within a synthetic matrix, Proc. Natl Acad. Sci., 110 (2013) 4563.

[39] I.B. Robertson, D.B. Rifkin, Regulation of the Bioavailability of TGF-β and TGF-β-Related Proteins, CSH Perspect. Biol., 8 (2016).

[40] B.F. Boyce, M.J. Zuscik, L. Xing, Chapter 11 - Biology of Bone and Cartilage, in: R.V. Thakker, M.P. Whyte, J.A. Eisman, T. Igarashi (Eds.) Genetics of Bone Biology and Skeletal Disease (Second Edition), Academic Press, 2018, pp. 173.

Chapter VI

Human platelet lysate-based nanocomposite bioink for bioprinting hierarchical fibrillar structures

Chapter VI

Human platelet lysate-based nanocomposite bioink for bioprinting hierarchical fibrillar structures

ABSTRACT

Three-dimensional (3D) bioprinting holds the promise to fabricate tissue and organ substitutes for regenerative medicine. However, the lack of bioactive inks to fabricate and support functional living constructs is one of the main limitations hindering the progress of this technology. In this study, a biofunctional human-based nanocomposite bioink (HUink) composed of platelet lysate hydrogels reinforced by cellulose nanocrystals is reported. When combined with suspended bioprinting technologies, HUink allows the biofabrication of 3D freeform constructs with high resolution and integrity, mimicking the hierarchical nano-to-macro fibrillary composition of native tissues. Remarkably, HUink supports bioprinting of stem cells with high viability immediately after extrusion and over long-term cell culture without the need for additional biochemical or animal-derived media supplementation. As opposed to typical polymer-based bioinks, the pool of growth factors, cytokines and adhesion proteins in HUink boosts cell spreading and proliferation, stimulating the fast production of cell-secreted extracellular matrix. This innovative bioprinting platform with unpaired biofunctionality allows the fabrication of complex freeform cell-laden constructs that can ultimately be applied in the development of xeno-free 3D tissue models for in vitro research or to develop tissue and organ surrogates for clinical applications.

This chapter is based on the following publication: ***B. B Mendes****, M. Gómez-Florit, A. G. Hamilton, M. S. Detamore, R. M. A. Domingues, R. L. Reis, M. E. Gomes. Human platelet lysate-based nanocomposite bioink for bioprinting hierarchical fibrillar structures. Biofabrication. 12 (1), 015012.*

VI-1. INTRODUCTION

Three-dimensional (3D) bioprinting technology, in particular extrusion-based systems, have been receiving considerable attention in tissue engineering and regenerative medicine as a cutting-edge technique to fabricate functional tissue and organ surrogates [1, 2]. However, commonly used bioinks, i.e. biomaterials that contain biological molecules and/or cells, are often limited to the "biofabrication window", in which the proposed hydrogel inks cannot be printed with high resolution and under cytocompatible conditions, delaying the clinical translation of personalized bioprinted structures [3, 4]. The main limitations of traditional hydrogel-based bioinks are generally related to the high polymer concentration and crosslinking density needed for the biofabrication of constructs with high printing fidelity, which compete with their biocompatibility and leads to detrimental effects over cell survival, spreading and nutrient diffusion [3, 5]. In order to overcome these limitations, current research has focused on the development of advanced bioinks based on supramolecular, multimaterial and nanocomposite hydrogels, a topic which has been widely covered by recent reviews [2, 3]. Another key aspect of advanced bioinks is their biofunctionality, as they should ideally be able to build or recreate the organization of extracellular matrix (ECM) in the native tissues and its role in supporting the cell survival, organization and differentiation of embedded cells. The functionalization of hydrogel polymers with cell-adhesion peptide sequences, stimuli responsive moieties or incorporation/conjugation of growth factors has been explored to improve the biological properties of bioinks [6]. Even though, the multiple synthesis steps required by such strategies as well as the need to use high doses of recombinant growth factors, due to their fast degradation and loss of bioactivity, represents prohibitive costs for widespread application [7]. Another important and generally overlooked limitation of hydrogels is that they are formed from crosslinked networks of polymer molecules which do not mimic the fibrous nature of the ECM. The filamentous architecture of the ECM strongly influences normal cell and organ function because it has a fundamental impact over e.g. cells' phenotype, migration, mechanotransduction, growth factors signaling pathways and mass transport of nutrients and waste (due to the large pore size of their networks) [8-10]. To recreate the native ECM fibre-based architecture and topology, different bioinks have been developed based on decellularized ECM [11] or the self-assembly of biomolecules, e.g. peptide amphiphiles, into biomimetic 3D fibrillar hydrogels [12, 13]. However, decellularized ECM hydrogels are typically derived from animal tissues and show high variability, while the gelation mechanisms of self-assembled fibrillar hydrogels usually proceed in non-biocompatible conditions that together with intricate synthesis pathways and lack of intrinsic biofunctionality, still limits the potential of these biomaterials in this field. Overall,

most of the current bioinks are not yet able to mimic the native tissue's ECM fibrillar architecture across multiple length scales while simultaneously showing high biocompatibility and incorporating key cell instructive bioactive elements, which are critical to move 3D bioprinting a step towards the generation of functional tissues and organs.

Blood derivatives, such as platelet lysate (PL), have attracted great attention as an inexpensive milieu of bioactive molecules (e.g., growth factors, cytokines), self-assembling scaffolding proteins (e.g., fibrinogen, fibronectin, vitronectin), and antimicrobial peptides (e.g., platelet factor-4) capable of enhancing angiogenesis, stem cell recruitment, and tissue regeneration [14, 15]. To leverage these key biological cues, injectable PL-based nanocomposite fibrillar hydrogels were developed by triggering the natural in-situ clotting cascade in the presence of surface functionalized cellulose nanocrystals (CNC) [16]. These hydrogels self-supported serum free culture of encapsulated stem cells, which showed excellent adhesion, fast proliferation and production of their own ECM, mainly due to the hydrogel physicochemical cues and intrinsic biological properties, i.e. These hydrogels self-supported serum free culture of encapsulated stem cells, which showed excellent adhesion, fast proliferation and production of their own ECM, mainly due to the hydrogel physicochemical cues and intrinsic biological properties, i.e. presence of adhesion motifs in the fibrillar proteins and PL bioactive molecules. Here, we exploit this concept to develop and test a human-based bioink (HUink) for the freeform biofabrication of bioactive and biologically-relevant 3D structures. This advanced bioink enables the bottom-up biofabrication across multiple length scales into complex nano-to-macroscopic 3D fibrillar objects. Remarkably, human adipose-derived stem cells (hASCs) encapsulated in HUink present high cell viability after printing, while showing an exceptionally fast spreading, growth and synthesis of new ECM within the 3D construct over time in serum free culture conditions. Such physical and biofunctional properties demonstrate that HUink is a powerful bioink to print dynamic and personalized 3D living constructs that can be maturated *in vitro* in xeno-free conditions.

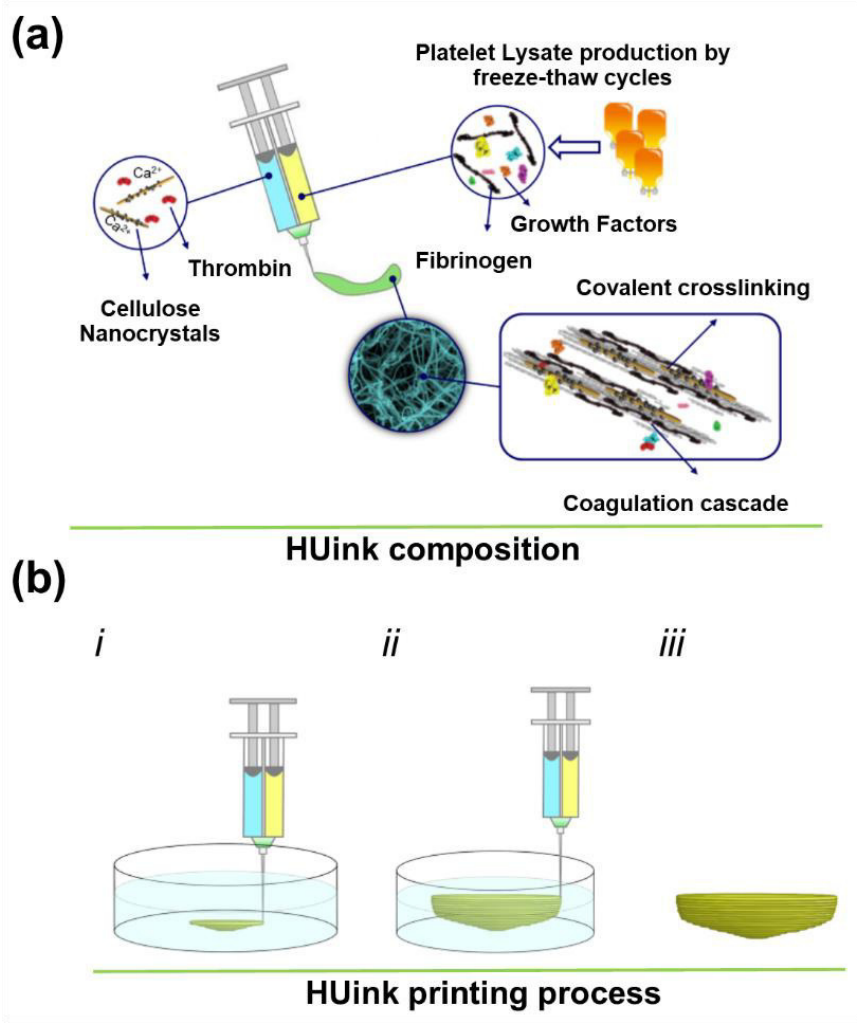

Scheme VI-1 HUink composition and bioprinting process. (a) Schematic illustration of HUink components and the crosslinking reaction. (b) Biofabrication process, namely HUink is extruded layer-by-layer into the agarose support bath (i), after the complete printing of the freeform construct and its full crosslinking (ii), the freeform 3D construct is removed from the support bath (iii).

VI-2. MATERIALS AND METHODS

VI-2.1. Precursors and bioinks preparation

VI-2.1.1. Platelet lysate preparation

Platelet concentrates were obtained from healthy human blood donors provided by Serviço de Imuno-Hemoterapia of Centro Hospitalar de S. João, EPE (Porto, Portugal). The procedures were approved by

the University of Minho Ethics Committee and all the platelet products were biologically qualified according to the Portuguese legislation. Platelet count was performed at HSJ and concentrates with a platelet count below 1 million platelet μL^{-1} were rejected. PL were prepared according to a previously established protocol [17]. Briefly, the pooled platelet concentrate samples (12 donors) were subject to three repeated temperature cycles (frozen with liquid nitrogen at −196 °C and heated at 37 °C water bath). Aliquots of PL were stored at −80 °C. Prior to use, the lysate was centrifuged at 4000 G for 5 minutes and filtered through a 0.45 μm pore filter to remove the platelet membrane fragments. For the concentration of PL, a reverse osmosis procedure using benzoylated cellulose dialysis membranes (2000 Da NMWCO, Sigma-Aldrich, USA) against poly(ethylene glycol) (average MW 20,000 kDa, Sigma-Aldrich, USA) was performed for 6 h at 4 °C.

VI-2.1.2. Aldehyde-CNC production

CNC were extracted from microcrystalline cellulose (MCC) powder (Sigma-Aldrich, USA) following the typical sulfuric acid hydrolysis according to Bondeson with minor modifications [18]. Concentrated sulfuric acid (95–98% from Sigma-Aldrich, USA) was added dropwise up to a final concentration of 64 wt.% and the obtained suspension was heated to 44 °C for 2 h. The final working suspension of modified CNC was collected and stored at 4 °C. Aldehyde CNC (a-CNC) were produced by sodium periodate ($NaIO_4$) oxidation [19]. In a typical experiment, $NaIO_4$ (Sigma-Aldrich, USA) was added to CNC aqueous suspension (1.5 wt.%) in a 1:1 molar ratio (NaIO4:CNC) for 12 hours preventing. The desired concentration of the working suspension was adjusted by concentrating it against poly(ethylene glycol) (average MW 20,000 kDa, Sigma-Aldrich, USA) using benzoylated cellulose dialysis membranes (2000 Da NMWCO, Sigma-Aldrich, USA). a-CNC were imaged using atomic force microscopy. Drops of the diluted CNC suspension (0.0015 wt.%) were deposited on freshly cleaved and carefully washed mica discs (9.9 mm diam. 0.27 thick). The suspension was left to adsorb for 15 minutes and the excess liquid was removed. The disc was washed two times with ultra-pure water and allowed to dry overnight. The samples were imaged in tapping mode with a MultiMode AFM (Bruker, USA) and the particle size distribution was determined with Gwyddion software (n=50).

VI-2.1.3. HUink preparation

Stock solutions of PL and a-CNC were produced and fully characterized as previously described. Double-barrel L-system syringes (1:1 ratio from Medmix, Switzerland) with a customized static mixer tip of 3 mm diameter and 6 mm height (102915, Medmix, Switzerland) were used to extrude the bioink. Barrel A was filled with PL (67-160 mg. mL^{-1} of total dry mass). Barrel B contained thrombin from human plasma (5 U. mL^{-1}, Sigma-Aldrich, USA), $CaCl_2$ (10 mM, Sigma-Aldrich, USA) and a-CNC water dispersion (0-2.88 wt.%). Concentrated PL (160 mg. mL^{-1}) and a-CNC at approximately 18 wt.% of PL total protein content (2.88 wt.%) were used to produce HUink, unless otherwise stated. Based on the typical fibrinogen concentration range in PL (454 ± 75 μg. mL^{-1}) 21 μg of Alexa Fluor® 488 conjugated fibrinogen from human plasma (Thermo Fisher Scientific, USA) were added to each 1 mL of PL solution (barrel A) for visualization of the fibrin network using confocal microscopy.

VI-2.1.4. Alginate and gelatin-methacrylate bioinks

A solution of 4% (w/v) sodium alginate and 0.4% (w/v) hyaluronic acid (MW 200,000, Lifecore Biomedical, USA) was prepared in PBS and stirred at 20 °C for 48 h, as previously described [20].

Gelatin-methacrylate (GelMA) was synthesized by reaction of gelatin (type-A, porcine skin, Sigma-Aldrich) with methacrylic anhydride (Sigma-Aldrich), as previously decribed [21]. The final bioink consisted in a solution of 10% (w/v) GelMA and 0.5% Irgacure 2959 (Sigma-Aldrich) dissolved in PBS. Right after printing, constructs were photopolymerized by exposure to ultraviolet light (320-500 nm, 1.2 mW cm^{-2}) for 60 s (Omnicure S2000).

VI-2.2. Support matrix preparation

The support fluid gel was prepared as described by Moxon et al.[22] with slight modifications. A 0.5 wt.% agarose (SeaKem, Lonza, USA) solution containing 11 mM $CaCl_2$ (Sigma-Aldrich, USA) was autoclaved and cooled down to 20 °C under constant shear using a magnetic stirrer rotating at 700 rpm in order to form agarose microparticles.

VI-2.3. 3D printing of complex constructs using HUink

All 3D printing was performed using a Creatr Dual-Extruder (Leapfrog, The Netherlands). One thermoplastic extruder was removed from the *xy*-axis carriage and the stepper motor was used to drive the plunger of a customized double-barrel syringe extruder. The custom syringe extruder was printed in acrylonitrile butadiene styrene (Leapfrog, The Netherlands) using the thermoplastic extruder of the same printer. 3D models were created using Autodesk Inventor (Adobe, USA) and exported to STL files. The file of the human femur was downloaded from NIH 3D Print Exchange and the leaf vasculature was downloaded from Thingiverse under creative commons licensing by Alajaz. The STL files were opened in Repetier-Host and sliced into 200-µm-thick layers by Sli3r software to generate the G-code for 3D printing. The printing was done at room temperature (20 °C) at a speed of 5 mm s^{-1}, unless otherwise stated, and different infill patterns and densities were used. To print inside of the support matrix, a custom post-processing script was added to Slic3r to move the *z*-stage and avoid the collision of the syringe with the petri dishes. HUink precursors were loaded into a double-barrel syringe capped with 27-gauge stainless steel needles (Nordson EFD, USA), unless otherwise stated. A container large enough to hold the construct was loaded with agarose support matrix and placed at the printing stage. The extruder was manually controlled from the Repetier software to push the plunger to initiate the extrusion right before start printing to avoid clogging in the nozzle. Constructs were allowed to full crosslink for 2 h before gently replacing the support matrix for PBS or culture media.

VI-2.4. Scanning electron microscopy

Printed hydrogels were fixed in 2.5% glutaraldehyde (Merck, Germany) for 30 minutes. After fixation, samples were solvent exchanged from water to ethanol (ethanol gradient from 25, 50, 75 and 99.9 vol%) for 4 hours and then critical point dried with CO_2. After immersion in liquid nitrogen, the samples were freeze-fractured to expose their inner structures and sputter coated (30 seconds at 20 mA, Cressington) with gold prior to observation in a scanning electron microscope (JSM-6010LV, JEOL, Japan).

VI-2.5. Cell isolation

hASCs were obtained from lipoaspirate samples of the abdominal region of patients undergoing plastic surgery after the signature of an informed consent, under the scope of protocols established with

Hospital da Prelada (Porto, Portugal) with the approval of the Hospital and University of Minho Ethics Committee. The hASCs isolation and stemness characterization were performed as previously optimized and described [16, 23]. hASCs were loaded to PL solution at a density of $2x10^6$ cells per 1 mL of PL ($1x10^6$ cells per 1 mL of final hydrogel). In the alginate-based bioink and GelMA bioinks, hASCs were loaded at a density of $1x10^6$ cells per 1 mL of hydrogel. All cell culture assays of hASCs encapsulated in bioinks were performed using culture media without serum supplementation.

VI-2.6. *In vitro* cell culture studies

To assess the shape fidelity of the 3D bioprinted construcs over time, 1 x 1 x 0.25 cm square lattices with 50% infilling were printed. At 1, 2 and 9 d after printing, top-view pictures of the constructs were taken with a digital camera and its surface area was measured using ImageJ. The shape factor was calculated by dividing the area of the printed construct at each culture period by the area of the 3D model.

VI-2.6.1. Fluorescent staining

At 2 h and 72 h after printing, cellular viability was assessed using Calcein AM (Thermo Fisher Scientific, USA) and propidium iodide (Thermo Fisher Scientific, USA) to stain live and dead cells, respectively. After 9 d of culture, hydrogels were washed with PBS and then fixed in 10% formalin (Thermo Fisher Scientific, USA) for 15 min at RT and permeabilized using 0.2 vol.% Triton-X100 (Sigma-Aldrich, USA). After washing, samples were incubated with 1:200 v/v rhodamine-conjugated phalloidin (Sigma-Aldrich, USA) for 10 minutes and 1:1000 v/v 4', 6-diamidino- 2-phenylindole (DAPI, Sigma-Aldrich, USA) for 20 minutes (dilutions in PBS). For collagen type I staining, samples were blocked using 3 w/v.% BSA and incubated with 1:500 v.% solution of specific primary antibody (ab90395, Abcam, UK). Then, samples were incubated with 1:200 v/v Alexa Fluor® 488 conjugated secondary antibody (Thermo Fisher Scientific, USA). For some experiments, hASCs were labelled with Calcein AM or with cell tracker CM-DiI dyes, prior to bioprinting. The HUink constructs were observed under a confocal microscope TCS SP8 (Leica Microsystems, Germany).

VI-2.6.2. Metabolic activity

Metabolic activity in the different bioinks was assessed at 1, 2 and 7 d using Alamar Blue assay (Bio-Rad, USA), following the manufacturer's instructions.

VI-2.7. Rheology

A Kinexus Pro Rheometer (Malvern Instruments, United Kingdom) was used to measure the viscoelastic properties of the materials. Time-sweep tests were applied to study polymerization kinetics of HUink. Immediately after dispensing 320 µL of extruded solution on the bottom plate, a 20 mm diameter top plate was lowered to a final gap of 1 mm (parallel plate set up). A thin film of mineral oil was poured over the exposed surface to reduce water evaporation. This time point was defined as the starting time (t=0). Time-sweep assays were performed at a strain amplitude of 1% and frequency of 1 Hz, and storage modulus values were monitored continuously at 10 seconds intervals. In shear sweep tests a 40 mm 4° cone and plate geometry was used. The solutions viscosity was measured in response to the increasing of shear rate from 0.001 to 100 s^{-1}. The same rheological set-up was used to perform frequency-sweep tests in the agarose support matrix with slight modifications from Moxon's work [22]. In stress-weep tests, agarose microparticles were subjected to a shear stress of 0.1-100 Pa at a constant oscillatory frequency of 1 Hz. All measurements were performed in triplicate. The shear stress (τ (Pa)) was calculated using Equation VI-1. Shear rate was calculated using Equation VI-2: [24, 25].

$$\tau = \eta\dot{\gamma}$$

Equation VI-1 Quantification of shear stress. Where η (Pa s) is viscosity and $\dot{\gamma}$ (s^{-1}) the shear rate in the nozzle during extrusion

$$\dot{\gamma} = \frac{3n+1}{n}\frac{Q}{\pi R^3}$$

Equation VI-2 Quantification of shear rate. Where Q ($m^3 s^{-1}$) is the flow, R (m) the radius of the nozzle and n is the flow behavior index derived from the slope of the shear stress to shear rate graph using the Power-Law equation from 1 to 100 s^{-1}.

VI-2.8. Diffusion of molecules through the bioinks

HUink and alginate-based bioink were produced as previously described and injected in the central chamber of a chemotaxis µ-slide (Ibidi, Germany) and the side chambers of the slide were filled with 10

mM $CaCl_2$ allowing the hydrogels crosslinking to proceed for 2 h. Then, the left chamber was filled with 25 µg. mL^{-1} of 20 kDa dextran-FITC (Sigma-Aldrich, USA) in PBS and the right chamber with PBS. Fluorescence microscopy (Axio Observer, Zeiss, Germany) with incubation to simulate cell culture conditions (37 °C, 5% CO_2) was used to observe the diffusion of dextran-FITC through the bioinks over time (images were acquired every 3 min for 2 h). The mean fluorescence intensity on a selected region of interest (ROI) in the right chamber was plotted against time.

VI-3. RESULTS AND DISCUSSION

VI-3.1. Bioprinting concept and characterization of the nanocomposite bioink

HUink is obtained using a simple double barrel injection system filled with PL in one compartment and with thrombin, calcium and aldehyde-functionalized CNC (1.22-2.88 wt.%) in the other (Squeme VI-1A and Supplementary Figure VI-1). We first optimized the bioink precursors to obtain adequate viscosity and polymerization kinetics that allow for extrusion at low printing pressures (i.e. shear-thinning behaviour) and simultaneously leading to a self-assembled and crosslinked fibrillar matrix (Figure VI-1A and B) by the activation of the fibrin polymerization with thrombin and calcium and the formation of Schiff base bonds between a-CNC and amine groups of PL proteins (Squeme VI-1A) [16]. PL was produced by the well-stablished method of repeated freeze/thaw cycles of platelet concentrates, which promotes platelet disruption and the release of the bioactive protein content [14]. To increase the protein content in the nanocomposite bioink, the initial PL was concentrated by reverse osmosis. The resulting solutions had a protein content of 67 and 160 mg. mL^{-1}, respectively, a process that had no significant impact on its viscosity (Figure VI-1A). Among the tested formulations, we selected the conditions that result in printed structures with mechanical integrity and stability (i.e. PL 160 mg. mL^{-1} and CNC 2.88 wt.%) (Supplementary Figure VI-2). Our bioprinting system was implemented in a broadly accessible 3D printing technology, which includes a commercially available Creatr 3D printer (Leapfrog), standard open source 3D printing software, and a modified stepper motor-driven thermoplastic extruder adapted to drive the plunger of 1.5 mL double barrel syringes (1:1) coupled with a nozzle equipped with a static mixer (Squeme VI-1A). Although HUink was easily extrudable through thin nozzles (150-250 µm), its low viscosity and gelation kinetics do not allow building layer-by-layer 3D objects (Figure VI-1A and B). Interestingly, recent works have shown that suspended manufacturing techniques allow for fabrication of 3D freeform hydrogel

constructs with outstanding complexity and with minimal dependence on hydrogel rheological properties [20, 22, 26]. Following this concept, we used an agarose microparticles support matrix, [22] which behaves as a viscoelastic fluid and can self-heal after nozzle movement (Figure VI-1C and D), as a 3D writing paper for HUink bioprinting. Simultaneously, the support matrix keeps our bioink in the printed position of the 3D space with minimal diffusion. Additionally, it enables the complete self-polymerization of HUink filaments while integrating the multiple printed layers by covalent crosslinking at crossing interfaces, resulting in high-fidelity constructs. Once the hydrogel crosslinking process is complete (reaches the steady state after ~1 hour, at 37° C; Figure VI-1B), agarose can easily be washed out using PBS or culture media (SquemeVI-1B).

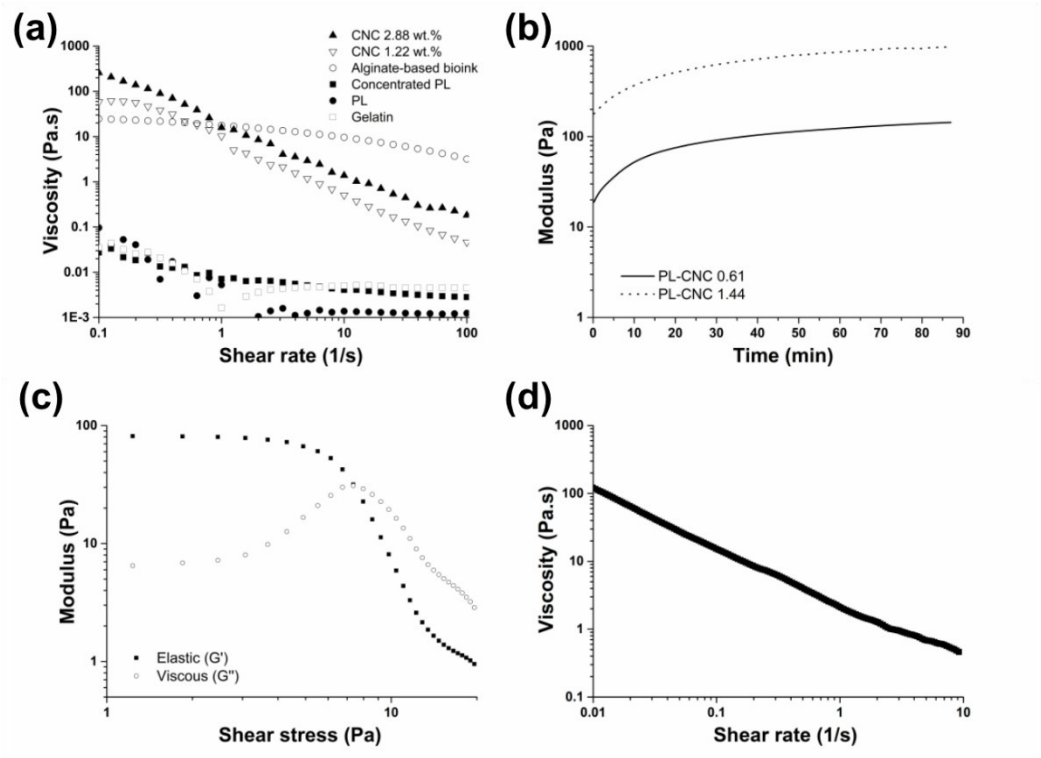

Figure VI-1 Rheological characterization. (a) Bioink precursor's viscosity in response to increasing shear rates from 0.1 to 100 s^{-1}. (b) Polymerization of PL-CNC biomaterial with different precursors concentrations, PL-CNC 0.61 data obtained from [16]. Agarose microparticulate bath rheological properties, namely (c) elastic and viscous modulus in response to increasing shear stress and (c) viscosity in response to increasing shear rates.

VI-3.2. HUink printability and hierarchical structure

The printability of the developed bioink was assessed by printing single filaments into the support matrix using different printing parameters. In order to observe the structure of the 3D printed hydrogel using confocal microscopy, fluorescent-labelled fibrinogen was added to PL. The diameter of the printed filaments (102.3±21 to 443.3±71.9 µm) could be controlled depending on the printing speed (5 to 30

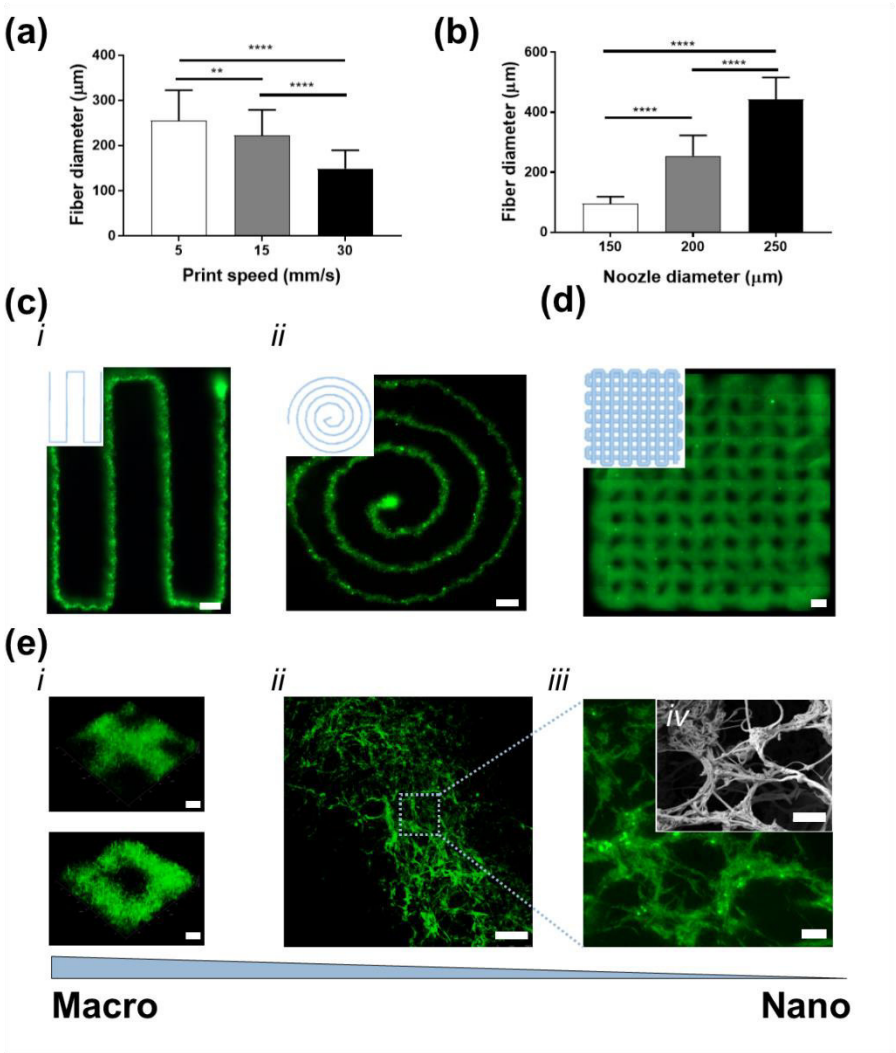

Figure VI-2 HUink bioprinting performance and fibrillar hierarchical structure. Filaments with different widths were printed into the agarose support bath (a) from a 27-gauge needle and varying the velocity and (b) with a velocity of 5 mm/s and modifying the needle diameter. (c) HUink printed into a continuous filament (i) or a concentric circle (ii) 2D pattern. (d) Thick 3D square lattice construct (30 layers). (e) Hierarchical fibrous structure from the macroscale pattern (i) of micro filaments (ii) composed of self-assembled fibrin nanofibrils (iii-iv). Staining in (c-e): fibrin-AlexaFluor 488 (green). Statistical differences: evaluated by one-way ANOVA using Tukey's multiple comparisons: ** $P < 0.01$ and **** $P < 0.0001$. Scale bars: (c) 250 µm, (d) 1 mm, (e-i) 200 µm, (e-ii) 100 µm, (e-iii) 10 µm and (e-iv) 2 µm.

mm. s^{-1}) and nozzle size (25G to 28G, corresponding to 250 to 150 µm internal diameter) (Figure VI-2A and B, Supplementary Figure VI-4). Among tested conditions, the filaments printed with 27-gauge needle and at 5 mm. s^{-1} showed the highest fidelity and processability, and were therefore applied in the subsequent bioprinting assays. We could continuously print simple rectilinear lines in one axis, as well as patterns in two degrees of freedom with a rapid hydrogel deposition and minimal diffusion (Figure VI-2C). Moreover, we were able to print in the 3D space constructs with multiple layers, e.g. a thick (5 mm) square lattice structure (Figure VI-2D). HUink enabled the biofabrication of interconnected hierarchical fibrillar architectures spanning multiple length scales, starting from the nano self-assembled fibrin\CNC

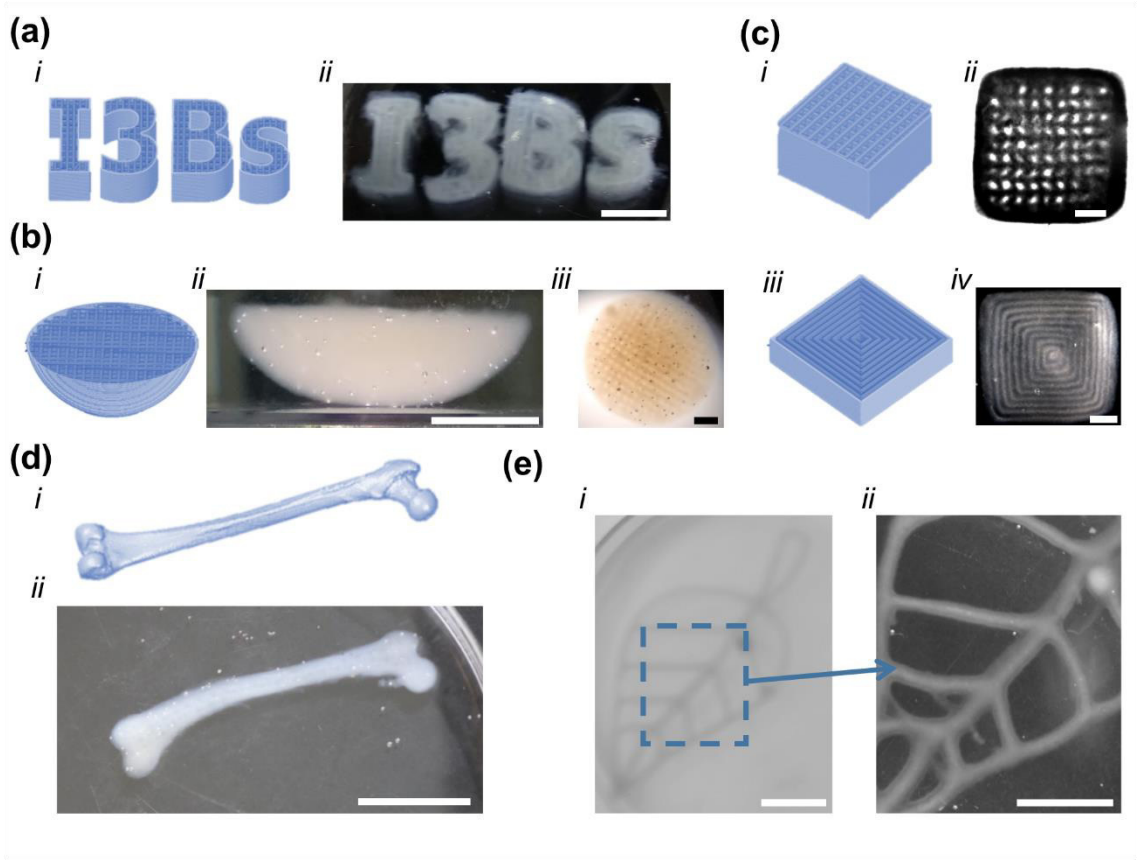

Figure VI-3 Examples of 3D printed constructs using HUink. (a) A 3D model of the letters "I3BS" printed layer-by layer (i) in the respective printed 3D construct with high integrity (ii). (b) A hemisphere model processed to print a freeform 3D structure (i), viewed from lateral (ii) and top down (iii) views. (c) A standard square model with 50% linear (0-90 °) (i) or 100% concentric infill pattern (iii) used to fabricated 3D constructs with 32 (ii) and 14 (iv) layers. (d) A scaled-down human femur model was printed using HUink (i) and after removal from the agarose bath (ii), it closely resembles the 3D model. (e) A leaf vasculature embedded in the agarose support bath (i) and a zoomed-in view of the leaf structural network (ii). Scale bars: (a-i) 10 mm, (b-ii) 10 mm, (b-iii) 5 mm, (c) 2 mm and (d-e) 10 mm.

fibrils (52.7±11.5 nm) bundled into fibres (260.3±102.1 nm) up to the macro infill patterns (Figure VI-2E). By recapitulating the hierarchical and topographical architecture of the native fibrillar ECM, our system will certainly benefit the biological outcomes of bioprinted tissues and organs when compared to other typical polymer-based hydrogel bioinks [27].

To show the versatility of HUink, we printed a variety of structures, including complex and large aspect ratio 3D objects, with different geometries and infill patterns (Figure VI-3). These large-scale structures showed a high shape and mechanical integrity due to the fibrin self-assembly process that induced covalent fusion between deposited filaments, avoiding the common delamination between layers observed in 3D printed hydrogels using polymers that crosslink right after extrusion (Figure VII-3) [28]. Moreover, leveraging on the printing technology using supporting materials, the 3D printing process is not limited to standard layer-by-layer self-supported constructs and allows freeform fabrication according to the intended computer-aided design. To demonstrate the freeform fabrication potential of the system,

we printed a freestanding convex hemisphere with a radius of ~12 mm that can maintain the complex printed geometry after removal of the supporting bath (Figure VI-3B). Next, to show the construction of biologically-relevant structures, we printed a scaled-down human femur reconstructed from medical images (Figure VI-3D) and a vasculature-like network from a leaf model (Figure VI-3E). The intrinsic self-assembly and hierarchical ECM-mimetic network of HUink combined with the precise control over structure and material deposition provided by the supporting matrix, demonstrate its potential for the biofabrication of personalized human-size constructs.

VI-3.3. Bioprinting performance and biofunctionality of HUink

The bioprinting and biological performance of the bioink was tested using hASCs. These cells are harvested from adipose tissue in large numbers and have been studied as an excellent and widely available multipotent cell source for different tissue engineering applications [29, 30]. To demonstrate the outstanding HUink biofunctionality, we compared it with alginate-based and GelMA bioinks, two widely used hydrogel material in this field due to their convenient crosslinking mechanisms based on the use of calcium ions or UV light, respectively [20, 24, 31, 32]. Furthermore, to show that HUink can self-support the culture of the bioprinted constructs, all cellular assays were performed without any type of serum supplementation. All the produced bioinks laden with hASCs were printed using the same conditions. Shortly after extrusion (2 hours), cells in HUink showed significantly higher viability (> 90%) than in alginate constructs (> 60%) and similar to GelMA (> 80%) (Figure VI-4A and B). These results confirm that the favourable rheological properties of HUink precursors (low viscosity of PL and marked shear-thinning behaviour of CNC) decrease the shear stress exerted over the cells in the nozzle during extrusion in comparison to the alginate-based bioink (32 and 1161 Pa, respectively), similar to the results obtained using GelMA (4 Pa). The shear stress, which is known to affect the short and long-term cell signaling and behavior, [24, 33, 34] exerted by HUink in combination with the cell-friendly printing process had a positive impact on post-printing cell viability. Notably, after 3 days in culture media hASCs already showed considerable cell spreading and spindle-like morphology whereas in alginate, cells maintained their original non-proliferative round shape, as would be expected from a hydrogel matrix without cell adhesion motifs. Moreover, although containing cell-binding motifs, cells in GelMA bioink also showed a similar

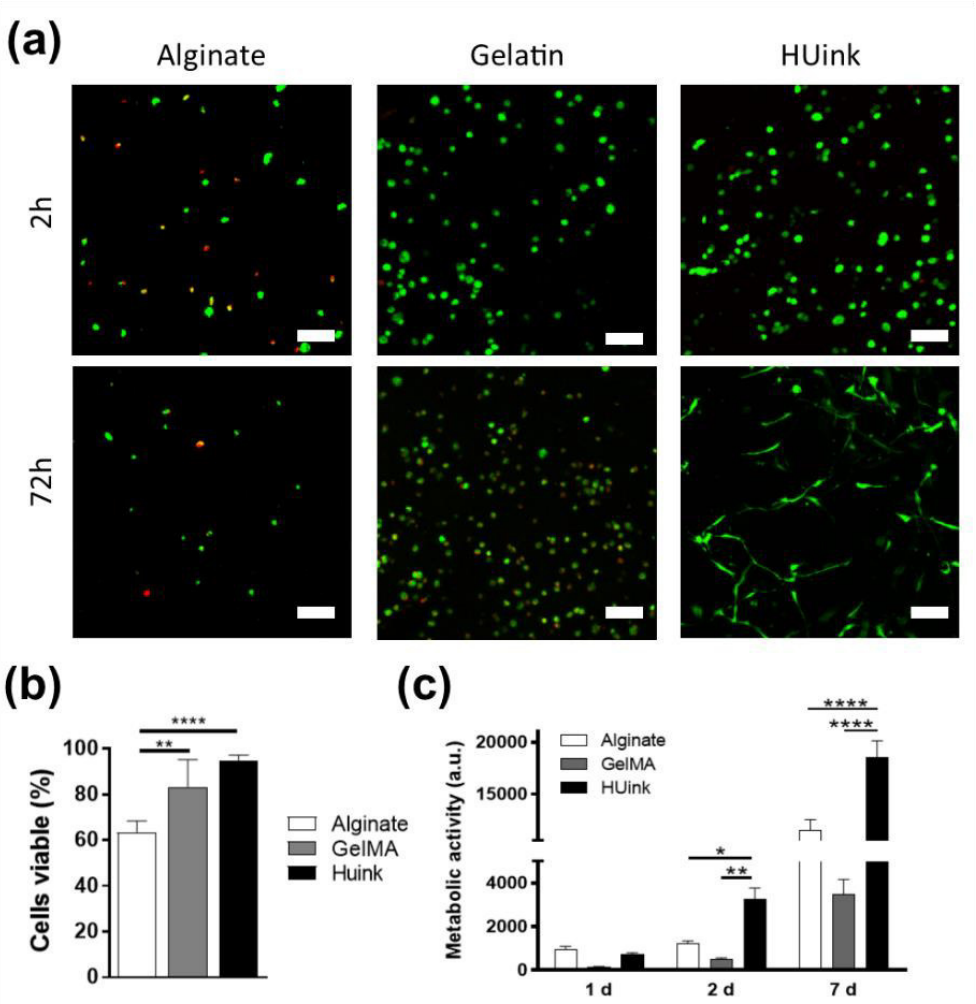

Figure VI-4 Biocompatibility and metabolic activity after bioprinting using hASCs. (a) Cell viability in alginate, GelMA and HUink 3D printed constructs with Live (green) / Dead (red) staining at 2 and 72 hours after printing. (b) Measurement of viable cells (live cells from Live/Dead staining) 2 hours after the printing process (n=3). (c) Metabolic activity of cells in the different bioinks over time. Statistical differences evaluated by (b) t-test: **** $P < 0.0001$; (c) one-way ANOVA using Tukey's multiple comparisons: * $P < 0.05$, ** $P < 0.01$ and **** $P < 0.0001$. Scale bars: (a) 100 μ m.

round shape morphology observed in cells encapsulated in the alginate-based bioink. Unlike these commonly used polymer matrices, the enriched bioactive milieu of HUink contains key temporary ECM proteins (e.g. fibrin, fibronectin and vitronectin) with native cell binding motifs, and growth factors with strong mitogenic action (e.g. platelet-derived growth factor and fibroblast growth factor 2) that favour cell adhesion and fast proliferation, respectively [14, 35]. This is reflected in the significantly higher metabolic activity of cells in HUink compared to the other two bioink materials (Figure VI-4C). In addition, although in this study pooled PL batches were prepared in house, the increasing trend on the use of standardized clinical grade human PL as xeno-free alternative to animal-derived serum in cell culture, [36, 37] represents an advantage over similar materials such as ECM bioinks (e.g. GelMA or decellurarized matrix), [11, 38] which are typically of xenogenic origin, a significant barrier for clinical translation, and present

high variability on the biochemical, topological and viscoelastic properties depending on the decellularization protocol. This further strengthens HUink concept, not only for research purposes, but also in terms of compliance with good manufacturing practices and clinical relevance.

After 9 days of culture, a high-density cellular network was formed independently of the infill pattern (50% or 100%) (Figure VI-5A), demonstrating that HUink promotes an unusual fast cell proliferation and cell-to-cell contact that contributes towards construct cellular densification. To further prove HUink superior bioactivity, GelMA constructs were printed and cultured in similar conditions and, as demonstrated in Figure VI-4A, they show lower cellularity and cell spreading, in agreement with their comparatively lower cell metabolic activity (Figure VI-4C). This unprecedented bioactive properties and ECM mimetic porous network represent a clear advantage over current biofabrication strategies, which typically depend on the use of perfusable channels or low infill patterns to minimize the diffusion limits of nutrients, metabolite and waste to sustain cell survival [26, 39, 40]. This was confirmed by comparing the differences between the diffusion of a model molecule through HUink and the alginate-based bioink (Supplementary Figure VI-3). Remarkably, hASCs encapsulated in HUink deposited considerable amounts of collagen type I after just 9 days of culture, showing that cells are able to remodel the hydrogel network and replace it by their own ECM (Figure VI-5B), contributing to the structural consolidation and integrity of the maturated constructs (Figure VI-5D and Supplementary Figure VI-5). To support this, we measured the shape factor of the 3D bioprinted constructs. These presented considerable shape fidelity to the 3D model right after printing (shape factor at day 0 = 1.1) although they show some contraction after 1 day (shape factor at day 1 = 0.8) but their dimensions and printed shape are well preserved through the following 9 days of culture (shape factor at day 9 = 0.8), closely maintaining the height of the original 3D model (0.26 vs 0.25 mm, respectively). Even though these constructs were bioprinted with 50% infilling,

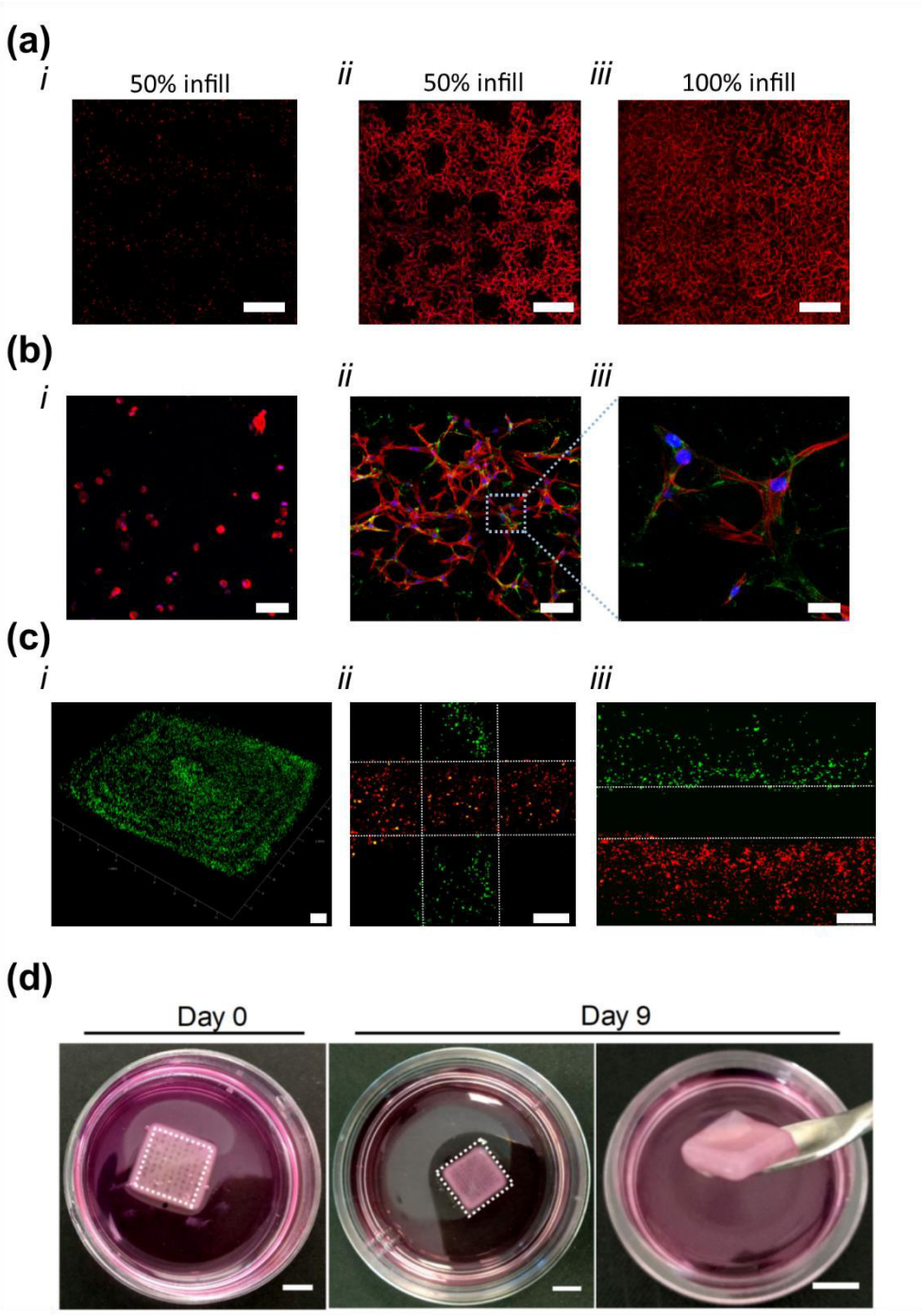

Figure VI-5 ECM remodeling and structural integrity. (a) Fluorescence microscopy images showing cytoskeleton (red) organization of 3D square constructs with 50% (i-ii) and 100% (iii) infill patterns printed using GelMA (i) or HUink (ii-iii). (b) Collagen I deposition (green), nuclei (blue) and cytoskeleton (red) in GelMA (i) and HUink (ii-iii) after 9 days in culture. (c) Control over the spatial arrangement of cells in 3D space using Calcein (green) (i) and over the 3D patterning using cells labeled with Calcein (green) and CM-DiI (red) in perpendicular (ii) and parallel (iii) deposition. (d) Structural integrity of HUink constructs over culture time. Scale bars: (a) 500 μ m, (b-i-ii) 75 μ m, (b-iii) 25 μ m, (c) 1 mm and (d) 0.5 cm. The dotted square in (d) represents the size of the initial 3D model.

their shape integrity over culture time follows a similar trend to the observed for casted PL-CNC hydrogels with comparable PL:CNC proportion and cell content evaluated in our previous work [16]. On the other

hand, cells in GelMA secreted minor amounts of collagen type I during this time period (Figure VI-5B), even though the constructs remained with a high shape integrity (shape factor at day 9 = 1.1) after 9 days of culture (Supplementary Figure VI-6), reflecting the low remodelling of this matrix by cells cultured under the serum-free conditions. Furthermore, hASCs labelled with two different cell trackers were printed in discrete locations of the 3D space, providing proof-of-concept for the potential of the system to recreate patterns of heterocellular tissues (Figure VI-5C).These results demonstrate that HUink not only possess outstanding biofunctional properties that can mimic the dynamics, composition and structure of native ECM and promote cell–cell communication, but collectively also results in the biofabrication of 3D living constructs, which are mechanically stabilized by a fast and newly deposited cell secreted matrix.

VI-4. CONCLUSIONS

We have developed a unique bioactive human-based bioink that can be successfully used with the suspended manufacturing technology to biofabricate complex 3D freeform structures. This combined bioprinting platform has the capacity to print diverse freestanding constructs with hierarchical fibrillar architecture, high resolution, structural integrity and biocompatibility. The bioactivity of HUink scaffolding proteins and soluble factors, the low diffusional limitations provided by the fibrillar matrix and their susceptibility for cell remodelling can remarkably boost cell proliferation and colonization of 3D printed structures in culture conditions without any type of serum supplementation. The HUink concept is further supported by the increasing standardised production of clinical grade human PL as a powerful alternative to animal-origin serum for human mesenchymal stem cell expansion in future cell factories. Therefore, HUink unleashes many potential strategies to fabricate complex and personalized living constructs that can faithfully mimic tissue anatomy, which combined with straightforward bioprinting strategies and xeno-free culture conditions, supports its potential both as a singular platform for in vitro 3D studies as well as for translation from bench-to-bedside.

VI-5. SUPPLEMENTARY INFORMATION

VI-5.1. Supplementary results

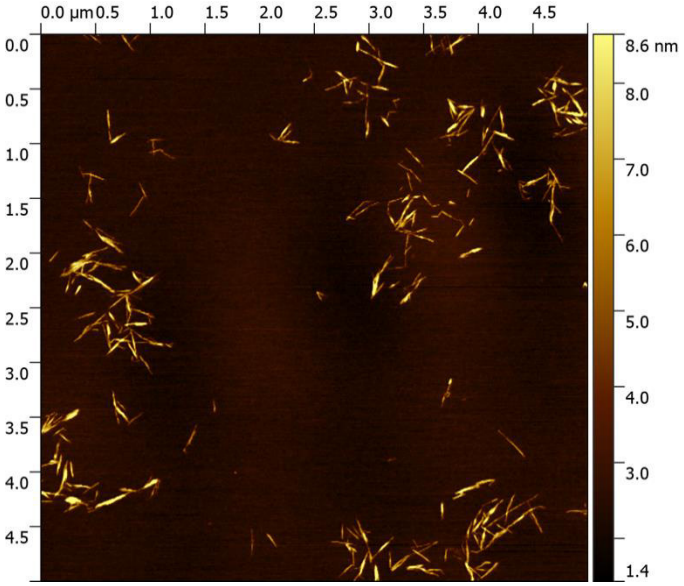

Supplementary Figure VI-1 Atomic force microscope images of CNC. They exhibit a typical rod-like shape morphology with an average length of 217±59 nm and height of 3.7±1.0 nm.

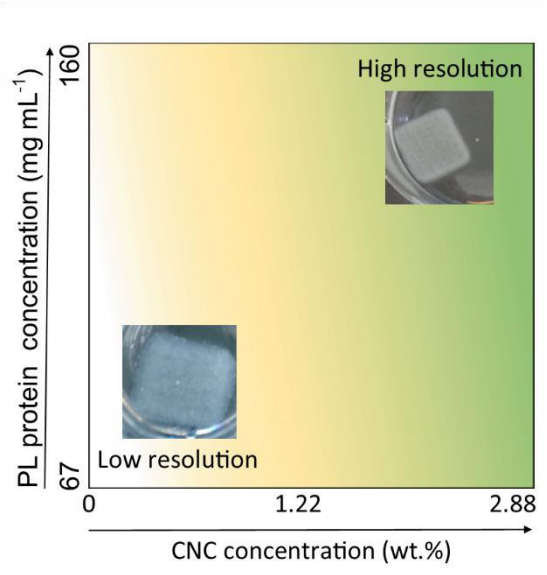

Supplementary Figure VI-2 Optimization of HUink components concentration to obtain constructs with high resolution. The combination of concentrated PL and 2.88 wt.% CNC allowed to print constructs with higher resolution. The concentrations of the individual components in the final bioink formulations correspond to half of their initial concentration before mixing.

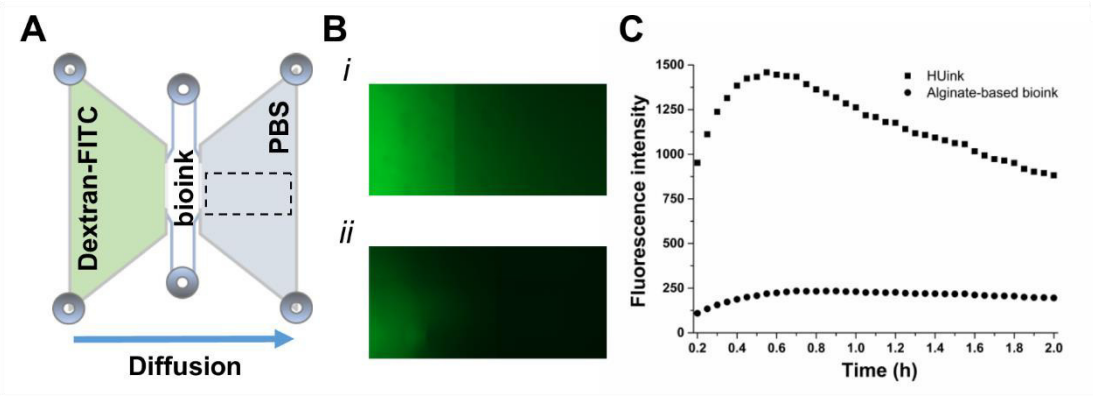

Supplementary Figure VI-4 Diffusion of model molecules through the bioinks. (A) Schematic design of the chemotaxis µ-slide and the experimental setup. The dashed box indicates the region of interest (ROI). (B) Picture of the ROI in (i) HUink and (ii) alginate-based bioink after 30 min incubation. The green color corresponds to 20 kDa dextran-FITC. (C) Mean fluorescence intensity in the ROI plotted against time.

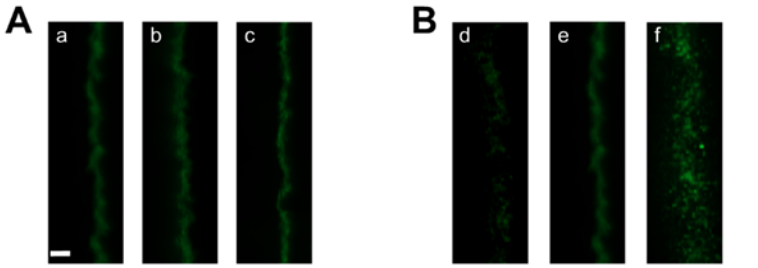

Conditions	Print speed (mm/s)
a	5
b	15
c	30

Conditions	Diameter (µm)
d	150 (28 G)
e	200 (27 G)
f	250 (25 G)

Supplementary Figure VI-3 Filaments with different widths were printed into the agarose support bath A) from a 27-gauge needle and varying the velocity and B) with a velocity of 5 mm. s^{-1} and modifying the needle diameter.

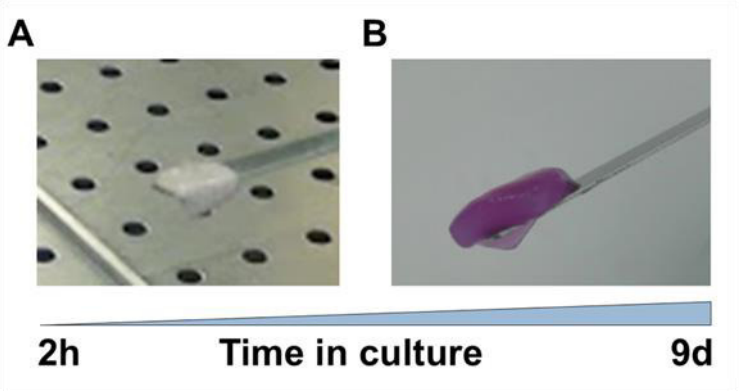

Supplementary Figure VI-5 (A) A square (1x1x0.5 cm) was 3D bioprinted using HUink and hASCs. (B) 3D bioprinted constructs were structurally consolidated after 9 days of culture in media without external supplementation.

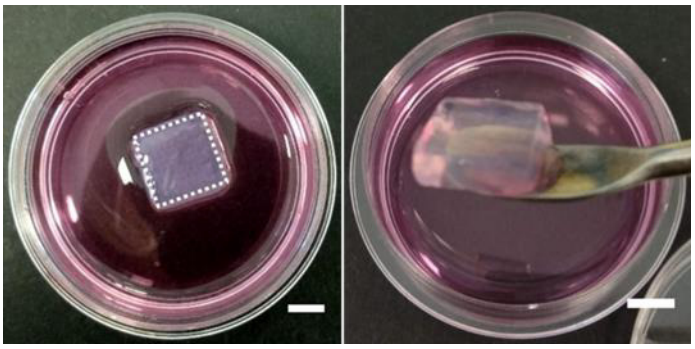

Supplementary Figure VI-6 A square (1x1x0.5 cm) was 3D bioprinted using GelMA and hASCs. 3D bioprinted constructs showed high shape integrity after 9 days of culture in media without external supplementation. The dotted square represents the size of the initial 3D model. Scale bar: 0.5 cm.

VI-6. REFERENCES

[1] M. Santoro, J. Navarro, J.P. Fisher, Micro- and Macrobioprinting: Current Trends in Tissue Modeling and Organ Fabrication, Small Methods, 2 (2018) 1700318.

[2] L. Moroni, J.A. Burdick, C. Highley, et al., Biofabrication strategies for 3D in vitro models and regenerative medicine, Nat. Rev. Mater., 3 (2018) 21.

[3] D. Chimene, K.K. Lennox, R.R. Kaunas, et al., Advanced Bioinks for 3D Printing: A Materials Science Perspective, Ann. Biomed. Eng., 44 (2016) 2090.

[4] J. Malda, J. Visser, F.P. Melchels, et al., 25th Anniversary Article: Engineering Hydrogels for Biofabrication, Adv. Mater., 25 (2013) 5011.

[5] H. Katja, L. Shengmao, T. Liesbeth, et al., Bioink properties before, during and after 3D bioprinting, Biofabrication, 8 (2016) 032002.

[6] S.M. Bittner, J.L. Guo, A.G. Mikos, Spatiotemporal control of growth factors in three-dimensional printed scaffolds, Bioprinting, (2018) e00032.

[7] K. Lee, E.A. Silva, D.J. Mooney, Growth factor delivery-based tissue engineering: general approaches and a review of recent developments, J. R. Soc. Interface, 8 (2011) 153.

[8] R.O. Hynes, The extracellular matrix: not just pretty fibrils, Science, 326 (2009) 1216.

[9] V. Vogel, Unraveling the Mechanobiology of Extracellular Matrix, Annu. Rev. Physiol., 80 (2018) 353.

[10] K.H. Vining, D.J. Mooney, Mechanical forces direct stem cell behaviour in development and regeneration, Nat. Rev. Mol. Cell Biol., 18 (2017) 728.

[11] D. Choudhury, H.W. Tun, T. Wang, et al., Organ-Derived Decellularized Extracellular Matrix: A Game Changer for Bioink Manufacturing?, Trends Biotechnol., 36 (2018) 787.

[12] C.L. Hedegaard, E.C. Collin, C. Redondo-Gómez, et al., Hydrodynamically Guided Hierarchical Self-Assembly of Peptide–Protein Bioinks, Adv. Funct. Mater., 28 (2018) 1703716.

[13] E. Prince, E. Kumacheva, Design and applications of man-made biomimetic fibrillar hydrogels, Nat. Rev. Mater., (2019).

[14] B.B. Mendes, M. Gomez-Florit, P.S. Babo, et al., Blood derivatives awaken in regenerative medicine strategies to modulate wound healing, Adv. Drug Deliv. Rev., 129 (2018) 376.

[15] N. Faramarzi, I.K. Yazdi, M. Nabavinia, et al., Patient-Specific Bioinks for 3D Bioprinting of Tissue Engineering Scaffolds, Adv. Healthc. Mater., 7 (2018) 1701347.

[16] B.B. Mendes, M. Gómez-Florit, R.A. Pires, et al., Human-based fibrillar nanocomposite hydrogels as bioinstructive matrices to tune stem cell behavior, Nanoscale, (2018).

[17] V.E. Santo, M.E. Gomes, J.F. Mano, et al., Chitosan-chondroitin sulphate nanoparticles for controlled delivery of platelet lysates in bone regenerative medicine, J. Tissue Eng. Regen. Med., 6 (2012) 47.

[18] D. Bondeson, A. Mathew, K. Oksman, Optimization of the isolation of nanocrystals from microcrystalline celluloseby acid hydrolysis, Cellulose, 13 (2006) 171.

[19] R.M.A. Domingues, M. Silva, P. Gershovich, et al., Development of Injectable Hyaluronic Acid/Cellulose Nanocrystals Bionanocomposite Hydrogels for Tissue Engineering Applications, Bioconjugate Chem., 26 (2015) 1571.

[20] T.J. Hinton, Q. Jallerat, R.N. Palchesko, et al., Three-dimensional printing of complex biological structures by freeform reversible embedding of suspended hydrogels, Sci Adv, 1 (2015) e1500758.

[21] M. Akbari, A. Tamayol, V. Laforte, et al., Composite Living Fibers for Creating Tissue Constructs Using Textile Techniques, Adv. Funct. Mater., 24 (2014) 4060.

[22] S.R. Moxon, M.E. Cooke, S.C. Cox, et al., Suspended Manufacture of Biological Structures, Adv. Mater., 29 (2017) 1605594.

[23] P.P. Carvalho, X. Wu, G. Yu, et al., The effect of storage time on adipose-derived stem cell recovery from human lipoaspirates, Cells Tissues Organs, 194 (2011) 494.

[24] A. Blaeser, D.F. Duarte Campos, U. Puster, et al., Controlling Shear Stress in 3D Bioprinting is a Key Factor to Balance Printing Resolution and Stem Cell Integrity, Adv. Healthc. Mater., 5 (2016) 326.

[25] L.J. Pourchet, A. Thepot, M. Albouy, et al., Human Skin 3D Bioprinting Using Scaffold-Free Approach, Adv. Healthc. Mater., 6 (2017) 1601101.

[26] C.B. Highley, C.B. Rodell, J.A. Burdick, Direct 3D Printing of Shear-Thinning Hydrogels into Self-Healing Hydrogels, Adv. Mater., 27 (2015) 5075.

[27] S.V. Murphy, A. Atala, 3D bioprinting of tissues and organs, Nat. Biotech., 32 (2014) 773.

[28] N.A. Sears, D.R. Seshadri, P.S. Dhavalikar, et al., A Review of Three-Dimensional Printing in Tissue Engineering, Tissue Eng. Part B Rev., 22 (2016) 298.

[29] J.M. Gimble, A.J. Katz, B.A. Bunnell, Adipose-derived stem cells for regenerative medicine, Circ. Res., 100 (2007) 1249.

[30] T. Rada, R.L. Reis, M.E. Gomes, Adipose Tissue-Derived Stem Cells and Their Application in Bone and Cartilage Tissue Engineering, Tissue Eng. Part B Rev., 15 (2009) 113.

[31] L. Jung-Seob, H. Jung Min, J. Jin Woo, et al., 3D printing of composite tissue with complex shape applied to ear regeneration, Biofabrication, 6 (2014) 024103.

[32] G. Cidonio, M. Glinka, J.I. Dawson, et al., The cell in the ink: Improving biofabrication by printing stem cells for skeletal regenerative medicine, Biomaterials, 209 (2019) 10.

[33] P.A. Galie, D.-H.T. Nguyen, C.K. Choi, et al., Fluid shear stress threshold regulates angiogenic sprouting, Proc. Natl. Acad. Sci. U S A, 111 (2014) 7968.

[34] R. Busch, A. Strohbach, M. Pennewitz, et al., Regulation of the endothelial apelin/APJ system by hemodynamic fluid flow, Cell. Signal., 27 (2015) 1286.

[35] A.M. Rosales, K.S. Anseth, The design of reversible hydrogels to capture extracellular matrix dynamics, Nat. Rev. Mat., 1 (2016).

[36] V. Becherucci, L. Piccini, S. Casamassima, et al., Human platelet lysate in mesenchymal stromal cell expansion according to a GMP grade protocol: a cell factory experience, Stem Cell Res. Ther., 9 (2018) 124.

[37] C. Saury, A. Lardenois, C. Schleder, et al., Human serum and platelet lysate are appropriate xeno-free alternatives for clinical-grade production of human MuStem cell batches, Stem Cell Res. Ther., 9 (2018) 128.

[38] G.S. Hussey, J.L. Dziki, S.F. Badylak, Extracellular matrix-based materials for regenerative medicine, Nat. Rev. Mater., 3 (2018) 159.

[39] D.B. Kolesky, K.A. Homan, M.A. Skylar-Scott, et al., Three-dimensional bioprinting of thick vascularized tissues, Proc. Natl. Acad. Sci. U S A, 113 (2016) 3179.

[40] A.K. Miri, A. Khalilpour, B. Cecen, et al., Multiscale bioprinting of vascularized models, Biomaterials, (2018).

Chapter VII

Injectable platelet lysate-derived granular hydrogels for biomedical applications

Chapter VII

Injectable hyaluronic acid and platelet lysate-derived granular hydrogels for biomedical applications

ABSTRACT

Towards the repair of damaged tissues, numerous scaffolds have been fabricated to recreate the complex extracellular matrix (ECM) environment to support desired cell behaviors; however, it is often challenging to design scaffolds with the requisite cell-anchorage sites, mechanical stability, and dynamic properties necessary for many applications. To address this and to improve on the properties of hyaluronic acid (HA) hydrogels, we combined photocrosslinkable norbornene-modified HA (NorHA) with human platelet lysate (PL). These PL-NorHA hybrid hydrogels supported the adhesion of cells when compared to NorHA hydrogels without PL, exhibited modular physicochemical properties based on the concentration of individual components, and released proteins over time. Using microfluidic techniques with on-chip mixing of NorHA and PL and subsequent photocrosslinking, spherical PL-NorHA microgels with a hierarchical fibrillar network were fabricated that exhibited the sustained delivery of PL proteins. Microgels could be jammed into granular hydrogels that exhibited shear-thinning and self-healing properties, enabling ejection from syringes and the fabrication of stable 3D constructs with 3D printing. Again, the inclusion of PL enhanced cellular interactions with the microgel structures, Overall, the combination of biomolecules and fibrin self-assembly arising from the enriched milieu of PL-derived proteins improved the bioactivity of HA-based hydrogels, enabling the formation of dynamic systems with modular design. The granular systems can be engineered to meet the complex demands of functional tissue repair using versatile processing techniques, such as with 3D printing.

This chapter is based on the following publication: ***B. B Mendes****, A. C. Daly, R. L. Reis, R. M. A. Domingues, M. E. Gomes, J. A. Burdick. Injectable hyaluronic acid and platelet lysate-derived granular hydrogels for biomedical applications (Submitted).*

VII-1. INTRODUCTION

Living tissues are hierarchically structured over different length scales and comprise multiple cell populations surrounded by a dynamic and bioactive extracellular matrix (ECM) [1]. ECM is a complex network of fibrous structural proteins (e.g., collagen, elastin); glycoproteins (e.g., laminin, fibronectin); glycosaminoglycans (GAGs) (e.g., heparan-sulfates, hyaluronic acid (HA)) covalently linked to core proteins to form proteoglycans (e.g., aggrecan, versican) with exception of HA; and ECM-associated proteins (e.g., growth factors, cytokines) [2, 3]. These ECM components are actively interconnected to establish unique compositions and topographies, which are crucial to provide structural and biochemical support to cells and to ultimately control cell behaviors, such as proliferation, growth, migration and differentiation [4]. Particularly, GAGs due to their high negative charge can establish strong electrostatic interactions with several soluble factors [5], which is further enhanced with van der Waals forces, hydrogen bonds, and hydrophobic interactions [6]. Thereby, ECM can dynamically and locally modulate the spatio-temporal presentation of soluble and immobilized molecules, and their subsequent signaling mechanisms [5]. In the context of tissue engineering and regenerative medicine (TERM) strategies, it is of utmost importance to develop effective engineered matrices that recapitulate such hierarchical fiber-based architectures and that introduce key cell instructive elements [7, 8].

Hydrogels have been widely exploited as mimics of the ECM due to their hydrated network and unique physicochemical properties that can be tuned to precisely regulate cellular behaviors [9]. Additionally, hydrogels can be engineered to be injectable or in situ gelling, enhancing their clinical translation through the use of minimally invasive approaches while homogenously incorporating cells and bioactive elements within any defect size (or shape) [10, 11]. Despite these advances, the majority of injectable hydrogels do not meet the complex demands of tissue repair since they do not recreate the organization, bioactivity, and mass transport properties of the native ECM [10, 11].

Several research groups have recently proposed bottom-up engineering strategies to process hydrogels as hydrogel microparticles (HMPs, or microgels) [12, 13]. The advantages of HMPs over traditional bulk hydrogels include: significant porosity (or void space); enhanced surface area; building blocks with modular design (e.g., composition, size, and contents); and a controlled mechanical response that depends on the polymer type and crosslinking degree [12]. Moreover, HMPs have gained interest in broader TERM through the creation of physicochemical gradients and tissue/disease models [13-16].

It was recently demonstrated that the agglomeration of HMPs in the jammed state produces granular hydrogels [12], enabling their combination with printing techniques to produce three-dimensional (3D) structures [17]. Cells in microgel-based systems can move within the porosity of the packed structure and spread out fully [18], thereby maximizing cell–cell interactions and synthesis of endogenous ECM, already at an early stage of the assembled constructs [19]. To take advantage of the potential benefits of granular systems to envision clinical applications, it is pivotal that the design of these advanced strategies recreates the physicochemical features of the native tissues [12, 13]. These includes cell anchorage sites and other bioactive cues, biodegradability, and xeno-free and clinically translatable processing.

Our study engineers HA-based hydrogels with improved cell adhesion, bioactivity, and tunable chemical and physical properties by incorporating platelet lysate (PL) that is recognized as an inexpensive source of biological molecules (e.g., growth factors, cytokines, self-assembling scaffolding proteins like fibrinogen) [20]. Specifically, PL was incorporated within a photocrosslinked norbornene-modified HA (NorHA) network with clotting factors to trigger fibrinogen polymerization (Scheme VII-1). We aimed to demonstrate that the system (1) possesses a similar fiber-based architecture to the native ECM due to the self-assembly of fibrinogen monomers; (2) contains an enriched milieu of key temporary ECM proteins with natural cell binding motifs; (3) preserves PL-derived protein bioactivity and fibrin polymerization; and (4) can be processed into relevant structures (e.g., microgels with microfluidics) and with precision technologies (e.g., 3D printing of granular hydrogels). In hydrogel and microgel formats, we evaluate the presence of an ECM-mimetic hierarchical fibrin matrix; characterize mechanical and rheological properties; analyze the degradation profiles and the subsequent release of therapeutically-relevant biomolecules; and assess the adhesion and spreading of mesenchymal stromal cells (MSCs).

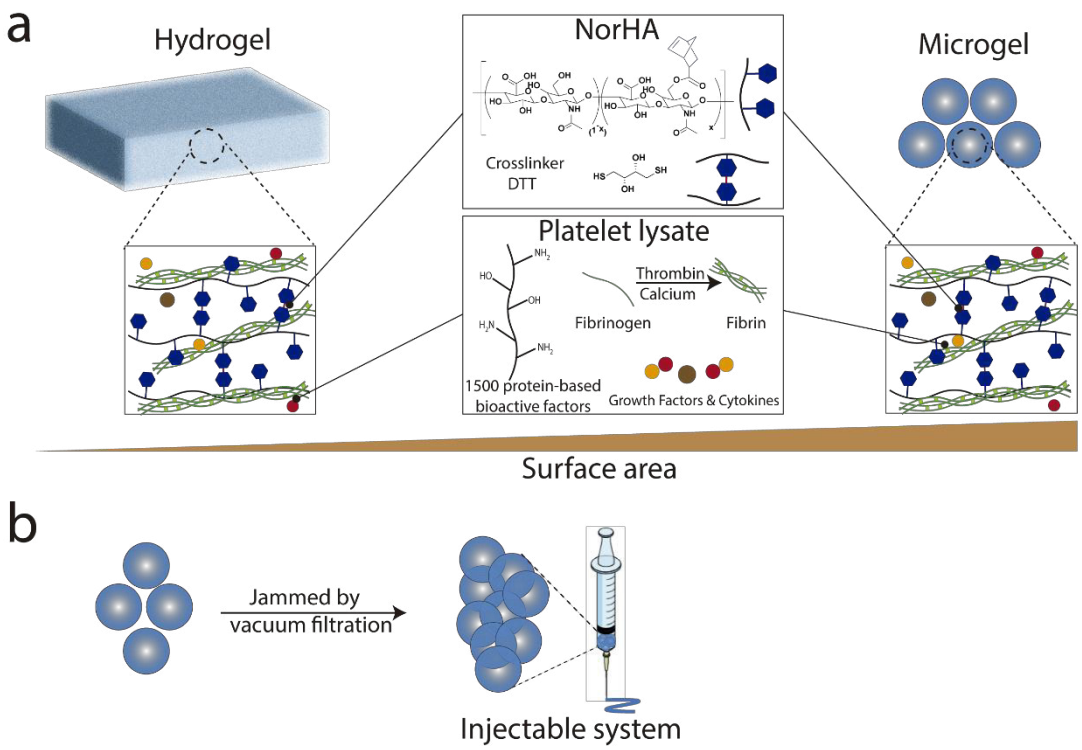

Scheme VII-1 Fabrication of platelet lysate-based hyaluronic acid hydrogels and microgels. a) Schematic representation of networks formed via the homogenous mixing of norbornene-modified hyaluronic acid (NorHA, ≈31% modification) and human platelet lysate. NorHA undergoes photocrosslinking through a thiol-ene reaction in the presence of a di-thiol (DTT) crosslinker, a visible light photoinitiator, and exposure to visible light. Fibrinogen polymerization within the PL is initiated by adding thrombin and calcium ions. b) Microgels can be jammed through vacuum filtration into a solid that can be extruded from a syringe or processed with 3D printing.

VII-2. MATERIALS AND METHODS

VII-2.1. Hydrogel and microgel synthesis and fabrication

VII-2.1.1. Synthesis of norbornene-modified hyaluronic acid

Prior to NorHA synthesis, sodium hyaluronate was converted to its tetrabutylammonium salt (HA-TBA), as previously described [21]. Briefly, sodium hyaluronate (75 kDa, Lifecore Biomedical) was dissolved in deionized (DI) water at 2 wt.% and 3 g of Dowex 50W hydrogen form exchange resin (Sigma-Aldrich) was added to 1 g of sodium hyaluronate for 2 h. The resin was filtered off by vacuum filtration and the filtrate was titrated with diluted TBA hydroxide solution (TBA-OH, Thermo Fisher Scientific) to a

pH of ≈7.03-7.05, and then frozen and lyophilized. Proton nuclear magnetic resonance spectroscopy (1H NMR, DMX 360 MHz, Bruker) was used to characterize the final product.

NorHA was synthesized by coupling HA-TBA with 5-norbornene-2-methylamine (3 molar ratio to HA-TBA repeat units, Tokyo Chemical Industry) in the presence of ditert-butyl dicarbonate (Boc2O, 0.4 molar ratio to HA-TBA repeat units, Sigma-Aldrich) and 4-(dimethylamino)pyridine (DMAP, 1.5 molar ratio to HA-TBA repeat units, Sigma-Aldrich), and dissolved in anhydrous dimethyl sulfoxide (DMSO, Sigma-Aldrich). The mixture was stirred for 20 h at 45 °C under a nitrogen atmosphere. Then, cold water (5x) was added to quench the reaction and the solution was dialyzed against 1 L of DI water with 0.25 g of sodium chloride (NaCl) for 4 days. After dialysis, 0.75 g of NaCl was added to 100 mL of dialyzed solution and it was precipitated into 10-fold excess cold acetone. The pellet was resuspended in cold DI water, dialyzed for 3 days, frozen and lyophilized. 1H NMR was used to determine the functionalization of HA by norbornene (≈ 31% of HA repeat units were modified with norbornene groups).

VII-2.1.2. Platelet lysate preparation

Human PL (PLTMax®, Mill Creek Life Sciences) was defrosted at room temperature (RT), aliquoted and stored at -80 °C. Prior to use, PL solution was defrosted at RT and briefly spun down to remove any platelet fragments. The mean fibrinogen level was 350 ± 124 μg mL^{-1} (experiment was conducted by Mill Creek Life Sciences), which is similar to the previously reported fibrinogen concentration in PL prepared from freeze-thaw cycles of pooled human expired platelets batches [22].

VII-2.1.3. Hydrogel fabrication

Hydrogels across various compositions were prepared from separate precursor solutions at 1:1 volume ratio. For precursor solution 1, NorHA was dissolved in PBS (2 or 4 w/v) in the presence of dithiothreitol (DTT, Sigma-Aldrich) at 0.8 mol of thiols to 1 mol of norbornenes and 0.1 w/v lithium phenyl(2,4,6-trimethylbenzoyl)phosphinate (LAP, Tocris Bioscience). Precursor solution 2 consisted of either phosphate-buffered saline (PBS, Sigma-Aldrich) or human PL solution.

Specific compositions are as follows:

1. NorHA hydrogel via mixing of precursor solution 1 and PBS (precursor solution 2).

2. NorHA hydrogel with cell-adhesive RGD oligopeptide (GenScript) via the addition of 4 mM of thiolated RGD motifs to precursor solution 1 (NorHA) and PBS (precursor solution 2), as previously described [23]

3. NorHA hydrogel with PL proteins in solution via mixing of precursor solution 1 and PL (precursor solution 2), without induction of the coagulation cascade.

4. PL-NorHA hydrogels embedded with fibrillar structures, clotting factors via the addition of thrombin from human plasma (4 U mL^{-1}, Sigma-Aldrich) and calcium chloride (10 mM, MERCK) to solution 1 and mixing with PL (precursor solution 2), to induce PL coagulation cascade.

Both precursor solutions (1 and 2) were homogeneous mixed and hand extruded onto glass coverslips to form hydrogel films. The mixture was incubated for 20 minutes at RT to allow PL matrix polymerization, and then the hydrogels were cured by visible light exposure (Exfo Omnicure S1500 lamp, 400-500 nm filter, 26 mW cm^{-2}) for 5 minutes. The final hydrogels were composed of 50 vol.% of PL (or PBS) and 1 or 2 w/v NorHA concentrations, and the hydrogel experimental groups were named NorHA, NorHA RGD, NorHA proteins and PL-NorHA.

VII-2.1.4. Microfluidic device fabrication and microgel formation

The mold of the microfluidic device was fabricated by micro-resolution stereolithography (MicroFine Green Resin, Proto Labs) and the desired microfluidic device was further produced by polydimethylsiloxane (PDMS, SylgardTM 184, Ellsworth adhesives, USA) replica molding process as previously optimized [17]. Device features include four inlets (precursor solution 1 and 2, and two-side inlets for oil flow) and one outlet for droplets, a T-junction for the creation of polymer aqueous droplets into the oil flow, and a serpentine path to allow the mixing of the precursor solutions.

Mineral oil (light Fisher Chemical, Thermo Fisher Scientific) supplemented with 2 vol.% span 80 (Sigma-Aldrich) at flow rate of 5 µL min^{-1} (syringe pump, World Precision Instruments) was first introduced in the microfluidic device. Then, precursor solution 1 (NorHA or NorHA with clotting factors) and 2 (PBS or PL) were introduced at 1 µL min^{-1} and 2 µL min^{-1} flow rates, respectively. The precursor solutions were the same as described above for hydrogel formation. While flowing through the tubing at outlets (≈ 28 cm), the coagulation cascade was initiated and then the formed polymer droplets were cured by visible light exposure (Exfo Omnicure S1500 lamp, 400–500 nm filter, 290 mW cm^{-2}). Microgels collected with

mineral oil were centrifuged (1000 G for 5 min), purified by sequential washing steps with PBS and stored at 4 °C until further use. The microgel experimental groups were NorHA and PL-NorHA.

VII-2.2. Jammed granular hydrogels

VII-2.2.1. Jammed microgel morphology

Thiolated fluorophores (GCKK-RHO) were prepared through standard solid phase peptide synthesis (PS3 automated peptide synthesizer, Protein Technologies) [22]. The fluorescent peptide (final concentration of 2 mM) was incubated in microgels suspension for 30 min, coupled via thiol-norbornene photochemistry (0.05 w/v Irgacure 2959, Sigma-Aldrich) during UV light curing (Omnicure S1500, 320–390 nm filter, ≈5 min) and washed three times with PBS. Microgels were jammed by vacuum-driven filtration and then imaged with the confocal microscope.

VII-2.2.2. Jammed microgels inks and printed structure stability

A modified stepper motor-based extruder with a 3D printer Revolution XL printer (Quintessential Universal Building Device, Inc.) was used for 3D printing [25]. Printing paths were processed into G-code by Slic3r and printed using Repetier hardware. Jammed microgel inks were loaded into a syringe (Microliter, Hamilton) and extruded through a 25 G needle at 40 mm min^{-1} printing speed. Single line filaments, lattice and cuboid structures were printed on a glass surface. Then, 3D printed structures were immersed in PBS and the maintenance of their printed shape was evaluated for 7 days. The morphologies of single line filaments, lattice and cuboid structures were observed by fluorescence microscopy.

VII-2.3. Hydrogel and microgel characterization

VII-2.3.1. Microgel morphology

Fluorescein isothiocyanate (FITC)-Dextran (1 mg mL^{-1}, ≈2 MDa, Sigma-Aldrich) was added to the precursor solution 1 and fluorescence microscopy (Olympus BX51) was used to analyze microgel morphology after the PBS washing steps. Microgel diameter and roundness were further quantified by ImageJ software (National Institutes of Health).

VII-2.3.2. Fibrin network analysis

For visualization of the fibrin networks within hydrogels, 9 μg of Alexa Fluor® 488 conjugated fibrinogen from human plasma (Thermo Fisher Scientific) was added to 1 mL of PL solution (precursor solution 2), and then images were acquired on with confocal microscopy (SP5, Leica Microsystems). The fibrin networks within microgels were visualized by reflectance confocal microscopy (SP5, Leica Microsystems), using scattered light instead of fluorescence.

VII-2.3.3. Rheological characterization

Rheological measurements were performed using an AR2000 stress-controlled rheometer (TA Instruments) fitted with a 20 mm diameter acrylic cone (59 min 42 s angle) and plate geometry using 27 μm (for hydrogel tests) or 1 mm (for microgel tests) gaps. For hydrogel rheological analysis, hydrogels were formulated as described above and precursor solutions were mixed immediately prior to testing. Time sweep tests were applied to study the polymerization kinetics of different formulations (0.5% strain, 1.0 Hz). After 20 min, hydrogels were cured by visible light (Exfo Omnicure S1500 lamp, 400–500 nm filter, 26 mW cm-2) for 5 min. Frequency sweep tests (1% strain, 0.01 Hz to 100 Hz) were conducted after the hydrogel modulus platequed and only the storage modulus (G′) values from 0.1 to 10 Hz frequencies are graphically represented. For microgel rheological properties, microgels were first jammed by vacuum-driven filtration and then placed on the rheometer for time sweep (0.5% strain, 1 Hz) and strain sweep (0.5% to 500% strain, 1 Hz) tests. To demonstrate self-recovery properties, the storage modulus (G′) values were evaluated under cycling strains (0.5% or 500% for 2 min each strain, 1 Hz).

VII-2.3.4. Degradation behavior

Hydrogels were produced as described above (60 μL) and incubated in 300 μL of PBS, either alone or with hyaluronidase from bovine tests (Type IV-S, 750-3000 U mg^{-1} solid, Sigma-Aldrich) at 0.005 mg mL^{-1} (HAse low) or 0.01 mg mL^{-1} (HAse high) at 37 °C. Jammed microgels (60 μL) were fabricated as described above and incubated in 300 μL of PBS or hyaluronidase at 0.005 mg mL^{-1} at 37 °C. At desired times, samples were centrifuged (1200 G for 15 min), releasate buffer was collected and replaced with fresh solution, and the releasate was stored at −20 °C. After one week, samples were fully degraded in hyaluronidase at 1 mg mL^{-1}. HA release was determined using a uronic acid assay and PL-derived proteins

were quantified via Pierce Bicinchoninic Acid Assay Kit (Thermo Fisher Scientific) according to the manufacturer's instructions [26]. Degradation and protein release are represented as the cumulative release over time.

VII-2.4. *In vitro* cell culture studies

MSCs (passage 3, Lonza) were cultured in α-MEM (Gibco) supplemented with 10% fetal bovine serum (FBS, Gibco) and 1% penicillin/streptomycin solution (Invitrogen) at 37 °C and 5% CO2. Cells were trypsinized with 0.05 % Trypsin (Gibco) and then resuspended in culture media without FBS. Hydrogels were produced as described above and incubated for 30 min in 150 µL medium before $3x10^3$ cells cm^{-2} MSCs (final volume of 300 µL per condition) were seeded and cultured for either 4 or 24 hours. For immunofluorescence staining, samples were washed with PBS, fixed in 10% formalin (Thermo Fisher Scientific) for 15 min, washed with PBS and then permeabilized using 0.2 vol% Triton-X100 in PBS for 10 min (Sigma-Aldrich). After washing, the samples were incubated with 1:200 v/v rhodamine-conjugated phalloidin (Sigma-Aldrich, hydrogels) and 1:2000 v/v Hoechst 33342 (Life Technologies) for 20 minutes. After washing, the samples were imaged with a fluorescence microscopy. For measurements of cell spread area and cell aspect ratio, fluorescence images were converted to binary images to identify individual cells and a mean threshold was applied in ImageJ.

For microgel cell studies, rhodamine-thiol-tethered microgels were homogeneous mixed with MSCs at $1x10^6$ cells mL^{-1}, centrifuged at 1000 G for 5 min, jammed by vacuum-driven filtration and cultured for 1 or 7 days. Cells were labelled with Cell Tracker™ fluorescent probes (Green-CMFDA, 5µM) for 30 minutes prior to mixing for visualization. After culture, samples were washed in PBS and then imaged using confocal microscopy. Images represent z-stacks (~300µm total depth, 5 µm per slice). The 3D analysis was performed at LASX software (Leica).

VII-2.5. Statistical analysis

All statistical analysis was performed using Graphpad Prism 7 software. Data were presented as mean ± standard deviation in triplicate. Statistical analysis was conducted using Shapiro-Wilk normality test and one-way analysis of variance (ANOVA) was used to analyze experimental data, followed by the Tukey's post hoc or Krustal-Wallis test for multiple comparisons.

VII-3. RESULTS AND DISCUSSION

VII-3.1. Biologically-active hydrogels

VII-3.1.1. Hydrogel synthesis and characterization

HA is a non-sulfated GAG component in the native ECM that is expressed throughout the body at a concentration and molecular weight that varies by tissue source and body location [27, 28]. Due to its crucial role in the ECM function, HA has been widely explored in the design of engineered biomaterials [29]. Numerous chemical modifications have been made to HA, which allows it to crosslink into hydrogels, with the selection of the chemical modification, the concentration of modification, and extend of crosslinking defining hydrogel properties (e.g., mechanics). As one example, HA has been crosslinked into hydrogels through thiol-norbornene click chemistry, with HA modified with norbornenes (NorHA) and di-thiol crosslinkers. This approach provides cytocompatibile conditions for cell incorporation, fast reaction kinetics and enables facile tuning of the physical properties by adjusting NorHA and di-thiol crosslinker concentration [21]. These features are essential in the modular design of multi-functional hydrogels; thus, we used NorHA at 31% modification of disaccharide repeat units and incorporation of dithiothreitol (DTT) crosslinker and visible light for hydrogel formation (Scheme VII-1A). The formulation could also be combined with clotting agents and PL and incubated for 20 minutes prior to light exposure to trigger a coagulation cascade.

For the analysis of the fibrillar structure, fluorescent fibrinogen was added to the PL solution and visualized by confocal microscopy (Figure VII-1AI and II). Hydrogels at NorHA concentrations of 1 wt.% and 2 wt.% exhibited an interconnected and homogenous fibrillar architecture that resembles a typical hierarchical fibrin matrix. The induction of the coagulation cascade mimics the physiological process that occurs after injury - initiated by thrombin cleavage, which exposes the central domain of fibrinogen binding sites to induce the self-assembly of fibrin monomers and the formation of half-staggered two-stranded protofibrils [30]. When protofibrils achieve a threshold length, they start to associate laterally to form fibers that branch into a 3D network. The introduction of these multiscale properties recreates the complexity of the hierarchical organization of the native ECM from the nanoscale (e.g., fibrin fibrils) to the microscale (e.g., fibrin fibers), which is difficult to recreate using synthetic biomaterials.

To better understand the gelling kinetics and network properties of the produced hydrogel, their gelation process and viscoelastic properties were analyzed (Figure VII-BI and II). Before visible light irradiation (at 20 minutes), NorHA, NorHA proteins (i.e., without clotting agents) and PL-NorHA (i.e., addition of clotting agents) conditions exhibited a low storage modulus, with similar mechanics (G' ≈ 1-2 Pa and G'' ≈ 0.4-1 Pa). These results are in agreement with previous studies on scaffolds solely based on PL exhibit limited stability and low mechanical properties [20]. However, the elastic and viscous moduli increased when exposed to visible light due to the covalent photocrosslinking process via thiol-ene reaction and reached a storage moduli plateau within seconds (Figure VII-1BI and II).

The PL-NorHA hydrogels (G': 591.76 ± 15.73 Pa – 1 wt.% and G': 3536 ± 158.40 Pa – 2 wt.%) exhibited a lower storage modulus than hydrogels with only NorHA (G': 1648.33 ± 237.01 Pa – 1 wt.% and G': 4838.67 ± 383.76 Pa – 2 wt.%) or NorHA with proteins (G': 1564 ± 76.14 Pa – 1 wt.% and G': 5284.67 ± 767.52Pa – 2 wt.%). The reduction in moduli with the addition of PL and coagulation are potentially explained by the self-assembly of fibrinogen derived from the PL solution, which produces an interconnected network before HA photocrosslinking. This may create some steric hindrance to reduce HA macromer mobility or phase separation that limits the continuity of the HA hydrogel, impairing thiol-ene crosslinking after light exposure. Since both networks are entangled with each other, we can leverage this mechanism to modulate hydrogel mechanical properties.

VII-3.1.2. Release of proteins from PL-containing hydrogels

HA biosynthesis and tissue turnover is regulated by three synthases and several hyaluronidases that can naturally catabolize HA with times ranging from hours to days [31, 32] depending on the local enzyme concentration [33]. In our study, the *in vitro* degradation profiles of the hydrogels were evaluated either in buffer or in the presence of hyaluronidase at 0.005 mg mL^{-1}, with quantification of either uronic acid or total proteins over time (Figure VII-1C). After 7 days, hyaluronidase was added to the remaining hydrogel for complete degradation. As expected, the overall time and rate of hydrogel degradation was faster in the presence of hyaluronidase (Figure VII-1CI and III). There was also a correlation between the degradation time and crosslinking density, with the higher concentration of 2 wt.% degrading more slowly than the lower concentration of 1 wt.% (Figure VII-1CI and III). Additionally, the PL-NorHA hydrogels degraded faster than NorHA. As previously reported, when the network becomes loosely crosslinked, the degradation rate increases due to the rapid solubilization of HA and facilitated matrix diffusion of the

enzyme [34]. Therefore, these findings are in agreement with our previous observations that the fibrin matrix formation decreases thiol-ene crosslinking density.

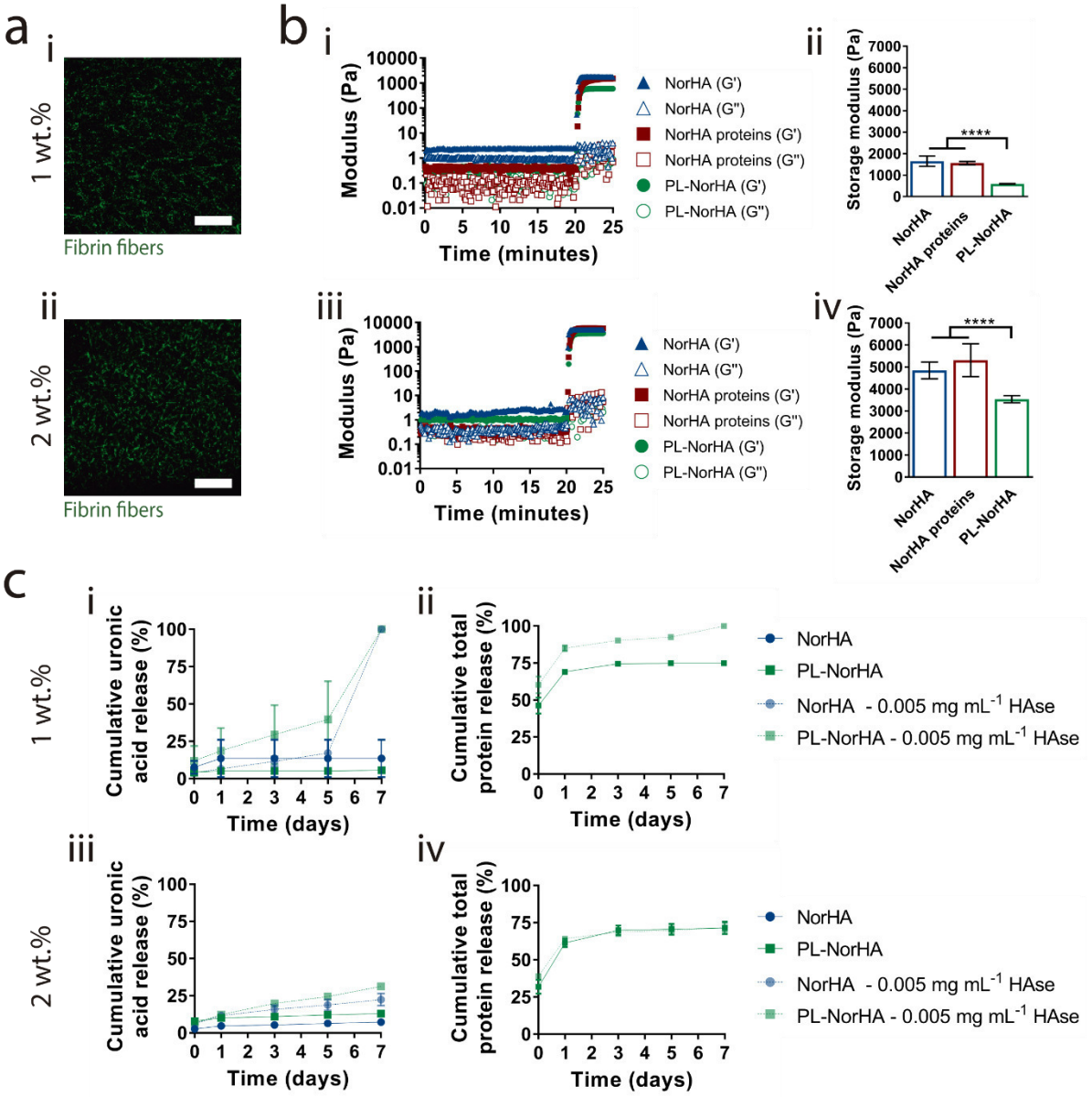

Figure VII-1 Characterization of the mechanical and degradation behaviors of hydrogels. a) Fibrin (green) polymerized within (i) 1 wt.% and (ii) 2 wt.% PL-NorHA (NorHA plus coagulation cascade induction of fibrinogen from PL) hydrogels. b) Representative time sweeps (1.0 Hz, 0.5% strain, light introduced at 20 minutes) of the polymerization of NorHA, NorHA proteins (NorHA plus PL-derived proteins) and PL-NorHA hydrogels and average plateau storage moduli (G') at concentrations of (i) 1 wt.% and (ii) 2 wt.% from time-sweep tests (1.0 Hz, 0.5% strain, 28 to 30 min). c) Cumulative uronic acid and total protein release during the degradation of (i, ii) 1 wt.% and (iii, iv) 2 wt.% hydrogels when incubated in PBS alone or with hyaluronidase at 0.005 mg mL-1. Scale bars: 50 μm (a). **** $P < 0.001$.

Unsurprisingly, the previously discussed hydrogel physical properties have a measurable impact on the temporal and spatial release of therapeutically-relevant PL proteins (Figure VII-1CII and IV). In PL-based hydrogels, there is an obvious burst release of proteins at early times, followed by a general plateau

until hydrogels reached complete degradation (or the end of the assay is reached). Inherently, formulations with a low crosslink density exhibited a higher initial release of PL-derived proteins (92.49 ± 1.15 %) than formulations with 2 wt.% NorHA concentration (71.79 ± 2.40 %) in presence of hyaluronidase. The protein release profile for 1 wt.% PL-NorHA formulations followed the uronic acid release behavior, whereas no correlation was observed with 2 wt.% PL-NorHA, indicating that HA macromer concentration is a parameter that can be explored to modulate the release of the hydrogel therapeutic cargo in a controlled and spatiotemporal manner. Moreover, it was observed that protein release occurred faster than uronic acid release, which is likely a combination of the initial diffusion of un-bound proteins and the surface hydrogel erosion behavior.

VII-3.1.3. *In vitro* cell response to hydrogels

HA bioactivity and adhesive properties have been improved through the incorporation of RGD or bioactive proteins in order to maximize biomaterial-cell interactions and to develop efficacious cell-instructive biomaterials [29, 31, 35, 36]. Most of the HA hydrogels modified with proteins are based on chemical crosslinking methods (e.g., 1-ethyl-3-(3-dimethylaminopropyl)-carbodiimide (EDC) crosslinkers) and processing techniques (e.g., glutaraldehyde treatment) that produce potential toxic products and require extensive washing steps, which jeopardizes cytocompatibility and protein bioactivity [29, 31, 37, 38]. The advantage of our strategy is the straightforward incorporation of therapeutically-relevant biomolecules and PL bioactivity within NorHA hydrogels without any further chemical modifications.

MSCs were seeded on NorHA, NorHA-RGD and PL-NorHA hydrogels under serum-free conditions and their morphology was assessed after 4 hours and 1 day of in vitro culture (Figure VII-2). As a result of the enriched environment of protein-based bioactive factors, we explored the release of PL as substitute to bovine serum during culture. Similar to fetal bovine serum (FBS), PL provides important nutritional and macromolecular factors that exhibit important growth-promoting and transport properties [39]. These include albumin (represents ≈40 % of total PL proteins) that supports cell growth [40, 41] and growth factors (e.g., platelet-derived growth factor, transforming growth factor-β, basic fibroblast growth factor) [42] that are responsible for numerous cell responses such as proliferation [43], chemotaxis [44] and

angiogenesis promotion [45]. The culture of MSCs without serum supplementation strengthens the clinical translation of the proposed biomaterial strategy.

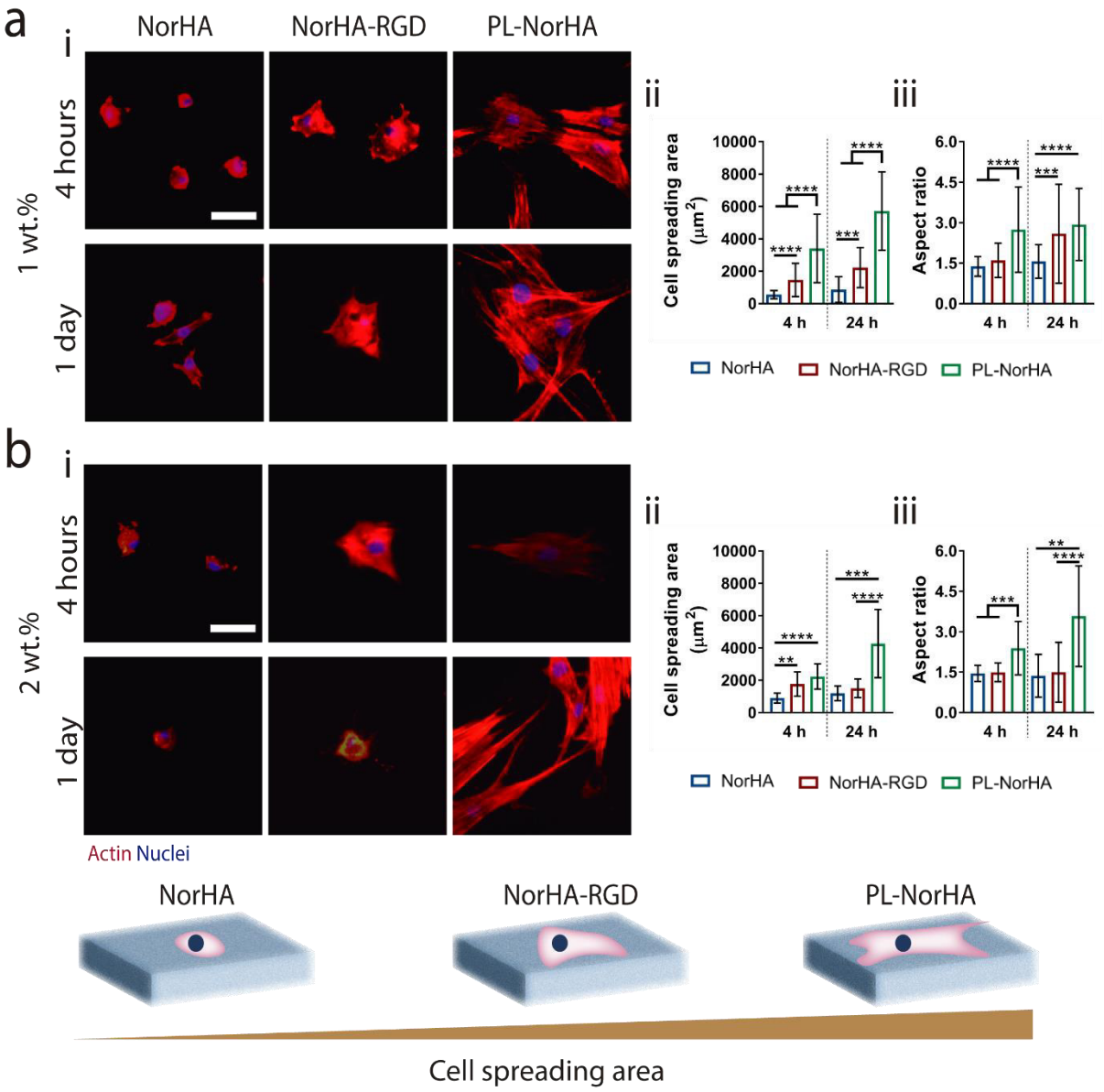

Figure VII-2 In vitro evaluation of human MSC interactions with hydrogels. a) Representative fluorescence images (actin: red, nuclei: blue) and quantification of cell spreading and aspect ratio for MSCs cultured for either 4 hours or one day in serum-free medium on (i-iii) 1 wt.% or (iv-vi) 2 wt.% NorHA, NorHA-RGD (NorHA containing 2 mM RGD motifs) or PL-NorHA (NorHA plus coagulation cascade induction of fibrinogen from PL hydrogels. b) Schematic representation of cell adhesion on hydrogel surfaces with various hydrogel formulations. Scale bar: 50 μm (a). ** P < 0.01, *** P < 0.001 and **** P < 0.0001.

Cells seeded on NorHA hydrogels exhibited generally rounded morphologies with some protrusions at 1 wt.% and 2 wt.% concentrations, displaying comparable cell spreading areas and aspect ratios over time (Figure IV-2A). As expected, the incorporation of RGD cell-binding motifs into NorHA hydrogels (1 wt.% and 2 wt.% NorHA-RGD) greatly enhanced cell spreading areas, although modest changes in aspect

ratios were observed. Changes in MSC behavior were further observed in PL-NorHA formulations (1 wt.% and 2 wt.%), where cells adhered, spread, and assumed a spindle-like morphology after only 4 hours in culture (Figure VII-2A and B). After 1 day in culture, MSCs exhibited thin and elongated protrusions and produced an interconnected network with adjacent cells. In contrast to previous reports, cell adhesion and spread areas in 2D did not increase as a function of increasing hydrogel stiffness [46, 47], indicating that hydrogel mechanical properties are not the driving force for the differences in cell response or that the magnitude changes are not great enough to observe an altered behavior. These results can be potentially explained by the fibrillar network that not only provides a provisional hierarchical ECM that confers mechanical support and ECM topography, but also contains numerous binding domains that mediates interactions with cells, ECM proteins and secreted growth factors [48-50].

VII-3.2. Biologically-active microgels

VII-3.2.1. Microgel synthesis and characterization

The assembling of building blocks into 3D scaffolds has emerged as a promising new approach to engineer hydrogels endowed with modular biochemical and biophysical cues [12]. As one example, hydrogel microparticles or microgels can be fabricated and packed together to build up 3D structures, permitting injectability or processing with techniques like 3D printing. Therefore, the previously optimized PL-NorHA approach was modified to produce microgels, and thus increase the potential TERM applications of the hydrogel.

A previously developed microfluidic device was modified to produce water-in-oil droplets of PL-NorHA or NorHA at 1 wt.% and 2 wt.% macromer concentrations (Figure VII-3A) [17]. NorHA (containing clotting factors) and PL were introduced in the Y-shaped microfluidic chip through two separate channels at varying flow rate ratios, converging into a single channel with laminar flow. The physical separation of both solutions is crucial to avoid clogging in the microfluidic channels due to the enzymatic cleavage of fibrinogen that starts the self-assembly of fibrin. This process typically takes around 5-10 minutes, but its initial triggering is sufficient to promote the agglomeration of fibrin fibers throughout the tubing and device channels [30, 51]. This single channel was then pinched-off by the immiscible continuous phase (i.e., oil with nonionic surfactant) to produce water-in-oil droplets. The introduction of a serpentine path then improves the mixing within the droplets through chaotic advection [52], while increasing the residence

time on chip to allow fibrin polymerization. The droplets were transferred through tubing and crosslinked with visible light to form microgels, which were subsequently washed from oil and surfactant into buffer.

The incorporation of fluorescein-labeled dextran during microgel formation allowed the analysis of their morphology, including size and roundness (Figure VII-3B and C). As previously demonstrated in PL-NorHA hydrogels, microgels containing PL produced a homogeneous and hierarchical fibrin network that was visualized by confocal reflectance (Figure VII-3BII). Spherical microgels had an average diameter of 120.04 ± 12.00 µm (1 wt.% NorHA), 126.35 ± 16.82 µm (1 wt.% PL-NorHA), 99.60 ± 7.97 µm (2 wt.% NorHA) and 118.94 ± 21.22 µm (2 wt.% PL-NorHA), (Figure VII-3CI and II). Previous studies reported that microgel dimensions are readily altered through the size of microchannels or precursor flow rates [12, 53]. Although not tested here, alterations in the size and morphology of microgels could be used to meet the requirements of specific biomedical applications.

Microgel degradation was assessed for over one week through the release of uronic acid and total proteins, including in the presence of hyaluronidase (Figure VII-3D). As shown with hydrogels, microgels exhibited degradation in the presence of hyaluronidase, which was faster with the lower NorHA concentration (Figure VII-3DI and III). Moreover, the majority of PL-NorHA microgels degraded at a faster rate than NorHA formulations and generally microgels degraded more quickly than hydrogels of the same formulations (Figure VII-1C). PL-NorHA microgels were further characterized for the release of total proteins (Figure VII-3DII and IV). Microgels generally exhibited a lower initial release of proteins than PL-NorHA hydrogels (11.01 ± 2.71 %, 2 wt.% PL-NorHA microgels without hyaluronidase), which can be explained by the initial removal of the unbound proteins during the several washing steps from oil into buffer. After the first timepoint, a steady release of PL-derived proteins was observed from PL-NorHA microgels, corresponding to the inherent protein diffusion and degradation of the polymeric networks. At the end of 7 days, 41.21 ± 6.49 % and 69.36 ± 2.55 % of the total proteins were released from 2 wt.% PL-NorHA microgels in absence or with 0.005 mg. mL^{-1} of hyaluronidase, respectively. Thus, we observed

that microgel stability and the rate of therapeutic-relevant proteins delivery can be tailored by varying the crosslink density microgels, as well as, the local hyaluronidase concentration.

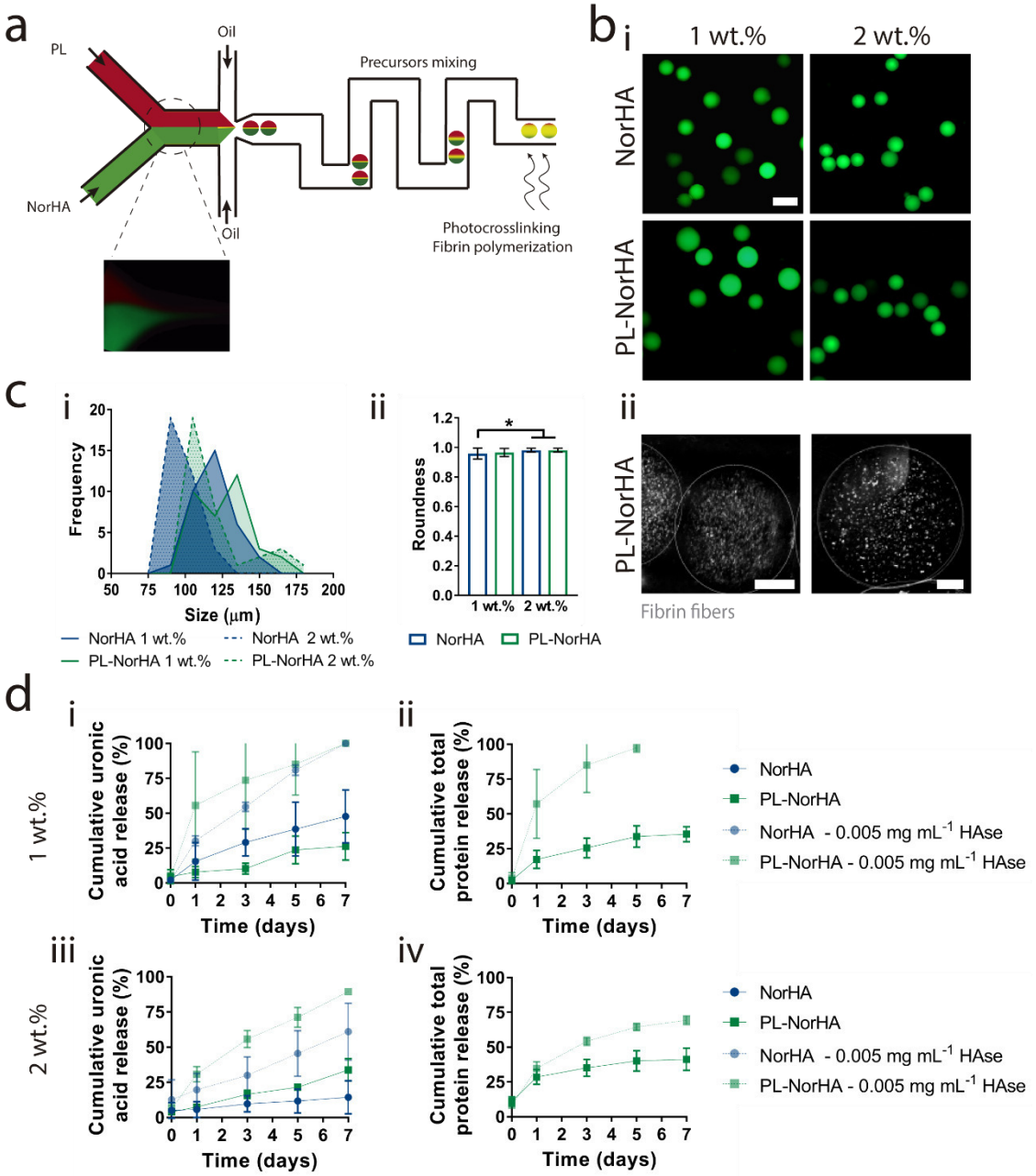

Figure VII-3 Microgel fabrication and characterization. a) Schematic of the microfluidic device for the formation of water-in-oil droplets, where the PL (or PBS for NorHA alone microgels (red) and NorHA (with clotting factors) (green) solutions are introduced and mixed down a serpentine path for fibrin polymerization and subsequently crosslinked with light exposure. b) Representative (i) fluorescent images of FITC-dextran (green) labeled 1 wt.% and 2 wt.% NorHA and PL-NorHA microgels and (ii) confocal reflectance images to detect fibrin fibers (gray) for 1 wt.% and 2 wt.% PL-NorHA microgels. c) Quantification of microgel (i) diameter distributions and (ii) roundness. d) Cumulative uronic acid and total protein release during the degradation of (i, ii) 1 wt.% and (iii, iv) 2 wt.% microgels when incubated in PBS alone or with hyaluronidase (HAse) at 0.005 mg mL^{-1}. Scale bars: 200 μm (b-i), 50 μm (b-ii and iii). * $P < 0.05$.

There are a number of parameters that can be modulated for more complex delivery profiles, such as the combination of microgels of varying stability and composition to recreate a microenvironment with modular properties over time [19]. Moreover, PL contains structural proteins (e.g., fibrinogen and fibronectin) [20] that are known to bind growth factors and control their sequestering, which could further be used to alter the presentation of biological signals to cells [54, 55].

VII-3.2.2. Granular hydrogel rheological characterization

Injectable systems have received significant attention in TERM due to their ability to reach tissue defects and ease administration with minimal surgical wounds [56]. Further, injectability can be useful in the processing of hydrogels with techniques such as 3D printing [57]. To process the hydrogels into injectable formulations, microgels were jammed by vacuum filtration into granular hydrogels to allow physical interactions between the microgels so that they behave as solid extrudable materials [12]. To better understand these systems rheological behavior and structure of granular hydrogels were investigated (Figure VII-4).

Oscillatory shear rheometry results demonstrated that the increase in concentration of NorHA polymer from 1 to 2 wt.% within microgels increased the granular hydrogel storage modulus by up to one order of magnitude (Figure VII-4AI and IV). In agreement with observations in hydrogels, the presence of PL significantly decreased the granular hydrogel storage modulus (from 766.80 ± 2.59 Pa to 233.82 ± 1.74 Pa, 2 wt.% NorHA and PL-NorHA, respectively); however, solid-like properties (G' > G'') were observed in all tested conditions. Similar to our previous studies [17], granular hydrogels behaved rheologically as shear-thinning and self-healing materials, allowing their extrusion using minimal force without altering their initial properties. Both granular hydrogels concentrations (1 wt.% and 2 wt.%) exhibited shear yielding with increased strains (Figure VII-4AII and V). When subjected to high strains, jammed microgels demonstrated disruption of the contacts between particles as evident by the decreased storage moduli [17]. The self-recovery behavior was observed in all granular hydrogels through a series of high (500%) and low (0.5%) strains. After being subjected to high strains, the materials exhibited a rapid recovery of the solid-like behavior (Figure VII-4AIII and VI). Based on their mechanical stability and mechanical recovery properties, granular hydrogels are suitable for several potential applications, including as inks for 3D printing or as injectable formulations for rapid localized delivery in a clinical or emergency setting.

An adequate pore space between microgels is needed for the transport of oxygen, metabolites and nutrients to sustain cell survival [58]. The analysis of the packing density of granular hydrogels was determined by incubating microgels before jamming with rhodamine thiols, Figure VII-4B. After vacuum filtration, 1 wt.% NorHA and PL-NorHA as well as 2 wt.% PL-NorHA formulations showed a denser microgel packing than 2 wt.% NorHA conditions, with increased deformation of microgels within the granular hydrogel structure.

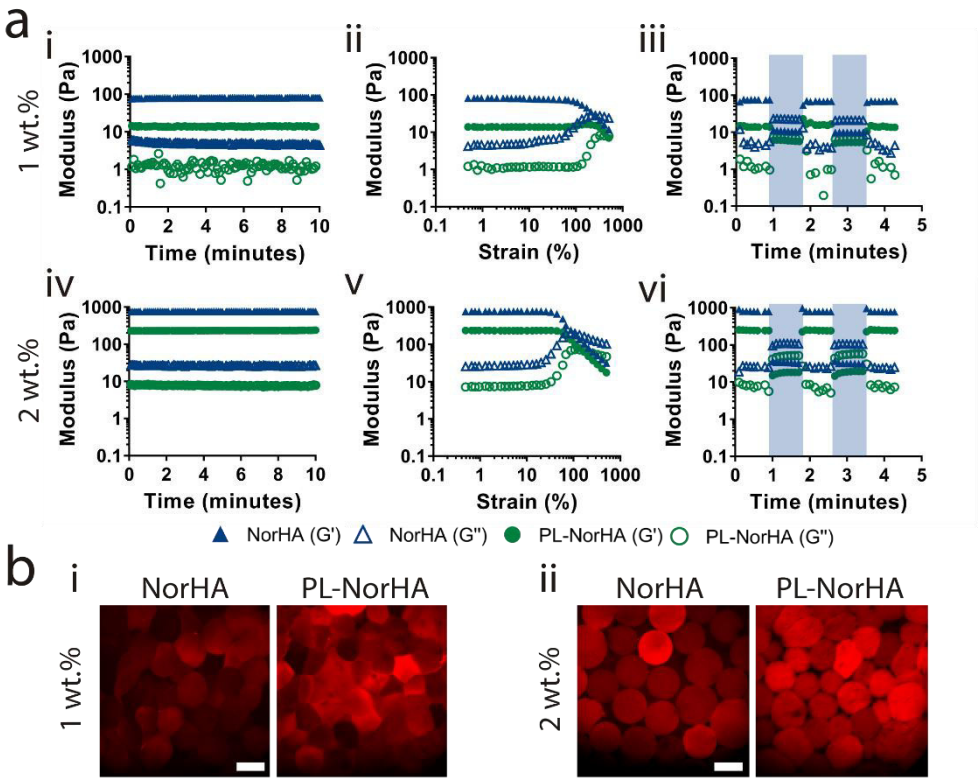

Figure VII-4 Rheological and morphological characterization of jammed NorHA and PL-NorHA granular hydrogels. a) Oscillatory shear rheometry including time sweeps (1 Hz and 0.5% strain), strain sweeps (0.5% to 500% strain and 1 Hz) and cycles through low (0.5% strain, 1 Hz, unshaded) and high (500% strain, 1 Hz, shaded) strains for granular hydrogels from (i-iii) 1 wt.% and (iv-vi) 2 wt.% microgels. b) Representative fluorescence images of rhodamine-labelled (red) granular hydrogels from (i) 1 wt.% and (ii) 2 wt.% NorHA and PL-NorHA microgels. Scale bars: 100 µm (b).

VII-3.2.3. Granular printed constructs and *in vitro* cell response

Microgels were jammed into granular hydrogels and used as injectable inks for 3D printing. To assess the printability of the microgels inks, single filaments that contained microgels with FITC-dextran were printed onto a glass surface and visualized by fluorescence microscopy (Figure VII-5A). Due to their granular structure, the microgel inks were easily extruded to form a uniform filament that displayed a

densely packed microgel morphology. Jammed microgels inks were further 3D printed to fabricate 3D constructs, as previously optimized [17]. The softer jammed microgels resulted in stable 3D constructs for up to seven days in buffer (Figure VII-5BI, II and IV); however, jammed microgels inks from more highly

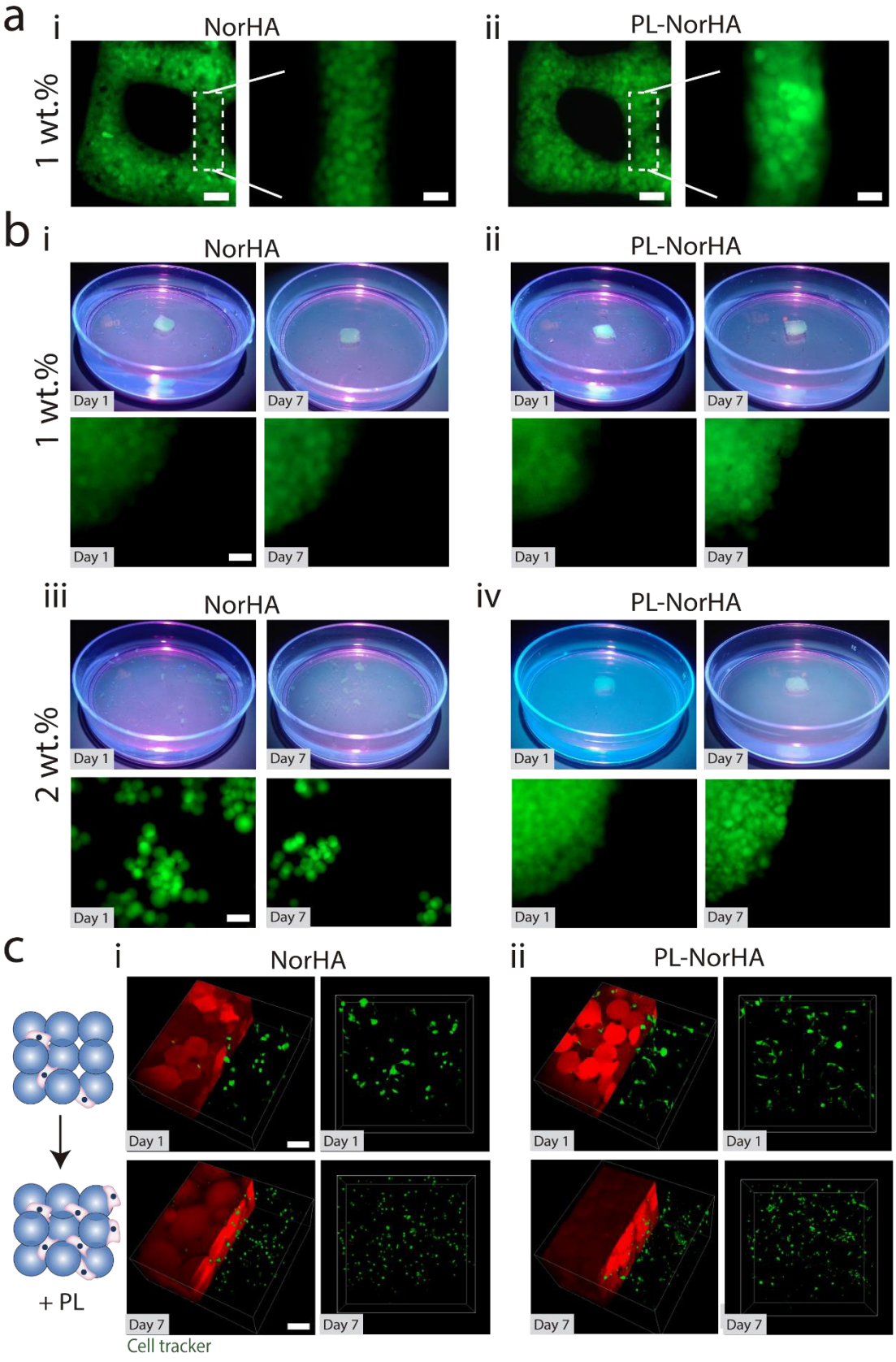

Figure VII-5 3D printed structure stability and interactions with MSCs. a) Fluorescent images of lattice structures from 3D printed granular hydrogels from 1 wt.% microgels containing FITC-dextran (green) from (i) NorHA or (ii) PL-NorHa. b) Macroscopic and fluorescent images of printed cuboid structures after 1 or 7 days of incubation in buffer, when fabricated from granular from (i-ii) 1 wt.% and (iii-iv) 2 wt.% NorHA or PL-NorHA microgels. c) Representative fluorescence images of MSCs (Cell Tracker™ fluorescent: green) after 1 or 7 days of serum-free culture in granular hydrogels from 1 wt.% microgels containing rhodamine (red) from (i) NorHA or (ii) PL-NorHA (note: granular hydrogels from 2 wt. % microgels were not stable with culture for NorHA, so this was not performed). Scale bars: 500 µm (a-i and ii), 200 µm (a-i inset and ii inset, b), 100 µm (c).

crosslinked NorHA particles (2 wt.%) resulted in structures that were easily disrupted (Figure VII-5BIII). Thus, the jamming process is adequate to obtain stable granular hydrogels in which the microporous structure is maintained without needing further processing, as long as the microgels are soft enough to deform when packed together (Figure VII-5B). Several groups have also proposed a variety of chemistries to anneal microgels to maintain their initial structure, namely enzymatic, light induced radical polymerization, and/or carbodiimide chemistry [12, 58].

As an initial proof of concept of using these granular cells to support cell culture, 1 wt.% NorHA and PL-NorHA microporous scaffold constructs were cultured with MSCs under serum-free conditions and their morphology was assessed after 1 and 7 days of *in vitro* culture (Figure VII-5C). Cells were seeded throughout granular hydrogels by mixing the cells with microgels before jamming.

At the beginning of the culture, cells were uniformly distributed throughout the granular hydrogels. MSCs seeded on NorHA microgels exhibited rounded morphologies (Figure VII-5CI), similar to that observed in NorHA hydrogels (Figure VII-2A). On the other hand, after only 1 day in culture, the interconnected microporous space in PL-NorHA microgels promoted substantial cell spreading and the formation of 3D cellular networks (Figure VII-5CI and II). Besides the crucial role of PL-derived proteins on promoting efficient cell adhesion and survival, it is also important to highlight the importance of the hierarchical fibrin network that provides numerous cell-anchorage sites. These results demonstrated that the proposed bioinstructive platform provides an ECM mimetic porous network and human-derived biomolecules reservoir that could modulate a number of complex cellular responses at the single cell level.

VII-4. CONCLUSIONS

In this study, we developed an efficient and unique approach to incorporate bioactive and therapeutically-relevant molecules that mimic the hierarchical fibrillar architecture and composition of the native ECM into hydrogels and microgels. Specifically, this was achieved through the incorporation of PL into covalently crosslinked HA hydrogels, where the physical properties and bioactive protein delivery stemming from PL were modulated by varying the HA concentration. These bioactive cues contributed to greater MSC spreading when compared to hydrogel formulations without PL. Jammed microgels of these formulations displayed shear-thinning and self-healing properties, enabling administration through minimally invasive approaches as well as processing into structures with 3D printing. Finally, the incorporation of PL into printed constructs enhanced the in vitro culture of MSCs under serum-free conditions.

VII-5. REFERENCES

[1] R. Perez-Castillejos, Replication of the 3D architecture of tissues, Mater. Today, 13 (2010) 32.

[2] J.K. Mouw, G. Ou, V.M. Weaver, Extracellular matrix assembly: a multiscale deconstruction, Nat. Rev. Mol. Cell Biol., 15 (2014) 771.

[3] R.O. Hynes, A. Naba, Overview of the matrisome–an inventory of extracellular matrix constituents and functions, CSH Perspect. Biol., 4 (2012) a004903.

[4] K.H. Vining, D.J. Mooney, Mechanical forces direct stem cell behaviour in development and regeneration, Nat. Rev. Mol. Cell Biol., 18 (2017) 728.

[5] L. Macri, D. Silverstein, R.A.F. Clark, Growth factor binding to the pericellular matrix and its importance in tissue engineering, Adv. Drug Deliv. Rev., 59 (2007) 1366.

[6] N.S. Gandhi, R.L. Mancera, The Structure of Glycosaminoglycans and their Interactions with Proteins, Chem. Biol. Drug Des., 72 (2008) 455.

[7] V. Vogel, Unraveling the Mechanobiology of Extracellular Matrix, Annu. Rev. Physiol., 80 (2018) 353.

[8] R.O. Hynes, The Extracellular Matrix: Not Just Pretty Fibrils, Science, 326 (2009) 1216.

[9] A.S. Hoffman, Hydrogels for biomedical applications, Adv. Drug Deliv. Rev., 54 (2002) 3.

[10] X. Tong, F. Yang, Recent Progress in Developing Injectable Matrices for Enhancing Cell Delivery and Tissue Regeneration, Adv. Healthc. Mater., 7 (2018) 1701065.

[11] R. Dimatteo, N.J. Darling, T. Segura, In situ forming injectable hydrogels for drug delivery and wound repair, Adv. Healthc. Mater., 127 (2018) 167.

[12] A.C. Daly, L. Riley, T. Segura, et al., Hydrogel microparticles for biomedical applications, Nat. Rev. Mater., 5 (2020) 20.

[13] M.D. Neto, M.B. Oliveira, J.F. Mano, Microparticles in Contact with Cells: From Carriers to Multifunctional Tissue Modulators, Trends Biotechnol., 37 (2019) 1011.

[14] S. Xin, J. Dai, C.A. Gregory, et al., Creating Physicochemical Gradients in Modular Microporous Annealed Particle Hydrogels via a Microfluidic Method, Adv. Funct. Mater., 30 (2020) 1907102.

[15] D.R. Griffin, W.M. Weaver, P.O. Scumpia, et al., Accelerated wound healing by injectable microporous gel scaffolds assembled from annealed building blocks, Nat. Mat., 14 (2015) 737.

[16] S. Xin, D. Chimene, J.E. Garza, et al., Clickable PEG hydrogel microspheres as building blocks for 3D bioprinting, Biomater. Sci., 7 (2019) 1179.

[17] C.B. Highley, K.H. Song, A.C. Daly, et al., Jammed Microgel Inks for 3D Printing Applications, Adv. Sci., 6 (2019) 1801076.

[18] J. Koh, D.R. Griffin, M.M. Archang, et al., Enhanced In Vivo Delivery of Stem Cells using Microporous Annealed Particle Scaffolds, Small, 15 (2019) 1903147.

[19] M.D. Neto, M.B. Oliveira, J.F. Mano, Microparticles in Contact with Cells: From Carriers to Multifunctional Tissue Modulators, Trends Biotechnol., (2019).

[20] B.B. Mendes, M. Gómez-Florit, P.S. Babo, et al., Blood derivatives awaken in regenerative medicine strategies to modulate wound healing, Adv. Drug Deliv. Rev., 129 (2018) 376.

[21] W.M. Gramlich, I.L. Kim, J.A. Burdick, Synthesis and orthogonal photopatterning of hyaluronic acid hydrogels with thiol-norbornene chemistry, Biomaterials, 34 (2013) 9803.

[22] S.T. Robinson, A.M. Douglas, T. Chadid, et al., A novel platelet lysate hydrogel for endothelial cell and mesenchymal stem cell-directed neovascularization, Acta Biomater., 36 (2016) 86.

[23] C. Loebel, R.L. Mauck, J.A. Burdick, Local nascent protein deposition and remodelling guide mesenchymal stromal cell mechanosensing and fate in three-dimensional hydrogels, Nat. Mater., 18 (2019) 883.

[24] J.E. Mealy, J.J. Chung, H.-H. Jeong, et al., Injectable Granular Hydrogels with Multifunctional Properties for Biomedical Applications, Adv. Mater., 30 (2018) 1705912.

[25] C.B. Highley, C.B. Rodell, J.A. Burdick, Direct 3D Printing of Shear-Thinning Hydrogels into Self-Healing Hydrogels, Adv. Mater., 27 (2015) 5075.

[26] T. Bitter, H.M. Muir, A modified uronic acid carbazole reaction, Anal. Biochem., 4 (1962) 330.

[27] B.P. Toole, Hyaluronan: from extracellular glue to pericellular cue, Nat. Rev. Cancer, 4 (2004) 528.

[28] J.A. Burdick, G.D. Prestwich, Hyaluronic Acid Hydrogels for Biomedical Applications, Adv. Mater., 23 (2011) H41.

[29] C.B. Highley, G.D. Prestwich, J.A. Burdick, Recent advances in hyaluronic acid hydrogels for biomedical applications, Curr. Opin. Biotechnol., 40 (2016) 35.

[30] E.A. Ryan, L.F. Mockros, J.W. Weisel, et al., Structural origins of fibrin clot rheology, Biophys. J., 77 (1999) 2813.

[31] K.J. Wolf, S. Kumar, Hyaluronic Acid: Incorporating the Bio into the Material, ACS Biomater. Sci. Eng., (2019).

[32] K.T. Dicker, L.A. Gurski, S. Pradhan-Bhatt, et al., Hyaluronan: A simple polysaccharide with diverse biological functions, Acta Biomater., 10 (2014) 1558.

[33] J.C. Houck, R.H. Pearce, The mechanism of hyaluronidase action, Biochim. Biophys. Acta, 25 (1957) 555.

[34] J.A. Burdick, C. Chung, X. Jia, et al., Controlled Degradation and Mechanical Behavior of Photopolymerized Hyaluronic Acid Networks, Biomacromolecules, 6 (2005) 386.

[35] Y. Zhang, P. Heher, J. Hilborn, et al., Hyaluronic acid-fibrin interpenetrating double network hydrogel prepared in situ by orthogonal disulfide cross-linking reaction for biomedical applications, Acta Biomater., 38 (2016) 23.

[36] Y.D. Park, N. Tirelli, J.A. Hubbell, Photopolymerized hyaluronic acid-based hydrogels and interpenetrating networks, Biomaterials, 24 (2003) 893.

[37] A.B. Moshnikova, V.N. Afanasyev, O.V. Proussakova, et al., Cytotoxic activity of 1-ethyl-3-(3-dimethylaminopropyl)-carbodiimide is underlain by DNA interchain cross-linking, Cell. Mol. Life Sci., 63 (2006) 229.

[38] P.R. Umashankar, P.V. Mohanan, T.V. Kumari, Glutaraldehyde treatment elicits toxic response compared to decellularization in bovine pericardium, Toxicol. Int., 19 (2012) 51.

[39] S. Kandoi, P.k. L, B. Patra, et al., Evaluation of platelet lysate as a substitute for FBS in explant and enzymatic isolation methods of human umbilical cord MSCs, Sci. Rep., 8 (2018) 12439.

[40] V. Pavlovic, M. Ciric, V. Jovanovic, et al., Platelet Rich Plasma: a short overview of certain bioactive components, Open Med., 11 (2016) 242.

[41] S.G. Boswell, B.J. Cole, E.A. Sundman, et al., Platelet-Rich Plasma: A Milieu of Bioactive Factors, Arthroscopy, 28 (2012) 429.

[42] H. Hemeda, B. Giebel, W. Wagner, Evaluation of human platelet lysate versus fetal bovine serum for culture of mesenchymal stromal cells, Cytotherapy, 16 (2014) 170.

[43] C.R. Silva, P.S. Babo, M. Gulino, et al., Injectable and tunable hyaluronic acid hydrogels releasing chemotactic and angiogenic growth factors for endodontic regeneration, Acta Biomater., 77 (2018) 155.

[44] M.C. Phipps, Y. Xu, S.L. Bellis, Delivery of platelet-derived growth factor as a chemotactic factor for mesenchymal stem cells by bone-mimetic electrospun scaffolds, PLoS One, 7 (2012) e40831.

[45] M. Matsui, Y. Tabata, Enhanced angiogenesis by multiple release of platelet-rich plasma contents and basic fibroblast growth factor from gelatin hydrogels, Acta Biomater., 8 (2012) 1792.

[46] D.E. Discher, D.J. Mooney, P.W. Zandstra, Growth Factors, Matrices, and Forces Combine and Control Stem Cells, Science, 324 (2009) 1673.

[47] T. Yeung, P.C. Georges, L.A. Flanagan, et al., Effects of substrate stiffness on cell morphology, cytoskeletal structure, and adhesion, Cell Motil. Cytoskeleton, 60 (2005) 24.

[48] N. Laurens, P. Koolwijk, M.P.M. De Maat, Fibrin structure and wound healing, J. Thromb. Haemost., 4 (2006) 932.

[49] A.C. Brown, T.H. Barker, Fibrin-based biomaterials: Modulation of macroscopic properties through rational design at the molecular level, Acta Biomater., 10 (2014) 1502.

[50] V.K. Lishko, N.P. Podolnikova, V.P. Yakubenko, et al., Multiple Binding Sites in Fibrinogen for Integrin αMβ2 (Mac-1), J. Biol. Chem., 279 (2004) 44897.

[51] B.B. Mendes, M. Gómez-Florit, R.A. Pires, et al., Human-based fibrillar nanocomposite hydrogels as bioinstructive matrices to tune stem cell behavior, Nanoscale, 10 (2018) 17388.

[52] H. Song, J.D. Tice, R.F. Ismagilov, A Microfluidic System for Controlling Reaction Networks in Time, Angew. Chem. Int. Ed., 42 (2003) 768.

[53] L.P.B. Guerzoni, J.C. Rose, D.B. Gehlen, et al., Cell Encapsulation in Soft, Anisometric Poly(ethylene) Glycol Microgels Using a Novel Radical-Free Microfluidic System, Small, 15 (2019) 1900692.

[54] M.M. Martino, P.S. Briquez, A. Ranga, et al., Heparin-binding domain of fibrin(ogen) binds growth factors and promotes tissue repair when incorporated within a synthetic matrix, Proc. Natl. Acad. Sci. U S A, 110 (2013) 4563.

[55] V. Llopis-Hernández, M. Cantini, C. González-García, et al., Material-driven fibronectin assembly for high-efficiency presentation of growth factors, Sci. Adv., 2 (2016) e1600188.

[56] L. Yu, J. Ding, Injectable hydrogels as unique biomedical materials, Chem. Soc. Rev., 37 (2008) 1473.

[57] M. Shin, K.H. Song, J.C. Burrell, et al., Injectable and Conductive Granular Hydrogels for 3D Printing and Electroactive Tissue Support, Adv. Sci., 6 (2019) 1901229.

[58] E. Sideris, D.R. Griffin, Y. Ding, et al., Particle Hydrogels Based on Hyaluronic Acid Building Blocks, ACS Biomater. Sci. Eng., 2 (2016) 2034.

SECTION 4

CONCLUSION

Chapter VIII

General Conclusions and Future Perspectives

Chapter VIII

General conclusions and Future Perspectives

VIII-1. FINAL REMARKS

In the past few years, Tissue Engineering and Regenerative Medicine (TERM) drew heavily on an explosion of new knowledge that broadens the range of potential diagnostic and therapeutic strategies. In particular, *in vitro* three-dimensional (3D) platforms for drug discovery, nanoengineered scaffolds with tailored properties, microfabrication technologies for 3D multifunctional tissues production or bioprinting for personalized therapies have defined the path for innovative TERM strategies and applications [1, 2]. Nevertheless, TERM still faces significant challenges - both scientific and social, as for example, finding appropriate cell sources and obtaining large cell quantities; replacement of animal origin products in cell culture media protocols; design of biomaterials with tailorable and intrinsic bioactive properties; enabling vascularization of tissue engineered constructs; and a number of other clinical translational issues [1].

In this thesis, we addressed some of the above mentioned TERM challenges by exploiting the intrinsic bioactivity of human platelet lysate (PL) based biomaterials. PL includes biologically-relevant proteins for *in vitro* cell culture; microbicidal proteins for antimicrobial host defense; potent pro-angiogenic proteins to promote vascularization; and structural proteins with key cell instructive cues capable of enhancing cell-material interactions and/or inducing specific cellular responses [3]. However, the use of biomaterials solely based on PL exhibit limited mechanical properties, fast in *vitro/in vivo* biomolecules degradation, and short-term storage stability, which limits its potential application in several TERM strategies. In order to improve PL-based biomaterial physicochemical and stability properties, we have developed 3D PL-based systems through different processing techniques and methodologies. We incorporated (1) aldehyde-modified cellulose nanocrystals (a-CNC), which get entrapped along the fibrin fibers of the PL systems and crosslinks through reversible Schiff base bonds (***Chapter 3 and 6***), or (2) norbornene-modified hyaluronic acid (NorHA) that covalent-crosslinked through thiol-norbornene photochemistry (***Chapter 7***). Such intrinsically bioactive micro/nano-structured scaffolds can find multiple applications in relevant research and clinical RM strategies such as injectable hydrogels, bioinks, or hemostatic agents.

Throughout this thesis, we discussed in detail how to explore the full potential of PL-derived proteins by i) improving its structural integrity and short-term stability; ii) tailoring biomolecules sequestering and

spatio-temporal release; iii) modulating the physical properties of PL-based scaffolds; iv) controlling its retractile effect upon cell encapsulation while v) preserving PL-derived proteins biological function. In addition, PL was used as an alternative to fetal bovine serum (FBS) in all the *in vitro* cell culture conditions, which clearly strengthens the clinical translation of the proposed PL-based systems. Accordingly, the main contributions of this thesis are the following:

- Mimic of the hierarchical and fibrillar architecture of the native ECM. ECM hierarchical structure is formed by the coordinated supramolecular assembly of individual proteins such as e.g. elastin, collagen and fibronectin [4]. In a biomimetic and bottom-up strategy, we trigger the natural *in situ* clotting cascade. The incorporation of CNC or HA polymers along the fibrinogen self-assembly recapitulates the spatial organization and hierarchical nano-to-macro fibrillary composition of native tissues, which are difficult to recreate by using typical synthetic polymer biomaterials.

We showed that the biomimetic ECM fibrillary architecture is crucial to allow the mass transport of nutrients, metabolites and waste to sustain cell survival (***Chapter 6***), while simultaneously empowering the commitment of the encapsulated cells towards different/specific phenotypes ***(Chapter 3)*** and matrix remodeling (***Chapter 3 and 6***). Mimicking the porous ECM-architecture represents a clear advantage over current biomaterials that typically depend on the use of perfusable channels to improve cell viability in large size scaffolds.

We also demonstrated that by adjusting fibrinogen, thrombin and calcium concentration, as well as adding CNC and NorHA polymers, we circumvent the typically highly dense branched fibrin fibers networks with low interfiber space, which is obtained in scaffolds solely based on PL.

- Engineer scaffolds with tailorable biophysical and biochemical properties. The physical and chemical properties of the resulting tissue engineered scaffolds strongly affects cell responses and its further TERM applications. It is well-known that scaffolds with cell-responsive biodegradability dynamically regulate cell migration, and the mechanical information in the cell-hydrogel interface modulates cell proliferation [5]. Therefore, we developed multifunctional PL-based systems that allows a precise control over microstructural and final mechanical properties of the fibrillar structure, as well as its dynamic biochemical microenvironment.

The incorporation of CNC and HA polymers greatly improves the structural stability and mechanical properties of PL-based gels (***Chapter 3, 4 and 7***), enabling their use as effective human-based scaffolds. Besides the modulation of the bulk mechanical behavior, by changing macromer concentration and crosslinking density, we also showed that variation of CNC content can be explored to modulate the

mechanical properties at fiber level (*Chapter 3*). Previous literature reports showed that the tension exerted by stem cells on fibrils greatly affects cell response through molecular mechanosensing mechanisms at the cell scale [4]. In this thesis, we showed how the traction forces between the hydrogel fiber-like architecture and stem cells can alter cell behavior (e.g., gene expression).

Regarding the control over the dynamic biochemical environment, we demonstrated that the physical properties of the resulting scaffolds can hindered the inherent proteolytic degradation of PL-based systems (**Chapter 3, 4, 6 and 7**). Moreover, we showed that PL-based systems were able to modulate the dose and spatio-temporal delivery of platelet-derived biomolecules such as growth factors (GFs), *Chapter 3*. We also engineered CNC with variable sulfation degree as mimics of sulfated glycosaminoglycans in which CNC surface chemistries (e.g., amphiphilic character and sulfation degree) fine-tuned the solid-phase presentation of PL-derived proteins, *Chapter 5*.

- Design of protein-engineered biomaterials to modulate stem cell behavior. ECM is not simply a collection of proteins [6, 7]. Its composition and further organization confer specific tissue-specific roles to the ECM. Current regenerative strategies have design biomaterials that can modulate the ECM secreted by the cells in order to create engineered tissues [8]. Promising strategies relies on the tuning of biological ligands such as the functionalization with peptides or proteins [9, 10], and/or the modulation of physical properties of the materials at the nanoscale [5, 11].

In this work, we explored PL that comprises key temporary ECM proteins (e.g., fibrin, fibronectin and vitronectin) able to modulate cell behavior via native cell binding motifs and selective presentation of GFs. For example, fibrin and fibronectin interact with cell-surface integrins, and contain binding domains for ECM proteins and secreted GFs [4, 12]. We exploited the enriched bioactive milieu of PL, which in combination with CNC or HA polymers tunes physicochemical properties and produces a defined cell-instructive environment.

We demonstrated that the presence of platelet-derived biomolecules favors cell adhesion, fast cell proliferation, and migration *(Chapter 4)*. PL-based systems also showed to regulate the remodeling at the dynamic cell-hydrogel interface in which the engineered fibrillar network is degraded and remodeled with newly synthetized cell-origin ECM. In particular, we explored the deposition of the fibrillar collagens, namely collagen types I (*Chapter 6*), II (*Chapter 5*), and III (*Chapter 3*). Finally, we demonstrated how material's biophysical and biochemical cues can be exploited to direct stem cell differentiation (*Chapter 3 and 5*). We evaluated the effect of CNC with variable sulfation degree on the

potential cell commitment to three common mesenchymal lineages (chondrogenic, osteogenic and adipogenic), ***Chapter 5***.

- Engineering precision biomaterials for personalized therapies. The developed PL-based bioinks demonstrated their potential to fabricate complex and personalized bioprinted structures for *in vitro* 3D studies or clinical translation. The developed nanocomposite bioinks (***Chapter 6***) and microgels inks (***Chapter 7***) enable to print constructs with high shape fidelity, fiber-like architecture, biocompatibility, and structural integrity.

Strikingly, we can easily modulate inks physicochemical properties, which will have a direct impact on cellular response. By changing macromer concentration and crosslinking density, it would be able to regulate the porosity, mechanical properties and proteins profile release of the resulting 3D construct. We also envision the incorporation of patient-specific cells and/or the use of autologous PL-derived bioactive components (instead of PL preparation from pools of samples/donors) to tailor the medical treatment to the individual features of each patient.

- Clinical translation potential of PL-based systems. Throughout this thesis, we developed different nanocomposite scaffolds based on the simple one-pot polymerization (i.e., coagulation cascade induction) and crosslinking method (i.e., reversible Schiff base bonds). This simple mechanism clearly potentiates the fast *in situ* gelation for rapid localized injectable delivery in a clinical or emergency setting (***Chapter 3***) and for 3D bioprinting applications (***Chapter 6***). The continued refinement of hemostatic materials composition to promote tissue regeneration endows our off-the-shelf PL-CNC cryogels with a great potential to improve the current clinical practices (***Chapter 4***). Besides the multiple applications and processing techniques that can be exploited from the same concept, various material´s properties can be customized to meet patient-specific needs. We believe on the potential for clinical translation of these intrinsically bioactive systems and have therefore filed a patent on the developed concept (***Appendix 1***).

Moreover, PL has been used as a prevailing supplement for cell culture in replacement of animal-derived serum (i.e., FBS) due to its standardized clinical grade preparation method. The use of serum-free cell culture conditions in our PL-based systems represents an advantage not only for research purposes, but also in terms of compliance with good manufacturing practices and clinical relevance. Indeed, in the preparation of the proposed PL-based systems, we used reproducible and standardize protocols to reduce the protocol-related variability and to produce more controllable systems. Moreover, the use of fibrinogen-derived from human PL samples voids the exposure to xenogeneic-derived products and associated risks.

VIII-2. FUTURE PERSPECTIVES

The biological questions and applications that can harness such PL-based platforms to match the complex bidirectional interactions between cells and the engineered ECM, and the heterogeneous biophysical and biochemical cues of the ECM are manifold. Recent studies showed that stem cells quickly modify their surrounded microenvironment as soon as four hours after encapsulation [13]. Therefore, we believe that is of utmost interest to explore in future studies the cell-derived ECM and cell-mediated material remodeling to better understand the impact of PL proteins presentation to guide cell behavior.

In this thesis, we demonstrated that our proposed PL-bases strategies take advantage of the inexpensive enriched milieu of bioactive factors that are typical release from platelets [14]. These factors include clotting agents, cytokines/chemokines, structural proteins, microbicidal proteins, ions, membrane proteins and GFs [3, 15]. Thus, we could exploit the spatio-temporal release of these PL-derived biomolecules to simultaneously introduce more than one desirable biological function such as cell migration and vascularization. Moreover, we could confer additional control over the human-based nanocomposite systems through the design of magnetic responsive scaffolds and/or bioinks by decorating CNC with magnetic nanoparticles, for example.

Throughout this thesis, we developed different bioactive materials that can find application on the regeneration of different tissues but that were not explored on a specific regenerative strategy. For example, *in chapter 5*, we demonstrated that the adsorption of PL-derived biomolecules depends on CNC sulfation degrees, and how these formulations are able to modulate the *in vitro* biological response. Therefore, an interesting scale-up of this 2D concept would be the introduction of these different CNC formulations in the previous developed 3D strategies (*Chapter 3* and *6*) to guide cell fate decisions and explore a particular TERM application.

In addition, most of the proposed systems are based on a-CNC as modulators of the PL gels properties. Although the use of this polymer in TERM applications have received exponential attention, humans do not have enzymes that can easily degrade cellulose, which can be an obvious limitation to our system. In a parallel project, we already tested how to incorporate cellulase into nanocomposite systems, in order to improve and modulate their degradability in *in vitro* and *in vivo* settings. In fact, these strategies have been already implemented on nanocellulose based hydrogels for 3D cell cultures such as GrowDex® commercial products. Undoubtedly, this will be an interesting and bioorthogonal strategy that would contribute to minimize the potential risks associated with the biopersistence of cellulose-based biomaterials when implanted *in vivo*.

Under the scope of this thesis, we developed innovative human-based strategies that offer an excellent control over chemical and physical properties of the scaffold. Along their intrinsic bioactivity and their hierarchical filamentous nature, these approaches have shown to be a multifunctional and versatile concept. Hopefully, the developed biomaterials strategies and processing techniques will provide useful insights towards new ECM-mimetic hydrogels for *in vitro* 3D cell cultures, and for personalized therapies to guide tissue regeneration *in vivo*.

VIII-3. REFERENCES

[1] A. Shafiee, A. Atala, Tissue Engineering: Toward a New Era of Medicine, Ann. Rev. Med., 68 (2017) 29.

[2] M.E. Gomes, M.T. Rodrigues, R.M.A. Domingues, et al., Tissue Engineering and Regenerative Medicine: New Trends and Directions-A Year in Review, Tissue Eng. Part B Rev., 23 (2017) 211.

[3] B.B. Mendes, M. Gómez-Florit, P.S. Babo, et al., Blood derivatives awaken in regenerative medicine strategies to modulate wound healing, Adv. Drug Deliv. Rev., 129 (2018) 376.

[4] E. Prince, E. Kumacheva, Design and applications of man-made biomimetic fibrillar hydrogels, Nat. Rev. Mater., 4 (2019) 99.

[5] Y. Li, Y. Xiao, C. Liu, The Horizon of Materiobiology: A Perspective on Material-Guided Cell Behaviors and Tissue Engineering, Chem. Rev., 117 (2017) 4376.

[6] J.K. Mouw, G. Ou, V.M. Weaver, Extracellular matrix assembly: a multiscale deconstruction, Nat. Rev. Mol. Cell Biol., 15 (2014) 771.

[7] C. Bonnans, J. Chou, Z. Werb, Remodelling the extracellular matrix in development and disease, Nat. Rev. Mol. Cell Biol, 15 (2014) 786.

[8] U. Blache, M.M. Stevens, E. Gentleman, Harnessing the secreted extracellular matrix to engineer tissues, Nat. Biomed. Eng., (2020).

[9] D.G. Belair, N.N. Le, W.L. Murphy, Design of growth factor sequestering biomaterials, Chem. Commun., 50 (2014) 15651.

[10] S.P.B. Teixeira, R.M.A. Domingues, M. Shevchuk, et al., Biomaterials for Sequestration of Growth Factors and Modulation of Cell Behavior, Adv. Func. Mater., (2020) 1909011.

[11] C.F. Guimarães, L. Gasperini, A.P. Marques, et al., The stiffness of living tissues and its implications for tissue engineering, Nat. Rev. Mater., 5 (2020) 351.

[12] A.C. Brown, T.H. Barker, Fibrin-based biomaterials: Modulation of macroscopic properties through rational design at the molecular level, Acta Biomater., 10 (2014) 1502.

[13] C. Loebel, R.L. Mauck, J.A. Burdick, Local nascent protein deposition and remodelling guide mesenchymal stromal cell mechanosensing and fate in three-dimensional hydrogels, Nat. Mater., 18 (2019) 883.

[14] S. Sorrentino, J.-D. Studt, O. Medalia, et al., Roll, adhere, spread and contract: Structural mechanics of platelet function, Eur. J. Cell Biol., 94 (2015) 129.

[15] R. Flaumenhaft, Chapter 18 - Platelet Secretion, in: A.D. Michelson (Ed.) Platelets (Third Edition), Academic Press, 2013, pp. 343.

Appendix I

Blood derivatives composite material, methods of production and uses thereof

Appendix I

Blood derivatives composite material, methods of production and uses thereof

ABSTRACT

The present disclosure relates to a blood derivatives-based nanocomposite material incorporating comprising oxidized cellulose nanocrystals, methods for their production, and uses thereof. Also disclosed herein is a method for the production of oxidized cellulose nanocrystals with gradients of sulfation degree and their use to modulate the affinity of protein content of blood derivatives/cellulose nanocrystals nanocomposite materials. Therefore, the present disclosure is useful use in regenerative medicine and/or tissue engineering.

This appendix corresponds to a patent application: ***B. B Mendes****, R. M. A. Domingues, P. Babo, R. L. Reis, M. E. Gomes. Blood derivatives composite material, methods of production and uses thereof. Patent application: WO 2018/078586 A1, EP 3532114 A1 and US 2019/0282621 A1. Priority date: 27 Oct 2016, PT.*

Patent request that is directly related to the chapters 3, 4, 5 and 6 of this Thesis.

IX-1. DESCRIPTION

IX-1.1. Technical field

The present disclosure relates to a blood derivatives nanocomposite material comprising oxidized cellulose nanocrystals, methods for their production, and uses thereof. Also disclosed herein is a method for the production of oxidized cellulose nanocrystals with gradients of sulfation degree and their use to modulate the affinity of protein content of blood derivatives/cellulose nanocrystals nanocomposite materials.

IX-1.2. Background

Blood is composed of different cellular, sub-cellular and molecular components that are involved in essential stages of wound healing and regenerative processes. The separation of blood components results on different blood derivative (BD) formulations. BD have shown promising features as an autologous and natural reservoir of supra-physiological doses of growth factors (GFs), cytokines, and extracellular matrix (ECM) precursors which are known to significantly modulate cell behavior. Among the ECM precursors present in BD are fibrinogen and fibronectin. Fibrinogen of BD has been commonly activated by calcium, collagen and exo- or/and endogenous thrombin, which promote the polymerization of fibrinogen producing a stable fibrin matrix.

The use of different types of BD has shown positive clinical effects in several fields of regenerative medicine such as in the treatments of tendon injures and pathologies, cartilage disorders, as well as in bone, periodontal and soft tissue wound healing. BD have been incorporated within polymeric matrices or used as biomaterials by self-crosslinking of its protein content in order to improve or tune the biological response of these biomaterials. Traditional methods of BD application in tissue engineering (TE) strategies rely on the activation of BD by thrombin and calcium activation in order to form a clot.

Currently, BD-based strategies have several limitations, including lack of standardization, limited mechanical properties, fast degradation of the biological active substances, limited *in vitro/in vivo* stability, without sufficient control over bioactive molecules release and low retention at the injury site.

There is a need to overcome BD-based strategies namely, shrinkage upon cellular encapsulation, modulation in the temporal and spatial demands of GF release, control over scaffold degradation rate and

improved native tissue integration. The development of more controllable systems for the delivery of well characterized populations of biomolecules will certainly improve the clinical outcomes of the use of BD.

In native ECM microenvironments, GFs are protected and stabilized via their binding to different ECM components that regulate their availability and signaling. In a biomimetic strategy, researchers have combined BD with different biomaterials to modulate the delivery of bioactive molecules in order to guide the wound healing process.

Cellulose nanocrystals (CNC) present outstanding characteristics namely high biocompatibility, low density, high surface area, high mechanical properties and a reactive surface which enables different surface chemical modifications. The nanodimensions and superior strength of CNC make it an ideal reinforcing material to a low strength matrix. Biomaterials containing surface sulfated CNC can exhibit specific or unspecific interactions with the pool of GFs released from PL. These interactions of platelet-released GFs and other proteins with the sulfated CNC within the biomaterial matrix may increase their local concentration/specificity within the 3D microenvironment, thus enhancing/tuning their effect over encapsulated stem cells. However, the use of CNC with a gradient of surface SO_3-half-ester groups as mimicry of ECM sulfated GAGs, has not been previously proposed.

WO2014077854 A1 discloses a system and method for the production of a fibrin matrix that incorporates CNC and/or oxidized CNC. WO2013116791 A1 discloses the use of biomaterials in combination of blood products. These facts are disclosed in order to illustrate the technical problem addressed by the present disclosure.

IX-1.3. General description

The present disclosure discloses use of CNC as a biomaterial or precursor in combination with BD component.

The present disclosure also described the use of BD as an intermediate component of the process to produce biomaterials, namely sponges and hydrogels, to be used as scaffolds or cell carries in TE applications.

Biomaterials containing surface sulfated CNC can exhibit specific or unspecific interactions with the pool of GFs released from PL. These interactions of platelet-released GFs and other proteins with the sulfated CNC within the biomaterial matrix may increase their local concentration/specificity within the 3D microenvironment, thus enhancing/tuning their effect over encapsulated stem cells. It was

surprisingly observed, the use of CNC with a gradient of surface SO3- half-ester groups as mimicry of ECM sulfated GAGs.

In the present disclosure, a BD component is any therapeutic substance prepared from human blood. These includes whole blood; blood components; and plasma derivative. In particular platelet, platelet released content, platelet-rich plasma, or their combinations.

An aspect of the present disclosure relates to a composition comprising:

a BD component;

a CNC as a filler comprising carbonyls at the CNC surface;

wherein such CNC comprises a sulfation degree of at least 50 mmol. Kg^{-1}; between 80 and 500 mmol. Kg^{-1}; more preferably between 100 and 300 mmol. Kg^{-1}; even more preferably between 120 and 300 mmol. Kg^{-1}.

It was surprisingly found that certain sulfation degree promotes favored non-covalently interactions with the protein content derived from BD formulations. The sulfation degree of the CNC may be measured by the method conductometric titration.

In an embodiment for better results, the composition may comprise 0.05-2% w/v of CNC; preferably 0.1-1 % w/v; more preferably 0.15-0.61 % w/v.

In an embodiment for better results, the composition may comprise $0.5x10^4$ platelets/µL -$1x10^8$ platelets/µL of BD platelet concentration; preferably $1x10^5$ - $1x10^7$ platelets/µL; more preferably $1x10^6$ - $5x10^6$ platelets/µL.

In an embodiment for better results, the composition may comprise thrombin, calcium, calcium salts, or mixtures thereof. It was surprisingly found that thrombin and calcium may be used to the activation of the coagulation cascade to convert fibrinogen contained in the BD into fibrin.

In an embodiment for better results, the composition may comprise 0.1 U. mL^{-1} - 50 U. mL^{-1} of thrombin preferably 0.5 U. mL^{-1} - 5 U. mL^{-1}; more preferably 1 U. mL^{-1} - 3 U. mL^{-1}.

In an embodiment for better results, the composition may comprise 0.1mM - 25mM of calcium or calcium derivate; preferably 0.5 mM - 10 mM; more preferably 1mM - 5mM.

In an embodiment for better results, the composition may comprise an amount of carbonyl groups at the surface of the CNC between .01 - 8 mmol. g-1; preferably 0.1 - 4 mmol. g^{-1}; more preferably 0.4 - 0.9 mmol. g^{-1}.

In an embodiment for better results, the composition may further comprise one or more active ingredient or biomolecule.

In an embodiment for better results, the composition may comprise as an active ingredient or biomolecule: active ingredient or biomolecule is: a drug; an active ingredient, a growth hormone, a cell attractant, a drug molecule, a cell, a bioactive glass, a tissue growth promoter, a cell attractant, or combinations thereof.

In an embodiment for better results, the drug molecule may be an anti-inflammatory, antipyretic, analgesic, anticancer agent, or mixtures thereof.

In an embodiment for better results, the wherein cells may be selected from: osteoblasts, osteoclasts, osteocytes, pericytes, endothelial cells, endothelial progenitor cells, bone progenitor cells, hematopoietic progenitor cells, hematopoietic stem cells, neural progenitor cells, neural stem cells, mesenchymal stromal/stem cells, induced pluripotent stem cells, embryonic stem cells, or combinations thereof.

In an embodiment for better results, the composition may further comprise one or more pharmaceutically acceptable excipient. In particular an additive, a binder, a disintegrant, a diluent, a lubricant, a plasticizer, or mixtures thereof.

In an embodiment for better results, the average length of the CNC is between 40 - 2500 nm; preferably 100 - 500 nm; more preferably 200 - 300 nm.

In an embodiment for better results, average width of the CNC is between 2 - 50 nm; preferably 3 - 20 nm; more preferably 4 - 15 nm.

In an embodiment for better results, the BD component may be a fraction of blood including red blood cells, white blood cells, buffy coat, plasma or platelet rich plasma, or an extract of blood including growth factors or extracellular matrix proteins purified or released from blood, blood fractions, or combination thereof. More preferably a platelet, platelet released content, platelet-rich plasma, or combinations thereof.

In an embodiment for better results, the BD component may be obtainable by centrifugation, by apheresis, or combinations thereof.

Another aspect of the present disclosure relates to the use of the composition of the present disclosure in medicine, veterinary or cosmetic, namely for use in tissue engineering, tissue regeneration or regenerative medicine, or in cellular therapy.

In an embodiment for better results, the composition may be use the treatment or therapy of wound healing or a tissue injury defect. In particular, the treatment or therapy of defects of skin wound, orthopedic injury, pain, nerve disease, dental injury, bone injury; or diabetic wound healing.

In an embodiment for better results, the composition may be use as an injectable formulation.

In an embodiment for better results, the composition is an injectable formulation, in particular an in situ injection.

Another aspect of the present disclosure relates to a hydrogel comprising the composition of the present subject-matter and comprising a BD component reinforced with modified CNC (or oxidized CNC) of a certain sulfation degree and, thrombin and/or calcium addition.

In an embodiment for better results, hydrogels with higher CNC content showed lower degradation rate. In fact, CNC incorporation lead to an improvement of PL stability (Figure IX-6).

In an embodiment for better results, the hydrogel may be an in situ crosslinked injectable hydrogels at physiological conditions.

Another aspect of the present disclosure relates to a sponge or scaffold comprising the composition described in the present disclosure comprising a BD and modified CNC of a certain sulfation degree.

Another aspect of the present disclosure relates to a sponge or scaffold comprising the composition described in the present disclosure comprising a BD and modified CNC of a certain sulfation degree, and, thrombin and/or calcium addition.

In an embodiment for better results, sponge or scaffold may be casted to the desired mold shape.

In an embodiment for better results, the sponge or scaffold may further comprise encapsulated cell and/or cells.

In an embodiment for better results, the cell or cells may be encapsulated or seeded.

Another aspect of the present disclosure relates to a method for producing scaffolds including injectable hydrogels, hydrogels and sponges for regeneration of biological tissues based on the use of BD and modified cellulose based-biomaterial.

In an embodiment for better results, the production method may further comprise oxidation of sulfated CNC by sodium periodate reaction or 2,2,6,6-tetramethylpiperidine-1-oxyl radical.

In an embodiment for better results, the production method may further comprise a hydrothermal treatment to produce CNC with a gradient of sulfation degrees.

In an embodiment for better results, a method for producing sponge biomaterials for any tissue engineering application includes mixing BD with an aqueous suspension of oxidized CNC of a certain sulfation degree, incubating the mixture for a certain period of time, freezing and freeze-drying the crosslinked nanocomposite material.

In an embodiment for better results, the method may comprise an aqueous oxidized CNC solution of a certain sulfation degree covalently crosslinks with the amine groups of the protein content released from BD formulations.

In an embodiment for better results, the method may comprise an aqueous oxidized CNC solution of a certain sulfation degree interacts electrostatically with the positive groups of the protein content released from BD formulations.

In an embodiment for better results, a method for producing sponge biomaterial for any TE application includes mixing BD with an aqueous suspension of oxidized CNC of a certain sulfation degree, thrombin, and calcium, incubating the mixture for a certain period of time, freezing and freeze-drying the crosslinked nanocomposite material.

In an embodiment for better results, wherein oxidized CNC of a certain sulfation degree covalently crosslinks with the amine groups of the protein content derived from BD formulations.

In an embodiment for better results, wherein oxidized CNC of a certain sulfation degree interacts electrostatically with the positive groups of the protein content derived from BD formulations.

In an embodiment for better results, wherein thrombin and calcium activation of the coagulation cascade is used to convert fibrinogen contained in the BD into fibrin.

In an embodiment for better results, a method for producing hydrogels for any TE application includes mixing BD with an aqueous suspension of oxidized CNC of a certain sulfation degree, thrombin and calcium, incubating the mixture for a certain period of time, producing in situ crosslinked hydrogels.

In an embodiment for better results, wherein oxidized CNC of a certain sulfation degree covalently crosslinks with the amine groups of the protein content derived from BD formulations.

In an embodiment for better results, wherein oxidized CNC of a certain sulfation degree interacts electrostatically with the positive groups of the protein content derived from BD formulations.

In an embodiment for better results, wherein thrombin and calcium activation of the coagulation cascade is used to convert fibrinogen contained in the BD into fibrin.

IX-1.4. Brief description of the drawings

The following figures provide preferred embodiments for illustrating the description and should not be seen as limiting the scope of invention.

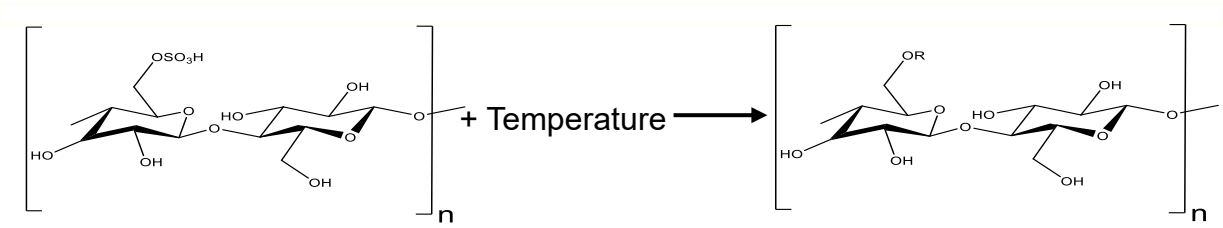

Figure IX-1 Decrease of sulfate group content of oxidized CNC by thermal degradation.

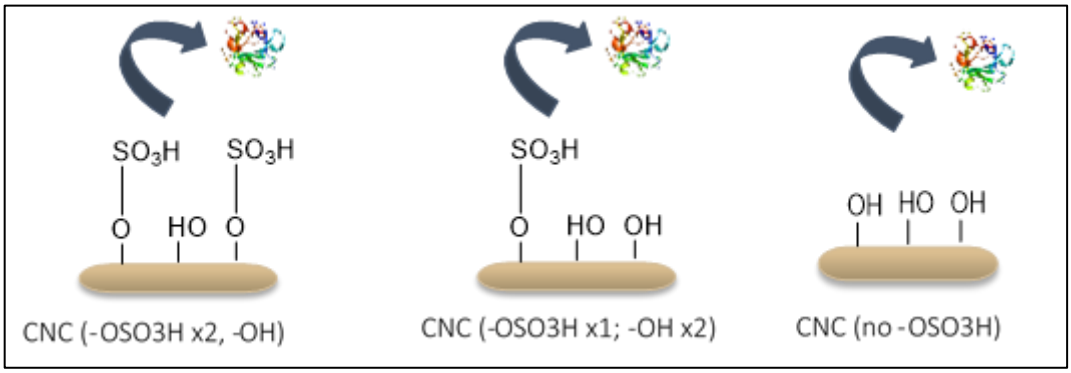

Figure IX-2 Schematic representation of the affinity between CNC surface and PL - derived proteins.

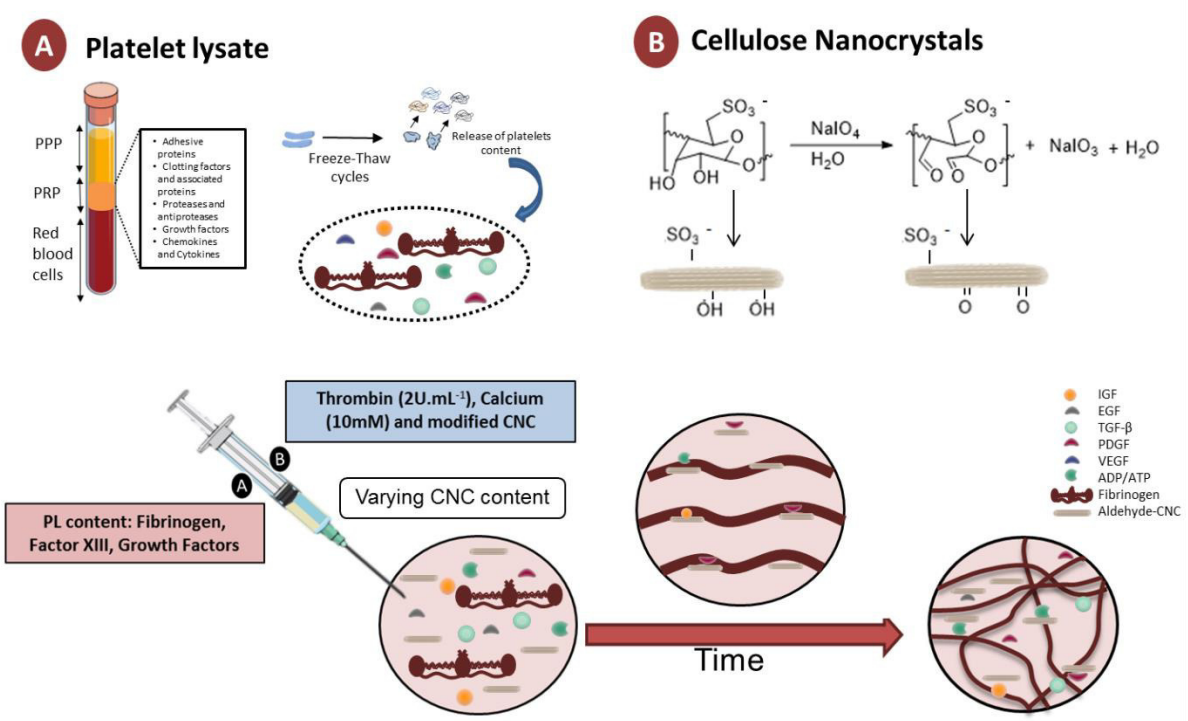

Figure IX-3 Schematic representation of the preparation of PL enriched CNC injectable hydrogels. A) PL and B) oxidized CNC and preparation of PL-CNC hydrogel.

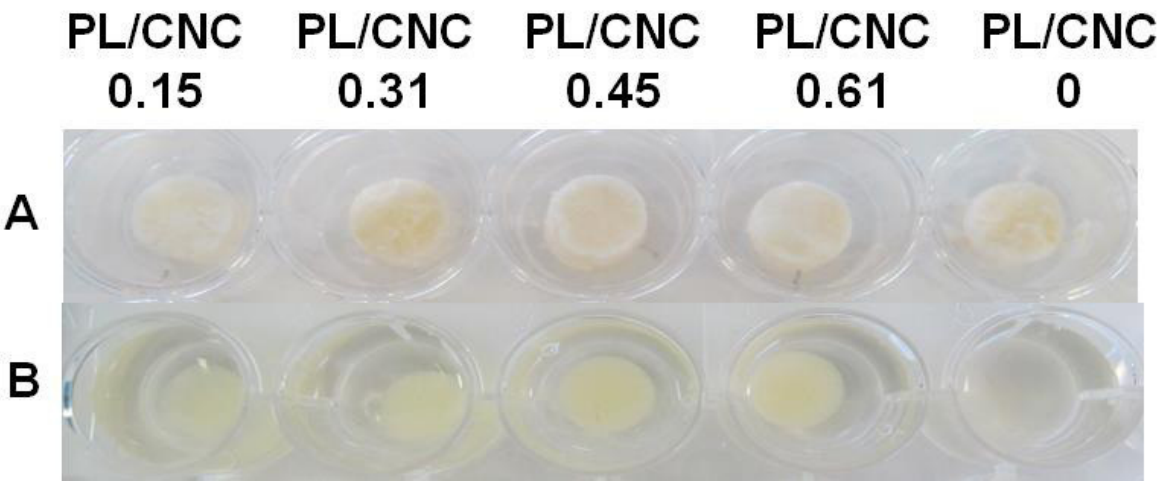

Figure IX-4 Freeze dried spongy hydrogels (A) before and (B) after immersion in PBS with varying CNC content wherein the CNC concentration is 0% w/v (PL-CNC 0), 0.15 % w/v (PL-CNC 0.15), 0.31 % w/v (PL-CNC 0.31), 0.45 % w/v (PL-CNC 0.45), and 0.61 % w/v (PL-CNC 0.61) in 50% PL composition.

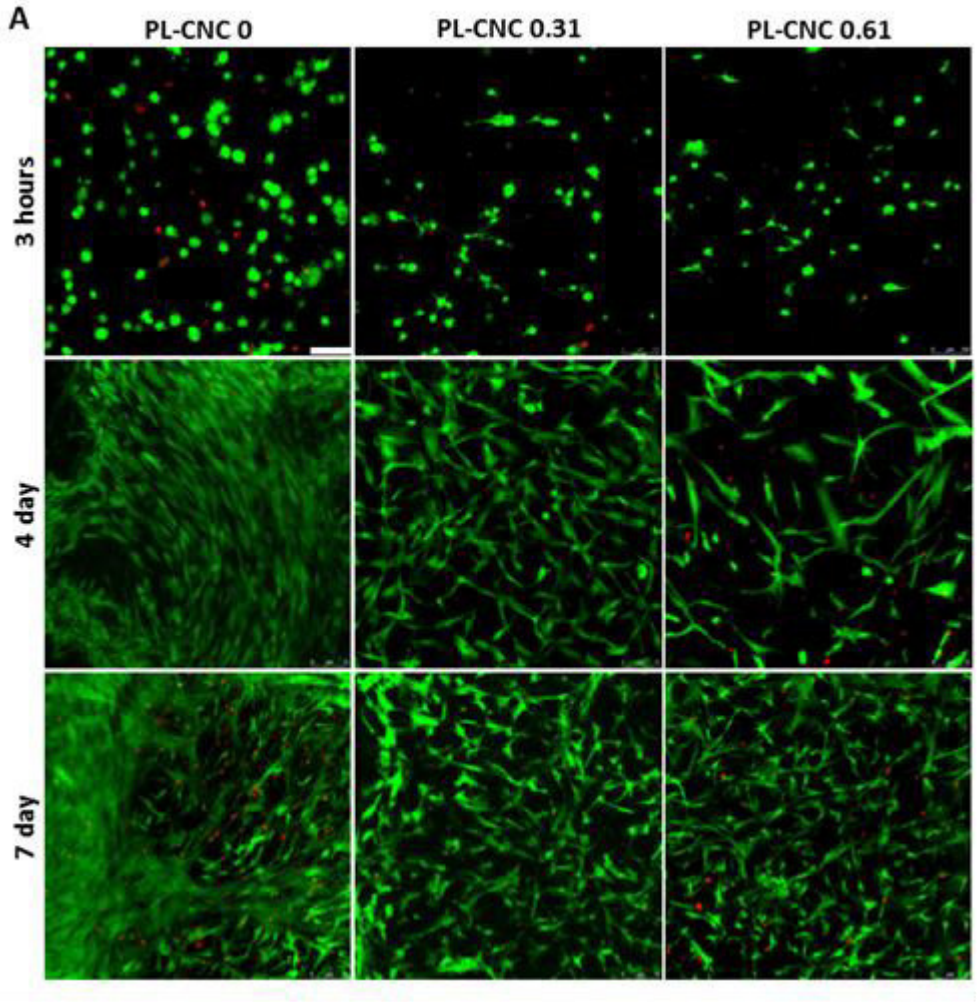

Figure IX-5 *In vitro* evaluation of cell supportive properties. Live/Dead staining with Calcein AM/PI (green: live cell; red: dead cell) of hASCs encapsulated in PL/CNC hydrogels

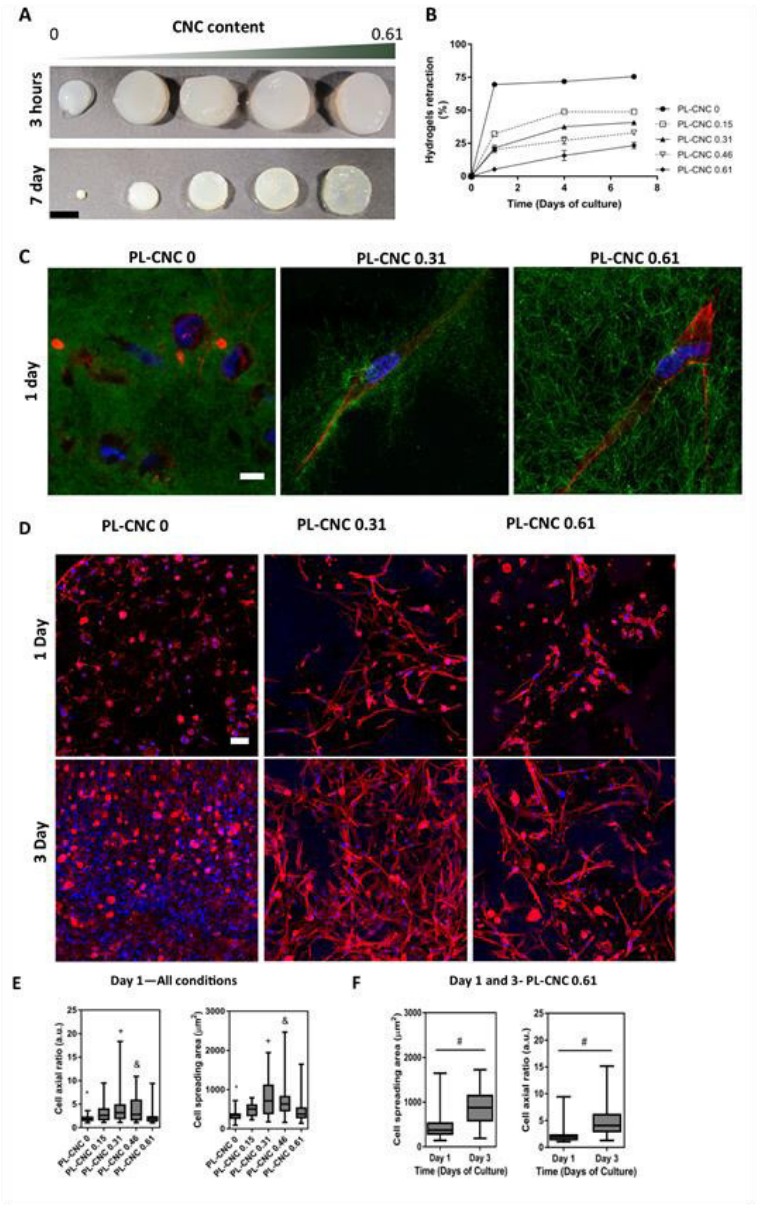

Figure IX-6 Hydrogels retraction upon hASCs encapsulation and analysis of adhesion and morphology of hASCs encapsulated. Photographs of PL-CNC hydrogels after 3 hours and 7 days in culture (A). Hydrogels retraction in percentage at 1, 4 and 7 days (B). Fluorescence microscopy images showing cytoskeleton organization in the fibrin matrix after 1 day in culture (C). Fluorescence microscopy images showing cytoskeleton organization after 1 and 3 days in culture (D). Cell axial ratio and cell spreading area after 1 day of culture were quantified for all conditions (E) and cell axial ratio and cell spreading area after 1 and 3 day of culture were quantified for PL-CNC 0.61 (F). Staining fibrinogen (green), actin (red) and nuclei (blue). Statistical differences: $P<0.05$, * $P<0.05$ PL-CNC 0 vs PL -CNC (0.15-0.46). + $P<0.05$ PL-CNC 0.31 vs PL-CNC (0.61). & $P<0.05$ PL-CNC 0.46 vs PL-CNC 0.61. # $P<0.05$ between 1 and 3 days in culture. Scale bars: 4 mm (A); 10 μm (C); 50 μm (D).

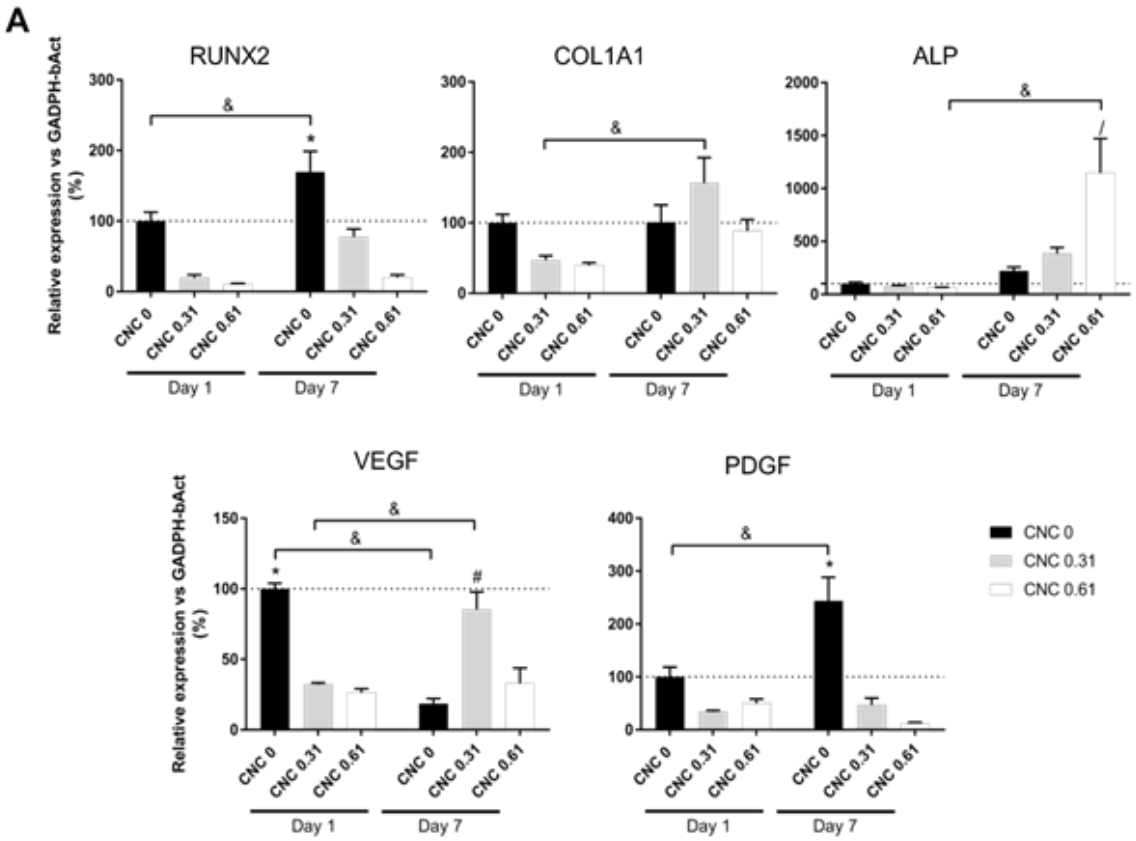

Figure IX-7 hASCs were assessed for the expression of chondrogenic (Sox-9 and COMP), osteogenic (Runx2, Cola1 and ALP), adipogenic (LPL) and angiogenic markers (PDGF and VEGF) on PL-CNC 0, 0.31 and 0.61 hydrogels (A). * P<0.05 PL-CNC 0 vs PL -CNC (0.31-0.46). # P<0.05 PL-CNC 0.31 vs PL-CNC 0. / P<0.05 PL-CNC 0.61 vs PL-CNC (0-0.31). & P<0.05 between 1 and 7 days in culture.

IX-1.5. Detailed description

The present disclosure comprises the use of CNC as multifunctional nanofillers in BD-based material that can act as 1) reinforcing nanofillers and crosslinkers of the protein matrix and as 2) sulfated glycosaminoglycan mimetic entities to reversibly sequester platelet-derived GFs and/or other soluble biomolecules in a three-dimensional (3D) microenvironment.

In an embodiment, the present disclosure enables the use of BD not only as growth factors cocktail but also as scaffolding biomaterial by crosslinking its protein content with oxidized CNC.

In an embodiment, platelet concentrates (PC) were obtained from different platelet collections produced by plasmapheresis. The platelet count was performed using the COULTER® LH 750 Hematology Analyzer and the sample volume adjusted to 1 million platelets. μL^{-1}.

In an embodiment, PC batches were subjected to three repeated temperature cycles (frozen with liquid nitrogen at −196°C and melt in a 37°C water bath), lysing the platelets and releasing their protein content. The lysate was then centrifuged at 4000 G for 5 min at 5°C and filtered through a 0.45 µm pore filter to reduce platelet membrane fragments. Aliquots of PL were stored at −80 °C until final use.

In an embodiment, CNC can be extracted from microcrystalline cellulose (MCC) powder, in particular from cotton, wood, or other suitable sources (following the typical sulfuric acid hydrolysis).

In an embodiment, 42 g of MCC were suspended in 189 ml of deionized water (DI) cooled in an ice bath using a mechanical agitator (500 rpm) during 10 minutes. Concentrated sulfuric acid (95%-97%, 188.3 mL) was added dropwise up to a final concentration of 64 wt.% under mechanical stirring. The reaction was performed under continuous stirring at 44 °C for 120 min, stopped by addition of 5 fold excess cold water and left to decant at 4 °C. The supernatant was discarded, and the remaining suspension was centrifuged three times for 10 min at 9000 rpm and 5 °C. The supernatant was successively replaced with DI water and the suspension subjected to centrifugation cycles until the supernatant became turbid. The resulting suspension was collected and extensively dialyzed against DI water until neutral pH. After dialysis the content was sonicated for 10 min using an ultrasound probe at 60% of amplitude output, under ice cooling to prevent overheating. The cloudy suspension was centrifuged one last time to remove big particulates and the final supernatant containing the CNC was stored at 4 °C until further use.

In an embodiment, oxidation was performed to convert CNC surface hydroxyls to carbonyls. The carbonyls are expected to induce covalent crosslinking between CNC and platelet-derived proteins.

In an embodiment, aldehyde functionalized CNC were produced by sodium periodate oxidation. In a preferred embodiment, sodium periodate is added to CNC aqueous suspension (1.5 wt.%) in a 1:1 molar ratio (sodium periodate /anhydroglucose equivalents). The mixture is allowed to stir at room temperature for 12 hours preventing from light exposure. Unreacted periodate was quenched by the addition of ethylene glycol. The mixture is transferred into a dialysis membrane and dialyzed against ultrapure water for 3 days with regular water replacement. The final suspension is then collected and stored at 4 °C until further use.

In an embodiment, CNC suspensions were submitted to a hydrothermal treatment process to reduce the surface sulfate content of the initial condition, Figure IX-1. An aqueous suspension of CNC (1 wt.%) was added to an autoclave. The autoclave was sealed and heated to 120°C and held at the desired temperature for different time periods (4h to 20h) in order to obtain different sulfation gradients. After

cooling the autoclave to room temperature, CNC suspension was collected and stored at room temperature in sealed glass vials until further characterization was performed.

In an embodiment, CNC suspension was further characterized by conductometric titration, based on Beck and co-workers method [1], where a certain sulfation degree is obtain 100 mmol. Kg^{-1} to 300 mmol. Kg^{-1} (mmol sulfate groups per 1 kg of cellulose).

In an embodiment, conductometric titration was determined. The carbonyl group content of the oxidized aldehyde CNC (a-CNCs) was determined by conductometric titration according to [2]. In a typical run, 3.6 mL of a-CNC aqueous suspension (1.39 wt. %, 0.050 g) and 0.025 g (0.62 mmol) of NaOH were dispersed in a final volume of 10 mL of ultra-pure water. 0.193 g of silver (I) oxide were added to the solution which was allowed to stir overnight and selectively oxidize the aldehyde groups to carboxylic acids. 5 mL of the oxidized reaction mixture were diluted with 80 mL of ultra-pure water and the pH was adjusted to c.a. 3.5 with HCl 1M. Finally, the solution was titrated using 0.01M NaOH. The total amount of carboxyl groups corresponding to the carbonyl content or degree of oxidation (DO) was calculated from:

$$DO = \frac{162C(V_2 - V_1)}{w - 36C(V_2 - V_1)}$$

Equation IX-1 Quantification of the degree of oxidation. Where C is the NaOH concentration (mol. L^{-1}), V_1 and V_2 are the amount of NaOH, and w (g) is the weight of a-CNC.

In an embodiment, CNC dimensions were analyzed by Atomic Force Microscopy (AFM). CNC produced were analyzed by AFM to determine the particles size distribution. Drops of the diluted CNC suspension (0.0015 wt. %) were deposited on freshly cleaved and carefully washed mica discs (9.9 mm diam. 0.27 thick). The suspension was left to adsorb for 15 minutes and the excess liquid was removed. The disc was allowed to dry overnight. The samples ware imaged in tapping mode with a MultiMode AFM connected to a NanoScope V controller, both from Veeco, USA, with non-contact silicon nanoprobes (c.a. 300 kHz) from Nanosensors (Switzerland). The particle size distribution was determined with Gwyddion software.

IX-1.5.1. Nanocomposite formulations

In an embodiment, nanocomposite formulation of the present disclosure, physiologically stable and mechanically reinforced BD loaded in CNC nanocomposites, can be produced by combining oxidized CNC suspensions with a different degree of sulfation with BD formulations.

In an embodiment, the aldehyde groups of oxidized CNC reversible react with amine groups of platelet-derived proteins through Schiff's base reaction and crosslink the protein matrix.

In a particular embodiment, thrombin and calcium may be used to maximize the crosslinking of platelet-derived proteins (fibrinogen) and to allow for the production of injectable nanocomposite materials that can crosslink in situ at physiological conditions.

Table IX-1 Components concentration in the final formulation

Values	a-CNC % w/v	Thrombin U. mL^{-1}	Calcium mM	Blood Derivatives Platelets.μL^{-1}	Sulfation degree of a-CNC mmol. Kg^{-1}
Minimum	0.05	0.1	0.1	$0.5x10^{4}$	50
Studied	0.15 - 0.61	1	5	$1x10^{6}$	100 - 300
Maximum	2	50	25	$2x10^{8}$	500

IX-1.5.1.1 *Example 1*

In an embodiment, sponges were prepared at room temperature using a double-barrel syringe fitted with a static mixer to ensure an effective mixing of the nanocomposite components.

Barrel A was filled with PL and barrel B with oxidized CNC presenting a certain sulfation degree (100 mmol. Kg^{-1} to 300 mmol. Kg^{-1}).

Aqueous suspensions of CNC with varying concentrations of 0% w/v (PL-CNC 0), 0.15 % w/v (PL-CNC 0.15), 0.31 % w/v (PL-CNC 0.31), 0.45 % w/v (PL-CNC 0.45), and 0.61 % w/v (PL-CNC 0.61) in 50% PL composition.

The PL/CNC mixtures were frozen and freeze-dried to produce PL/CNC nanocomposite sponges.

PL/CNC nanocomposite sponges were prepared in cylindrical acrylic molds of 9 mm diameter and 5 mm height. Alternatively, the PL/CNC mixtures may be poured into any form or mold having the desired final material shape.

In an embodiment, CNC incorporation lead to an improvement of PL stability (Figure IX-4) and hydrogels with higher CNC content showed lower degradation rate.

In an embodiment, CNC incorporation leads to a more organized microstructure with smaller pores.

In an embodiment, the porosity (vol.%) increases from 64.6 to 75.1 with increasing of CNC content. Increasing CNC content significantly improved the mechanical properties (compression modulus and strength) of PL/CNC spongy hydrogels.

Fast recover of initial shape upon unloading demonstrate the high elastic nature of PL/CNC spongy hydrogels.

PL/CNC conditions demonstrated cellular viability after 9 days in culture.

IX-1.5.1.2 *Example 2*

In an embodiment, sponges were prepared at room temperature using a double-barrel syringe fitted with a static mixer to ensure an effective mixing of the nanocomposite components.

Barrel A was filled with PL and barrel B with oxidized CNC presenting a certain sulfation degree (100 mmol. Kg-1 to 300 mmol. Kg-1), calcium, and thrombin.

Aqueous suspensions of CNC with varying concentrations of 0% w/v (PL-CNC 0), 0.15 % w/v (PL-CNC 0.15), 0.31 % w/v (PL-CNC 0.31), 0.45 % w/v (PL-CNC 0.45), and 0.61 % w/v (PL-CNC 0.61) in 50% PL composition.

The precursor solutions were then hand extruded into cylindrical acrylic molds of 9 mm diameter and 5 mm height and incubated at 37 °C for a certain period of time to allow fibrin fibrillation to proceed. Alternatively, the PL/CNC mixtures may be poured into any form or mold having the desired final material shape.

The PL/CNC mixtures were frozen and freeze-dried to produce crosslinked PL/CNC nanocomposite sponges.

IX-1.5.1.3 *Example 3*

In an embodiment, hydrogels were prepared at room temperature using a Double-barrel syringe (1:1) with a mixer tip was used to produce this system (L-System, Medmix, Switzerland). promoting the in situ PL-clotting via thrombin and calcium activation along with the CNC/protein covalent crosslinking.

Barrel A was filled with PL (67.6 mg. mL^{-1} of total protein) composed of albumin, growth factors, cytokines and structural proteins (such as fibrinogen, vitronectin and fibronectin) [3, 4].

Barrel B was composed of thrombin (2 U. mL^{-1}), calcium (10 mM) and a-CNC water dispersions presenting a certain sulfation degree (100 mmol. Kg-1 to 300 mmol. Kg^{-1}).

Aqueous suspensions of CNC with varying concentrations of 0% w/v (PL-CNC 0), 0.15 % w/v (PL-CNC 0.15), 0.31 % w/v (PL-CNC 0.31), 0.45 % w/v (PL-CNC 0.45), and 0.61 % w/v (PL-CNC 0.61) in 50% PL composition.

The precursor solutions were then hand extruded into cylindrical acrylic molds of 9 mm diameter and 5 mm height and incubated at 37 °C for a certain period of time to allow fibrin fibrillation to proceed. Alternatively, the PL/CNC mixtures may be poured into any form or mold having the desired final material shape or be injectable extruded in the tissue injury defect.

In an embodiment, the gelation, microstructural, mechanical, swelling, degradation and protein release profiles of the hydrogels were fully characterized.

In optimized conditions for PL gelation (1 U. mL^{-1} thrombin and 5 mM $CaCl_2$), incorporation of up to 0.61 % w/v CNC considerably improved the microstructural organization, stability and degradation rate of the hydrogels. Moreover, the proposed strategy did not hinder a fast gelation process while markedly increased the hydrogels mechanical properties up to an impressive 2 orders of magnitude higher storage modulus compared to control (maximum G' of 1.2 kPa) and improved their ability to sequester native PL bioactive factors.

In an embodiment, at nanoscale dimensions using AFM measurements, CNC incorporation leads to higher young's modulus in PL-CNC hydrogels. In PL-CNC 0 formulation was 2.2 kPa being very similar of the values obtained along the fibers (1.3 kPa). The increased bundle thickness and sample heterogeneity in PL-CNC 0.46-0.61 was correlated with higher fiber rigidity. Differences between gel and fiber rigidity are higher when higher CNC concentration are obtained, which indicates the incorporation of CNC along the fibers. Cell-scale measurements, as well as, bulk rheological properties, showed increased stiffness

for higher CNC loading. As expected, mechanical properties can be modulated by tailoring CNC concentration and network densities.

In an embodiment, PL-CNC 0 hydrogels rapidly degraded over this time in comparison of PL-CNC (0.15-0.61) formulations. To examine the ability to sequester native PL bioactive factors from degradation within PL-CNC hydrogels, total protein released was quantified. The hydrogels were incubated in PBS and each day fresh PBS was replaced. After 6 days in PBS, PL-CNC 0 matrix was almost completely degraded. In contrast, in PL-CNC 0.61 around 61% of the protein hydrogel is maintained over 7 days. Altogether these data indicate that different matrix architectures and composition can influence the interactions and released of PL bioactive molecules from within the hydrogel.

In an embodiment, concerning proliferative capacities of the PL-CNC hydrogels, it is visible that improving structure stability leads to higher number of cells encapsulated over time (Figure IX-5). After 7 days in culture, metabolic activity normalized with DNA content showed that CNC incorporation improves cell activity.

In an embodiment, upon hASCs encapsulation, PL hydrogel has a manifold densification of the fibrin network referred to as clot retraction. PL-CNC 0 exert a modest contractile effect that results in 75% reduction in total diameter (Figure IX-6).

In an embodiment, concerning chondrogenic differentiation, it was studied sex-determining region Y-box 9 protein (SOX-9), as a key transcription factor in early chondrogenesis and cartilage oligomeric matrix protein (COMP), which is one of the major matrix molecules in articular cartilage (Figure IX-7). In order to study osteogenic potential, human adipose derived-stem cells (hASCs) were examined for the expression of gene expression during early phases, runt-related transcription factor 2 (RUNX2), collagen Type I Alpha 1 Chain (COL1A1) and alkaline phosphatase (ALP). Specifically, RUNX2 is crucial for the generation of a mineralized tissue, COL1A1 is the main constituent of the bone organic part of the extracellular matrix (ECM) and ALP is responsible for the mineralization of the ECM [5]. In vitro osteogenic differentiation can also be predicted by the ratio between RUNX2 and SOX-9, since SOX9 directly interacts with Runx2 and represses its activity [6]. The increased expression of osteogenic markers (ALP and COL1A1), downregulation of chondrogenic-related markers (SOX9 and COMP) RUNX2/ SOX-9 ratios showed significant higher values on Day 7 compared on Day 1 in PL-CNC incorporated CNC suggested that presence of CNC tend to differentiate hASCs in osteogenic lineage which is in agreement within the established paradigm of stiffness-directed stem cells differentiation [7].

In an embodiment, the disclosure platform allows therefore using PL as stable injectable formulations for either the delivery of biological factors as well as a cell carrier matrix. Overall, this platform open new avenues to explore PL based hydrogels in TE applications, enabling a controlled modulation of the physical and chemical cellular microenvironments in in vitro settings, as well as upon in vivo injection. Their 3D in vitro biological performance was assessed using encapsulated hASCs. Hydrogels formulations showed cell supportive properties, such as viability, metabolic activity, and proliferation rate.

In an embodiment, the materials of the present disclosure rely on the production of structures composed of PL reinforced with varying contents of aldehyde-modified CNC and a certain sulfation degree. Aldehyde-modified CNC baring surface aldehyde groups reversibly react with terminal amine groups of proteins, which improve the spongy hydrogel structural integrity and mechanical properties. The present disclosure discloses the feasibility of incorporating modified CNCs into PL-based scaffolds and shown its structural and biological performance.

In an embodiment, the hydrogel produced using this method may be used as an injectable biomaterial able to crosslink in physiological conditions.

In an embodiment, the injectable PL/CNC may be applied as a cell carrier or as an acellular material in medical applications.

The term "comprising" whenever used in this document is intended to indicate the presence of stated features, integers, steps, components, but not to preclude the presence or addition of one or more other features, integers, steps, components or groups thereof.

Where singular forms of elements or features are used in the specification of the claims, the plural form is also included, and vice versa, if not specifically excluded. For example, the term “a cell” or “the cell” also includes the plural forms “cells” or “the cells,” and vice versa. In the claims articles such as “a,” “an,” and “the” may mean one or more than one unless indicated to the contrary or otherwise evident from the context. Claims or descriptions that include “or” between one or more members of a group are considered satisfied if one, more than one, or all of the group members are present in, employed in, or otherwise relevant to a given product or process unless indicated to the contrary or otherwise evident from the context. The invention includes embodiments in which exactly one member of the group is present in, employed in, or otherwise relevant to a given product or process. The invention also includes embodiments in which more than one, or all of the group members are present in, employed in, or otherwise relevant to a given product or process.

Furthermore, it is to be understood that the invention encompasses all variations, combinations, and permutations in which one or more limitations, elements, clauses, descriptive terms, etc., from one or more of the claims or from relevant portions of the description is introduced into another claim. For example, any claim that is dependent on another claim can be modified to include one or more limitations found in any other claim that is dependent on the same base claim.

Furthermore, where the claims recite a composition, it is to be understood that methods of using the composition for any of the purposes disclosed herein are included, and methods of making the composition according to any of the methods of making disclosed herein or other methods known in the art are included, unless otherwise indicated or unless it would be evident to one of ordinary skill in the art that a contradiction or inconsistency would arise.

Where ranges are given, endpoints are included. Furthermore, it is to be understood that unless otherwise indicated or otherwise evident from the context and/or the understanding of one of ordinary skill in the art, values that are expressed as ranges can assume any specific value within the stated ranges in different embodiments of the invention, to the tenth of the unit of the lower limit of the range, unless the context clearly dictates otherwise. It is also to be understood that unless otherwise indicated or otherwise evident from the context and/or the understanding of one of ordinary skill in the art, values expressed as ranges can assume any subrange within the given range, wherein the endpoints of the subrange are expressed to the same degree of accuracy as the tenth of the unit of the lower limit of the range.

The disclosure should not be seen in any way restricted to the embodiments described and a person with ordinary skill in the art will foresee many possibilities to modifications thereof.

The above described embodiments are combinable.

The following claims further set out particular embodiments of the disclosure.

IX-2. CLAIMS

1. A composition comprising:

   a blood derivative component;

   a cellulose nanocrystal as a filler comprising carbonyls at the cellulose nanocrystal surface,

   wherein such cellulose nanocrystal comprises a sulfation degree of at least 50 mmol. Kg^{-1}.

2. The composition according to the previous claim wherein the sulfation degree is between 80 and 500 mmolKg-1; more preferably between 120 and 300 mmol. Kg^{-1}.

3. The composition according to any one of the previous claims wherein the blood derivative component is platelet-rich plasma, platelet cellular component, platelet lysate and/or platelet released content.

4. The composition according to any one of the previous claims comprising 0.05 - 2% w/v of cellulose nanocrystal, preferably 0.1 - 1 % w/v, more preferably 0.15 - 0.61 % w/v.

5. The composition according to any one of the previous claims comprising $0.5x10^{4}$ platelets. μL^{-1} - $2x10^{8}$ platelets. μL^{-1} of blood derivative platelet concentration, preferably $1x10^{5}$ - $1x10^{7}$ platelets. μL^{-1}, more preferably $1x10^{6}$ - $5x10^{6}$ platelets. μL^{-1}.

6. The composition according to the previous claims further comprising thrombin, calcium, calcium salts, or mixtures thereof.

7. The composition according to the previous claim comprising 0.1 U. mL^{-1} -50 U. mL^{-1} of thrombin preferably 0.5 U. mL^{-1} - 5 U. mL^{-1}, more preferably 1 U. mL^{-1} - 3 U. mL^{-1}.

8. The composition according to any one of the previous claims comprising 0.1mM-25mM of calcium or calcium derivate, preferably 0.5 mM-10 mM, more preferably 1mM-5mM.

9. The composition according to any one of the previous claims comprising an amount of carbonyl groups at the surface of the cellulose nanocrystals between 0.01 - 8 $mmol.g^{-1}$; preferably 0.1 - 4 mmol. g^{-1}; more preferably 0.4 - 0.9 mmol. g^{-1}.

10. The composition according to any one of the previous claims further comprising one or more active ingredients or biomolecules.

11. The composition according to any one of the previous claims wherein such active ingredient or biomolecule is: a drug; an active ingredient, a growth hormone, a cell attractant, a drug molecule, a cell, a bioactive glass, a tissue growth promoter, a cell attractant, or combinations thereof.

12. The composition according to any one of the previous claims wherein the drug molecule is an anti-inflammatory, antipyretic, analgesic, anticancer agent, or mixtures thereof.

13. The composition according to any one of the previous claims wherein cells are selected from: osteoblasts, osteoclasts, osteocytes, pericytes, endothelial cells, endothelial progenitor cells, bone progenitor cells, hematopoietic progenitor cells, hematopoietic stem cells, neural progenitor

cells, neural stem cells, mesenchymal stromal/stem cells, induced pluripotent stem cells, embryonic stem cells, or combinations thereof.

14. The composition according to any one of the previous claims further comprising one or more pharmaceutically acceptable excipients.
15. The composition according to any one of the previous claims wherein such pharmaceutically acceptable excipient is: an additive, a binder, a disintegrant, a diluent, a lubricant, a plasticizer, or mixtures thereof.
16. The composition according to any one of the previous claim wherein the average length of the cellulose nanocrystal is between 40 - 2500 nm, preferably 100 - 500 nm, more preferably 200 - 300 nm.
17. The composition according to any one of the previous claims wherein the average width of the cellulose nanocrystal is between 3 - 50 nm; preferably 3 - 30 nm.
18. The composition according to any one of the previous claims wherein the blood derivative component is obtainable by centrifugation or by apheresis.
19. The composition according to any one of the previous claims for use in medicine, veterinary or cosmetic.
20. The composition according to any one of the previous claims for use in tissue engineering, tissue regeneration, regenerative medicine, or in cellular therapy.
21. The composition according to any one of the previous claims for the use in the treatment or therapy of wound healing or a tissue injury defect.
22. The composition according to any one of the previous claims for the use in the treatment or therapy of defects of skin wound, orthopedic injury, pain, nerve disease, dental injury, bone injury, or diabetic wound healing.
23. The composition according to any one of the previous claims, wherein the composition is an injectable formulation.
24. A hydrogel comprising the composition described in any of the previous claims comprising a blood derivative component, oxidized cellulose nanocrystals of a certain sulfation degree, thrombin and/or calcium through chemical crosslinking.

25. The hydrogel according to any one of the previous claims wherein the cells are encapsulated or seeded.

26. The hydrogel according to the previous claim wherein the hydrogel is an in situ crosslinked injectable hydrogel at physiological conditions.

27. The hydrogel according to any one of the previous claim wherein the hydrogel is casted to the desired mold shape or be in situ injectable extruded.

28. A sponge or scaffold comprising the composition described in any of the previous claims comprising a blood derivative component reinforced with oxidized cellulose nanocrystals of a certain sulfation degree.

29. The sponge or scaffold according to the previous claim further comprising a cell, oxidize cellulose nanocrystals, thrombin and/or calcium through chemical crosslinking.

30. The sponge or scaffold according to any one of the previous claim wherein the sponge is casted to the desired mold shape.

31. The sponge or scaffold according to any one of the previous claims wherein the cells are encapsulated or seeded.

32. A method for the preparation of the composition described in any of the previous claims, comprising the following steps:

obtaining oxidized cellulose nanocrystals comprising a sulfation degree of at least 50 mmol. Kg^{-1}, preferably the sulfation degree is obtained by a hydrothermal treatment of the oxidized cellulose nanocrystal;

mixing a blood derivative component with the oxidized cellulose nanocrystal.

33. The method according to the previous claim further comprising the addition of calcium and/or thrombin to the mixture.

34. The method according to any one of the previous claims wherein the blood derivative component is platelet-rich plasma, platelet cellular component, platelet lysate and/or platelet released content.

IX-3. REFERENCES

The following references should be considered here with incorporated in their entirety:

[1] S. Beck, M. Méthot and J. Bouchard, General procedure for determining cellulose nanocrystal sulfate half-ester content by conductometric titration, Cellulose, 22 (2015) 101.

[2] R.M.A. Domingues, M. Silva, P. Gershovich, et al., Development of Injectable Hyaluronic Acid/Cellulose Nanocrystals Bionanocomposite Hydrogels for Tissue Engineering Applications, Bioconjugate Chem., 26 (2015) 1571.

[3] N. Fekete, M. Gadelorge, D. Furst, et al., Platelet lysate from whole blood-derived pooled platelet concentrates and apheresis-derived platelet concentrates for the isolation and expansion of human bone marrow mesenchymal stromal cells: production process, content and identification of active components, Cytotherapy, 14 (2012) 540.

[4] R. Crespo-Diaz, A. Behfar, G.W. Butler, et al., Platelet lysate consisting of a natural repair proteome supports human mesenchymal stem cell proliferation and chromosomal stability, Cell Transplant., 20 (2011) 797.

[5] C. Granéli, A. Thorfve, U. Ruetschi, et al., Novel markers of osteogenic and adipogenic differentiation of human bone marrow stromal cells identified using a quantitative proteomics approach, Stem Cell Res., 12 (2014) 153.

[6] C. Loebel 1, E. M Czekanska, M. Bruderer, et al., In vitro osteogenic potential of human mesenchymal stem cells is predicted by Runx2/Sox9 ratio, Tissue Eng. Part A, 21 (2014) 115.

[7] D. E. Discher, D. J. Mooney and P.W. Zandstra, Growth factors, matrices, and forces combine and control stem cells. Science, 324 (2009) 1673.

[8] X. Zhang, E. E. Brown. Nanocrystalline cellulose materials and methods for their preparation. WO2014077854A1.

[9] P. D. Martiner, M. Stanton, A. Kazantsev, et al., Biomaterials for delivery of blood extracts and methods of using same. WO2013116791A1.